

**AN EFFICIENT VIRTUAL TESTING FRAMEWORK TO SIMULATE THE
PROGRESSION OF DAMAGE IN NOTCHED COMPOSITE LAMINATES**

by

Mina Shahbazi

B.Sc., Isfahan University of Technology, 2008

M.Sc., Isfahan University of Technology, 2010

A THESIS SUBMITTED IN PARTIAL FULFILLMENT OF
THE REQUIREMENTS FOR THE DEGREE OF

DOCTOR OF PHILOSOPHY

in

THE FACULTY OF GRADUATE AND POSTDOCTORAL STUDIES
(Civil Engineering)

THE UNIVERSITY OF BRITISH COLUMBIA

(Vancouver)

August 2017

© Mina Shahbazi, 2017

Abstract

The progression of damage in composite laminates is influenced by the interactions of several failure/damage mechanisms including matrix cracking, fibre breakage, splitting and delamination. In capturing detailed prediction of various damage modes, it is important to maintain the efficiency of the computational models so that they can be readily used by engineers for damage tolerant design of composite components. Continuum damage models are commonly employed to simulate the smeared response of certain failure modes such as matrix cracking and fibre failure due to their higher numerical efficiency in comparison with discrete damage models. However, application of continuum damage based models for accurate prediction of the onset and propagation of macro-discrete damage modes (i.e. splitting and delamination) and their interactions with other failure modes is limited.

This work presents an efficient methodology to capture the interacting effect of discrete and smeared cracks based on a combination of the continuum and discrete approaches. Here, delamination is the only damage mode captured by a discrete approach (cohesive zone interface), while all intra-laminar forms of damage including splitting are modelled using the non-local composite damage model (CODAM2) in a mesoscopic context. Through placement of discrete delamination interfaces and synchronizing the onsets of delamination and matrix cracks, the computational effort is markedly reduced. The effect of ply thickness and constraints imposed by neighbouring plies on initiation of intra-laminar matrix damage modes is also considered. A novel methodology involving a combination of physical and virtual tests on notched laminates is proposed to calibrate the in-situ fracture energies of intra-laminar damage modes.

The numerical simulations are conducted using an enhanced version of CODAM2, implemented in the explicit finite element software, LS-DYNA, as a user-defined model (UMAT), together with a built-in tie-break cohesive interface in LS-DYNA to model delamination. The proposed approach is validated using various layups and notched specimen geometries under tensile loading. The reasonable agreement of the predictions with experiments in terms of global behaviour and detailed damage patterns proves the efficiency and applicability of the presented methodology for damage tolerant assessment of composite laminates.

Lay Summary

The industrial application of composite materials has experienced rapid growth in the last few decades. Starting in the late 1970's application of composites expanded widely including aircraft and aerospace structures, automotive components, sporting goods and underground pipes. The progression of damage in composite laminates under mechanical loads is influenced by the interactions of several damage mechanisms. This work presents an efficient numerical tool to predict the evolution of damage in composite materials and provide details of damage pattern progressing at level of the constituent plies and interfaces of the composite laminate. The methodology established in this research provides an engineering approach to model the response of composite laminates to loads that cause significant damage. The model parameters come from a set of standard tests as well as a few specialized tests that in a novel way are combined with numerical analysis to extract the required input to the model.

Preface

This thesis entitled "An Efficient Virtual Testing Framework to Simulate the Progression of Damage in Notched Composite Laminates" presents the research conducted by Mina Shahbazi. The research was supervised by Dr. Reza Vaziri at the University of British Columbia.

Some of the contents of Chapter 2 are published as a book chapter entitled "An Overview of Continuum Damage Models used to Simulate Intra-laminar Failure Mechanisms in Advanced Composite Materials", Chapter 6 in "Numerical Modelling of Failure in Advanced Composite Materials", Editors: Hallet S.R. and Camanho P.P., Woodhead Publishing, 2015, pp. 151-173 [73]. The chapter was co-authored by Dr. Alireza Forghani, and reviewed/revised by Dr. Navid Zobeiry, Professor Reza Vaziri and Professor Anoush Poursartip.

A version of the contents of Chapter 3, Chapter 4, and Chapter 5 is included in a paper entitled "An Engineering Approach to Numerical Simulation of Damage Progression in Tensile Loading of Notched Composite Laminates" that is going to be submitted as a journal article. These sections include the proposed methodology and formulations, the calibration and validation of the method using over-height compact tension (OCT) test configurations. The paper is reviewed by Professor Reza Vaziri and Dr. Navid Zobeiry.

Some of the contents of Chapter 6 on simulation of OCT quasi-isotropic laminates were presented and published in a paper entitled "An Efficient Virtual Testing Framework to Simulate the Interacting Effect of Intra-laminar and Inter-laminar Damage Progression in Composite Laminates" at the 31st Technical Conference of American Society for Composites (ASC-31st), Virginia, USA, September 2016 [219]. This paper was reviewed by Professor Reza Vaziri, Dr. Navid Zobeiry and Dr. Alireza Forghani.

Some of the contents of Chapter 6 is included in a paper entitled "Simulation of the Open-hole Tensile Response of Composite Laminates using a Combined Discrete and Continuum Damage Approach" that is under preparation for submission as a journal article. These sections include

the validation of the proposed methodology for progression of damage in open-hole tensile (OHT) test configurations.

Parts of the contents of Chapter 6 on simulation of OHT test for quasi-isotropic laminates were accepted for presentation and publication in a paper entitled "Simulation of Open-Hole Tension Tests on Composite Laminates using Combined Discrete and Continuum Damage Approach", at the 10th Canadian-International Conference on Composites (CANCOM-2017), to be held in Ottawa, Canada, July 2017.

Some parts of Chapter 6 on the size effect problem in simulation of OHT specimens are also accepted for a conference paper entitled "Simulation of Open-Hole Tension Tests on Composite Laminates using Combined Discrete and Continuum Damage Approach" for the 21st International Conference on Composite Material (ICCM-21st) to be held in Xian, China, August 2017.

The experimental tests that are used for calibration and validation purposes in Chapter 5 are selected from the work by Li et al. [154]. The test panels for these specimens were provided by the University of Bristol. The tests were conducted by Xiaodong Li at the University of British Columbia (UBC) to study the progressive damage behaviour of different layups. Later, C-scans were conducted by Navid Zobeiry at UBC for further observation of delamination zones in a few post-mortem specimens. The results of these C-scans are used in Figure 5.3, Figure 6.4 and Figure 6.7. The experimental test results that are used in Chapter 6 for validation purpose are adopted from the work by Green et al. [82] at the University of Bristol.

Table of Contents

Abstract	ii
Lay Summary	iii
Preface	iv
Table of Contents	vi
List of Tables	x
List of Figures	xii
List of Symbols	xvii
List of Abbreviations	xx
Acknowledgements	xxi
Chapter 1: Introduction	1
1.1 Objectives.....	6
1.2 Outline.....	7
Chapter 2: Literature Review	9
2.1 Introduction	9
2.2 Initiation of failure mechanisms	13
2.2.1 Fibre failure	15
2.2.2 Matrix failure.....	16
2.2.3 Delamination	20
2.3 Progression of damage	22
2.3.1 Continuum approach.....	23
2.3.1.1 Ply discount methods	23
2.3.1.2 Continuum damage-based methods	25
2.3.2 Discontinuous approach.....	29
2.3.2.1 Interface elements/surfaces.....	32
2.3.2.2 Partition of unity finite element method.....	33
2.4 Status of numerical methods in composite structural design	35
2.4.1 World-Wide Failure Exercise (WWFE)	37
2.4.2 Composite Materials Handbook (CMH-17): Crashworthiness Section.....	39
2.4.3 Damage tolerance design principles (DTDP) program.....	40

2.5	Summary	41
Chapter 3: Intra-laminar Damage Modelling.....		49
3.1	Introduction	49
3.2	UBC composite damage Model- CODAM2	52
3.2.1	Formulation	52
3.2.2	Non-local averaging.....	58
3.2.2.1	Orthotropic non-local averaging.....	59
3.2.2.2	Isotropic non-local averaging	60
3.2.3	Limitations of the fully continuum damage modelling approach	62
3.2.4	Damage characterization and model calibration at the sub-laminate (macro) level..	63
3.3	Enhanced CODAM2 material model.....	67
3.3.1	Intra-laminar damage	68
3.3.1.1	Damage initiation.....	70
3.3.1.2	Damage saturation.....	72
3.3.2	Effect of ply thickness and constraints on matrix crack initiation	74
3.3.2.1	Shear-lag theory	74
3.3.2.2	Estimation of in-situ strength properties	77
3.3.3	In-plane shear behaviour	80
3.3.4	Stiffness matrix in damaged state.....	82
3.4	Summary	85
Chapter 4: Inter-laminar Delamination Modelling		87
4.1	Introduction	87
4.2	Cohesive zone model.....	92
4.2.1	Cohesive element size requirement	96
4.3	Summary.....	100
Chapter 5: Model Calibration		101
5.1	Inter-laminar model parameters	101
5.1.1	Inter-laminar damage initiation- numerical calibration	101
5.1.2	Inter-laminar damage progression- Experimental calibration.....	103
5.2	Intra-laminar model parameters	104
5.2.1	Intra-laminar damage initiation- Experimental calibration.....	104

5.2.2	Intra-laminar damage progression- Review of existing experimental methods.....	105
5.2.2.1	Intra-laminar fibre fracture energy.....	105
5.2.2.2	Intra-laminar matrix fracture energy.....	107
5.2.3	Intra-laminar damage progression- Numerical calibration	110
5.2.3.1	Calibration of intra-laminar fracture energies for IM7/8552 CFRP	111
5.2.3.1.1	Numerical model setup for OCT simulation.....	113
5.2.3.1.2	OCT simulation of blocked cross-ply laminates $[90_4/0_4]_{2s}$	115
5.2.3.1.3	OCT simulation of dispersed cross-ply laminates $[0/90]_{8s}$	121
5.3	Summary.....	125
Chapter 6: Model Validation.....		128
6.1	OCT tests on quasi-isotropic laminates	128
6.1.1	Simulation results and discussions	129
6.2	Open-hole tensile (OHT) tests on quasi-isotropic laminates	137
6.2.1	Test setup.....	139
6.2.2	Model setup.....	141
6.2.3	Simulation results	142
6.2.3.1	Ply-thickness size-effect.....	145
6.2.3.2	In-plane size effect	154
6.3	Summary.....	157
Chapter 7: Conclusions and Future Work.....		159
7.1	Conclusions	159
7.2	Contributions	163
7.3	Future works.....	163
Bibliography.....		165
Appendices		187
Appendix A - Derivation of IDEFs in shear lag theory		187
Appendix B - Correlation of intra-laminar fracture energy with input fracture energy density and non-local radius		192
Appendix C - General introduction to user defined features in LS-DYNA		197
C.1	User material subroutines.....	198
C.2	Load curves in user material subroutines.....	200

Appendix D - Material card for the enhanced CODAM2 user material model.....	203
Appendix E - Post-processing a user-defined material	208
Appendix F - Pseudo-code	211

List of Tables

Table 2-1: Fibre failure criteria in tension.....	15
Table 2-2: Fibre failure criteria in compression	15
Table 2-3: Matrix failure criteria in tension	18
Table 2-4: Matrix failure criteria in compression.....	19
Table 2-5: Failure criteria for delamination	22
Table 2-6: Ply discount models used in literature [101]	24
Table 2-7: Criteria for growth of delamination	32
Table 2-8: An overview of the ongoing research on simulation of damage in composites at various research institutes and finite element vendors around the world including sample articles/references and model scales as well as their capabilities and applications, extended from [73].....	43
Table 3-1: Damage initiation criteria based on Hashin’s failure theory [94,95].....	71
Table 4-1: Estimated cohesive zone length (l_{cz}) and equivalent value for M in Equation (4.14).....	97
Table 5-1:A summary of experimental studies on measurement of intra-laminar matrix fracture energy for various material systems in unidirectional laminates.....	109
Table 5-2: Elastic and damage material parameter (tensile) for plies for $[90_4/0_4]_{2s}$ and $[90/0]_{8s}$ OCT laminates in meso-modelling approach	115
Table 6-1: Inter-laminar damage material parameters for $[45_4/90_4/-45_4/0_4]_s$ and $[45/90/-45/0]_{2s}$ laminates in the combined damage modelling approach for OCT specimens	129
Table 6-2: Calibrated damage material parameters for $[45/90/-45/0]_{2s}$ laminate using the original sub-laminate based (macroscopic) CODAM2 [289]	136
Table 6-3: Experimental gross average failure stresses for laminates (MPa)(cv,%), reference [82]	141
Table 6-4: Damage material parameters for $[45_m/90_m/-45_m/0_m]_{ns}$ laminates in the combined damage modelling approach for OHT specimens.....	143
Table 6-5: Finite element predicted gross average failure stresses for $[45_m/90_m/-45_m/0_m]_{ns}$ laminates (MPa)(difference with average experimental results,%).....	143

Table B-1: The material properties of IM7/8552 carbon-epoxy unidirectional lamina [121].....	185
Table B-2: The predicted fracture energy from the simulations of a unidirectional 90° OCT laminate with different non-local radii and element sizes. The effective length scale and its ratio to r are also presented.	193
Table B-3: The predicted fibre fracture energy from the simulations of a unidirectional 0° OCT laminate for a given input fracture energy density of 230 N/mm ² , different non-local radii and element sizes. The effective length scale and its ratio to r are also presented.....	195
Table D-1: *MAT_USER_DEFINED_MATERIAL_MODELS_CODAM2.....	194
Table D-2: Definition of material constants in the enhanced user material model of CODAM2.....	203
Table E-1: History variables for the enhanced CODAM2 model	208

List of Figures

Figure 1.1: A schematic of different damage modes	2
Figure 2.1: The three scales of damage analysis in composite laminates	11
Figure 2.2: Delamination induced by inter-laminar stresses at zones highlighted by dotted circles, adapted from [206].....	21
Figure 2.3: Fracture process zone in cohesive crack models- adapted from [176]	31
Figure 2.4: Application of continuum and lumped interface elements in a discontinuous approach, adapted from [274].....	32
Figure 2.5: Building Block pyramid	36
Figure 3.1: (a) Schematic of an RVE for a cross-ply laminate at three stages: (1) before the damage starts (2) formation of microcracks mainly in the matrix and fibre (3) microcracks merge and form a through crack in the laminate. (b) schematic nominal stress vs. nominal strain behaviour of the RVE under applied deformation, adapted from [267]	50
Figure 3.2: (a) A four-layer quasi-isotropic sub-laminate subjected to uniaxial tensile strain and its typical stress-strain response, (b) the typical stress-strain response of individual layers in both the fibre direction and transverse to the fibre direction	53
Figure 3.3: (a) The stiffness reduction factor vs damage, (b) Damage parameter vs equivalent strain parameter.....	56
Figure 3.4: The averaging zone in non-local approach for (a) orthotropic averaging method and (b) for isotropic averaging method	60
Figure 3.5: Distribution of non-local averaging weight function in x-direction (parallel with notch direction in an OCT configuration) calculated from Equations and (3.12) and (3.14) over a circular averaging domain	61
Figure 3.6: A symmetric laminate with transverse cracks in the mid-ply constrained by adjacent plies	75
Figure 3.7: Schematic in-plane nonlinear shear behaviour	81
Figure 3.8: In-plane nonlinear shear behaviour and the contribution of elastic shear strain to fracture energy	82
Figure 4.1: Inter-laminar stresses in a ply of a symmetric balanced laminate under axial loading, adapted from [111].....	88

Figure 4.2: Effect of ply thickness on the onset of delamination onset strain, adapted from [186]	89
Figure 4.3: Inter-laminar stresses due to matrix cracks in off-axis plies	90
Figure 4.4: Mixed-mode traction separation law, adapted from [158]	92
Figure 5.1: Exploded through-thickness view of the region close to the notch tip of OCT specimen showing contact interface between adjacent dissimilar plies modelled using 3D solid or thick shell elements. The averaged interface shear and normal stresses, t_{avg}^S and t_{avg}^N , inside a zone of 'n' elements close to the notch tip will be extracted from an elastic (undamaged) tied contact interface. At a time step when intra-laminar matrix damage in adjacent plies initiates (i.e. $\omega_2 > 0$ in L^k or L^{k+1}), the averaged normal and shear stresses are used as the calibrated maximum inter-laminar stresses, t_{max}^S and t_{max}^N , for the cohesive-based contact interface.	103
Figure 5.2: Experimentally obtained force vs. pin-opening displacement (POD) curves for both dispersed $[0/90]_{8s}$ and blocked $[0_4/90_4]_{2s}$ cross-ply laminates in OCT specimens [154]	112
Figure 5.3: C-Scan results showing the delaminated zone in OCT specimens of (a) blocked-ply $[0_4/90_4]_{2s}$ laminate, and (b) dispersed-ply $[0/90]_{8s}$ laminate [154]	112
Figure 5.4: (a) OCT specimen geometry and (b) the FE mesh	114
Figure 5.5: Comparison of the experimental and predicted force-displacement curves for $[0_4/90_4]_{2s}$ laminate with different values of matrix fracture energy and fibre fracture energy of 150 kJ/m^2 [154]	118
Figure 5.6: Predicted damage patterns for each ply of the $[0_4/90_4]_{2s}$ OCT laminate with $G_2^f = 2.6 \text{ kJ/m}^2$ at $\text{POD} = 4.8 \text{ mm}$, (a) matrix damage in 0^0 layer, (b) fibre damage in 0^0 layer, (c) matrix damage in 90^0 layer and (d) fibre damage in 90^0 layer	118
Figure 5.7: Comparison of (a) the predicted delamination zone at $0^0/90^0$ interface of the $[0_4/90_4]_{2s}$ OCT laminate at $\text{POD} = 5 \text{ mm}$ with (b) the final measured delamination zone from the C-scan results	119
Figure 5.8: Comparison of the predicted split length over half of the specimen height from the notch to the upper boundary in the 0^0 ply for intra-laminar matrix fracture energy values ranging from 0.65 to 6.5 kJ/m^2 for the $[0_4/90_4]_{2s}$ blocked-ply OCT laminate	119

Figure 5.9: (a) An non-structured mesh configuration ahead of the notch tip for the $[0_4/90_4]_{2s}$ OCT laminate, (b) predicted matrix damage in 0^0 layer, (c) predicted matrix damage in 90^0 layer for $G_2^f = 2.6 \text{ kJ/m}^2$ at $\text{POD}=4.8\text{mm}$ 120

Figure 5.10: Comparison of the experimental and predicted force-displacement curves for the $[0/90]_{8s}$ OCT laminates for a low and a high value of intra-laminar matrix fracture energy and fibre fracture energy of 150 kJ/m^2 [154]..... 122

Figure 5.11: Predicted damage patterns for each ply of the $[0/90]_{8s}$ OCT laminate with $G_2^f = 2.6 \text{ kJ/m}^2$ at $\text{POD}=3.8 \text{ mm}$, (a) matrix damage in 0^0 layer, (b) fibre damage in the 0^0 layer, (c) matrix damage in 90^0 layer, and (d) fibre damage in 90^0 layer 122

Figure 5.12: Comparison of (a) the predicted delamination zone at $0^0/90^0$ interface of the $[0/90]_{8s}$ OCT laminate with $G_2^f = 2.6 \text{ kJ/m}^2$ at $\text{POD}=3.8 \text{ mm}$ with (b) the final measured delamination zone from the C-scan results 123

Figure 5.13: Predicted damage patterns for each ply of the $[0/90]_{8s}$ OCT laminate with $G_2^f = 6.5 \text{ kJ/m}^2$ at $\text{POD}=3.8 \text{ mm}$, (a) matrix damage in 0^0 layer, (b) fibre damage in the 0^0 layer, (c) matrix damage in 90^0 layer, and (d) fibre damage in 90^0 layer 123

Figure 5.14: Comparison of the experimental and predicted force-displacement curves for the $[0/90]_{8s}$ OCT laminates with $G_2^f = 2.6 \text{ kJ/m}^2$ and a range for fibre fracture energy values, G_1^f [154]. 125

Figure 6.1: Comparison of the experimental and predicted force-displacement curves for (a) $[45_4/90_4/-45_4/0_4]_s$ and (b) $[45/90/-45/0]_{2s}$ laminates under OCT loading geometry [154]..... 130

Figure 6.2: Predicted matrix damage pattern (ω_2 distribution) for each ply of the blocked-ply $[45_4/90_4/-45_4/0_4]_s$ laminate at $\text{POD}=2.2\text{mm}$ 131

Figure 6.3: Predicted length of matrix damage versus pin opening displacement (POD) for each ply of the blocked-ply $[45_4/90_4/-45_4/0_4]_s$ laminate under OCT loading..... 131

Figure 6.4: Predicted projected delamination zone for $[45_4/90_4/-45_4/0_4]_s$ laminate at $\text{POD}=2.2\text{mm}$ and the experimental C-scan result obtained from a corresponding post-mortem specimen..... 132

Figure 6.5: Predicted matrix damage pattern (ω_2 distribution) for each ply of the $[45/90/-45/0]_{2s}$ laminate at $\text{POD}=2.2 \text{ mm}$ for (a) the first and (b) second sub-laminates (from the mid-plane to the free surface) 132

Figure 6.6: Predicted fibre damage pattern (ω_1 distribution) for each ply of the $[45/90/-45/0]_{2s}$ laminate at $POD=2.2$ mm for (a) the first and (b) second sub-laminates (from the mid-plane to the free surface)	133
Figure 6.7: Predicted projected delamination zone for $[45/90/-45/0]_{2s}$ laminate at $POD=2.2$ mm and the experimental C-scan result obtained from a corresponding post-mortem specimen.....	133
Figure 6.8: Comparison of the experimental [154] and predicted force-displacement curves for $[45/90/-45/0]_{2s}$ OCT laminate with different values of fracture energy for fibre damage mode	134
Figure 6.9: Comparison of the experimental and predicted force-displacement curves with and without accounting for delamination for (a) blocked-ply $[45_4/90_4/-45_4/0_4]_s$ and (b) dispersed-ply $[45/90/-45/0]_{2s}$ laminates [154,289].....	136
Figure 6.10: Specimen geometry of the open hole tensile laminates	140
Figure 6.11: Finite element mesh around the hole with width and height of $2.5D$ for specimens with (a) $D=3.175$ mm, (b) $D=6.35$ mm, (c) $D=12.7$ mm.....	142
Figure 6.12: Predicted load versus displacement curves of OHT laminates with different laminate thicknesses: (a) ply-level scaled and (b) sub-laminate-level scaled specimens $[45_m/90_m/-45_m/0_m]_{ns}$ with $D=3.175$ mm	144
Figure 6.13: Predicted load versus displacement curves of OHT laminates with different laminate thicknesses: (a) ply-level scaled and (b) sub-laminate-level scaled specimens $[45_m/90_m/-45_m/0_m]_{ns}$ with $D=6.35$ mm	144
Figure 6.14: Predicted load versus displacement curves of OHT laminates with different laminate thicknesses for a ply-level scaled and a sub-laminate-level scaled specimens $[45_m/90_m/-45_m/0_m]_{ns}$ with $D=12.7$ mm	145
Figure 6.15: Comparison between numerical and experimental strength values for ply-level scaled specimens for $D=3.175$ mm and $D=6.35$ mm.....	146
Figure 6.16: Predicted load-displacement curves for 4mm thick specimens with (a) $D=3.175$ mm, (b) $D=6.35$ mm and (c) $D=12.7$ mm hole size made of single and quadruple ply thickness.....	147
Figure 6.17: State of fibre damage in 0° plies for a time step after failure (marked with red squares in Figure 6.16(a)) for $[45/90/-45/0]_{4s}$ specimen with hole size $D=3.175$ mm	147
Figure 6.18: State of matrix damage in all the plies for a time step after failure (marked with red squares in Figure 6.16(a)) for $[45/90/-45/0]_{4s}$ specimen with hole size $D=3.175$ mm	148

Figure 6.19: State of delamination in all the interfaces for a time step after failure (marked with red squares in Figure 6.16(a)) for $[45/90/-45/0]_{4s}$ specimen with hole size $D=3.175\text{mm}$	149
Figure 6.20: State of matrix damage for all plies and delamination at each interface for $[45_4/90_4/-45_4/0_4]_s$ specimen with $D=3.175\text{mm}$ at a time step after the first and second load drop (marked with red squares in Figure 6.16(a)).....	151
Figure 6.21: State of matrix damage for all plies and delamination at each interface for $[45_4/90_4/-45_4/0_4]_s$ specimen with $D=6.35\text{mm}$ at a time step after the first load drop (marked with red squares in Figure 6.16(a)).....	152
Figure 6.22: Effect of specimen size on the strength of 4-mm thick specimens of $[45/90/-45/0]_{4s}$ and $[45_4/90_4/-45_4/0_4]_s$ laminates with different hole diameter size both in experiments and the predicted results. The strength of thin-ply laminates show a decreasing trend, while the thick-ply laminates exhibit an increasing trend as the hole diameter increases.	155
Figure 6.23: Effect of specimen size on the strength of 4-mm thick specimens of $[45/90/-45/0]_{4s}$ with different hole diameter. Comparison of the predictions of the current methodology and LEFM with experiments.....	156
Figure B.1: (a) OCT specimen geometry and (b) the FE mesh with element size 0.25mm and 0.5mm ahead of notch tip.....	193
Figure B.2: Dissipated energy calculated from the area below the load vs. pin-opening displacement (POD) curve.....	194
Figure C.1: Schematic of user defined material in LS-DYNA.....	198

List of Symbols

\mathbf{Q}^d	In-plane stress stiffness matrix of laminate
\mathbf{Q}_k^d	In-plane stress stiffness matrix of k th lamina
\mathbf{C}_k^d	Three dimensional stiffness matrix of k th lamina
$\mathbf{T}_k^{*T}, \mathbf{T}_k$	Strain and Stress transformation matrices
t_k	Lamina thickness
t	Laminate thickness
n	Total number of layers in a sub-laminate
$R_\alpha (\alpha \in 1,2)$	Stiffness reduction factor (fibre and matrix)
R_{12}	Shear stiffness reduction factor
$\omega_\alpha (\alpha \in 1,2)$	Damage parameter (fibre and matrix)
$\varepsilon_\alpha^{eq} (\alpha=1,2)$	Local equivalent strain (fibre and matrix)
$\bar{\varepsilon}_\alpha^{eq} (\alpha=1,2)$	Non-local averaged equivalent strain (fibre and matrix)
$\varepsilon_\alpha^i (\alpha=1,2)$	Initiation value for equivalent strain (fibre and matrix)
$\varepsilon_\alpha^s (\alpha=1,2)$	Saturation value for equivalent strain (fibre and matrix)
ρ^{eff}	Effective radius used in orthotropic averaging
r_1, r_2	Longitudinal and transverse non-local averaging radii
d_1, d_2	Components of the vector connecting the source point to a generic point in the orthotropic non-local averaging
r	Radius for isotropic non-local averaging
W	Non-local averaging weight function
Ω_X	Non-local averaging domain around point X.
\mathbf{x}, \mathbf{X}	Position vectors
G_{FE}^f	Predicted fracture energy from simulation of OCT specimen used in model calibration
$h_c^{effective}$	Effective length scale
l_e	Finite element size
G^f	Experimentally measured laminate's in-plane fracture energy
h^{exp}	Experimentally measured damage height perpendicular to the crack growth path
g^f	Fracture energy density of laminate (area under the strain-softening curve of laminate)
ΔU	Change in the strain energy

ΔW	Change in the external work
Δa	Crack length advancement
G_2^f	Intra-laminar matrix cracking fracture energy
G_1^f	Intra-laminar fibre breakage fracture energy
g_2^f	Intra-laminar matrix cracking fracture energy density
g_1^f	Intra-laminar fibre breakage fracture energy density
$\gamma_{12}, \gamma_{12}^e, \gamma_{12}^p$	Shear strain, elastic shear strain, inelastic shear strain
γ_{12}^*	Maximum shear strain experienced during the loading
$\tau(\gamma_{12})$	In-plane nonlinear shear stress of a ply as a function of shear strain
$G_{12}(\gamma_{12})$	In-plane shear stiffness of a ply as a function of shear strain
$\varepsilon_{11}, \varepsilon_{22}$	In-plane longitudinal and transverse strains of a ply
E_1, E_2	In-plane longitudinal and transverse modulus of a ply
G_{12}^0	In-plane initial shear modulus of a ply
ν_{12}, ν_{21}	Major and minor Poisson's ratio of a ply
E_{lam}	Initial modulus of the laminate
E^*	Modulus of the delaminated laminate
F_1	Failure initiation criterion for fibre damage
F_2	Failure initiation criterion for matrix damage
X_T	Longitudinal strength of ply in tension
Y_T	Transverse strength of ply in tension
S_L	In-plane shear strength of ply
Y_T^{is}	In-situ tensile transverse strength
S_L^{is}	In-situ in-plane shear strength
σ_2^{eq}	Matrix equivalent stress
T	Matrix equivalent stress at initiation of matrix damage
t_i	Components of tractions between the top and bottom surfaces of the interface, $i = 1, 2, 3$
δ_i	Components of the relative displacement between the top and bottom surfaces of the interface, $i = 1, 2, 3$
t^N, t^S	The normal and tangential tractions of the interface,
t_{max}^N and t_{max}^S	The peak normal and tangential (shear) traction values in pure mode I and mode II separation
δ_I	The normal relative displacement between the top and bottom surface of the interface

δ_{II}	The resultant shear relative displacement between the top and bottom of surfaces of the interface
δ_m	The relative mixed-mode displacement
$\delta_I^0, \delta_{II}^0$	The normal and relative tangential (shear) displacement between the top and bottom of surfaces of the interface at initiation of pure mode I and pure mode II separation
δ_m^0, δ_m^f	The initiation and final values of mixed-mode displacement
β	The mixed-mode ratio
E_I, E_{II}	The stiffness components corresponding to pure mode I and mode II traction-separation law
G_{Ic} and G_{IIc}	The mode I and mode II inter-laminar fracture energy values
G_I and G_{II}	The mode I and mode II inter-laminar energy release rates
ω_α	Damage parameter associated with interface delamination
α	The power coefficient in power law mixed-mode cohesive formulation
n_D	Number of delaminated interfaces through-thickness
$\bar{\mathbf{S}}^{(2)}, \hat{\mathbf{S}}^{(2)}$	The compliance matrix for damaged and undamaged status of the cracked ply in shear lag model
$\mathbf{S}^{*(2)}$	The difference between compliance matrix for undamaged and damaged status of the cracked ply in shear lag model
$\bar{\mathbf{Q}}^{(2)}, \hat{\mathbf{Q}}^{(2)}$	The stiffness matrix for damaged and undamaged status of the cracked ply in shear lag model
$\mathbf{Q}^{*(2)}$	The difference between stiffness matrix for undamaged and damaged status of the cracked ply in the shear lag model
$\bar{\boldsymbol{\varepsilon}}^{(2)}, \bar{\boldsymbol{\sigma}}^{(2)}$	The macro-stress and strains of the cracked ply in the shear lag model
$\tilde{\boldsymbol{\varepsilon}}^{(2)}, \tilde{\boldsymbol{\sigma}}^{(2)}$	The micro-stress and strains of the cracked ply in the shear lag model
$\Lambda_{ij}^{(2)}$	The in-situ damage effective functions for the cracked ply in the shear lag model
$D^{(2)}$	The crack density in the cracked ply of the shear lag model
$h^{(1)}, 2h^{(2)}$	Thickness of the constraining layer and the cracked layer in the shear lag model
s	Half of crack spacing in the shear lag model
L	Length of open hole specimens
D	Hole diameter in open hole specimens

List of Abbreviations

FPZ	Fracture process zone
OCT	Over-height compact tension test
CC	Compact compression test
CDM	Continuum damage mechanics
CZM	Cohesive zone model
PUFEM	Partition-of-unity finite element method
XFEM	Extended finite element method
PNM	Phantom node method
FNM	Floating node method
WWFE	World-wide failure exercise
VCCT	Virtual crack closure technique
RVE	Representative volume element
OHT	Open hole tensile test
4PBT	Four-point bending test
3PBT	Three-point bending test
DCB	Double cantilever beam
DEN	Double edge notch
MBT	Mixed bending tension
CODAM	Composite damage model
RVE	Representative volume element
POD	Pin-opening displacement
IDEFs	The in-situ damage effective functions
FD	Fibre damage
MD	Matrix damage

Acknowledgements

I would like to express my sincere thanks and appreciation to my supervisor Professor Reza Vaziri, for his support, guidance and criticism throughout this challenging project. Without his positive attitude and encouragements and his commitment to discuss my work in detail, I would not have been able to go through this path on my own.

I would like to especially thank members of the UBC Composites Research Network (CRN), Professor Anoush Poursartip, Navid Zobeiry, Alireza Forghani, and Ofir Shor for their helpful discussions, useful tips and encouragement during these years. I acknowledge members of University of Bristol, Professor Stephen R. Hallett and Xiaodong Li for conducting many useful experiments that were used in this thesis as a basis to validate my work.

I gratefully acknowledge the Natural Sciences and Engineering Research Council (NSERC) of Canada and the Four-Year Fellowship Grant (4YF), for their financial support for this research. I would like to thank the technical support team of the Livermore Software Technology Corporation, and in particular, Ushnish Basu and Jim Day for their assistance in responding to numerous technical questions related to LS-DYNA.

I would like to thank my family members: my parents, my sister and my boyfriend for their unconditional love, encouragement and moral support throughout this journey.

Chapter 1: Introduction

The application of composite materials has experienced a rapid growth in the last few decades. Starting in the late 1970s application of composites expanded widely including aircraft and aerospace structures, automotive components, sporting goods, underground pipes and biomedical products. Increasing use of composites in new aircraft programs, such as Boeing 787, Airbus A350, is the major driving force of putting the aerospace industry on the frontline of this field. In automotive industry, OEMs are continuously looking for innovative materials to reduce vehicle weight and achieve fuel efficiency and carbon emission targets. BMW has taken on a leading role for mass production of composite vehicles.

The basic advantage of composite materials lies in their high specific strength and stiffness, and that complex shape and large scale structures can be manufactured in one piece thus reducing costly assembly requirements. Fibre-reinforced composites in the form of multidirectional laminates with stacks of plies oriented in different directions enable material optimization to achieve minimum weight and required mechanical properties. However, the numerous available options and the heterogeneous nature of composites make the process more involved and their analysis more complex. Unlike conventional engineering materials, development of analytical models and procedures for determining material properties for prediction of structural behaviour of composite laminates is very challenging. By increasing the load beyond the elastic level, laminated composites exhibit intricate behaviour. This is due to the various modes of failure that emerge and the extreme anisotropy of the laminate constituents, i.e. plies.

The progression of damage in composite laminates is highly influenced by the interactions of several failure/damage mechanisms including matrix cracking, fibre breakage, splitting and delamination (see Figure 1.1). Given difficulties associated with numerical simulation of damage and failure in composites, in the recent decade many studies have been dedicated to improve numerical analysis of damage tolerance in such structures. A reliable prediction of the complex behaviour of composite materials must include the interaction of distinct failure mechanisms such as matrix cracking, fibre breakage, splitting and delamination. Such numerical tools, if validated, enable engineers to reduce the number of experimental tests at the coupon level and

probably sub-component level with virtual tests. However, as it was shown by the extensive studies in the so-called World-Wide Failure Exercise (WWFE) [100,123,228], developing computational models that yield quick and reliable results is still challenging and requires numerous validation case studies to identify their capabilities and limitations.

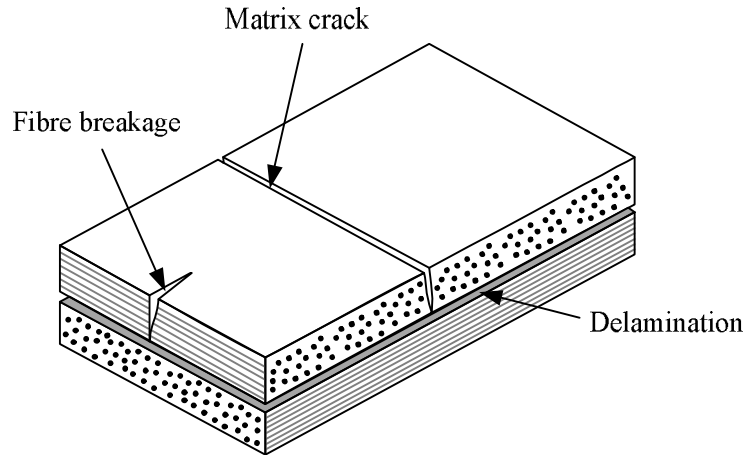


Figure 1.1: A schematic of different damage modes

Among the various approaches to model fracture and damage in solids, methods of continuum damage mechanics (CDM) have gained the most attention [73]. This is mainly due to the convenience of their implementation in general purpose finite element software. In continuum approaches, the effect of material degradation due to fracture and damage in the fracture process zone (FPZ) is modelled in a smeared manner and by reducing the apparent stiffness of the material (strain-softening) inside the FPZ. Although strain-softening is not a real physical phenomenon at the microscale of the material, it provides an appealing framework to simulate the effect of damage on the macroscopic structural response.

Since the Boeing-lead program for Advanced Technology Composite Aircraft Structure (ATCAS) in the early to mid-1990s, strain-softening approaches for simulation of damage in composite structures have gained notable attention. The Boeing collaboration with the Composites Group at the University of British Columbia that included testing of notched laminated composite panels with various materials and geometric configurations, provided a comprehensive experimental and strain-softening based modelling framework to simulate

damage and failure in laminated composites (see Dopker et al., 1994; Ilcewicz et al., 1993, 1996; Kongshavn and Poursartip, 1999; Williams and Vaziri, 1995, 2001).

When there is no single isolated crack that dominates the zone of damage, one may consider the effect of multiple micro-cracks smeared into a locally homogeneous continuum field in a CDM approach. To characterize the damage state of this field, the quantities that define the stiffness degradation of the material within that zone need to be identified. This modelling approach is used extensively in finite element analysis due to its straightforward implementation and numerical efficiency. A successful example of a fully continuum damage model is the sub-laminate based approach that was first introduced by Williams et al. [267] at UBC known as COmposite DAmage Model (CODAM). The application of this model leads to reasonably accurate modelling of damage in quasi-brittle materials, for cases where damage is not dominated by macro discrete failure modes (i.e. splits and delamination) (see [73,75,171-173]). More recently, the second generation of this material model (CODAM2) was introduced by Forghani et al. ([75,76]), equipped with a non-local regularization limiter scheme to address the mesh dependency. The required material properties for this material model are obtained with a characterization scheme developed by Zobeiry et al. [289,290]. This technique identifies the optimum effective strain-softening curve of the locally homogenized damaged zone of the laminate. For material characterization in tension, they used the over-height compact tension (OCT) test configuration that was originally designed by Kongshavn and Poursartip [129] in order to have a stable crack growth.

For cases where failure is governed by discrete macro-crack propagation such as large splits and delamination, continuum damage models often fail to correctly capture the propagation of damage through the structure. Discrete macro-cracks redistribute the stresses around the damage zone and consequently alter the load paths within the structure. For instance, delamination which is usually accompanied by intra-laminar discrete matrix cracks close to notches or general discontinuities potentially blunts the damage front and reduces the stress concentration. In these cases the mesoscopic models are more suited as they attempt to capture both intra-laminar (within the plies) and inter-laminar (between the plies) damage modes. However, the challenge is to understand the sequence of different damage modes in ply-scale and defining physical

parameters in material's constitutive laws that determine which mode will dominate. The behaviour of a laminate depends on the interplay of different failure processes which complicates the development of computational models.

This work presents a combination of discrete and continuum damage models in a mesoscopic approach that leads to an acceptable prediction of the structural response whether or not the delamination is a dominant damage mechanism. Compared to fully discrete methods, this method offers a much higher numerical efficiency by only modeling delaminations discretely. The intra-laminar damage modes including splitting are captured using a non-local continuum model rather than a discrete model. However, application of this methodology requires guidance from experimental studies of damage mechanisms in order to properly characterize and calibrate the required material properties. A significant contribution of this work is to address this need.

In the proposed methodology, the intra-laminar modes of damage including matrix cracking and fibre fracture are captured with an enhanced form of the non-local CODAM2 material model. The non-local averaging technique is very effective in predicting the trajectory of in-plane macro-cracks irrespective of the mesh orientation. Therefore, the need to introduce pre-inserted discrete elements to capture the growth of discrete cracks is eliminated and the computational cost is reduced significantly. The enhancements in the original CODAM2 formulation are described in order to relate the damage initiation and progression of individual delaminated plies to the mechanical properties of unidirectional laminates. The enhanced CODAM2 material model formulation is implemented as a user-defined material model (UMAT) in the commercial finite element software package, LS-DYNA [158].

A common cause of delamination is the inter-laminar stresses induced at the tip of matrix cracks [232] which highlights the importance of proper estimation of the onset of matrix cracking. Many studies show that the formation of transverse matrix cracks in a ply depends on the constraining effects of its neighboring plies as well as the thickness of the ply [191,217]. For example, experiments show higher transverse tensile and shear strengths for a 90° ply constrained by plies with different orientations in comparison with a unidirectional 90° laminate (see [10,45,82,127,191]). Based on these observations, some researchers differentiate between

the behaviour of a unidirectional lamina and that of a lamina embedded within a laminate [52,70,227]. In this work, Hashin's failure criteria [94,95] are used to identify the onset of intra-laminar matrix and fibre damage modes. The constraining effect of the immediate neighboring plies and the ply thickness are also considered through an approximate analytical model based on combination of linear elastic fracture mechanics and a shear lag theory introduced by Zhang et al. [278,279].

From a numerical point of view, the explicit modelling of delamination as a macro-crack separation of plies at the interface enables the split in the separated ply to grow independently of the remainder of the laminate. Therefore, in combination with CODAM2 model which captures the intra-laminar damage (including the splits), a mixed-mode cohesive-based contact formulation available in LS-DYNA [158] is used to model the delamination between all dissimilar plies. A common drawback of cohesive methods is that robust and accurate simulations require very fine finite element spatial discretization to accurately represent the tractions in the cohesive zone. This will inevitably affect the computational efficiency of the mesoscopic models which is addressed in this work. A methodology is introduced to calibrate the material properties of the cohesive model such that it automatically takes into account the size of in-plane elements and the inter-laminar stress distribution in a region close to the notches where the matrix cracks and delamination are expected to occur first. With this technique, one can eliminate the need to have very fine mesh size to obtain accurate prediction using the cohesive interfaces. Moreover, it implicitly accounts for the effect of ply thickness on the initiation of delamination since the initiation of delamination is indirectly linked to the matrix cracking which is in turn influenced by ply thickness.

A significant contribution of this work is to introduce a methodology to obtain the in-situ material properties associated with initiation and progression of intra-laminar damage modes. Most of these properties including the elastic moduli and strength properties can be gathered from the standard tests. However, the main challenge is to obtain the fracture energies associated with the progression of fibre and matrix damage modes. While there is more literature available on the characterization of fibre fracture energy, less work has been done for characterization of intra-laminar matrix fracture energy. This is a quantity which may not be

directly measured from standard experiments on unidirectional laminates and is considered to be essential in continuum representation of multiple matrix cracks that are confined to an off-axis ply constrained between stiff layers. A systematic and novel procedure has been proposed to extract the intra-laminar fracture energies of the material system of interest in tension from a few experiments on OCT specimens with specific layups. The intent is to implicitly account for the interaction of matrix cracks with delamination and damage in neighboring plies. These are the type of interacting mechanisms that do not show up in conducted tests on unidirectional laminates.

In this work the input material properties of the enhanced CODAM2 material model in mesoscopic context are calibrated for IM7/8552 carbon-fibre/epoxy (CFRP) material system using the test results conducted by Li et al. [154]. The proposed mesoscopic numerical approach is examined for two tensile notched geometries including OCT and open-hole tensile (OHT) test configurations. In the first case, cross-ply and quasi-isotropic laminates with dispersed-ply and blocked-ply laminate layups are studied. In the second case, OHT specimens made of quasi-isotropic with various size and laminate thicknesses are examined.

1.1 Objectives

The main objective of this work is to present a numerical methodology to simulate the progression of damage in laminates that are prone to macro-discrete damage modes (i.e. splitting and delamination). The proposed approach must also be applicable to laminate layups and loading geometries where the effect of delamination is negligible. The goal is to capture the global behaviour and detailed damage response of the laminate without compromising the efficiency of the methodology. To achieve this goal, firstly the material model formulation needs to have the capability of modeling different modes of damage and their interactions. Secondly, the key material parameters associated with intra-laminar and inter-laminar damage modes need to be identified and their effects on the material model behaviour understood. Finally, these parameters are required to be calibrated such that they represent the effective behaviour of the constituent plies within a multi-directional laminate.

1.2 Outline

The layout of the thesis is as follows:

Chapter 2 provides a review of the existing numerical approaches and computational methods in simulation of initiation and progression of different damage mechanisms in continuous fibre-reinforced composites.

Chapter 3 first presents a summary of the second generation of the sub-laminate-based (macroscopic) non-local CODAM model (i.e. CODAM2) developed by Forghani et al. ([75,76]). Second, the mesoscopic version of this model is introduced to capture the intra-laminar damage mechanisms at ply-level. The modifications in the material model formulation associated with prediction of initiation and progression of damage at individual plies are described in detail.

Chapter 4 provides a brief summary of the widely used cohesive zone model (CZM) to capture delamination between the plies. A common drawback of cohesive-based models and the available solutions in literature are discussed which motivates the solution proposed in the following chapter.

Chapter 5 provides a brief summary of existing experimental methods for characterization of damage properties of unidirectional laminates. The detailed methodology for calibration of the intra-laminar (enhanced non-local CODAM2) and inter-laminar (CZM) models for IM7/8552 CFRP material system is provided.

Chapter 6 shows the performance of the presented methodology in predicting the progression of damage in OCT and OHT geometry configurations for the same material system calibrated in Chapter 5. The predicted overall response and the damage patterns are shown and compared against the experimental results for various laminate layups, ply thickness and specimen sizes. This purpose is to assess the efficiency of the presented framework for reliable prediction of laminate failure from its initiation through evolution to complete failure.

Chapter 7 wraps up the thesis with summary, conclusion remarks, contributions and future works.

Appendix A provides detailed formulation of the shear lag theory used in Chapter 3. Appendix B establishes the relationship between the experimental intra-laminar fracture energy and the input fracture energy density for the enhanced non-local CODAM2 model in mesoscopic context. Appendix C provides a general guideline for the structure of the user material model subroutines in LS-DYNA. Appendices D and E include the introduced material model's input parameters and their definitions, as well as some notes on post processing the outcome of the material model. Appendix F provides the pseudo code and the implementation of the material model.

Chapter 2: Literature Review

2.1 Introduction

The heterogeneous nature of fibre-reinforced composite laminates that gives rise to multiple crack types interacting as failure progresses makes the prediction of failure complicated. These damage mechanisms may lead to significant redistribution of stresses and thus affect the load level, at which final structural failure occurs. Therefore, there is a need for models, capable to simulate the entire damage process from its initiation through evolution to complete failure of the composite structure.

Although composite laminates may be considered to be homogeneous macroscopically, they show various heterogeneities at microscopic level. Formation and propagation of damage in composite structures is a multiscale event in nature. It usually initiates with microscale cracking in the matrix typically accompanied by small-scale delamination at the layer interfaces. Further increase of the load results in growth of matrix cracks to mesoscale cracks and delamination, which eventually leads to macroscale cracks and fibre breakage. Therefore, it is required to study their behaviour at various scales. With a rapid growth in computational power of computers, multi-scale modelling of fibre-reinforced composites has become an important means of understanding the behaviour of such materials. A multi-scale approach considers three scale levels for the analysis of heterogeneous composite materials [277] described below (see Figure 2.1):

1. **Micro-scale:** The micro-scale is the lowest material scale taking into account the behaviour of constituents (fibres and matrix) of the material. Here, fibre and matrix phases and their interface are modelled separately, and the average properties of a single reinforced layer are determined based on properties of individual constituent using a homogenisation technique. Interaction between constituents and the resulting behaviour of the composite (micro-strain and –stress fields) is the main concern at this scale [83,273,281]. Although the microscale models have been shown to be very successful in predicting the properties of the undamaged material and also in predicting the onset of

damage, they are unable to predict damage evolution. This is due to the fact that the representative volume assumed for predicting the behaviour of the virgin material in a microscale model cannot be used as a representative volume for the extensively damaged material. In other words, in a damaged material, smearing and homogenization cannot be performed at the same scale that is performed in the undamaged material.

2. **Meso-scale:** The meso-scale considers the ply as a basic homogeneous continuum entity for mechanical analysis of, and failure prediction in laminated composites [128,138,161,201,238,250,266,268]. Each ply is modelled separately as a homogeneous material and the fibre direction is taken into account in terms of orthotropy of the homogeneous material. This scale can be much more easily implemented in analysis of large structures than the micro-scale due to lower computational effort. After the pioneering work by Ladevèze [136] and Matzenmiller [166], Pinho et al. [197,198], Maimi et al. [161,162], Laurin et al. [145] and Camanho et al. [33] proposed the stiffness degradation models and different damage evolution laws for different damage modes of the constitutive plies which can be used in a mesoscopic approach. The ply's mechanical and elastic properties can be determined through experimentation, but modelling at this scale does not provide any information about a character of interaction between the constituents. Considering the fact that the standard test methods suggested for characterization of unidirectional laminates often exhibit instability (or catastrophic failure), the behaviour observed in such a test would not represent the behaviour of a ply in a multidirectional laminate. In a multidirectional laminate, neighbouring plies provide structural support to the damaged layers and introduce alternative load paths to the structure. Therefore, the effective behaviour of a ply, when placed in a multidirectional laminate, have been considered in some meso-models [34,217].
3. **Macro-scale:** The macro-scale is defined at the level of components at which the structure is a completely homogeneous continuum and its material behaviour is described by an anisotropic constitutive law. The macroscale models are typically not capable of predicting the details of the damage events in the layers. Main advantages of macroscale models are their simplicity as well as capability to be adapted to large scale problems.

The sub-laminate-based approach, which was first introduced by Williams et al. [267], takes the sub-laminate as the building block of the laminated composite structure. This approach considers the sub-laminates as the representative volume and as the base level for constructing the damage model. In this approach, in contrast with the ply-based approach, an element in the numerical simulation represents a sub-laminate. The goal of the sub-laminate approach is to predict, in a smeared manner, the essence of the overall nonlinear response of a laminated composite structure (e.g., its stiffness, load-carrying capacity, stability and post-peak behaviour) due to progressive damage caused by a given loading condition. In general, the main drawback of macro-scale models is that since the interface of plies is not modelled explicitly, the actual damage mechanisms especially large matrix macro-cracks and delamination are not captured, leading to an arguable lack of physical representativeness. This issue will be more discussed in this thesis.

Multi-scale modelling transfers the damage information from lower to higher scale to predict the final failure of laminates. However, multi-scale failure analysis using the finite-element models combining coarse meshes and finer meshes at the macro and micro levels respectively is still computationally costly because of a large volume of calculations. Therefore, meso- and macro-level models coupled with continuum damage mechanics still works well in design and failure prediction of composite laminates and it is also employed in this work.

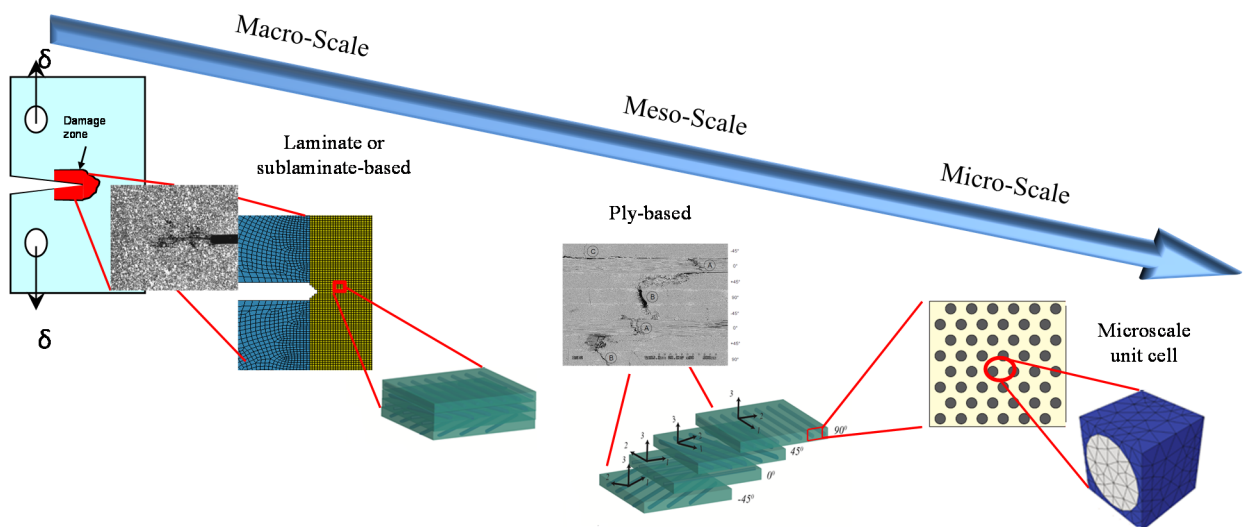


Figure 2.1: The three scales of damage analysis in composite laminates

The most promising and suitable tool for modeling damage progression in composite materials is a computational approach based on the finite-element method (FEM). This approach has the potential to model the complex damage process, initiating from matrix cracking, evolving in delamination and fibre breakage to composite structural ultimate failure. However, the development of proper numerical model representing the physics of damage mechanisms is a challenging task [251]. Reliable and accurate simulations of discrete damage behaviour of composite laminates require guidance from experimental and theoretical studies of damage mechanisms. Understanding a sequence of different damage modes and defining physical parameters in material's constitutive laws that determine which mode will dominate is a challenge of respective simulations. The strength of a laminate depends on the interplay of different failure processes which complicates the development of computational models. For example, laminate strength does not linearly scale with increasing the thickness of the laminate. In fact, the failure type may change completely when the thickness of the plies is changed [82]. Moreover, characterization of the effect of manufacturing-induced defects such as residual stresses on mechanical performance of composites can be quite challenging. The material properties are evolving during processing and an accurate estimation of these defects requires the consideration of the processing history of the material system, e.g. [67,68,117,151,284,288].

Cox and Yang [44] have pointed out that the main challenge in damage modeling of composites is to categorize and characterize possible mechanisms of damage and represent them in a model in a realistic and physical way. Moreover, understanding the origins of numerical instabilities that often occur in simulations of heterogeneous materials adds another challenge. It is important to know whether these instabilities are due to numerical approximations or rather they represent the actual unstable progression of damage as it is often observed in experiments. Modelling of damage mode sequences and their interaction successfully in a computationally cost-effective way is of key motivation to developing tools for use as virtual tests.

In order to characterize the onset and progression of damage for analysis of composite structures, various approaches are implemented in finite-element models. In the next section, various damage analysis approaches based on numerical techniques are presented. The damage in composite laminates is a complex phenomenon and results in various failure modes that interact

with each other. Usually, failure of the first ply represents the damage initiation, but does not lead to the ultimate structure failure. Numerous existing composites failure and damage methodologies can include one or two parts, one being focused on the prediction of initiation of different damage mechanisms and the second dealing with prediction of the progression of damage in a composite laminate leading to its ultimate failure. Theories and models at these two stages of damage (initiation and progression) are reviewed separately in following Sections 2.2 and 2.3.

2.2 Initiation of failure mechanisms

The first component for damage progression prediction in composite laminates is to identify the initiation of various failure mechanisms such as fibre breakage, matrix cracking and delamination. The need to predict failure initiation in composites has led to the proposal of several failure criteria. There is numerous number of failure theories in the literature of which some predict initiation of an individual damage mode while some predict failure in a general sense. Some of these failure theories are associated with intra-laminar failure modes while the others focus on inter-laminar failure modes.

Most of these criteria are expressed in terms of the stress components and strength properties referred to as strength-based criteria. In application of the strength criteria, the material is said to be damaged once these criteria are satisfied. The strength-based failure criteria can be expressed in terms of stress components relevant to a specific damage mode. They can also be expressed in terms of other internal variables such as strain, displacement or rotations. The strength-based criteria only characterize damage for its initiation and not the propagation of the existing damaged region.

A selection of the failure criteria commonly used in literature is presented here that are categorized based on the approach used in their derivations [61,190]: non physically-based (or not associated with the failure modes, or non-phenomenological) and physically-based (or associated with the failure modes, or phenomenological).

- 1. Non physically-based failure criteria.** These are criteria in which a failure envelope is defined by using a mathematical expression, usually a polynomial, which predicts failure by interpolating between a few experimental points. No attempt is made to predict which failure mode is taking place, and the criterion itself is not the result of a physically-based failure model.
- 2. Physically-based failure criteria.** These are criteria which result from models that try to describe the physics of the failure process. These criteria can predict the type of failure mode.

The former criteria are developed from the theories originally developed for metals and updated for anisotropic materials. These criteria are usually expressed as a polynomial in terms of stress components and the experimentally determined strength values. The most common polynomial failure criteria is proposed by Tsai and Wu [242]. Other failure theories of this category can be found in the reviews by Nahas [181] or by Paris [190]. The advantage of these criteria is the simplicity of their implementation in finite element methods and their smooth envelopes.

In physically-based failure criteria, on the other hand, the distinction between failure modes is considered. The failure envelopes corresponding to these criteria are therefore not always smooth, and the vertices correspond usually to a change in the failure mode. Hashin and Rotem [95] are the pioneers to establish a failure theory that accounts for failure of different constituents of a ply and to predict each of them separately. In this category of stress-based criteria, Hashin and Rotem's work in 1973 [95] and later Hashin's work in 1980 [94] have inspired considerable research in failure-mode oriented criteria. Depending on the failure mode, the following subsections summarize the common failure criteria for different intra- and inter-laminar failure modes.

2.2.1 Fibre failure

For composite laminates, fibre failure in tension is usually expressed in terms of a maximum stress or maximum strain criterion at each ply, with the material limit values extracted from experimental results. Hashin [95] uses a stress-based criterion, while Puck and Schürmann [204] use a criterion with a stress magnification factor applied to transverse normal stress. Common failure criteria for fibre failure in tension are summarized in Table 2-1.

Fibre failure in compression is mostly due to microbuckling and the formation of kink bands [195]. Most researchers have only used a maximum stress or maximum strain criteria using limit values from experimental characterization, while only some of them have tried to incorporate the effects of microbuckling and kinking [195]. These criteria are summarised in Table 2-2.

Table 2-1: Fibre failure criteria in tension

Criterion	Formulation	Notes
Max stress	$\sigma_1 \geq X_T$	
Max strain	$\varepsilon_1 \geq \varepsilon_T$	
Hashin-2D [95]	$\left(\frac{\sigma_1}{X_T}\right)^2 \geq 1$	
Hashin-3D [95]	$\left(\frac{\sigma_1}{X_T}\right)^2 + \frac{1}{S_{12}^2}(\tau_{12}^2 + \tau_{13}^2) \geq 1$	1,2,3 stand for material principal directions
Puck [204]	$\frac{1}{\varepsilon_T} \left(\varepsilon_1 + \frac{\nu_{f12}}{E_{1f}} m_{f\sigma} \sigma_2 \right) \geq 1$	Subscript f indicates fibre values $m_{f\sigma}$: stress scale factor

Table 2-2: Fibre failure criteria in compression

Criterion	Formulation	Notes
Max stress	$\sigma_1 \geq X_C$	
Max strain	$\varepsilon_1 \geq \varepsilon_C$	
Puck [204]	$\frac{1}{\varepsilon_C} \left(\varepsilon_1 + \frac{\nu_{f12}}{E_{1f}} m_{f\sigma} \sigma_2 \right) \geq 1 - (10\gamma_{12})^2$	Subscript f indicates fibre values $m_{f\sigma}$: stress scale factor

Table 2-2: Fibre failure criteria in compression

Criterion	Formulation	Notes
LaRC03 [52]	$\text{for } \sigma_{22}^m < 0: \left\langle \frac{ \tau_{12}^m + \eta_{12} \sigma_{22}^m}{S_{12, is}} \right\rangle \geq 1$ $\text{for } \sigma_{22}^m > 0: (1-g) \left(\frac{\sigma_{22}^m}{Y_{T, is}} \right) + g \left(\frac{\sigma_{22}^m}{Y_{T, is}} \right)^2 + \left(\frac{\tau_{12}^m}{S_{12, is}} \right)^2 \geq 1$	$\sigma_{22}^m, \tau_{12}^m$: stresses in 2D kinking frame, at angle ϕ $g = G_{Ic} / G_{IIc}$
LaRC04 [195]	$\text{for } \sigma_{22}^m < 0:$ $\frac{ \tau_{12}^m }{S_{12, is} - \eta_{12} \sigma_{22}^m} \geq 1$ $\text{for } \sigma_{22}^m > 0:$ $(1-g) \left(\frac{\sigma_{22}^m}{Y_{T, is}} \right) + g \left(\frac{\sigma_{22}^m}{Y_{T, is}} \right)^2 + \frac{\Lambda_{23}^0 \tau_{23}^{m\psi} + \chi(\gamma_{12}^m)}{\chi(\gamma_{12, is}^m)} \geq 1$	$\sigma_{22}^m, \tau_{12}^m, \tau_{23}^{m\psi}$: are stresses in 3D kinking frame, at angles ϕ, ψ 3D kinking angles found by iteration $g = G_{Ic} / G_{IIc}$
Maimí-et-al. [161]	$\left\langle \frac{ \tau_{12}^m + \eta_{12} \sigma_{22}^m}{S_{12}} \right\rangle \geq 1$	$\sigma_{22}^m, \tau_{12}^m$: stresses in 2D kinking frame, at angle ϕ

2.2.2 Matrix failure

Matrix failure in laminated composites can be in the form of cracks initiating from defects or can occur as the fibre–matrix debonding and splitting. Accumulation of the cracks and their coalescence leads to failure across a critical fracture plane. Many researchers have developed approaches for predicting the initiation of matrix cracks and predicting the fracture plane angle under a variety of loading conditions.

Criteria for matrix failure in tension involve an interaction of the traction components on a critical fracture plane in the transverse tension direction. Apart from the maximum stress and maximum strain criteria, the simplest proposal is the quadratic interaction criterion of Hashin and Rotem [95] and further developments include in-situ transverse tensile and shear strengths of the ply, use of through-thickness shear strength terms [195] as shown in Table 2-3.

The criteria for matrix failure in compression are given in Table 2-4. Hashin and Rotem [95] assumed the fracture plane was in the transverse direction and proposed a simple quadratic

interaction criterion using the transverse normal and in-plane shear components. Hashin [94] later used similar approach but included the effect of the through-thickness strength.

Puck took the basic idea of the Hashin criteria for Inter Fibre Failure (IFF) and extended it [204]. Following the idea of a Mohr Coulomb type of failure, a fracture plane is identified. IFF is assumed to occur on a plane parallel to the reinforcing fibres. There are three tractions acting on the fracture plane, the normal traction and the two shear tractions. Only those three components of stress will contribute to failure. The failure criteria are therefore written in terms of fracture plane stresses. The computational effort for finding the critical angle can be cumbersome. The concept of the fracture plane was already proposed by Hashin in 1980 but not pursued due to the lack of computing power. The main criticism of the Puck failure theory has been the comparatively large number of required parameters. It is sometimes claimed that those parameters are of empirical nature and require extensive experimental material characterization procedures [108].

Davila and Camanho [52] extended the Puck theory by suggesting ply thickness dependent strength parameters. Fracture mechanics based analysis was employed to derive the influence of the ply thickness on the strength. In particular, thin and thick embedded plies were investigated. The idea was further developed by Pinho et al. [195] for three-dimensional stress states.

In parallel with Puck, Cuntze and Freund [48] developed the failure mode concept. The fundamental assumptions for both theories are identical, but Cuntze defines his failure criteria in terms of stress invariants and avoids therefore a search for the critical fracture plane orientation. Cuntze composes the failure surface by a set of three different failure criteria. Each failure criterion characterizes a certain failure mechanism and incorporates only one strength parameter. The first IFF mode is a tensile failure transverse to the fibre which is characterized by the transverse tensile strength Y_T . The second IFF mode is a shear failure which is characterized by the in-plane shear strength S_{12} . This failure results in a matrix crack which is oriented at $\theta_f = 0^\circ$ where θ_f is the angle of the fracture plane. The third IFF mode is characterized by transverse compressive strength Y_C and results in a fracture plane which is inclined by $\theta_f \neq 0^\circ$.

Table 2-3: Matrix failure criteria in tension

Criterion	Formulation	Notes
Max stress	$\sigma_{22} \geq Y_T$	
Max strain	$\varepsilon_{22} \geq \varepsilon_T$	
Hashin-Rotem-2D [95]	$\left(\frac{\sigma_{22}}{Y_T}\right)^2 + \left(\frac{\tau_{12}}{S_{12}}\right)^2 \geq 1$	
Hashin-Rotem-3D [94]	$\left(\frac{\sigma_{22} + \sigma_{33}}{Y_T}\right)^2 + \left(\frac{\tau_{23}^2 - \sigma_{22}\sigma_{33}}{S_{23}^2}\right) + \left(\frac{\tau_{12}^2 - \tau_{13}^2}{S_{12}^2}\right) \geq 1$	1,2,3 stand for material principal directions
Chang-Lessard [38], Ladaveze [136]	Use $d_2, \bar{\Psi}_2$ to indicate damage Total failure for $d_2 \geq 1$ or $\bar{\Psi}_2 \geq \bar{\Psi}_{2max}$ $d_2 = \langle \bar{\Psi}_2 - \bar{\Psi}_{2int} \rangle_+ / \bar{\Psi}_{2crit}$ $\bar{\Psi}_2(t) = \sqrt{\frac{\langle \sigma_{22} \rangle_+^2}{2E_2(1-d_2)^2}}$, $\bar{\Psi}_2 = \max \bar{\Psi}_2(t)$	$\langle a \rangle_+ = a$ if $a \geq 0$, else 0 material parameters: $\Psi_{2,max,crit,max}$: tension test on $[\pm 67.5]_{2s}$ coupon Also uses plasticity law
Puck [204]	$\sqrt{\left(\frac{\tau_{12}}{S_{21}}\right)^2 + \left(1 - P_{\perp\parallel}^{(+)} Y_T / S_{21}\right)^2 \left(\sigma_{22} / Y_T\right)^2} + \left(P_{\perp\parallel}^{(+)} \sigma_{22} / S_{21}\right) \geq 1 - \sigma_{11} / \sigma_{1D} $	$P_{\perp\parallel}^{(+)} = -\left(d\tau_{12} / d\sigma_{22}\right)_{\sigma_{22}=0}$ $\sigma_{1\sigma}$ is stress value for linear degradation
LaRC03 [52]	$(1-g)\left(\frac{\sigma_{22}}{Y_{T,is}}\right) + g\left(\frac{\sigma_{22}}{Y_{T,is}}\right)^2 + \left(\frac{\tau_{12}}{S_{12,is}}\right)^2 \geq 1$	Factor $g = G_{Ic} / G_{IIc}$
LaRC04 [195]	$(1-g)\left(\frac{\sigma_{22}}{Y_{T,is}}\right) + g\left(\frac{\sigma_{22}}{Y_{T,is}}\right)^2 + \frac{\Lambda_{23}^0 \tau_{23}^2 + \chi(\gamma_{12})}{\chi(\gamma_{12,is})} \geq 1$	$g = G_{Ic} / G_{IIc}$
Maimí-et-al. [161]	$\sigma_{22} > 0$: $\sqrt{(1-g)\left(\frac{\sigma_{22}}{Y_T}\right) + g\left(\frac{\sigma_{22}}{Y_T}\right)^2 + \left(\frac{\tau_{12}}{S_{12}}\right)^2} \geq 1$ $\sigma_{22} < 0$: $\left\langle \frac{ \tau_{12} + \eta_{12}\sigma_{22}}{S_{12}} \right\rangle \geq 1$	$g = G_{Ic} / G_{IIc}$. $\alpha_0 = 53^0$ $\eta_{12} = -\frac{S_{12} \cos 2\alpha_0}{Y_C \cos^2 2\alpha_0}$
Vogler [256]	$f_M = \alpha_1 I_1 + \alpha_2 I_2 + \alpha_3' I_3 + \alpha_{32}' I_3^2 > 1$ for $I_3 > 0$	$\alpha_1 = 1 / S_T^2$ $\alpha_1 = 1 / S_L^2$ $\alpha_{32}' = \frac{1 - Y_T / (2Y_{BT}) - \alpha_1 Y_T^2 / 4}{Y_T^2 - 2Y_{BT} Y_T}$ $\alpha_3' = \frac{1}{2Y_{BT}} - 2\alpha_{32}' Y_{BT}$
Cuntze [48]	$(I_1 + \sqrt{I_4}) / 2Y_T > 1$ $I_2 = \sigma_{22} + \sigma_{33}$, $I_2 = (\sigma_{22} - \sigma_{33})^2 + 4\tau_{23}^2$	

Table 2-4: Matrix failure criteria in compression

Criterion	Formulation	Notes
Max stress	$\sigma_{22} \geq Y_C$	
Max strain	$\epsilon_{22} \geq \epsilon_C$	
Hashin-Rotem-2D [95]	$\left(\frac{\sigma_{22}}{Y_C}\right)^2 + \left(\frac{\tau_{12}}{S_{12}}\right)^2 \geq 1$	
Hashin -3D [94]	$\sigma_{22} / Y_C \left[(Y_C / 2S_{23})^2 - 1 \right] + \left(\frac{\sigma_{22}}{2S_{23}}\right)^2 + \left(\frac{\tau_{12}}{S_{12}}\right)^2 \geq 1$	
Puck [204]	Mode B, $\theta_{fp} = 0^0$, $\frac{1}{S_{21}} (\sqrt{\tau_{12}^2 + (P_{\perp\parallel}^{(-)} \sigma_{22})^2} + P_{\perp\parallel}^{(-)} \sigma_{22}) \geq 1 - \sigma_{11} / \sigma_{1D} $ <i>for</i> $\sigma_{22} < 0$ and $0 \leq \sigma_{22} / \tau_{12} \leq R_{\perp\parallel}^A / \tau_{12c} $ Mode C, $\theta_{fp} \neq 0^0$, (refer to paper) $\left[\left(\frac{\tau_{12}}{2(1 + P_{\perp\parallel}^{(-)} S_{21})}\right)^2 + \left(\frac{\sigma_{22}}{Y_C}\right)^2 \right] \frac{Y_C}{(-\sigma_{22})} \geq 1 - \sigma_{11} / \sigma_{1D} $ <i>for</i> $\sigma_{22} < 0$ and $0 \leq \tau_{12} / \sigma_{22} \leq \tau_{12c} / R_{\perp\parallel}^A$	$P_{\perp\parallel}^{(-)} = -(d\tau_{21} / d\sigma_{22})_{\sigma_2=0}$ $R_{\perp\parallel}^A = Y_C / (2(1 + P_{\perp\parallel}^{(-)}))$ $P_{\perp\parallel}^{(-)} = P_{\perp\parallel}^{(-)} R_{\perp\parallel}^A / S_{21}$ $f_w = 1 - \sigma_1 / \sigma_{1D}$ $\sigma_{1\sigma}$ is stress value for linear degradation
LaRC03 [52]	$\sigma_{11} < Y_c: \left(\frac{\tau_{23,eff}^m}{S_{23}}\right)^2 + \left(\frac{\tau_{12,eff}^m}{S_{12,fs}}\right)^2 \geq 1$ $\sigma_{11} \geq Y_c: \left(\frac{\tau_{23,eff}^m}{S_{23}}\right)^2 + \left(\frac{\tau_{12,eff}^m}{S_{12,fs}}\right)^2 \geq 1$	$\alpha_0 = 53^0$ angle α found by checking $0 < \alpha < \alpha_0$ $\tau_{23,eff}^m, \tau_{12,eff}^m$: stresses in 2D kink frame at φ $S_{23} = Y_c \cos \alpha_0 \times (\sin \alpha_0 + \cos \alpha_0 / \tan 2\alpha_0)$
LaRC04 [195]	$\sigma_{11} \geq -Y_c: \left(\frac{\tau_{23}^\alpha}{S_{23} - \eta_{23} \sigma_n}\right)^2 + \left(\frac{\tau_{12}^\alpha}{S_{12,fs} - \eta_{12} \sigma_n}\right)^2 \geq 1$ $\sigma_{11} < -Y_c: \left(\frac{\tau_{23}^m}{S_{23} - \eta_{23} \sigma_n^m}\right)^2 + \left(\frac{\tau_{12}^m}{S_{12} - \eta_{12} \sigma_n^m}\right)^2 \geq 1$	$\alpha_0 = 53^0$ angle α found by checking $0 < \alpha < \alpha_0$ $\sigma_n, \tau_{23}^\alpha, \tau_{12}^\alpha$: stresses in fracture plane at α $\sigma_n^m, \tau_{23}^m, \tau_{12}^m$: stresses in 3D kink frame at ϕ, φ $S_{23} = Y_c \cos \alpha_0 \times (\sin \alpha_0 + \cos \alpha_0 / \tan 2\alpha_0)$ $\eta_{23} = -1 / \tan 2\alpha_0$ $\eta_{12} = \eta_{23} S_{12} S_{23}$
Maimi-et-al. [161]	$\sqrt{\left(\frac{\tau_{23,eff}}{S_{23}}\right)^2 + \left(\frac{\tau_{12,eff}}{S_{12}}\right)^2} \geq 1$ $\tau_{23,eff} = \langle -\sigma_{22} \cos \alpha_0 (\sin \alpha_0 - \eta_{23} \cos \alpha_0 \cos \theta) \rangle$ $\tau_{12,eff} = \langle \cos \alpha_0 (\tau_{12} + \eta_{12} \sigma_{22} \cos \alpha_0 \sin \theta) \rangle$	$\eta_{23} = -1 / \tan 2\alpha_0$ $\eta_{12} = -\frac{S_{12} \cos 2\alpha_0}{Y_c \cos^2 2\alpha_0}$ $S_{23} = Y_c \cos \alpha_0 \times (\sin \alpha_0 + \cos \alpha_0 / \tan 2\alpha_0)$
Vogler [256]	$f_M = \alpha_1 I_1 + \alpha_2 I_2 + \alpha_3^c I_3 + \alpha_{32}^c I_3^2 > 1$ <i>for</i> $I_3 < 0$	$\alpha_1 = 1 / S_T^2$ $\alpha_1 = 1 / S_L^2$ $\alpha_{32}^c = \frac{1 - Y_C / (2Y_{BC}) - \alpha_1 Y_C^2 / 4}{Y_C^2 - 2Y_{BC} Y_C}$ $\alpha_3^c = \frac{1}{2Y_{BC}} - 2\alpha_{32}^c Y_{BC}$

Table 2-4: Matrix failure criteria in compression

Criterion	Formulation	Notes
Cuntze [48]	$\left(b_{\perp}^r - 1\right) \frac{I_2}{Y_c} + \frac{b_{\perp}^r - I_4 + b_{\perp}^r I_3}{Y_c^2} > 1$ $I_2 = \sigma_{22} + \sigma_{33}, \quad I_3 = \sigma_{22}^2 + \sigma_{33}^2,$ $I_4 = (\sigma_{22} - \sigma_{33})^2 + 4\tau_{23}^2$	The parameters b characterize the slope of failure envelopes

2.2.3 Delamination

Delamination failure occurs as a result of inter-laminar shear stresses and through-thickness stresses, resulting in separation of adjacent layers with dissimilar fibre orientation. Delamination usually starts from stress concentrations which can be found at free edges, at ply-drops, at regions subjected to out-of-plane bending such as bending of curved beams (see Figure 2.2). In general, delamination initiation does not coincide with structural failure of the laminate. However, the initiated delamination may grow in an unstable manner and finally result in an interaction of in-plane failure modes which can cause a catastrophic final failure.

Delamination initiation criteria are based mainly on two approaches, stress based criteria and fracture mechanics based criteria. In the following, some of the proposed criteria for both approaches are introduced. A review of delamination initiation criteria for both, stress based and fracture mechanics based models, can be found in [46]

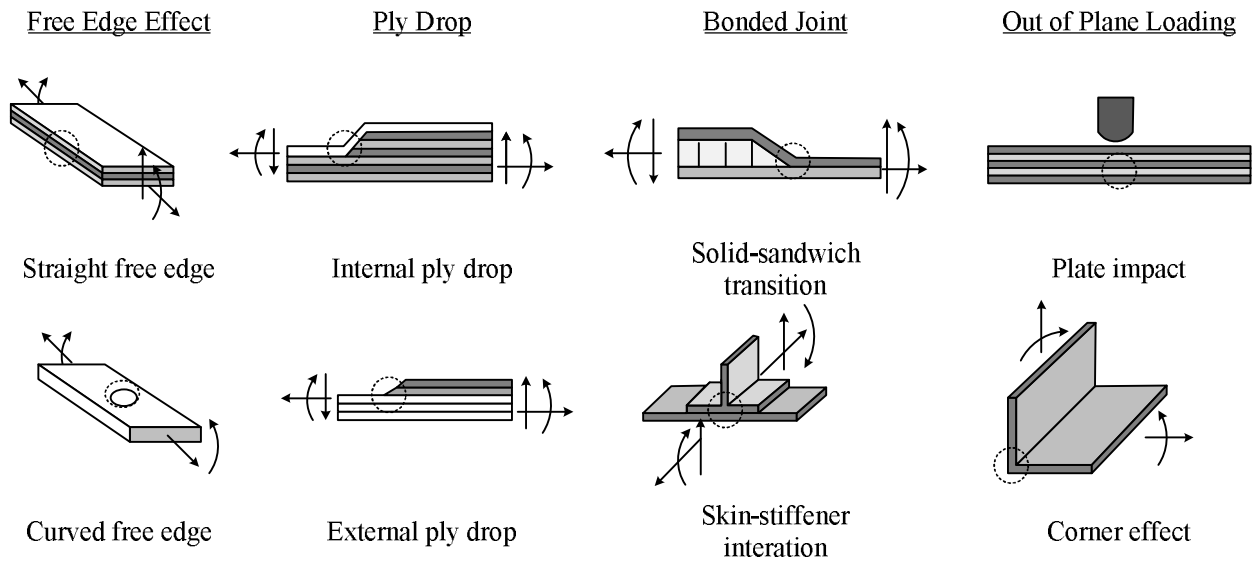


Figure 2.2: Delamination induced by inter-laminar stresses at zones highlighted by dotted circles, adapted from [206]

Several criteria are available to predict the initiation of delamination using the stress values of an interface element between plies as summarized in Table 2-5. These criteria all use combinations of the out of plane tensile and shear parameters, in linear, quadratic or curve-fit relationships.

Alternatively, delamination criteria can be formulated based on fracture mechanics. It is assumed that the material contains defects even before the onset of failure. The onset of delamination is therefore treated as a propagation of cracks which are already in the material. Strain energy release rates are calculated and failure is assumed to propagate if the strain energy release rate G reaches a critical energy release rate G_c . A simple example for this approach has been proposed by O'Brien [186]. He derived a simplified energy release rate G (energy per unit of delaminated area) as follows:

$$G = \frac{t\varepsilon^2}{2} (E_{lam} - E^*) \quad (2.1)$$

and compared it with a critical energy release rate G_c in order to find the critical strain, ε_c , for the initiation of delamination. In Equation (2.1), E_{lam} refers to the original longitudinal laminate Young's modulus and E^* refers to the longitudinal Young's modulus of the remaining sub-laminates after delamination. The variable t denotes the thickness of the laminate.

Today, the increasing use of FE solvers allows for more complex models and more accurate calculation of the energy release rates. However, in most applications stress based failure criteria are used to determine the onset of delamination and fracture mechanics based formulations find their application in the damage propagation laws that will be discussed in Section 2.3.

Table 2-5: Failure criteria for delamination

Criterion	Formulation
Max stress	$\sigma_{33} \geq Z_T, \tau_{31} \geq S_{31}, \tau_{23} \geq S_{23}$
Hashin [94]	$\left(\frac{\sigma_{33}}{Z_T}\right)^2 + \left(\frac{\tau_{23}}{S_{23}}\right)^2 + \left(\frac{\tau_{31}}{S_{31}}\right)^2 \geq 1$
Tsai [240]	$\left(\frac{\sigma_{33}}{Z_T}\right)^2 + \left(\frac{\tau_{23}}{S_{23}}\right)^2 + \left(\frac{\sigma_1^2 - \sigma_1\sigma_3}{X_T^2}\right) \geq 1$
Tong [240]	$\left(\frac{\sigma_{33}}{Z_T}\right)^2 + \left(\frac{\tau_{23}}{S_{23}}\right)^2 + \left(\frac{\sigma_1^2 - \sigma_1\sigma_3}{X_T X_C}\right) \geq 1$
Zhang [280]	$\sigma_{33} \geq Z_T$ and $\sqrt{(\sigma_{12}^2 + \sigma_{13}^2)} \geq S_{23}$
Goyal [81]	$\left(\frac{\langle \sigma_{33} \rangle}{Z_T}\right)^2 + \left(\frac{\tau_{23}}{S_{23}}\right)^\gamma + \left(\frac{\tau_{31}}{S_{31}}\right)^\gamma \geq 1, \gamma : \text{curve fit parameter}$

2.3 Progression of damage

The onset of damage in laminated composite materials does not usually lead to ultimate failure. Therefore, it is necessary to account for the progression of damage modes in order to accurately predict composite material performance in a damage tolerance analysis. Failure in a laminate may be caused by failure of individual laminae or plies within the laminate (intra-laminar failure) or by separation of contiguous laminae (inter-laminar failure) or both. Numerous models have been developed to represent the various damage mechanisms and these damage models have

been used both in conjunction with and independent of the failure criteria presented in the previous section for damage initiation.

From a computational point of view, different methods for the modelling progression of damage can be divided into two categories: the continuum approach and the discontinuous approach. In the continuum approach, the crack is smeared over a band with finite width. This is appealing because of its simple implementation in general finite element codes. However, in discontinuous approach, the crack is explicitly modelled as a displacement discontinuity in the continuum. The different types of these two approaches and related methods of implementation are briefly reviewed in the following.

2.3.1 Continuum approach

Incorporation of continuum models into the finite element framework is often straightforward as they are usually implemented in the relation between stress and strain. A continuum progressive damage methodology attempts to represent the accumulation of damage in a composite laminate by reducing selected material properties. The structure is loaded until a failure criterion is satisfied, at which point a corresponding material property or property set is reduced, and the analysis is continued. The degraded material property, most commonly stiffness, is selected so as to simulate the loss of load-carrying capacity in a particular direction. Hinton and Soden [101] have categorized the post-initial-failure models into two main groups: (a) instantaneous degradation using ply discount methods where the material is assumed to lose its entire stiffness and strength in the dominant stress direction or (b) progressive degradation using damage potential functions where the material is assumed to lose its stiffness and strength gradually in the failure direction.

2.3.1.1 Ply discount methods

Typically, for instantaneous degradation of stiffness properties once a failure criterion is reached, researchers usually apply knockdown factors that are either empirical or obtained from specific experiments [190]. Although this approach is simple, the instantaneous knockdown of properties

is particularly suited to the quasi-brittle nature of fibre-reinforced composites [102]. Examples of such methods are given in Table 2-6. However, the ply-discount progressive failure analysis of composites can underestimate laminate strength and stiffness because it does not recognize that the damage is localized and that a failed ply may have residual load-carrying capability.

Table 2-6: Ply discount models used in literature [101]

Researchers	Failure mode	Degradation of stiffness properties
Wolfe [269]	Matrix failure	$E_2 = 0, G_{12} = 0, \nu_{12} = 0$
Puck [204]	Cracking under tension Mode A	$E_2 = \eta E_2^0, G_{12} = \eta G_{12}^0, \nu_{12} = \eta \nu_{12}^0,$ η is a parameter which varies with stress
	Cracking under compression Modes B and C	$G_{12} = \eta_1 G_{12}^0, \nu_{12} = \eta_1 \nu_{12}^0,$ η_1 is smaller than η
Chamis [79,80]	Matrix failure	E_m is replaced with a negligible value and $E_1, E_2, G_{12}, \nu_{12}$ are computed from micromechanics
Sun [233,234]	Shear matrix failure	$E_2 = 0, G_{12} = 0$
	Transverse matrix failure	$E_2 = 0$
Tsai [133,155]	Matrix failure $\epsilon_{22} > 0$	$E_m = 0.15E_m^0, \nu_{12} = 0.15\nu_{12}^0$ E_2, G_{12} are computed from micromechanics
	Matrix failure $\epsilon_{22} \leq 0$	$E_2 = 0.01E_2^0, G_{12} = 0.01G_{12}^0,$ $\nu_{12} = 0.01\nu_{12}^0, E_1 = 0.01E_1^0$
Zinoviev [282]	Open cracks $\sigma_{22} > 0$	For $ \gamma_{12} < \gamma_{12}^* ,$ when (a) $\epsilon_2 < \epsilon_2^* : E_2 = \psi_2 E_2^0, G_{12} = \psi_3 G_{12}^0,$ (b) $\epsilon_2 = \epsilon_2^* : E_2 = 0, G_{12} = \psi_3 G_{12}^0,$ ψ is a function of strain For $ \gamma_{12} = \gamma_{12}^* ,$ when (a) $\epsilon_2 < \epsilon_2^* : E_2 = \psi_2 E_2^0, G_{12} = 0,$ (b) $\Delta \epsilon_2 > 0 : E_2 = 0, G_{12} = 0,$
	Closed cracks $\sigma_{22} \leq 0$	For $\Delta \epsilon_2 < 0 :$ (a) $ \gamma_{12} < \gamma_{12}^* : G_{12} = \psi_3 G_{12}^0$ (b) $\Delta \gamma_{12} < 0 : G_{12} = 0$

2.3.1.2 Continuum damage-based methods

A more straightforward option is the progressive degradation based on continuum damage mechanics (CDM). The loss of stiffness can be considered as the macroscopic representation of a series of distributed microcracks. The simplest formulation is by introducing phenomenological damage tensor $\mathbf{H}(\omega)$ relevant to failure modes written as [36]:

$$\boldsymbol{\sigma} = \mathbf{H}(\omega)\mathbf{C}^e \boldsymbol{\varepsilon} = \mathbf{C}(\omega)\boldsymbol{\varepsilon} \quad (2.2)$$

where $\mathbf{C}(\omega)$ is the stiffness tensor and the damage tensor, $\mathbf{H}(\omega)$, is in terms of damage parameters ω for different damage modes, which grows from 0 to 1 during failure. Generally, the stiffness degradation is computed explicitly from the strain, which make the implementation of continuum damage straightforward. Kachanov [119] introduced for the first time the concept of smearing damage due to microcracking over a continuous medium and representing this damage by single scalar variable to study creep in metals. Scalar damage representations are appropriate for isotropic damage, where the damage is randomly distributed, or in cases that the void density is small [179]. To describe anisotropic damage, a higher-order representation of damage is required. These tensor forms accommodate descriptions of damage that include damage in various directions as well as interactions of damage parameters in the different directions. Several damage models have been developed that describe damage as a second order tensor [36] or as a fourth order tensor [188,222,223].

The thermodynamic formulation is usually used as a general framework to formulate constitutive equations. The Helmholtz free energy per unit mass for a damaged solid is expressed in terms of internal state variables, namely damage parameters:

$$\rho\psi = \rho\psi(\boldsymbol{\varepsilon}_{ij}, H_{ij}) \quad (2.3)$$

where ψ is the free energy function which represent the elastic deformations and ρ is the density. The thermodynamic conjugate forces Y_{ij} corresponding to the internal variables H_{ij} (i.e. damage parameters) are expressed as:

$$\sigma_{ij} = \rho \frac{\partial \psi}{\partial \varepsilon_{ij}}, \quad Y_{ij} = \rho \frac{\partial \psi}{\partial H_{ij}} \quad (2.4)$$

The thermodynamic formulation gives the thermodynamic forces and the dissipation inequality equation but no information about the evolution laws for internal variables. The only restriction imposed by the continuum thermodynamics on the evolution laws is that the Clausius–Duhem dissipation inequality must be fulfilled, which takes the following form:

$$\gamma = -\rho \dot{\psi} + \sigma_{ij} \dot{\varepsilon}_{ij} \geq 0 \quad (2.5)$$

where γ is the power of dissipation due to damage and a dot denotes the rate with respect to time. From Equations (2.1)-(2.5), the dissipation inequality is expressed as

$$\gamma = Y_{ij} \dot{H}_{ij} \geq 0 \quad (2.6)$$

If the dissipation reaches the maximum, the damage evolution law is given by:

$$\dot{H}_{ij} = \dot{\lambda}^d \frac{\partial F^d}{\partial Y_{ij}} \quad (2.7)$$

where $F^d(H_{ij}, \varepsilon_{ij})$ is the damage potential function, $\dot{\lambda}^d \geq 0$ is called the consistency parameter and it is assumed to obey the Kuhn-Tucker consistency requirements:

$$\dot{\lambda}^d \geq 0, \quad F^d \leq 0, \quad \dot{F}^d = 0 \quad (2.8)$$

When the damage potential function $F^d(H_{ij}, \varepsilon_{ij})$ is determined, the damage evolution information can be acquired. Then, as the consistency parameter λ^d is derived, the damage tensor and internal variable as well as the consistent constitutive equations are obtained. A popular approach to formulate the evolution law is based on the hypothesis of maximum damage dissipation, which is analogous with the associate flow rule in plasticity. In this approach, the evolution of each damage parameter is governed by its work conjugate that are also called the energy release rate density parameters.

A more general approach motivated by the non-associated flow rule in plasticity defines a potential of dissipation function, $F^d(H_{ij}, \varepsilon_{ij})$, and damage evolution law is written in terms of the conjugates of each damage parameter with respect to the dissipation potential function. The choice of the dissipation potential function depends on the available test data and the purpose of

the damage model. The hypothesis of maximum damage dissipation can be seen as a special case where the Helmholtz free energy $\psi(\varepsilon_{ij}, H_{ij})$ is chosen as the dissipation potential.

Kwon and Liu [134], Schipperen [216], Maa and Cheng [159], Camanho et al. [33], Barbero and Vivo [17] established the thermodynamic models to describe the progressive failure properties and to interpret the stiffness degradation of composite laminates. In their models, the various failure modes were assumed and the relationships between the damage tensor, conjugate forces and internal stresses/strains were further formulated.

Based on the CDM theory, Ladevèze [136], Schapery [215], Hayakawa et al. , Basu et al. [19], Pinho et al. [197,198], Maimí et al. [161,162], Laurin et al. [145] and Camanho et al. [33] proposed the isotropic/anisotropic stiffness degradation models and damage evolution models. In these models, the relationships between the damage dissipation potential, the conjugate forces and the damage tensor were addressed, which were explained by different damage evolution laws for different damage modes. These models are well suited to be used as a mesoscopic model where intra-laminar damage modes in the plies are captured using CDM.

Apart from thermodynamically based damage laws, damage growth can also be related to statistical variations in the strength of a material. Damage is related to the probability that a given stress or strain state is likely to exceed the strength of the RVE. A common statistical approach to describing variations in the strength of materials is Weibull's formulation [261]. Weibull's probability distribution function has been implemented into a number of models [131,152,166,268]. An example is the damage in Matzenmiller's model defined in one dimension as:

$$\omega = 1 - \left(\frac{\varepsilon}{\varepsilon_f} \right)^e e^{\left[\frac{1}{me} \left(\frac{\varepsilon}{\varepsilon_f} \right)^m \right]} \quad (2.9)$$

where e is the exponential function, m is the Weibull modulus, and ε_f is the nominal failure strain. A major shortcoming of such models, however, is the difficulty in relating the statistical parameters to physical characteristics of the problem. Selection of the Weibull

modulus, m , can be quite challenging without a priori knowledge of the statistical variation of the nominal failure strain in the specific material examined.

Despite the advances in progressive damage modeling, recent studies indicate that CDM models coupled with cohesive zone models (CZM) in a mesoscopic context may not always represent laminate failure sequences properly [251]. These deficiencies are particularly evident when the observed fracture mode exhibits matrix splitting or when the fracture is characterized by a strong coupling between transverse matrix cracking and delamination. The deficiencies of the predictive capabilities can be attributed to several factors, including the incorrect prediction of the damage zone size normal to the fracture direction when using crack-band models, and the inability of local CDM models to reliably predict matrix crack paths. These limitations are mostly due to the fact that CDM models are usually implemented as “local” rather than “non-local” models [72,116,193,194] i.e., the evolution of damage in a local CDM model is evaluated at individual integration points without consideration of the state of damage at neighboring locations, and the inability of standard finite elements to represent localized shear bands. Therefore, the commonly used crack-band approach for regularizing CDM models cause the damage to localize into a band with a width equivalent to the element dimension and may not predict correctly the width of the damage zone nor the local stress field. Consequently, stress redistribution resulting from damage development may be inaccurately predicted and can potentially result in inaccurate representation of damage mode interactions and failure sequences. However, as will be discussed in this thesis, using the non-local methods for regularization of CDM models can significantly alleviate the above-mentioned problem.

In order to improve the predictability of CDM models in a mesoscopic approach, some researchers use aligned mesh structure for each ply of the composite laminate [183,229]. The edges of elements are parallel with the direction of the fibre orientation in each ply. This method has been successful to some extent by enforcing the matrix cracks to grow in parallel with the fibre direction [229].

2.3.2 Discontinuous approach

The alternative to smearing a crack over the continuum is to insert a discontinuity in the displacement field. Although this is a more intuitive approach to failure, since displacements really are discontinuous over a crack, it requires more fundamental changes to the finite element formulation. In general, the kinematical formulation has to be adapted to accommodate the discontinuity. One of the most common applications of discontinuous approach is in prediction of delamination growth.

One of the most popular tools for simulating the propagation of delamination in composites, are methods that are based on linear elastic fracture mechanics (LEFM) theory. It states that after the onset of delamination, the delamination propagation is not controlled by the through-thickness strength any more, but by the inter-laminar fracture toughness, mainly the critical strain energy release rate G_c . The basic numerical implementation of these methods usually involves computing the total strain energy release rate G , or in mode dependent models, G_I and G_{II} associated with normal opening mode and shear mode are computed separately. Comparing these values to some critical values G_c (G_{Ic} and G_{IIc} in case the model is mode dependent) usually serves as the delamination propagation criteria. Once the local value reaches the critical value, the delamination front will propagate.

LEFM based methods such as the J-integral proposed by Rice [211] which is limited to plane structures can be used to calculate the energy release rate. For complex 3D laminated structure, however, the virtual crack closure technique (VCCT) initially proposed by Rybicki and Kanninen [213] can calculate the fracture parameters at the crack tip for the mixed fracture modes more effectively than the J-integral. The main assumption in the finite element calculations using the VCCT is that the energy required for the crack propagation length Δa is equal to that required for closing two separate crack surfaces with the crack length Δa . Since using VCCT method does not require any information on the stress field around the crack tip, it does not require a very fine mesh around the crack front, which is a very important advantage in

comparison with J-integral method. A comprehensive review of the state-of-the-art of VCCT was recently presented by Kruenger [132].

However, the VCCT cannot be competent for the prediction of the failure initiation and subsequent evolution for the cracking composite laminates since the self-similar crack propagation mode is assumed. Accordingly, the cohesive zone models (CZM) are becoming more common, particularly for progressive failure analysis with non-self-similar crack growth.

Cohesive based approaches is based on the early work by Barenblatt [18], who showed that the fracture process zone in the region near the crack tip can be modelled as a lumped line with its nonlinear behaviour governed by a form of stress-displacement law which exhibits softening. The rest of the model is assumed to behave elastically. As shown in Figure 2.3, the variation of stress-strain is shown in the fracture process zone. The point with zero displacement is called the fictitious mathematical crack tip and the point at which the crack surface traction vanishes is called the physical crack tip. To control the amount of energy that is dissipated in the crack as it propagates and to remove the singularity from the stress field at the crack tip, cohesive forces are applied on the crack surface. This means that a second constitutive law is introduced besides the constitutive law for the continuum. This ‘cohesive law’ relates the cohesive traction \mathbf{t} to the size of the displacement jump over the crack $[[\mathbf{u}]]$ (i.e. $\mathbf{t} = \mathbf{t}([[\mathbf{u}]])$). Cohesive based approaches have the advantages to investigate both initiation and growth of damage in the same analysis, and to incorporate both strength and fracture mechanics theories. Also, as opposed to classical fracture mechanics, this approach does not require the assumption of an initial damage size or propagation direction for delamination, and eliminates the need to apply difficult and computationally expensive re-meshing to accommodate the propagating delamination front.

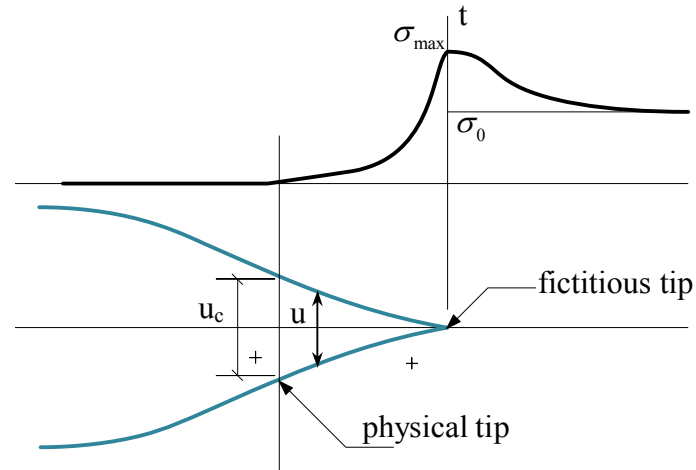


Figure 2.3: Fracture process zone in cohesive crack models- adapted from [176]

Following the earlier work of Dugdale [60] and Barenblatt [18], later Hutchinson and Suo [104], Tvergaard and Hutchinson [247], Allen and Searcy [13], Camanho et al. [32], Xie and Waas [275], Turon et al. [245] developed the cohesive theories which assume there is a process zone in front of the crack tip whose fracture properties are controlled by the cohesive traction-displacement discontinuity relationships, and allows non-self-similar crack propagation.

Delamination fracture tends to be a mixed-mode phenomenon. Camanho et al. [31] developed a cohesive law in which the fracture toughness is a phenomenological function of mode mixity as formulated by Benzeggagh and Kenane [28]. This cohesive law was improved for thermodynamical consistency by Turon et al. [243]. Alternative formulations have been proposed among others by Allix and Corigliano [14], Yang and Cox [276] and Jiang et al. [114]. Table 2-7 summarizes a number of criteria in cohesive law formulations for predicting the growth of pre-existing delamination. These criteria are all based on the fracture mechanics concept of a strain energy release rate, G , in crack growth, and combine the G components with the threshold G_c toughness values in the mode I, II and III directions.

Table 2-7: Criteria for growth of delamination

Criterion	Formulation	Notes
Single mode	$G_I \geq G_{Ic}, G_{II} \geq G_{IIc}, G_{III} \geq G_{IIIc}$	
Power law delamination [264]	$\left(\frac{G_I}{G_{Ic}}\right)^m + \left(\frac{G_{II}}{G_{IIc}}\right)^n + \left(\frac{G_{III}}{G_{IIIc}}\right)^p \geq 1$	m, n, p : curve fit linear: $n=m=p=1$ quadratic: $m=n=p=2$
Benzeggagh and Kenane [28]	$G_T \geq G_{Ic} + (G_{IIc} - G_{Ic}) \left[\frac{G_{II}}{G_I + G_{II}} \right]^\eta$	η : curve fit $G_T = G_I + G_{II} + G_{III}$

While it has been successfully used to predict the delamination failure mechanisms of dissimilar material interfaces, the cohesive theory extends rapidly to predict the failure initiation and damage evolution in the progressive failure analysis of composite laminates.

The implementation of cohesive zone models in finite element methods can be done either using interface elements/surfaces or using partition of unity finite element methods as described below.

2.3.2.1 Interface elements/surfaces

The most straightforward implementation of a discontinuous approach is to have the discontinuity between the elements. Duplicate nodes are used along the crack path to describe a jump in the displacement field (see Figure 2.4). Interface behaviour is determined by the constitutional relationship (mostly based on cohesive zone models) between the relative displacement of the two connected nodes, and the traction generated between them as a result.

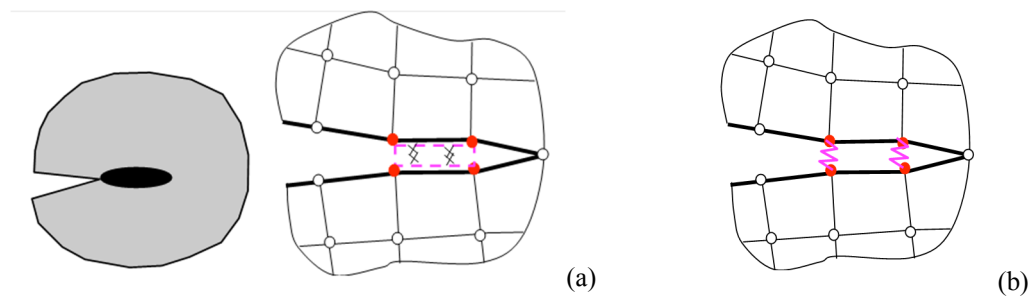


Figure 2.4: Application of continuum and lumped interface elements in a discontinuous approach, adapted from [274]

Cohesive zone models in the form of node to node 1D elements [47], or continuous interface elements [31], or cohesive contact formulations [29] are used to define the behaviour of an interface in finite element methods. These models are increasingly being applied by researchers to model delaminations and debonds in composite structures. After the element passes the strength limit of the material, the stiffness is reduced gradually. This continues until the interface has zero stiffness, at which point the substructures are completely separated, and the interface element acts only as a contact region to prevent any interpenetration of the two debonded surfaces. In the cohesive element formulation, the work done in reducing the material stiffness to zero is equal to the fracture toughness (G_c). This will incorporate fracture mechanics theories into the damage mechanics-based approach.

Wisnom, Hallett and coworkers have successfully studied behaviour of different notched and un-notched geometries using the interface elements to capture the effect of both intra-laminar damage modes and delamination [87,88,114,153,235]. This, however, requires fine and specific mesh arrangement for each ply and is less predictive as a result of pre-insertion of interface elements at priori known crack paths. Therefore, the direction of crack growth and the location of major macrocracks have to be known from the experiments in order to use the interface elements in an optimal way [87,88].

For the specific case of simulating delamination in composite material, it is known that the crack propagation plane is located in between dissimilar plies through the thickness of the laminate. This reduces the complexity of the problem by simply putting the cohesive elements in between the plies.

2.3.2.2 Partition of unity finite element method

An alternative class of methods for modelling of cracks is based on enrichment of the finite element solution basis with discontinuous functions, referred to as the Partition-of-Unity Finite Element Method (PUFEM) [16] or the eXtended Finite Element Method (XFEM) [176]. Based on the partition of unity property of the finite element shape functions, any function can be added to the basis functions in order to improve its accuracy. Belytschko and Black [27] and Moës et

al. [177] were among the first groups who added a discontinuous function in form of Heaviside function for the modelling of cracks. In this way, a discontinuity can be running through the elements, which obviously offers more flexibility for the crack path than interface elements.

Originally, asymptotic functions were used for enrichment around the crack tip to approximate the singular stress field. Alternatively, it is possible to add cohesive tractions on the crack surface, as proposed by Wells and Sluys [263] and Moës and Belytschko [176]. In this case the crack tip singularity is removed from the stress field.

Iarve et al. [105] used PUFEM to model matrix cracking in unidirectional composites with a smooth enrichment function instead of standard Heaviside functions. In this case, the matrix crack were inserted a priori without progressive damage modeling which was later added in [107] that includes the interaction with delamination as well. They used this approach to model the over-height compact tension tests [178], where they used a statistical strength distribution to obtain a random crack pattern and a CDM criterion to capture fibre breakage.

An alternative method has been proposed by Hansbo [90], in which two overlapping elements are introduced with independent displacement fields which are partially active. This method is commonly known as phantom node method (PNM). In other words, once an element is cut by a discontinuity, extra nodes are added to the original nodes and two superposing sub-elements are formed. Effectively, only part of the domain in each sub-element is active, and the stiffness and nodal force integration is only performed on this active part of the domain. When modelling a strong discontinuity, the PNM becomes equivalent to the XFEM with the Heaviside enrichment function [230]. Cohesive tractions were also applied in this method by Mergheim et al. [175]. An advantage of Hansbo's method over PUFEM is associated with its relatively easier implementation, because the method does not require any changes to be made in the elements adjacent to the cracked elements.

PNM in combination with cohesive interface elements have been shown to be able to model interaction of intra-laminar macroscopic matrix cracks and delamination. An example of this is the failure modelling of open-hole composite laminates by Van Der Meer et al. [253]. Another

example is the matrix cracking induced delamination modelled by PNM and breakable CZM cohesive elements [208] which combines discrete matrix cracking with cohesive interface failure in composite laminates under flexural loading.

While the PNM is well suited for modelling an individual discontinuity within an element, extensions which allow modelling more complex networks of discontinuities (such as multiple intersecting cohesive cracks) become considerably more challenging. Moreover, both XFEM and PNM introduce an error in the representation of the geometry of discontinuities while mapping the discontinuities from the physical to the natural space of the elements [36]. To prevent this issue, a new method called the floating node method (FNM) is introduced by Chen et al. [41], which is similar to the PNM in terms of computational methodology, where discontinuities within an element are modelled by partitioning the original element into sub-elements. However, the FNM directly uses crack boundary coordinates for the definition and transformation of the sub-elements, as opposed to PNM which uses the coordinates of the phantom nodes instead. This reduces the error in the representation of discontinuities in the natural coordinates associated with the PNM and XFEM. Additionally, FNM is more suited for modelling weak and cohesive discontinuities.

2.4 Status of numerical methods in composite structural design

The expansion of composites application in the industry has led to an increasing demand for an effective design methodology suitable for heterogeneous materials such as continuous fibre reinforced systems. An emerging idea represented by “integrated product development”, has been introduced in the Composite Materials Handbook-17 [1], which can be applied to the development of new products in most of the major industries. The collective judgment and insight for designing a new product can be obtained from an appropriate balance between the coordinated testing and analysis activities that are represented by the “integrated product development pyramid”, alternatively known as the “Building Block Approach”. A specific illustration related to aerospace products is shown in Figure 2.5.

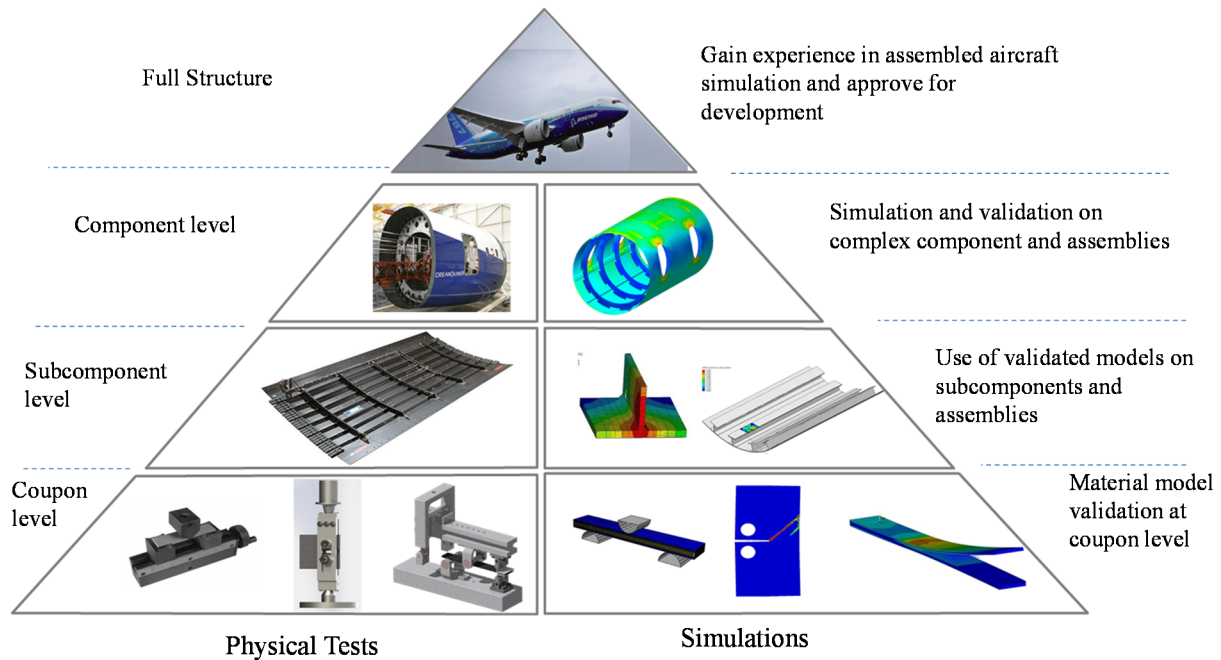


Figure 2.5: Building Block pyramid

The idea is to build the knowledge on the material and structural behaviours step by step, starting from the fundamental stage at the coupon level up to the full scale (i.e. the full wing or even the full aircraft). It is widely acknowledged that tests can be expensive when repeated several times for different material configurations (e.g. different stacking sequences) or when changes in the components geometry or loading are studied, and so using virtual testing can help reduce the product development costs. Physically insightful methods of analysis and thoroughly verified numerical methods can be employed as virtual test to replace some of the physical tests specifically at the coupon level. Having developed the material basis values and design allowable including some correlation with predictive methods at the coupon level, the critical subcomponents at higher level can be identified for test evaluation and analysis using the knowledge built at the coupon level. At higher levels, the verification of the structural integrity of the full-scale structure can be verified based on consideration of the most critical load conditions for the structure that has been determined by test/analysis correlation at previous levels. The numerical analysis at lower level, therefore, can be more useful in understanding the major mechanisms of damage that will be critical in subcomponent and complex assemblies.

In summary, effective product development usually depends to a large degree on the insight and judgment gained from integrated test and analysis efforts. Therefore, having a physically based analysis method that is fully verified and can be readily and efficiently used in practice is of great value. A summary of the ongoing methodologies and techniques adopted by various research groups around the world as well as those available in commercial FE software packages are listed in Table 2-8.

There have been some landmark studies to assess existing computational models in the field of composite materials. Three of the major studies that have been done so far are presented in the following.

2.4.1 World-Wide Failure Exercise (WWFE)

The so-called World-Wide Failure Exercise (WWFE) [102] was conducted as a landmark study on the effectiveness of numerical approaches including failure theories and constitutive models.

The goal was to (1) assess the predicting capability of the numerical approaches, (2) to close the knowledge gap between theoreticians and design practitioners in the field and (3) to provide design engineers with more robust and accurate failure prediction methods [102]. To do this, Hinton and Soden ('the organizers') laid out a plan for a unique blind study of failure theories for composite laminates. This was done in three stages. The first and second stages involved assessment of failure criteria in composite structures under 2D and tri-axial state of stresses [102]. The third world-wide failure exercise [120] was concerned with damage evolution under uniaxial, biaxial, bending and loading/unloading scenarios in combination with ply constraint, stacking sequence and thermal effects as well as interacting failure modes.

The organizers selected a number of test cases for the failure theories to examine. The test cases were limited to continuous fibre reinforced thermoset plastics, and specifically to two types of carbon fibres, two types of glass fibres (E-glass), and epoxy resin systems. The test cases included a wide range of lay-ups, a wide range of loading conditions, a variety of damage types, and behaviours that were linear and non-linear. For each lay-up and loading scenario, there were

requirements to determine failure stress envelopes, both initial failure and final failure, and stress-strain curves for loading in specific directions, depending on the case. Leading researchers in failure of composites were invited to participate and to present their approaches and predictions.

Hinton and Soden summarized and compared the similarities and the differences between predictive capabilities of the leading theories [100,101,122,227]. They assessed the performance of the participating theories in three ways. Qualitative assessments of the correlation between the theories and the experiments were made on a test-by-test basis and on a theory-by-theory basis, and they performed a quantitative assessment of the performance of the theories using 125 tests that they developed in five categories: the biaxial strength of unidirectional laminae (UD), the initial biaxial strengths of multidirectional laminates (MD), the final strengths of MD laminates, the deformation (stress-strain curves) of MD laminates, and the ability of the theory to predict general trends.

Of the theories that performed well, Zinoviev [282,283] and Puck [204] were phenomenological approaches, while the Tsai approach [133,155] is an interactive failure criterion approach. Those theories that performed poorly consisted of Sun [233,234], an interactive approach, Eckold [62], a design code approach, and McCartney [168,169], a damage mechanics approach. All three of these theories did not address all of the test cases, which significantly affected their ranking by the organizers.

The organizers developed a number of recommendations for designers on the basis of the results of the WWFE. They noted that for isolated laminae, the theories were fairly mature, and recommended using either Tsai or Puck for these types of analyses. In attempting to predict the initial strength of MD laminates, the theories were all fairly poor. In recommending approaches to predict initial failure, Zinoviev [282,283] and Wolfe [30,269] were recommended. A similarly poor performance exists for predicting the final strength of MD laminates. Puck, Zinoviev, Tsai, and Hart-Smith(3) [92,93] were recommended, but the organizers noted that the best a designer could hope for was $\pm 50\%$ accuracy. Deformation predictions were only reasonably accurate when fibre failure was the dominant mode of failure. Zinoviev and Puck were recommended.

The organizers noted that in this context, “lack of robustness is a feature”. For situations where the prediction of other features, such as the mode or sequence of failure, is required, once again Puck and Zinoviev were recommended.

Several lessons can be learned from the WWFE. Firstly, most criteria were unable to capture some of the trends in the experimental results. Secondly, most expressions proposed to predict each failure mode are still to some extent empirical. From the limited predictive capabilities of the most accurate analyses available, it is clear that further developments in failure models are required before any analysis approach can be used with confidence to predict the strength of a typical composite component. In conclusion, this exercise highlighted the gap between the theoreticians and designers. The designers need easy to use software tools to perform the analyses of composite laminates. Therefore, the theoreticians need to recognize the trade between a complex theory and a practical predictive tool.

2.4.2 Composite Materials Handbook (CMH-17): Crashworthiness Section

The Composite Materials Handbook-17 (CMH-17) is the product of another example of extensive studies done by experts from the industry, academia and regulators, which is supported by the Federal Aviation Administration (FAA) in the United States. It provides reliable guidelines and standards for design, fabrication, characterization, test and maintenance of composite materials and structures. A round-robin exercise was initiated in 2008 as part of the CMH-17 crashworthiness and energy management activities. Its main purpose was to assess the performance of various commercial FE codes, in predicting the crush response of a number of composite components. Commercial code vendors, academia and industry participants willing to participate in this exercise have attempted to use the current capabilities of explicit FE codes, LS-DYNA, Abaqus/Explicit, PAM-Crash, and Radioss, to tackle these challenging problems. This is an on-going simulation effort backed by testing program for their validation that is progressing from the base level of the building-block consisting of small scale and simple coupons through to sub-assemblies of configured composite components that are representative of crash absorbing structures.

2.4.3 Damage tolerance design principles (DTDP) program

More recently, Air Force Research Laboratory (AFRL) funded a program called “Damage Tolerance Design Principles (DTDP)” with the goal to evaluate existing technology in composite damage progression modeling and prediction, and evaluate them for application to future damage growth analysis needs. This program was limited to participants from analysis teams based in USA including: (1) the University of Michigan, who is running the NASA Glenn MAC/GMC software, Enhanced Schapery Theory, and NCYL, (2) AlphaSTAR, who is running their GENOA software, (3) Multiscale Design Systems, who is running their MDS-C software, (4) Autodesk, who is supporting LM Aero on the application of their ASCA software, (5) Vanderbilt University, who is running their Reduced-order Space-Time Homogenization software; (6) Global Engineering and Materials, Inc., who is running their X-FEM software, and (7) University of Dayton Research Institute, who is running their BSAM software.

The goal of this study was to assess the ability of emerging progressive damage analysis methods to predict the type and location of damage as a function of fatigue cycles and to predict the residual strength and stiffness after fatigue. This research project was expected to assess the ‘readiness’ of various progressive damage analysis tool for design application. This program conducted through four separate contracts. The largest was with Lockheed Martin Aeronautics Company who led the study for the first four analysis teams mentioned above. The other three teams were part of three separate contracts being led by the Aerospace Systems (RQ) and Materials and Manufacturing (RX) Directorates of AFRL.

In the first phase of the program, AFRL and Lockheed Martin (LM) assessed the ability of nine different analysis methods to predict the mechanical response of open-hole coupons made of IM7/977-3 with three different layups $[0/45/90/-45]_{2s}$, $[60/0/-60]_{3s}$ and $[30/60/90/-60/-30]_{2s}$ under static and fatigue tensile and compressive loading conditions. They were asked to blind predict the static strength of unnotched and notched coupons and once they delivered the predictions, they were allowed to review the test data and make “recalibrations” to their models if need be. The same process was repeated for notched fatigue coupons. Each analysis team ran simulations to predict the residual static properties, damage progression, and stiffness degradation as a

function of cycles. Some of the assessments are published by Engelstad and Clay [63,64] for fatigue test of open-hole laminate layup $[0/45/90/-45]_{2s}$, which indicates that the fatigue average blind prediction error in terms of residual stiffness and strength was 21%, and the recalibrated error was 10%, a factor of two improvement over the blind predictions.

Among the factors that they found essential in the predictions were, having finite element modeling expertise regardless of the level of complexity of the damage formulations, adjusting for mesh dependency in damage analysis, including the inter-laminar damage in the analysis. It is specifically noted that inter-laminar fatigue is an important failure mode for aircraft structure, and a focus on maturing this capability would be very important. Most of the micromechanics-based (multi-scale) analysis teams did not include discrete (cohesive based) inter-laminar damage in their analysis which led to loss of accuracy in the results.

2.5 Summary

In this chapter, different scales of damage in composite materials were discussed. An overview of the current failure theories for prediction of the initiation of various damage modes including fibre failure, matrix failure and delamination was provided.

Common computational methods to simulate the progression of damage in composite structures, namely the continuum and discontinuous approaches were presented in this chapter. Table 2-8 provided a summary of different research groups that pursue one or combination of the presented numerical methodologies in an attempt to address different attributes of composite structures including static, dynamic, impact and crash analysis.

Based on the landmark studies that were described in this chapter, there are still technology gaps in both experimental and computational methods. The objective of this study is to improve the computational modeling of progressive failure of composite laminates. The focus is primarily on the meso-level and we will work towards a framework in which different failure processes are taken into account. The main challenge is to account for the interaction of these damage processes without compromising the efficiency of the modeling framework. To formulate

physically based, reliable and robust models is one thing, but to characterize the input material properties and calibrate them is at least as challenging. This is therefore one of the main issues that has been tried to address in the development of the proposed framework.

Table 2-8: An overview of the ongoing research on simulation of damage in composites at various research institutes and finite element vendors around the world including sample articles/references and model scales as well as their capabilities and applications, extended from [73]

Research Group/FE Vendors	Sample References	Scales			Capabilities and Applications
		Micro	Meso	Macro	
University of Liege, Computational & Multiscale Mechanics of Materials	(Wu, Noels et al. 2012) [271] (Wu, Noels et al. 2013) [272]	x		x	2-phase composites with moderate fibre volume fraction (unidirectional)
Polytechnic University of Madrid	(Llorca, Gonzalez et al. 2011) [156]	x		x	2-phase unidirectional composites
Northwestern University Michigan University	(Smilauer, Hoover et al. 2011) [226]		x	x	2-phase braided composites
Ohio State University	(Ghosh, Bai et al. 2007) [78] (Raghavan, Li et al. 2004) [205]	x	x	x	Matrix with particle reinforcements
Luisiana State University	(Voyiadjis, Deliktas et al. 2001) [257]	x		x	Transverse matrix cracking
LMT-Cachan	(Lemaitre, Desmorat et al. 2000) [150] (Ladeveze 2004) [137] (Ladeveze, Nouy 2003) [139]		x x x		Examples shown for unidirectional and woven materials but applicable to various architectures
University of Illinois at Urbana- Champaign	(Inglis, Geubelle et al. 2008) [109]	x		x	Transverse crack in matrix
Delft University of Technology	(Nguyen, Stroeven et al. 2012) [182] (Van Der Meer, Moës 2012) [250]	x	x	x x	Can be applied to transverse matrix cracking Mixed cohesive-XFEM for Laminates

Table 2-8: An overview of the ongoing research on simulation of damage in composites at various research institutes and finite element vendors around the world including sample articles/references and model scales as well as their capabilities and applications, extended from [73]

Research Group/FE Vendors	Sample References	Scales			Capabilities and Applications
		Micro	Meso	Macro	
Columbia University	(Fish, Yu 2001) [69]	x	x	x	Transverse matrix cracking
Texas A&M University	(Singh, Talreja 2009) [224]	x	x		Matrix cracking in multi-directional laminate
University of Girona University of Porto	(Maimi, Camanho et al. 2007) [161]		x x	x	Ply-based (unidirectional lamina) Sub-laminate
NASA Lewis Research Centre NASA Glenn Research Centre	(Chamis, Murthy et al. 1996)[37]	x	x x	x	Multi-scale framework Part of the WWFE I
Clarkson University AlphaSTAR GENOA	(Abdi, Godines et al. 2015) [9]	x	x		Multi-scale progressive failure analysis involving damage and fracture evolution GENOA supports the following strength-based failure criteria: maximum stress/strain, Tsai-Wu, Tsai-Hill, Puck, Hoffman and Hashin. Various specific micromechanical degradation approaches are available to model matrix defects or residual stresses due to curing and manufacturing effects. Fibre failure in tension and compression can be modelled with probabilistic Weibull strength distribution. Standard CZM and VCCT features are implemented in GENOA. Constitutive modelling is available to implement subroutines in FORTRAN, C/C++ and PYTHON.
AutoDesk/LM Aero	(Dalgarno, Robbins 2012) [50]		x	x	Using constituent average stress states to predict damage and failure of the constituents Autodesk Simulation Composite Analysis (ASCA) software

Table 2-8: An overview of the ongoing research on simulation of damage in composites at various research institutes and finite element vendors around the world including sample articles/references and model scales as well as their capabilities and applications, extended from [73]

Research Group/FE Vendors	Sample References	Scales			Capabilities and Applications
		Micro	Meso	Macro	
Autodesk/Helios	http://www.autodesk.com/products/helios-composite/overview				<p>Autodesk Helios Composite is a standalone package that offers a collection of analytical tools for conceptual design of composite materials.</p> <p>Helios Progressive Failure Analysis (PFA) is an add-on for commercial FEA programs and provides multiscale simulation capabilities. It is compatible with Abaqus, Ansys and MSC products, Multiple failure criteria are available to enable users to view damage effects in the fibre and matrix and identify multiple modes of failure.</p>
Ansys Composite PrepPost	http://www.ansys.com/		x	x	<p>Various failure criteria are available: maximum stress/strain, Tsai-Wu, Tsai-Hill, Hashin, LaRC, Cuntze and Puck. Degradation is coupled with the Chang and Chang softening model [39]. VCCT capability is implemented.</p> <p>CZM interfaces can be defined in terms of maximum relative displacement at interface and critical fracture energy values.</p> <p>User defined material models can be implemented in UPFs (User-Programmable Features) written in C or FORTRAN.</p>

Table 2-8: An overview of the ongoing research on simulation of damage in composites at various research institutes and finite element vendors around the world including sample articles/references and model scales as well as their capabilities and applications, extended from [73]

Research Group/FE Vendors	Sample References	Scales			Capabilities and Applications
		Micro	Meso	Macro	
Abaqus Simulia	http://www.3ds.com/products-services/simulia/				<p>Damage initiation can be controlled by maximum stress/strain criterion or two-dimensional Hashin's criteria.</p> <p>Material degradation due to damage is governed by linear or exponential softening.</p> <p>CZM is available in the form of cohesive surfaces or elements in two- and three-dimensional applications.</p> <p>VCCT is implemented in combination with several linear, bilinear and mixed-mode fracture criteria.</p> <p>X-FEM is possible. A pre-crack (if existing) and a potentially cracked domain need to be defined by the user a priori.</p> <p>User defined constitutive modelling can be implemented in C or FORTRAN through USDFLD or UMAT subroutines for implicit solvers and VUSDFLD and VUMAT in explicit problems.</p>
LSDYNA	http://www.lstc.com/				<p>Initiation and progression of damage in composites is available through Chang and Chang's failure criteria with associated strength and stiffness degradation [39].</p> <p>Other failure criteria such as Tsai-Wu or maximum strain criterion are also available. Strain rate effects can additionally be considered.</p> <p>The material library is frequently updated in order to provide most recent developments such as the non-local sub-laminate based CDM approach (MAT219) or orthotropic continuum damage models (MAT261 and 262).</p> <p>Cohesive surfaces/elements are available in combination with mixed mode or trilinear traction-separation law.</p> <p>VCCT approach is implemented.</p>

Table 2-8: An overview of the ongoing research on simulation of damage in composites at various research institutes and finite element vendors around the world including sample articles/references and model scales as well as their capabilities and applications, extended from [73]

Research Group/FE Vendors	Sample References	Scales			Capabilities and Applications
		Micro	Meso	Macro	
MSC Patran/ Marc/ Mastran	http://www.mscsoftware.com/				Damage initiation can be determined by maximum stress/strain, Hill, Hoffman, Tsai-Wu, Hashin and Puck criteria. VCCT and CZM capabilities are implemented. User defined failure models can be incorporated through UFAIL subroutines.
University of Dayton Research Institute (UDRI)	(Iarve, Hoos et al. 2016) [107]		x	x	B-spline interpolated finite element approach Embedded mesh independent through thickness cracks or in-plane delaminations in a similar manner to X-FEM
University of California, Berkeley	(Matzenmiller, Lubliner et al. 1995) [166]		x		Unidirectional lamina
Technical University of Denmark Georgia Institute of Tech	(Talreja 1985) [238] (Talreja 1989) [237] (Lacy, McDowell et al. 1997) [135]		x		Unidirectional lamina Short fibre composites
University of Illinois at Chicago	(Krajcinovic 1985) [130]	x	x		Unidirectional lamina
NPL Materials Centre, UK	(McCartney 2005) [167]		x		Unidirectional laminate
Louisiana State University	(Voyiadjis, Deliktas 2000) [258]		x	x	Composite Laminates
RPI and Northwestern	(Cusatis, Beghini et al. 2008) [49]		x		Micro-plane based damage model for unidirectional lamina
US Airforce Materials Lab Hercules Materials Tech. Dept.	(Tan, Nuismer 1989) [239]			x	Matrix cracking in laminates

Table 2-8: An overview of the ongoing research on simulation of damage in composites at various research institutes and finite element vendors around the world including sample articles/references and model scales as well as their capabilities and applications, extended from [73]

Research Group/FE Vendors	Sample References	Scales			Capabilities and Applications
		Micro	Meso	Macro	
University of Bristol	(Hallett 2005) [86]		x	x	Ply-based simulation of laminates
	(Hallett, Green et al. 2009) [87]		x	x	
University of Alberta		x			Micro-mechanical models for matrix cracking and fibre-matrix interface failure in unidirectional laminates
	(Karihaloo, Xiao 2003) [126]	x			
	(Grufman, Ellyin 2007) [84]	x			
University of British Columbia	(Williams, Vaziri et al. 2003) [267]			x	Macro-scale modelling of laminated composites using sub-laminate approach MAT219 in LSDYNA
	(Forghani, Zobeiry et al. 2011) [76]				
	(Forghani, Zobeiry et al. 2013) [75]				

Chapter 3: Intra-laminar Damage Modelling

3.1 Introduction

Continuum damage mechanics (CDM) has been commonly used to simulate the damage behaviour of composite laminates. The main challenge in this approach is to describe the secant stiffness of the damaged orthotropic material in terms of damage parameters and to specify the growth law for damage modes.

The sub-laminate based approach that was first introduced by Williams et al. [267] known as Composite DAmage Model (CODAM) is a CDM approach where the reduction of the stiffness matrix is written in terms of a set of damage parameters. The model represents damage growth in a Representative Volume Element (RVE) as shown schematically in Figure 3.1. The height and width of the RVE are equal to the characteristic length of damage in each of these directions. The characteristic height of a quasi-brittle material is defined as the actual height the damage would grow to if experimentally tested under conditions that lead to stable self-similar damage growth. The thickness corresponds to the thickness of the sub-laminate. Defining the RVE thickness in such a way allows smearing the stiffness reduction effect of macro-cracks as well as making the model more computationally efficient. CODAM material model as a CDM approach provides a smeared representation of damage mechanisms and their growth within a damage zone which encompasses the matrix cracking and fibre breakage and minor delamination. The main purpose of this model is to predict the effect of damage on the macroscopic behaviour of the laminate such as its stiffness, load carrying capacity, post-peak behaviour and energy absorption. Damage growth in the RVE is represented by an overall decrease in the normalized secant modulus ($\bar{E} = E/E_o$, where E_o is the initial undamaged modulus). The modulus reduces with increasing amounts of damage, as indicated by three damage variables (ω) that represent the degradation of effective modulus in two perpendicular directions (in-plane principal directions) and the shear modulus in the same coordinate system (plane). The damage parameters in this model are explicitly written in terms of effective strain function (F). The effective strain is a function of the various strain components, which allows strain interactions to be incorporated

into the model. A damage growth curve (ω vs. F), is defined for each principal direction (x , y , and z) for both tension and compression (see [267] for further details). The damage parameter for the in-plane shear is defined based on the damage parameters in x and y directions. In this model a general multi-linear relation between the damage parameter and the equivalent strain function can be defined (see [267]). By changing ω vs. F curves, one can get a variety of stress-strain behaviours such as instantaneous failure and brittle fracture.

Figure 3.1 schematically shows an RVE of a laminate subjected to uniaxial strain. Figure 3.1(b) shows the typical nominal stress-strain behaviour of the sub-laminate RVE under the applied deformation.

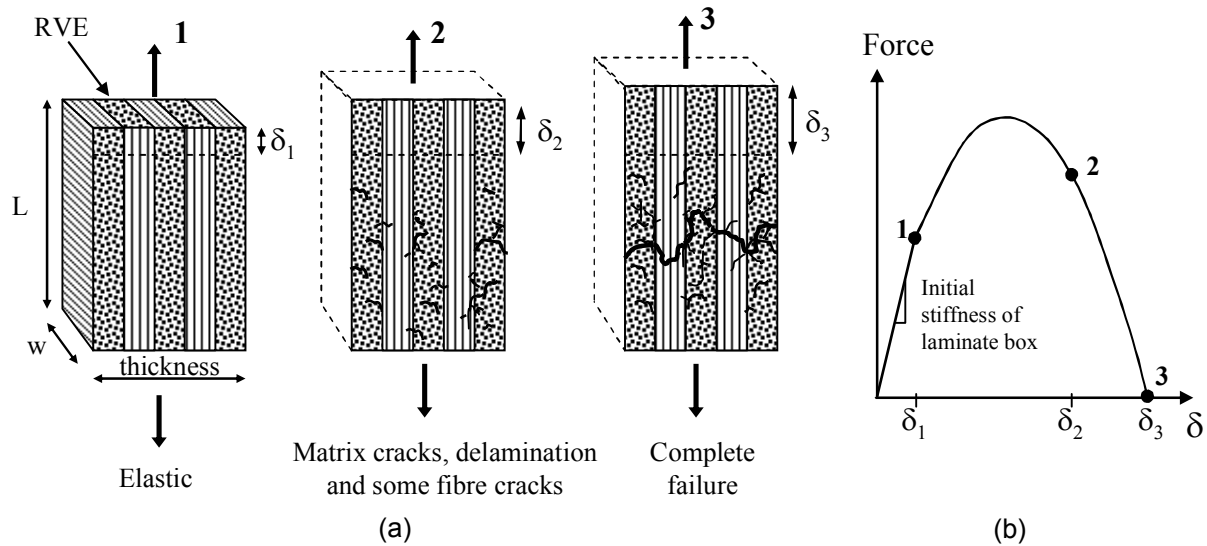


Figure 3.1: (a) Schematic of an RVE for a cross-ply laminate at three stages: (1) before the damage starts (2) formation of microcracks mainly in the matrix and fibre (3) microcracks merge and form a through crack in the laminate. (b) schematic nominal stress vs. nominal strain behaviour of the RVE under applied deformation, adapted from [267]

The ability of CODAM was demonstrated under various loading scenarios including:

- 1- Quasi-static loading of notched laminates [71,266,267,286,287]
- 2- Transverse impact of composite plates [266,268]
- 3- Axial impact of composite tubes [170,171,174]

Forghani [76] showed that the original formulation of CODAM has an unrealistic dependency on the choice of the coordinate system used to formulate it and it is not capable of predicting the damage-induced orthotropy. Therefore, Forghani [76] improved the formulation of CODAM by writing the formulation of damage potential functions in terms of the strain components in the direction of fibres and transverse to the fibres of the constituent plies. Therefore, the new formulation which is called CODAM2 has a direct relationship with the directional properties of the constituent layers inside the sub-laminate [76]. Bringing the fibre orientation into the damage formulation provides the opportunity to address the dependency of the model on the choice of material's coordinate system. Similar to the original formulation of CODAM, the sub-laminate is modelled as a whole unit (i.e. macroscopically) given that there is no major delamination in the sub-laminate. It should be noted that CODAM2 developed by Forghani [76] is not meant to predict the details of damage in the layers of the laminate. However, by assuming the effective behaviour of layers, the goal is to capture the overall behaviour of the laminate in a structure.

In using the sub-laminate as the building block, delamination within the sub-laminate cannot be explicitly simulated. As will be discussed in detail, the application of CODAM2 material model faces some limitations in applications where macroscopic matrix cracks (e.g. splits) are accompanied by large delamination zones. This brings a motivation for having a more general numerical approach in order to tackle not only the problems for which damage progression can be treated in a smeared continuum approach, but also for problems where large delaminations cannot be smeared using a fully continuum damage model.

In this chapter a brief description of the original CODAM2 material model formulation and its main limitation in addressing the response of composite laminates that are prone to delamination will be presented (see Section 3.2). As will be explained in this chapter, the discrete delamination damage mode will interact with the intra-laminar damage modes specifically the intra-laminar fibre/matrix splits. This effect can be captured by explicitly modelling discrete delamination using a cohesive interface approach (see Chapter 4) in combination with CODAM2 material model for treating intra-laminar damage modes. However, in order to use CODAM2 in the context of a mesoscopic model with the presence of delamination, its formulation is enhanced and presented in Section 3.2.4.

3.2 UBC composite damage Model- CODAM2

The CODAM2 material model developed by Forghani [76] is the second generation of the UBC CODAM model, which aims to address the material objectivity issue inherent in the original CODAM formulation.

Owing to the mismatch between the individual layer properties in laminated composites, the local stress and strain state in the laminate is very complex. The complexity increases when damage is introduced to the system as damage modes interact at smaller scales. The interaction between the layers and existence of various damage mechanisms affects the behaviour of a layer within the laminate significantly. CODAM2 acknowledges the fact that orientations of the layers play an important role in damage behaviour of the laminate. In CODAM2, the response of the laminate is based on the effective behaviour of the layers in the laminate. In the following subsections, the formulation of this material model as well as the characterization procedure for its main damage parameters will be explained.

3.2.1 Formulation

As mentioned before, the composite damage model (CODAM) is a macro-scale model in which the effect of damage propagation on the overall response of the laminate is described at the level of the RVE [267].

The necessity of being able to consider the exclusive effect of individual plies- associated with their fibre orientations and stacking sequence- on the propagation of damage has demanded development of the second generation of Composite Damage Model (CODAM2) [75]. The damage behaviour of the sub-laminate in CODAM2 is defined in terms of the effective strain of its constituent layers to account for the layup scheme of the sub-laminate. This is in contrast to the original formulation of CODAM where damage states were defined directly based on overall sub-laminate strains.

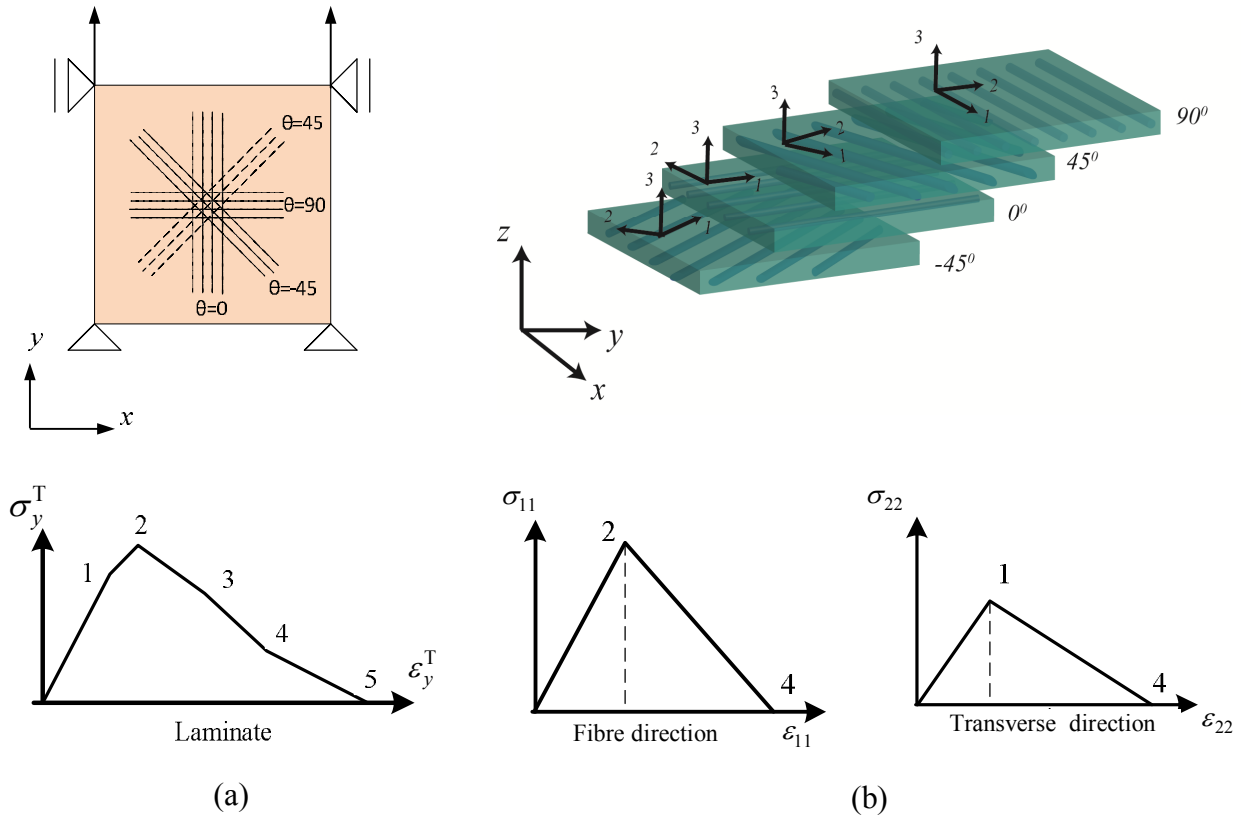


Figure 3.2: (a) A four-layer quasi-isotropic sub-laminate subjected to uniaxial tensile strain and its typical stress-strain response, (b) the typical stress-strain response of individual layers in both the fibre direction and transverse to the fibre direction

The basic concept behind CODAM2 is shown schematically in Figure 3.2. The stress-strain curve for a quasi-isotropic laminate subjected to a uniaxial tensile strain is shown in Figure 3.2(a). This curve is built-up of the bilinear stress-strain curves of individual plies as shown in Figure 3.2(b). The points on the laminate's stress-strain curve indicate different stages of damage within the constituent layers. For example under tensile loading, first at point #1 matrix damage in the 90° plies initiates. Later at point #2, the fibres in the 0° layer start to degrade. At point #3, fibre damage initiates in the $\pm 45^\circ$ layers while matrix damage of 90° layer has saturated. At point #4, fibre damage in the 0° is saturated and finally at point #5, the load carrying capacity of the laminate is exhausted through saturation of fibre damage in the $\pm 45^\circ$ layers.

In this material model, for a plane-stress condition the stiffness of the damaged laminate, \mathbf{Q}^d , is written as the summation of the effective contributions of the layers in the laminate.

$$\mathbf{Q}^d = \frac{1}{t} \sum_k t_k \mathbf{T}_k^{*T} \mathbf{Q}_k^d \mathbf{T}_k \quad (3.1)$$

where t_k is the k^{th} layer thickness, t is the laminate thickness, \mathbf{Q}^d is the effective reduced secant stiffness of the laminate, \mathbf{T}_k^{*T} and \mathbf{T}_k are the transformation matrices for strain and stress vectors and \mathbf{Q}_k^d is the damaged in-plane secant stiffness of the k^{th} layer in its principal material direction written as:

$$\mathbf{Q}_k^d = \begin{bmatrix} \frac{R_1 E_1}{1 - R_1 R_2 \nu_{12} \nu_{21}} & \frac{R_1 R_2 \nu_{12} E_2}{1 - R_1 R_2 \nu_{12} \nu_{21}} & 0 \\ & \frac{R_2 E_2}{1 - R_1 R_2 \nu_{12} \nu_{21}} & 0 \\ \text{sym} & & R_2 G_{12} \end{bmatrix}^{(k)} \quad (3.2)$$

A physically-based and yet simple approach is adopted to derive the damaged stiffness matrix. Two reduction coefficients, R_1 and R_2 , that represent the reduction of stiffness in the longitudinal (fibre) and transverse (matrix) directions have been employed. The shear modulus has also been reduced with the same matrix stiffness reduction parameters. The stiffness reduction parameters, $R_\alpha (\alpha \in 1, 2)$, are defined as linear functions of damage parameters, $\omega_\alpha (\alpha \in 1, 2)$, as shown in Figure 3.3 (a).

The damage parameters, $\omega_\alpha (\alpha \in 1, 2)$, are explicitly defined in terms of the maximum equivalent strains that the material has experienced throughout its loading history.

The damage parameters, $\omega_\alpha (\alpha \in 1, 2)$, are calculated as a function of the corresponding non-local equivalent strains. In CODAM2 the damage parameters are assumed to grow as a hyperbolic function (Figure 3.3 (b)) of the damage potentials (i.e. equivalent strains) such that when used in conjunction with stiffness reduction factors that vary linearly with the damage parameters

(Figure 3.3 (a)), they result in a linear strain-softening response (or a bilinear stress-strain curve) for each mode of damage. The explicit form of this relation is shown below:

$$\omega_\alpha = \frac{\varepsilon_\alpha^{eq} - \varepsilon_\alpha^i}{\varepsilon_\alpha^s - \varepsilon_\alpha^i} \frac{\varepsilon_\alpha^s}{\varepsilon_\alpha^{eq}}, \quad \text{for } (\varepsilon_\alpha^{eq} - \varepsilon_\alpha^i) > 0, \quad \alpha \in \{1, 2\} \quad (3.3)$$

where superscripts i and s denote, respectively, the damage initiation and saturation values of the strain quantities to which they are attached. The equivalent strain function that governs the fibre stiffness reduction parameter, ε_1^{eq} , is written in terms of the longitudinal normal strains as shown in Equation (3.4). The equivalent strain function that governs the matrix stiffness reduction parameter, ε_2^{eq} , is written in an interactive form in terms of the transverse and shear components of the local strain as shown in Equation (3.5).

$$\varepsilon_1^{eq} = |\varepsilon_{11}| \quad (3.4)$$

$$\varepsilon_2^{eq} = \sqrt{(\varepsilon_{22})^2 + \left(\frac{\gamma_{12}}{2}\right)^2} \quad (3.5)$$

The sign of the principal strain with maximum absolute value plays a role in initiation and growth of matrix damage since it indicates the compressive or tensile nature of the matrix damage driven by ε_2^{eq} . Whereas, the sign of strain in the fibre direction determines the compressive or tensile nature of fibre damage which is driven by ε_1^{eq} .

Damage is considered to be a monotonically increasing function of time, t , such that:

$$\omega_\alpha(t) = \max \left[\omega_\alpha(\tau) \mid \tau \leq t \right] \quad (3.6)$$

where $\omega_\alpha(t)$ is the damage parameter for the current time (load state), and $\omega_\alpha(\tau)$ represents the state of damage at previous time steps $\tau < t$.

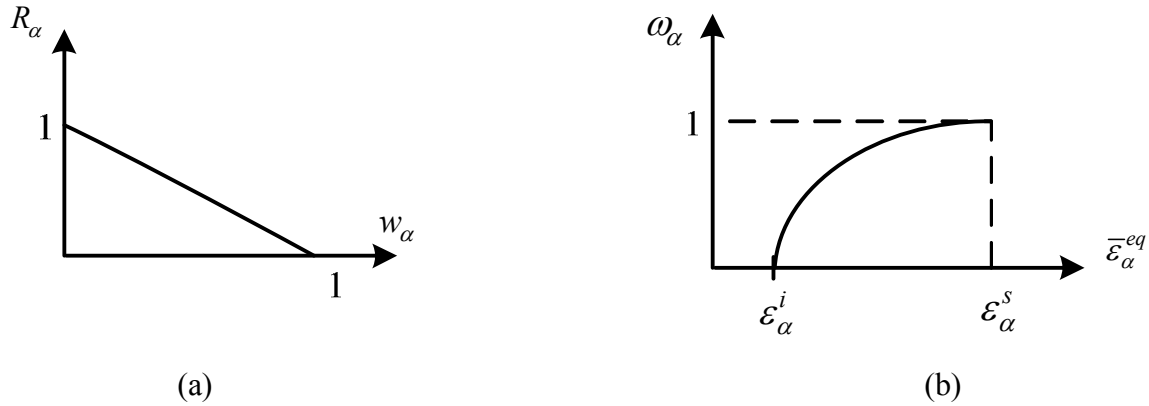


Figure 3.3: (a) The stiffness reduction factor vs damage, (b) Damage parameter vs equivalent strain parameter

The material formulation of CODAM2 was introduced by Forghani [76] in the finite element code, OOFEM [192]. OOFEM is an open-source code distributed under GNU General Public License. Later, this material model became available as a built-in material model, MAT219, in the commercial finite element software, LS-DYNA [158].

It is widely acknowledged that continuum damage models lead to the localization phenomenon. The solution for a structure made of a progressively damaging elastic solid predicts localization of damage over a surface of zero thickness leading to the energy dissipated by the damage process being equal to zero. This would happen regardless of the shape of the softening part of the stress-strain curve [115].

The above problem manifests itself as spurious mesh size dependency in the finite element solution. In such cases damage/crack pattern tends to localize to the smallest length scale of the model that is the height of one element. Therefore, with successive mesh refinement, damage localizes into a zone of zero volume and the numerical predictions fail to converge to a unique solution. Consequently, the global response of the system shows a strong dependency on the spatial discretization.

To address the localization issue, various solutions have been proposed. A simple approach that has been widely used in continuum damage-based methodologies is the crack-band method. In

this approach that was originally proposed by Bazant [24], the softening part of the stress-strain relation is scaled according to the height of the element to keep the energy dissipated during the damage progression constant and independent of element height. Assuming that g^f is the area under the stress-strain curve known as the fracture energy density, then the fracture energy, G^f , can be written in the following form:

$$G^f = g^f h^c \quad (3.7)$$

where h^c is a characteristic length scale of damage that can be related to the height of the damaged zone. In a finite element analysis where damage localizes into a single row of elements, h^c would be equal to the height of the element, h^e .

By scaling the fracture energy density according to the height of element, the crack-band method ensures that the fracture energy G^f remains constant and independent of the element size.

$$g_e^f = \frac{G^f}{h^e} = \frac{g^f h^c}{h^e} \quad (3.8)$$

The crack-band model can be seen as a representation of cohesive crack in a smeared sense where the traction-separation law is translated into a stress-strain law. In this case, opening of the crack faces is smeared over the height of an element and is represented by strain.

While simplicity and ease of implementation in commercial codes are the advantages of the crack-band approach, a few points should be taken into account when using this approach:

- Crack-band method works best in structured meshes with rectangular elements. Triangular elements and unstructured quadrilateral elements bring complications to the concept of height of element in the analysis.
- The damage pattern predicted using the crack-band approach does not represent the physical shape of the damage zone as its height is equal to the height of one element.
- Similar to cohesive crack models, this method is applicable to cases where in reality there is a distinct localization of damage and formation of a crack. Growth of damage and crack in a notched specimen under quasi-static loading is an example of such situation. In

very fast dynamic events such as blast and high-velocity impact loading where the damage takes a more spatially distributed form and thus a well-defined path for the crack propagation does not exist, the applicability of the crack band concept becomes questionable.

- The crack-band method cannot solve the mesh-orientation dependency problem associated with the local finite element solution.

Based on the limitations of this method, an alternative approach using the non-local averaging technique can be used in CODAM2 material model to address localization. This method that was introduced by Forghani [76] will be presented in the following subsection. This technique prevents the localization by implicitly introducing a length scale in the governing equations. Introduction of this length scale forces the damage to grow in a zone with a finite width that is independent of spatial finite element discretization. A detailed body of literature on different types of non-local damage formulations is available in [23,25,72].

3.2.2 Non-local averaging

In a damage formulation enhanced with a non-local scheme, unlike the local formulation, the state of stress at a point does not only depend on the state of strain and history parameters at that point, but also depends on the state of these parameters in a finite neighborhood of that point. Non-local averaging is a common approach among the non-local methods. In this method, a suitable parameter, β is averaged over a neighborhood of a generic point \mathbf{X}_i as follows:

$$\bar{\beta}(\mathbf{X}_i) = \frac{1}{W_i} \int_{\Omega_x} \beta(\mathbf{x}) W(\|\mathbf{X}_i - \mathbf{x}\|) d\Omega \quad (3.9)$$

$$W_i = \int_{\Omega_x} W(\|\mathbf{X}_i - \mathbf{x}\|) d\Omega$$

In this equation, $\bar{\beta}$ is the average of β over the zone Ω_x and W is a weighting function. It is critical to choose an appropriate parameter for averaging in a non-local formulation. Various case studies have shown that the equivalent strains ε_α^{eq} defined by Equations (3.4) and (3.5) are suitable parameters for averaging in CODAM2 formulation (see [72]). Therefore, the local

equivalent strains, ε_α^{eq} , in Equation (3.3) for calculation of damage will be replaced by their corresponding non-local values, $\bar{\varepsilon}_\alpha^{eq}$, leading to damage parameters in non-local CODAM2 material model being written as:

$$\omega_\alpha = \frac{\bar{\varepsilon}_\alpha^{eq} - \varepsilon_\alpha^i}{\varepsilon_\alpha^s - \varepsilon_\alpha^i} \frac{\varepsilon_\alpha^s}{\bar{\varepsilon}_\alpha^{eq}}, \quad \text{for } (\bar{\varepsilon}_\alpha^{eq} - \varepsilon_\alpha^i) > 0, \quad \alpha \in \{1, 2\} \quad (3.10)$$

Averaging is usually performed over a finite neighborhood of the original point using a weight function. In the following, two possible domains over which averaging can be performed are described.

3.2.2.1 Orthotropic non-local averaging

An orthotropic averaging scheme was introduced by Forghani [72] that was implemented in OOFEM for CODAM2 material model. The idea behind the orthotropic averaging is motivated by the physics of damage growth in a fibre reinforced composite medium. The neighboring points of a material point for which averaging is performed, have different contributions. It depends not only on the distance of the neighbour point from the material point but also on the alignment of the vector that connects it to the material point with respect to the fibre direction. Therefore, it is suggested to write the weight function for orthotropic averaging in terms of the effective distance (radius) as follows:

$$\rho^{eff} = r_1 \sqrt{\left(\frac{d_1}{r_1}\right)^2 + \left(\frac{d_2}{r_2}\right)^2} \quad (3.11)$$

where d_1 and d_2 are the components of the vector that connects a material point like ‘A’ shown in Figure 3.4(a) to its neighbor point ‘B’ in the x_1 and x_2 directions (parallel and perpendicular to the fibre directions). In this equation, r_1 is the non-local radius along the fibre direction and r_2 is the non-local radius in the transverse direction and $r_1 > r_2$. The weight function in the form of a bell function is written in terms of the effective radius, ρ^{eff} , defined as:

$$W(\rho^{eff}) = \left(1 - \left(\frac{\rho^{eff}}{r_1} \right)^2 \right)^2 \quad (3.12)$$

This method introduces two length scales, r_1 and r_2 , into the system. The predicted height of damage in the laminate would depend on these two averaging radii as well as the lay-up and the loading configuration.

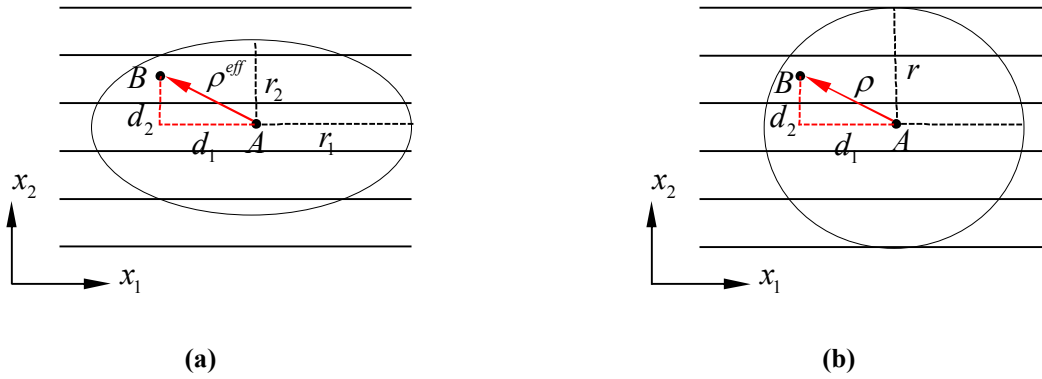


Figure 3.4: The averaging zone in non-local approach for (a) orthotropic averaging method and (b) for isotropic averaging method

3.2.2.2 Isotropic non-local averaging

The application of non-local averaging for the built-in CODAM2 material model in the commercial finite element software LS-DYNA (MAT219) is possible by using an implementation of non-local averaging based on the work by Bazant and Pijaudier-Cabot [25]. When the CODAM2 material model is used in conjunction with the non-local averaging capability of LS-DYNA, the averaged equivalent strains of each point will be computed similar to Equation (3.9):

$$\bar{\varepsilon}_\alpha^{eq}(\mathbf{X}_i) = \frac{1}{W_i} \int_{\Omega_x} \varepsilon_\alpha^{eq}(\mathbf{x}) W(\|\mathbf{X}_i - \mathbf{x}\|) d\Omega \quad (3.13)$$

where Ω_x is the averaging zone which in contrast to the orthotropic method introduced by Forghani [72] is a circle with radius, r , as shown in Figure 3.4(b). Therefore, the neighboring points of a material point have the same contribution irrespective of the alignment with respect to

the fibre direction of the vector that connects them to the material point. Thus, this method will be referred to as the isotropic non-local averaging method. The weight function available in LS-DYNA for this purpose is defined as:

$$W(\rho) = \frac{1}{\left[1 + \left(\frac{\rho}{r}\right)^p\right]^q} \quad \text{with } \rho = \sqrt{d_1^2 + d_2^2} \quad (3.14)$$

in which p and q are parameters that define the shape of the weight function. The variation of this function for different sets of p and q are shown in Figure 3.5. In the built-in version of CODAM2 material model available in LS-DYNA (MAT219), however, the weight function is similar to the Gaussian function of Equation (3.12) introduced by Forghani in OOFEM [72].

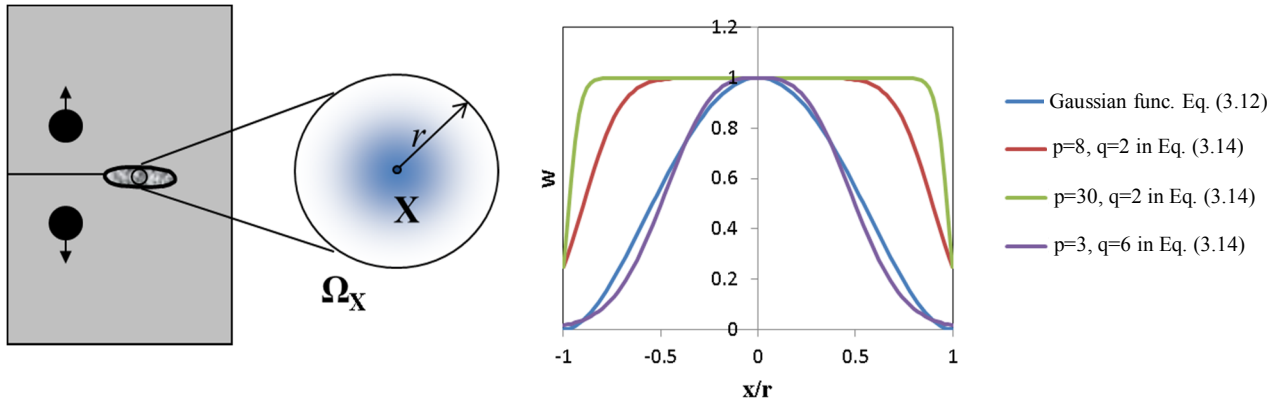


Figure 3.5: Distribution of non-local averaging weight function in x-direction (parallel with notch direction in an OCT configuration) calculated from Equations and (3.12) and (3.14) over a circular averaging domain

Although choosing a non-local approach may increase the computation time especially when the radius of averaging is much larger than the element size, it is a suitable approach to use in order to predict the height of damage and the direction of damage growth irrespective of the finite element discretization.

As will be described in Section 3.2.4, the isotropic non-local averaging feature available in LS-DYNA will be used in conjunction with the enhanced form of CODAM2 implemented as a user-defined material model. Therefore, in the enhanced CODAM2 model, the weight function is defined based on Equation (3.14). However, the parameters P and q are set to 3 and 6, respectively, such that Equation (3.14) yields a shape similar to the Gaussian function that was used by its predecessor (MAT219).

3.2.3 Limitations of the fully continuum damage modelling approach

For cases where failure is governed by discrete crack propagation such as large splits or delamination, continuum damage models often fail to correctly describe the propagation of damage through the structure. Discrete cracks redistribute the stresses around the damage zone and consequently alter the load paths within the structure. For instance, delamination which is usually accompanied by intra-laminar discrete matrix cracks close to notches or general discontinuities, potentially creates blunt damage fronts that reduce the stress concentration. An example of this can be found in open-hole tensile tests conducted by Green et al. [82] on quasi-isotropic laminates made of IM7/8552 carbon-fibre/epoxy prepregs. It is pointed out that the growth of delamination from the boundary of the hole leads to propagation of splits in the 0° plies that act as a crack-blunting mechanism. There are many other cases with similar susceptibility to large delamination zones and splits that can be caused by reasons related to the material properties, material layout and the geometry of the problem. Examples of these cases are schematically shown in Figure 2.2 and can be summarized as follows:

- Material systems with low inter-laminar strength that promotes delamination
- Laminates with layups that have blocked plies
- Geometries with free-edge or discontinuities that can promote edge delamination
- Notched subcomponents
- Subcomponents with holes and other geometric discontinuities
- Components with stiffeners and ply-drops
- Low velocity Impact

The effect of discrete macroscopic cracks such as delamination and large splits cannot be directly captured by merely using a continuum damage approach. Therefore, a combination of the continuum and the discrete approach at the mesoscopic scale can be used to tackle the problems where the effect of discrete cracks cannot be smeared. From a numerical point of view, the explicit modelling of delamination as a macro-crack separation of plies at the interface enables the split in the separated ply to grow independently of the remainder of the laminate. The separation from the laminate allows the split to grow so long as there is enough energy for such growth to occur.

In the proposed methodology, in combination with the continuum approach to capture the intra-laminar damage, a mixed-mode cohesive-based interface approach will be used to capture the delamination between dissimilar plies (see Chapter 4). The intra-laminar modes of damage, on the other hand, including matrix cracking and fibre fracture are captured with an enhanced form of the non-local CODAM2 material model in a mesoscopic context. The non-local averaging technique is very effective in predicting the trajectory of in-plane macro-cracks irrespective of the finite element discretization. Therefore, the need to introduce pre-inserted discrete elements to capture the growth of discrete cracks is eliminated. This aspect of the proposed approach offers a significant advantage and therefore utility by engineers. The enhancements in the original CODAM2 formulation are described in order to be able to link the initiation and progression of damage for individual delaminated plies to the mechanical properties of unidirectional laminates. As will be discussed, the effect of ply thickness and constraining conditions imposed by neighbouring plies will also be considered.

3.2.4 Damage characterization and model calibration at the sub-laminate (macro) level

Zobeiry et al. [285] have used the OCT specimen that was first introduced by Kongshavn and Poursartip [129] for estimating the strain-softening response of laminates made of unidirectional prepregs under tensile loading. This geometry can lead to a self-similar and stable damage growth which allows application of progressive fracture analysis to the material inside the damage zone. Similarly, a Compact Compression Test (CCT) is used for characterizing the strain-softening response under compressive loading.

Upon employing a digital image correlation (DIC) technique and analysis of the measured surface displacement/strain data, the effective strain-softening response of a sub-laminate can be constructed. The key parameters in characterization of a sub-laminate are the damage initiation strain of the laminate, the critical energy release rate or fracture energy of the sub-laminate and the height of damage growing in a self-similar manner.

The first step in this methodology is to identify the boundary of the damaged zone [285]. Assuming a virtual mesh on the surface of the specimen, the displacement vectors at the virtual nodes of the elements are measured from the high resolution images taken from the surface. The nodal forces for each element will be calculated assuming that the material within the element is elastic. The damage zone will then be the area in which the equilibrium of forces at the nodes cannot be satisfied within an acceptable tolerance. The damage initiation strain of the laminate, ε^i , will be the average of strain values at the boundary of the damaged zone. The fracture energy, G^f , associated with the laminate will also be calculated using the effective damage length and the area below the load-displacement curve. These damage properties are then used to calibrate the sub-laminate based damage model, CODAM2.

Using this approach, Zobeiry [286] characterized the stress-strain response of the damaged zone for a quasi-isotropic laminate with $[90/45/0/-45]_{4s}$ layup made of IM7/8552 carbon fiber/epoxy prepregs. The experimental results showed minor delamination with a self-similar damage zone with approximate height of 4-6mm. Forghani [72] used the isotropic non-local CODAM2 model to simulate the progression of damage for the same test. The predictions showed a good agreement with the experimental results in terms of the load-displacement response and the damage height. Later, Zobeiry et al. [289] used the same methodology to simulate the progression of damage for a similar laminate layup $[45/90/-45/0]_{4s}$ with the same material system and again good agreement was achieved.

Forghani [72] showed that the estimation of the damage saturation strain values has a relationship with the fracture energy that depends on the selected radius of averaging. In order to establish this relationship, he simulated the above mentioned OCT problem with an in-plane

finite element mesh of 0.25 mm close to the notch with varying radius of averaging. He calculated the predicted fracture energy value based on its fundamental definition, i.e. the change in the dissipated energy divided by the change in cracked surface area as the crack advances from one load state to the next. Then, he calculated an effective length scale, h^c , which is defined as the ratio of the predicted fracture energy from finite element simulation, G_{FE}^f , and the fracture energy density, g^f , as:

$$h^c = \frac{G_{FE}^f}{g^f} \quad (3.15)$$

with

$$G_{FE}^f = \frac{(\Delta W - \Delta U)}{t\Delta a} \quad (3.16)$$

where ΔW is the external work done and ΔU is the change in the strain energy of the system when the crack length advances by an amount Δa and t is the thickness of the laminate. He approximated the fracture energy density in Equation (3.15) from the simulation of a single element under uniaxial tensile strain. He showed that for two cases of $r = 1$ mm and $r = 2$ mm, h^c is approximately a constant factor of the radius of averaging (i.e. $h^c = 1.6r$). Moreover, the predicted height of damage was found to be approximately $2.5r$. Based on the latter finding, the radius of averaging can be selected based on the observed height of damage in experiments (i.e. $r = 0.4h^{\text{exp}}$ where h^{exp} is the experimental damage height perpendicular to the direction of crack growth).

Therefore, for a given laminate with known experimentally measured damage initiation strain, damage height and fracture energy, first the fibre and matrix damage initiation strains are approximated based on the damage initiation strain of the laminate. Second, the damage saturation strains can be approximated from the experimental fracture energy of the laminate with the help of Equation (3.15) where $h^c = 1.6r$ and r is a factor of the damage height (i.e. $r = 0.4h^{\text{exp}}$). The idea is to estimate values for the saturation strains such that the predicted

energy release rate agrees with the experimental measurements of fracture energy. An iterative procedure can be used to estimate the saturation strain values. In a multi-directional laminate, assuming that the damage saturation strain for the matrix and fibre are the same, they can be estimated using the effective length scale $h^c = 1.6r$ in Equation (3.15). The iterative process can be summarized as follows:

For a given experimental fracture energy value of the laminate, use a trial value for the fibre and matrix damage saturation strains:

- 1- Simulate a single element subjected to uniaxial strain and calculate the resulting area under the stress-strain curve (which represents the fracture energy density, g^f).
- 2- The resulting fracture energy can be approximated using Equation (3.15) (i.e. $G_{FE}^f = h^c g^f = 1.6r g^f$ where $r \approx 0.4h^{\text{exp}}$)
- 3- Compare the estimated fracture energy, G_{FE}^f , with the fracture energy measured from the OCT test, G^f . If the difference is not acceptable, the process needs to be repeated.

In the above calibration process, one should note that the suggested relationship between h^c and r is only an approximation based on fracture energy density response of a uniaxially loaded single element. In the actual model, the predicted average fracture energy density of damaged elements might be slightly lower or higher than what is predicted from a uniaxial tensile test of a single element. This is due to the fact that the initiation and saturation of damage in this material model is based on the non-local strains reaching a threshold rather than the local strains. Therefore, the stress-strain curve of an element damaged in an averaged zone is slightly different from that obtained from a single element loaded uniaxially. In testing a single element, damage state is not affected by neighbor elements as they are in a real model. For example, in a monotonic tensile loading of an OCT specimen, when the equivalent strains of a material point with a potential to get damaged is averaged, its non-local equivalent strains might be less than its local equivalent strains; therefore, damage in the element might be delayed. This may lead to

over-prediction of the peak stress and the overall peak force which can be unrealistic. However, this problem can be addressed by using the above mentioned iterative process.

The above mentioned iteration process can be avoided by introducing a more straightforward method for indication of the initiation and saturation strains of damage modes. In other words instead of approximating the damage initiation and saturation values from the local stress-strain behaviour of a single element followed by iterations, these values can be directly calculated as part of the material formulation. As will be shown in Section 3.2.4, using a set of stress-based failure criteria, the initiation of equivalent strains can be directly specified in order to automatically account for the effect of the stress-state at the initiation of damage. This will ensure that the maximum stress of the local stress-strain curves is not over-predicted. Moreover, the saturation values will also be directly calculated as part of the material formulation by inputting the fracture energy entities directly. These modifications have been carried out as part of the enhancement of CODAM2 material model which will be discussed in detail in Section 3.2.4.

3.3 Enhanced CODAM2 material model

In application of macroscopic CODAM2, as mentioned in the previous sections, the initiation and saturation of equivalent strains for fibre and matrix damage modes can be estimated by knowing the effective stress-strain (strain softening) curve of the sub-laminate and its fracture energy. However, when delamination is dominant, measurement of the sub-laminate's fracture energy in presence of extensive delamination zones between the plies becomes impossible. This is due to the fact that the notched experiments needed to characterize the fracture properties do not lead to self-similar and stable growth of damage. The estimation of the initiation of matrix cracking also becomes more complex as a result of its interaction with the adjacent plies through delamination. In fact, a common cause of delamination is the high inter-laminar stresses induced at the tip of matrix cracks [232] which highlights the importance of proper estimation of the onset of matrix cracking. Many studies have shown that the formation of transverse matrix cracks in a ply depends on the constraining effects of its neighboring plies as well as the thickness of the ply [191,217]. For example, experiments show higher transverse tensile and

shear strengths for a 90° ply constrained by plies with different orientations in comparison with a unidirectional 90° laminate (see [10,45,82,127,191]). Based on these observations, some researchers differentiate between the behaviour of a unidirectional lamina and that of a lamina embedded within a laminate [52,70,227]. Moreover, thicker transverse plies are more prone to matrix cracking and delamination. The interaction of splits and delamination in adjacent interfaces has also been the subject of extensive studies on matrix-crack induced delamination that promotes splits in the neighboring plies (see [10,82,87,127]).

In simulating the behaviour of laminates that are prone to delamination, the CODAM2 material model needs to be used in a meso-model context where intra-laminar damage modes in plies are captured by non-local continuum damage approach and delamination is captured by a discrete methodology. To achieve the first part, some enhancements are made to the original formulation of CODAM2. The added features to CODAM2 material model in addition to what is available in the built-in form of the original model in LS-DYNA (i.e. MAT219), are implemented in a user material model (UMAT) [158]. The enhanced formulation allows one to predict the growth of intra-laminar damage modes at plies that are separated from the sub-laminate as a result of delamination. This is essential in studying the behaviour of laminate layups or loading geometries that are prone to delamination.

The rest of this chapter will summarize all the modifications that are implemented in CODAM2 material formulation to be able to use the model in conjunction with a discrete approach. We may refer to this enhanced form of the material model, the mesoscopic non-local CODAM2 model to distinguish it from its predecessor which was used in macroscopic scale.

3.3.1 Intra-laminar damage

The CODAM2 material model is modified and implemented as a user material model for LS-DYNA in order to predict the initiation and progression of damage in the individual plies as the building blocks of the laminate.

Similar to the original formulation of CODAM2, the progression of intra-laminar damage modes are tracked by two damage parameters that are written in terms of the non-local averaged equivalent strain components, $\bar{\varepsilon}_\alpha^{eq}$ ($\alpha \in \{1, 2\}$), as follows (see Figure 3.3b):

$$\omega_\alpha = \left(\frac{\bar{\varepsilon}_\alpha^{eq} - \varepsilon_\alpha^i}{\varepsilon_\alpha^s - \varepsilon_\alpha^i} \right) \frac{\varepsilon_\alpha^s}{\bar{\varepsilon}_\alpha^{eq}}, \quad \alpha \in \{1, 2\} \quad (3.17)$$

where ε_α^i and ε_α^s indicate the strain values associated with damage initiation and saturation, respectively. Based on the concept of non-local continuum damage and the averaging feature available in LS-DYNA [158] for user-defined material models, the averaged equivalent strains, $\bar{\varepsilon}_2^{eq}$ and $\bar{\varepsilon}_1^{eq}$, at each integration point are obtained by averaging the local equivalent strains of all the integration points within a circular domain with radius, r (see Equation (3.13)). For user-defined material models, the weight function of non-local averaging is defined by Equation (3.14). In order to be consistent with the bell-shape Gaussian function that is used for the original formulation of CODAM2 in OOFEM and in the built-in MAT219 in LS-DYNA, the values of $p=3$ and $q=6$ are selected for the weight function defined in Equation (3.14). As can be observed from Figure 3.5, these values yield a weight function similar in shape to the Gaussian function.

The local equivalent strains, ε_1^{eq} and ε_2^{eq} , for fibre and matrix damage modes are defined as:

$$\varepsilon_1^{eq} = |\varepsilon_{11}| \quad (3.18)$$

$$\varepsilon_2^{eq} = \sqrt{(\varepsilon_{22})^2 + (\gamma_{12}^e)^2} \quad (3.19)$$

Note that in the equivalent strain equation for matrix damage, γ_{12}^e is the elastic part of the in-plane shear strain in cases where the in-plane shear behaviour is non-linear. It is well-known that the in-plane shear response in most unidirectional laminates is nonlinear and inelastic e.g. [140,195,254] among others. Therefore, this nonlinear in-plane shear stress vs strain constitutive behaviour has been implemented as part of the improvements made to CODAM2 material model. Using a linear in-plane shear behaviour as in the original CODAM2 material model may lead to premature matrix damage due to prediction of higher shear stress at a specific shear strain value. Since progression of damage is driven only by elastic internal energy at the onset of

matrix damage, only the elastic component of the total shear strain (γ_{12}^e) is taken into account in the matrix equivalent strain formulation. The implementation of nonlinear in-plane shear behaviour will be presented in more detail in Section 3.3.3.

3.3.1.1 Damage initiation

The original CODAM2 material model [75] is applicable to loading scenarios that leads to formation of a progressive damage zone small enough not to interact with the boundaries of the structure with minimal delamination at the ply interfaces. In those cases, the stiffness reduction in the laminate is mainly driven by progression of fibre breakage. However, in material layups and geometries that are marked by formation of large splits followed by discrete macro-delamination between the plies, fibre breakage will be delayed and the laminate stiffness reduction is mostly governed by the initiation of splits and delamination. Given the sensitivity of these types of response to initiation of damage (mainly matrix cracking and the ensuing delamination), it is important to have failure initiation criteria that consider the effect of in-situ strength properties of the plies. This enables one to account for the thickness and constraining effect of the neighboring plies on the initiation of matrix cracking. The interactive effect of transverse normal and shear stress components on matrix cracking combined with the inherent non-linear shear stress-strain response of unidirectional composites necessitates the use of stress-based criteria to signal initiation of matrix damage.

For simplicity, Hashin's failure criteria [94,95] in which the failure surface is expressed in terms of stress reaching a critical state is used here for initiation of intra-laminar matrix and fibre damage modes. It should be noted that any other failure initiation criteria can also be used but with Hashin's criteria minimum number of additional parameters will be required for the material model to be calibrated. The criteria for intra-laminar fibre and matrix failure initiation are listed in Table 3-1 only for tensile loading which are relevant to the simulation cases presented in this work. In Table 3-1, X_T and Y_T are tensile strengths in the fibre and transverse directions, S_L indicates the longitudinal shear strength, and σ_{ij} are the stress components.

Table 3-1: Damage initiation criteria based on Hashin's failure theory [94,95]

Damage mode	Failure Criterion
Fibre tension	$F_{1T} = \left(\frac{\sigma_{11}}{X_T} \right)^2 = 1$
Matrix tension	$F_{2T} = \left(\frac{\sigma_{22}}{Y_T} \right)^2 + \left(\frac{\tau_{12}}{S_L} \right)^2 = 1$

The initiation values of the equivalent strain components in Equation (3.17) will be determined when the failure criteria listed in Table 3-1 are satisfied for each damage mode. Therefore:

$$\varepsilon_1^i = \bar{\varepsilon}_1^{eq} \Big|_{@F_1=1} \quad (3.20)$$

$$\varepsilon_2^i = \bar{\varepsilon}_2^{eq} \Big|_{@F_2=1} \quad (3.21)$$

In the original formulation of CODAM2 material model, the damage initiation values for the equivalent fibre and matrix strains have to be predefined by the user. This estimation can be more difficult for the matrix equivalent strain since it is defined as a combination of transverse strain and shear strain. Depending on the loading scenario, the contribution of each component to the matrix equivalent strain varies. For example, in a problem where the in-plane shear strain is dominant, defining the initiation value of matrix equivalent strain based only on the transverse matrix strength may lead to premature prediction of matrix damage since the shear strength of the material is neglected. The higher strength in shear than transverse direction in many cases, as well as the nonlinearity of the material in shear can effectively delay the initiation of matrix damage. Therefore, the use of a stress-based criterion for indicating the initiation point of matrix damage will automatically consider the contribution of both shear stress and transverse stress in triggering the initiation of matrix damage.

3.3.1.2 Damage saturation

For the case of a bi-linear strain-softening curve, the damage saturation values for the matrix equivalent strain, ε_2^s , are calculated based on the associated value of intra-laminar matrix fracture energy as well as the transverse and shear stress components at the onset of damage. For this purpose, an equivalent stress corresponding to the equivalent matrix strain is introduced as follows:

$$\sigma_2^{eq} = \frac{(\sigma_{22}\varepsilon_{22} + \tau_{12}\gamma_{12}^e)}{\sqrt{(\varepsilon_{22})^2 + (\gamma_{12}^e)^2}} \quad (3.22)$$

The value of this equivalent stress at the initiation of matrix damage mode $T = (\sigma_2^{eq})|_{@F_2=1}$ is used to estimate the saturation strain for matrix damage such that:

$$\varepsilon_2^s = \frac{2g_2^f}{T} \quad (3.23)$$

where, g_2^f is the intra-laminar matrix fracture energy density. Similar to what was explained in Section 3.2.4 in the context of a sub-laminate, the value of g_2^f can be related to the experimental intra-laminar matrix fracture energy, G_2^f , through an effective length scale, h_2^c , such that $g_2^f = G_2^f / h_2^c$. With the use of non-local averaging technique, as discussed in Section 3.2.4, h_2^c is related to the radius of averaging. The radius of averaging will also affect the height of damage captured in the finite element predictions. In application of the original (macroscopic) non-local CODAM2 formulation for OCT simulations on a dispersed-ply quasi-isotropic laminate [75,289], the radius of averaging was selected to be $0.4 h^{\text{exp}}$ in order to predict the height of damage close to what was observed from the experiments. It was also shown that for a given mesh size of 0.25mm, $h^c \approx 1.6r$. Therefore, knowing the experimentally measured fracture energy of the sub-laminate, its fracture energy density required for the calculation of

fibre and matrix damage saturation strains could be obtained using Equation (3.15) with $h^c \approx 1.6r$.

In the mesoscopic application of the non-local CODAM2 model, we need to be able to capture the potential discrete matrix cracks in a continuum sense. Therefore, the non-local radius, r , used for averaging should be small enough to capture a narrow height of damage that is representative of the matrix cracks running parallel to the fibre direction. Thus, the value of r is limited to two times the finite element size to ensure that there is more than one integration point within the averaging zone and to prevent an excessively large width for discrete cracks perpendicular to its growth direction. In order to obtain the relationship between the fracture energy, G_2^f , and the fracture energy density g_2^f (i.e. the value of h_2^c), several simulations are performed on a unidirectional 90° laminate in an OCT specimen configuration with different element sizes and averaging radii (see Appendix B for details). For a given input of fracture energy density, the fracture energy of the UD 90° laminate is calculated using the area under the predicted force-displacement curve (energy dissipated during fracture) divided by the fractured area associated with crack growth. It is found that the ratio of the predicted G_2^f to the input fracture energy density, g_2^f , for a given mesh size is a constant factor of the radius of averaging (see Appendix B for details). This is similar to what was explained for the application of macroscopic CODAM2 for sub-laminates. Therefore, for an experimentally known intra-laminar matrix fracture energy, G_2^f , and a given mesh configuration, the input fracture energy density g_2^f is selected as G_2^f / h_2^c with h_2^c as a constant factor of r . To approximate this factor the procedure explained in Appendix B can be followed.

The equivalent strain value for fibre damage saturation is similarly calculated as follows:

$$\varepsilon_1^s = \frac{2g_1^f}{X} \quad (3.24)$$

where X is the strength in the fibre direction and g_1^f is the intra-laminar fibre fracture energy density. The relationship between g_1^f and G_1^f for the fibre damage mode can be established similar to what is done for the matrix fracture energy (see Appendix B for details).

3.3.2 Effect of ply thickness and constraints on matrix crack initiation

It is well known that the crack density and stiffness reduction of a cracked ply can be influenced by the thickness of the ply and the stiffness of the immediate neighboring plies [191,260]. Due to the stress singularity at the transverse crack tip, the exact solution of this problem cannot be derived, and only approximate analytical methods can be applied. A popular approach among these methods is the shear lag theory where the cracked ply is considered as a 2D unit cell between two consecutive cracks (see Figure 3.8). In the plane of a transverse crack, the transverse ply carries no load, while away from the crack part of the load is transferred to the transverse ply through shear stresses. The concept of shear lag theory has been used by Han and co-workers [89], Laws and Dvorak [146], Lee and Daniel [148], and Zhang et al [279]. In the present study, we use the latter work in order to obtain an approximation of the in-situ strength properties of the cracked plies using the combined concepts of shear lag and linear elastic fracture mechanics. In the following, the details of this method are presented.

3.3.2.1 Shear-lag theory

In a laminate, each layer can be considered as a homogeneous material with a distribution of microcracks which is constrained by the surrounding material through shear and normal forces on the contact surfaces with neighboring elements. In a shear lag theory, the constitutive equation of the constrained, piecewise homogeneous lamina in the in-situ microcracked state will be developed. In other words, the effects of the constrained cracked lamina on the behaviour of the laminate will be determined by developing the in-plane stiffness matrix $\bar{\mathbf{Q}}^{(k)}$ of the cracked lamina. The extensional stiffness, \mathbf{A} , bending stiffness, \mathbf{D} and coupling stiffness, \mathbf{B} , of composite laminates can then be determined using the classical laminate theory.

With the limitation of the micro-cracks to the transverse matrix cracking and not delamination, this model is proposed by Zhang et al. [279] for a cracked layer denoted here as Layer 2 with the ply angle θ constrained symmetrically by the homogeneous upper and lower equivalent constrained layers denoted as Layer 1 (see Figure 3.8). It is assumed that the constraining plies are intact. The laminate will be referred to the global xyz and local $x_1x_2x_3$ coordinate systems with x_1 directed along the fibres in the θ -layer (θ is the angle of fibres in the cracked ply with respect to the global x -axis). Matrix cracks are assumed to span the full width and the full thickness of Layer 2 and be spaced uniformly at a distance $2s$ with their crack surface being perpendicular to the lamina principal axes.

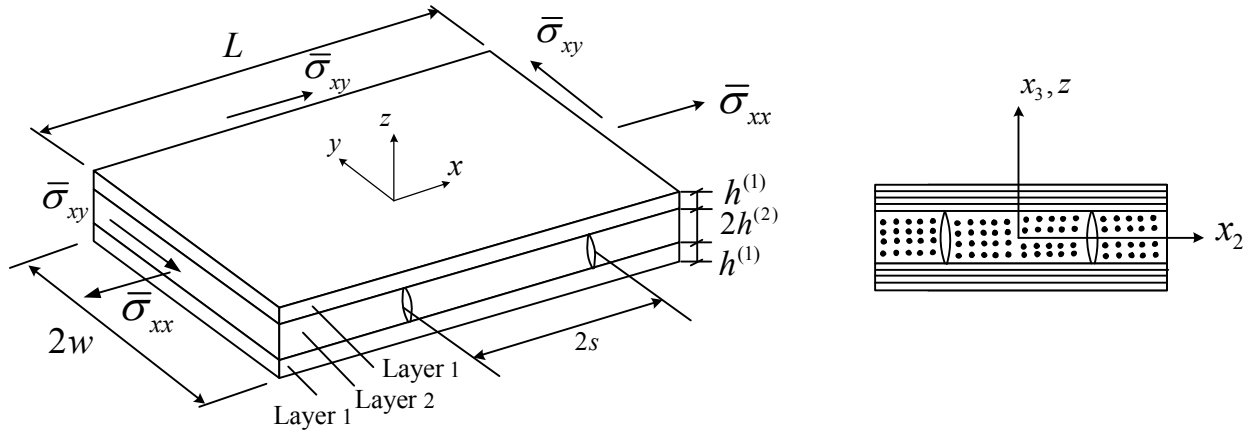


Figure 3.6: A symmetric laminate with transverse cracks in the mid-ply constrained by adjacent plies

The overall compliance of the cracked lamina (i.e. Layer 2) with micro-cracks can be expressed in the lamina coordinate system $x_1x_2x_3$ as:

$$\begin{aligned}\bar{\mathbf{S}}^{(2)} &= \hat{\mathbf{S}}^{(2)} + \mathbf{S}^{*(2)} \\ \bar{\boldsymbol{\varepsilon}}^{(2)} &= \bar{\mathbf{S}}^{(2)} \bar{\boldsymbol{\sigma}}^{(2)}\end{aligned}\tag{3.25}$$

or inversely as:

$$\begin{aligned}\bar{\mathbf{Q}}^{(2)} &= \hat{\mathbf{Q}}^{(2)} - \mathbf{Q}^{*(2)} \\ \bar{\boldsymbol{\sigma}}^{(2)} &= \bar{\mathbf{Q}}^{(2)} \bar{\boldsymbol{\varepsilon}}^{(2)}\end{aligned}\tag{3.26}$$

where $\hat{\mathbf{S}}^{(2)}$ and $\hat{\mathbf{Q}}^{(2)}$ are, respectively, the elastic compliance and stiffness matrices of the ply without damage, $\mathbf{S}^{*(2)}$ is an additional compliance dependent on the configurations and distribution of micro-cracks, and $\mathbf{Q}^{*(2)}$ is the reduction in stiffness matrix of the lamina due to damage.

With assumption of uniformly distributed cracks, only $S_{22}^{*(2)}$ and $S_{66}^{*(2)}$ are non-zero for in-plane loading conditions. Therefore, Equation (3.26) for the stiffness matrix of the Layer 2 can be written as:

$$\begin{bmatrix} \bar{Q}_{11}^{(2)} & \bar{Q}_{12}^{(2)} & 0 \\ \bar{Q}_{12}^{(2)} & \bar{Q}_{22}^{(2)} & 0 \\ 0 & 0 & \bar{Q}_{66}^{(2)} \end{bmatrix} = \begin{bmatrix} \hat{Q}_{11}^{(2)} & \hat{Q}_{12}^{(2)} & 0 \\ \hat{Q}_{12}^{(2)} & \hat{Q}_{22}^{(2)} & 0 \\ 0 & 0 & \hat{Q}_{66}^{(2)} \end{bmatrix} - \begin{bmatrix} (\hat{Q}_{12}^{(2)})^2 / \hat{Q}_{22}^{(2)} \Lambda_{22}^{(2)} & \hat{Q}_{12}^{(2)} \Lambda_{22}^{(2)} & 0 \\ \hat{Q}_{12}^{(2)} \Lambda_{22}^{(2)} & \hat{Q}_{22}^{(2)} \Lambda_{22}^{(2)} & 0 \\ 0 & 0 & \hat{Q}_{66}^{(2)} \Lambda_{66}^{(2)} \end{bmatrix} \quad (3.27)$$

in which $\Lambda_{ij}^{(2)}$ ($i, j = 2, 6$) are related to $S_{22}^{*(2)}$ and $S_{66}^{*(2)}$ as follows:

$$\begin{aligned} \Lambda_{22}^{(2)} &= \frac{\hat{Q}_{22}^{(2)} S_{22}^{*(2)}}{1 + \hat{Q}_{22}^{(2)} S_{22}^{*(2)}} \\ \Lambda_{66}^{(2)} &= \frac{\hat{Q}_{66}^{(2)} S_{66}^{*(2)}}{1 + \hat{Q}_{66}^{(2)} S_{66}^{*(2)}} \end{aligned} \quad (3.28)$$

where $\Lambda_{22}^{(2)}$ and $\Lambda_{66}^{(2)}$ are the in-situ damage effective functions (IDEF) that indicate the stiffness loss caused by the in-situ damage state of the cracked ply under the constraint conditions.

After the three-layer model for the cracked ply is built, a 2-D shear lag theory is used to obtain the IDEFs $\Lambda_{ij}^{(2)}$. These functions will be expressed using a series of microscopic parameters and constraint variables such as the crack density variable, $D^{(2)}$, the thickness ratios χ , and the

undamaged stiffness and compliance components of the cracked layer and the constraining layers. Therefore, we have:

$$\Lambda_{ij}^{(2)} = f(D^{(2)}, \hat{Q}_{ij}^{(2)}, \hat{S}_{ij}^{(1)}, \hat{S}_{ij}^{(2)}, \chi), \quad i, j = 1, 2, 6 \quad (3.29)$$

with

$$D^{(2)} = \frac{h^{(2)}}{s}, \quad \chi = \frac{h^{(1)}}{h^{(2)}} \quad (3.30)$$

where $h^{(2)}$ is the half-thickness of the cracked ply and $h^{(1)}$ is the thickness for each of the constraining plies and s is half of the distance between uniformly spaced cracks (see Figure 3.8). The derivation of IDEFs is presented in detail in Appendix A.

Once the in-plane stiffness matrix of the cracked ply $\bar{\mathbf{Q}}^{(2)}$ in the local coordinate system $x_1x_2x_3$ is determined using Equations (3.27) and (3.29) for any crack density value, it can be transformed to the global coordinate system xyz using standard tensor transformation functions (see Figure 3.8).

3.3.2.2 Estimation of in-situ strength properties

The total strain energy associated with matrix cracking in the cracked layer can be related to the IDEF rate, $d\Lambda_{ij}^{(2)} / dD^{(2)}$, which indicates the stiffness loss under the constrained in-situ condition.

Considering a unit cell with a finite length, L and width, $2w$ (Figure 3.8), the total area of cracked surface for the case of $\theta = 90^\circ$ will be $A = 2wLD^{(2)}$. The potential energy of this unit cell is:

$$\Pi = U - W = U - 2LHw\bar{\sigma}_i \bar{\epsilon}_i \quad (3.31)$$

where U is the total strain energy stored in the laminate unit cell. Using the constitutive equation of the cracked lamina given in Equation (3.27), we have:

$$U = \frac{1}{2} \left(4Lwh^{(2)} \bar{Q}_{ij}^{(2)} (\bar{S}_{im} \bar{\sigma}_m) (\bar{S}_{jl} \bar{\sigma}_l) + 4Lwh^{(1)} \bar{Q}_{ij}^{(1)} (\bar{S}_{im} \bar{\sigma}_m) (\bar{S}_{jl} \bar{\sigma}_l) \right) \quad (3.32)$$

where $\bar{S}_{ij}(i, j = x, y)$ are the laminate compliance matrix components, $\bar{Q}_{ij}^{(2)}$, $\bar{Q}_{ij}^{(1)}(i, j = x, y)$ are the stiffness components of the cracked ply and constraining plies and $\bar{\sigma}_i (i = x, y)$ are the applied stresses on the laminate in global coordinate system. The energy release rate is equal to the first partial derivative of the potential energy with respect to the crack surface area under fixed applied laminate load:

$$G = - \left. \frac{\partial \Pi}{\partial A} \right|_{\bar{\sigma}_i} = -2Lwh^{(2)} \frac{\partial \bar{Q}_{ij}^{(2)}}{\partial A} (\bar{S}_{im} \bar{\sigma}_m) (\bar{S}_{jl} \bar{\sigma}_l) \quad (3.33)$$

using $A = 2wLD^{(2)}$, we obtain:

$$G = -h^{(2)} \frac{\partial \bar{Q}_{ij}^{(2)}}{\partial D^{(2)}} (\bar{S}_{im} \bar{\sigma}_m) (\bar{S}_{jl} \bar{\sigma}_l) \quad (3.34)$$

Therefore, knowing the in-plane stiffness matrix of the cracked lamina, $\bar{Q}_{ij}^{(2)}(i, j = x, y)$, for a given crack density $D^{(2)}$, the energy release rate can be derived from Equation (3.34) in terms of the crack density and the applied loads $\bar{\sigma}_i (i = x, y)$.

Under pure tensile loading, $\bar{\sigma}_x$, applied perpendicular to the cracked 90° layer the energy release rate is equal to mode I inter-laminar fracture toughness, G_{IC} , at the onset of matrix cracking. Therefore, the laminate stress at the initiation point of matrix cracks, $(\bar{\sigma}_x)_{init}$, will be the root of the following equation when $D^{(2)} \rightarrow 0$, that is:

$$(\bar{\sigma}_x)_{init} = \text{root} \left(\lim_{D^{(2)} \rightarrow 0} \left(\frac{G_I(\bar{\sigma}_x, D^{(2)})}{G_{IC}} = 1 \right) \right) \quad (3.35)$$

The in-situ tensile strength of the 90^0 layer at the initiation point of matrix cracks can now be obtained using the laminate compliances and the constitutive equation of the cracked layer:

$$Y_T^{is} = \bar{Q}_{xx}^{(2)} \bar{S}_{xx} (\bar{\sigma}_x)_{init} + \bar{Q}_{xy}^{(2)} \bar{S}_{xy} (\bar{\sigma}_x)_{init} \quad (3.36)$$

Under pure shear loading, $\bar{\sigma}_{xy}$, the energy release rate is equal to mode II inter-laminar fracture toughness, G_{IIc} at the onset of matrix cracking. Therefore, the laminate stress at the initiation point of matrix cracks, $(\bar{\sigma}_{xy})_{init}$, will be the root of the following equation when $D^{(2)} \rightarrow 0$, that is:

$$(\bar{\sigma}_{xy})_{init} = \text{root} \left(\lim_{D^{(2)} \rightarrow 0} \left(\frac{G_{II}(\bar{\sigma}_{xy}, D^{(2)})}{G_{IIc}} = 1 \right) \right) \quad (3.37)$$

Therefore, the in-situ shear strength of the constrained cracked layer, S_L^{is} , will be:

$$S_L^{is} = \bar{Q}_{xy}^{(2)} \bar{S}_{xy} (\bar{\sigma}_{xy})_{init} \quad (3.38)$$

The Hashin's failure criterion for matrix in tension can now be expressed in terms of the ply stresses and the strength properties replaced by their in-situ equivalents, Y_T^{is} and S_L^{is} , obtained from Equations (3.36) and (3.38). Therefore:

$$F_{2T} = \left(\frac{\sigma_{22}}{Y_T^{is}} \right)^2 + \left(\frac{\sigma_{12}}{S_L^{is}} \right)^2 = 1 \quad (3.39)$$

where σ_{22} and σ_{12} are the transverse and shear stress components in the ply.

3.3.3 In-plane shear behaviour

Based on the experimental observations in the literature (and also in-house experiments carried out at UBC), the in-plane shear behaviour in most laminates is nonlinear and exhibit irreversible shear strains. Therefore, it is important to incorporate the nonlinearity in the shear stress vs strain response in CODAM2 material model formulation.

The shear behaviour of composite laminates during loading-unloading can be very complex. As experimental works show, some materials exhibits constant unloading modulus approximately equal to the initial modulus (see [140]), while others might exhibit a slight decrease in the unloading modulus (see [254]). Van Paepegem et al. [255] have introduced a model that includes both plasticity and damage with parameters that can be calibrated with respect to the measured loading and unloading stiffness as well as the permanent strain of the material in shear. For the sake of simplicity, similar to the model introduced in [195], it is assumed that the slope of unloading is identical to the initial shear modulus as shown in Figure 3.7. The loading curve for shear stress is defined as a function of shear strain which can be extracted from standard tests [15]. The in-plane shear stress-strain formulation before matrix damage initiates can be written as:

$$\tau_{12} = \begin{cases} \frac{|\gamma_{12}|}{\gamma_{12}} \tau(|\gamma_{12}|) & , \text{ for } |\gamma_{12}| = \gamma_{12}^* \\ \frac{|\gamma_{12}|}{\gamma_{12}} G_{12}^0 \langle |\gamma_{12}| - \gamma_{12}^p \rangle & , \text{ for } |\gamma_{12}| < \gamma_{12}^* \end{cases} \quad (3.40)$$

where $\tau(|\gamma_{12}|)$ is the curve that defines the nonlinear shear behaviour obtained from experiments and G_{12}^0 is the initial shear modulus. The operator $\langle \cdot \rangle$ is the Mc-Cauley bracket defined as $\langle x \rangle = \max\{0, x\}$, $x \in R$. Also, γ_{12}^* is the maximum shear strain (over time) and γ_{12}^p is the inelastic shear strain defined as follows:

$$\gamma_{12}^*(t) = \max_{\tau \leq t} \{ |\gamma_{12}(\tau)| \} \quad (3.41)$$

$$\gamma_{12}^p = \gamma_{12}^* - \tau_{12}^* / G_{12}^0$$

where $\tau_{12}^* = \tau(\gamma_{12}^*)$ is the value of shear stress at γ_{12}^* .

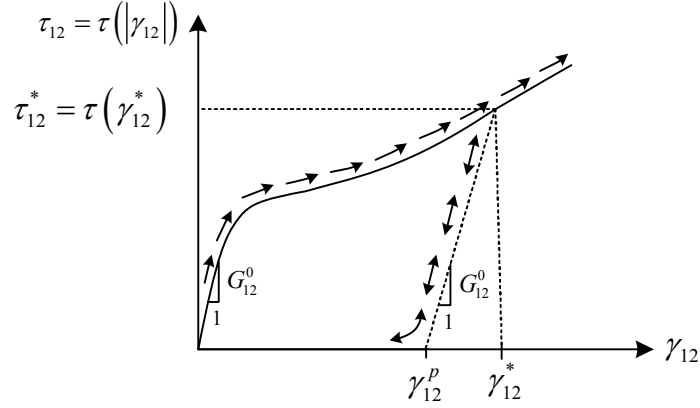


Figure 3.7: Schematic in-plane nonlinear shear behaviour

While some of the energy will be absorbed uniformly over all the specimen due to the nonlinear (irreversible) shear behaviour (see Figure 3.8), after the initiation of matrix cracks and formation of fractured surfaces, further energy will be absorbed which is proportional to the area created. Only the elastic internal energy in the element at onset of failure contributes to the fracture process. Therefore, the definition of the driving strain for matrix damage needs to consider only the elastic part of shear strain. This requires the following change in the equation for equivalent matrix strain in the enhanced CODAM2 as was shown in Equation (3.19):

$$\varepsilon_2^{eq} = \sqrt{(\varepsilon_{22})^2 + (\gamma_{12}^e)^2} \quad (3.42)$$

where γ_{12}^e is the elastic component of the in-plane shear strain of each layer calculated from the point where the matrix damage initiates:

$$\gamma_{12}^e = \gamma_{12} - \gamma_{12}^p \Big|_{@F_2=1} \quad (3.43)$$

where $\gamma_{12}^p \Big|_{@F_2=1}$ is the inelastic shear strain at the point when matrix damage initiates (i.e. when $F_2=1$). Once matrix damage initiates, the in-plane shear stress is calculated as:

$$\begin{aligned}\tau_{12} &= R_{12}G_{12}^0(\gamma_{12} - \gamma_{12}^p|_{@F_2=1}) \\ R_{12} &= (1 - \omega_1)(1 - \omega_2)\end{aligned}\quad (3.44)$$

where R_{12} is the shear stiffness reduction factor which is dependent on both fibre and matrix damage parameters. This is in contrast to the original formulation of CODAM2 material model where it was only dependent on the matrix damage parameter.

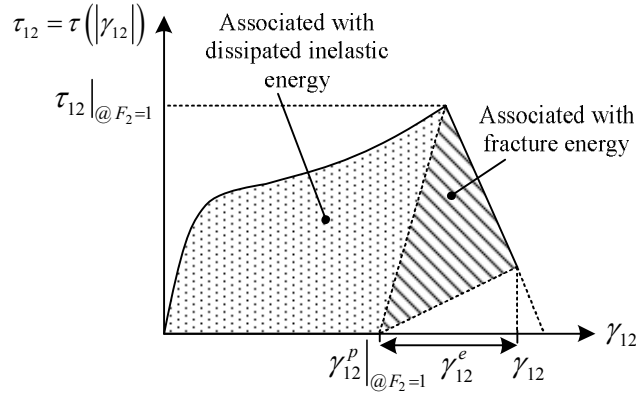


Figure 3.8: In-plane nonlinear shear behaviour and the contribution of elastic shear strain to fracture energy

3.3.4 Stiffness matrix in damaged state

Upon calculation of damage parameters, the nominal stresses in each ply are calculated from the reduced in-plane secant stiffness of the ply. For plane stress conditions, the damaged in-plane stiffness matrix, \mathbf{Q}^d , for each ply can be written:

$$\mathbf{Q}^d = \begin{bmatrix} \frac{R_1 E_1}{1 - R_1 R_2 \nu_{12} \nu_{21}} & \frac{R_1 R_2 \nu_{12} E_2}{1 - R_1 R_2 \nu_{12} \nu_{21}} & 0 \\ \frac{R_2 E_2}{1 - R_1 R_2 \nu_{12} \nu_{21}} & 0 & 0 \\ sym & & R_{12} G_{12}(\gamma_{12}) \end{bmatrix} \quad (3.45)$$

where E_1 , E_2 are the undamaged material moduli, ν_{12} , ν_{21} are undamaged major and minor Poisson's ratios, and $R_1 = (1 - \omega_1)$, $R_2 = (1 - \omega_2)$ are stiffness reduction factors in terms of damage parameters ω_1 , ω_2 in the longitudinal and transverse directions, respectively. Note that when the in-plane shear stress is nonlinear, the shear modulus, G_{12} , is not constant anymore. It is a function of the shear strain as defined by Equations (3.40) and (3.44). The shear stiffness reduction factor, $R_{12} = R_1 R_2$, as mentioned before is dependent on both fibre and matrix damage modes.

The above intra-laminar damage formulation is also extendable to a three-dimensional constitutive model suitable for three-dimensional elements available in LS-DYNA including the solid and thick-shell element formulations [158].

In problems where bending is significant, shell elements with a plane-stress constitutive formulation defined in Equation (3.45) will be adequate provided that there are enough number of integration points through the thickness of the element. This will ensure that the linear variation of in-plane strains through the thickness is captured. However, in plane stress constitutive formulations, it is assumed that the out-of-plane normal and shear stresses are zero. In order to obtain those stress components, one needs to use the equilibrium equations.

In applications where delamination between the layers is dominant, either due to free-edge induced out-of-plane stresses or bending deformations, elements with three-dimensional kinematics formulations can directly capture the out-of-plane stresses based on the three-dimensional Hooke's law. Therefore, a three-dimensional constitutive formulation for CODAM2 material model is required for such cases. In the current approach, delamination is modelled as an interface between the plies with a cohesive-based constitutive behaviour to describe the out-of-plane stress components (see Section 4.2). Therefore, in the three-dimensional constitutive formulation of CODAM2, the out-of-plane stiffness components of the plies are assumed to remain elastic and undamaged (i.e. no reductions are applied to the out-of-plane stiffness components). Instead, such reductions are applied indirectly through the inter-laminar cohesive-

based formulation. Accordingly, the 3-D damaged stiffness matrix for a single ply can be written as:

$$\mathbf{C}^d = \frac{1}{D} \begin{bmatrix} (1-R_2\nu_{23}\nu_{32})R_f E_1 & (\nu_{21} + \nu_{23}\nu_{31})R_1 R_2 E_1 & (\nu_{31} + R_2\nu_{21}\nu_{32})R_1 E_1 & 0 & 0 & 0 \\ & (1-R_1\nu_{31}\nu_{13})R_2 E_2 & (\nu_{32} + R_1\nu_{31}\nu_{12})R_2 E_2 & 0 & 0 & 0 \\ & & (1-R_1R_2\nu_{21}\nu_{12})E_3 & 0 & 0 & 0 \\ & & & DR_{12}G_{12}(\gamma_{12}) & 0 & 0 \\ & & & & DG_{23} & 0 \\ & sym. & & & & DG_{13} \end{bmatrix}$$

where

$$D = 1 - R_2\nu_{23}\nu_{32} - R_1R_2\nu_{12}\nu_{21} - 2R_1R_2\nu_{31}\nu_{12}\nu_{23} - R_1\nu_{31}\nu_{13} \quad (3.46)$$

This stiffness matrix is obtained by inverting the 3-D compliance matrix which (similar to the plane stress compliance matrix of CODAM2) follows the approach proposed by Matzenmiller et al. [166], to achieve a symmetric secant stiffness matrix. The compliance matrix is written as:

$$\mathbf{S}^d = \begin{bmatrix} \frac{1}{E_1 R_1} & -\frac{\nu_{21}}{E_2} & -\frac{\nu_{31}}{E_3} & 0 & 0 & 0 \\ -\frac{\nu_{12}}{E_1} & \frac{1}{E_2 R_2} & -\frac{\nu_{32}}{E_3} & 0 & 0 & 0 \\ -\frac{\nu_{13}}{E_1} & -\frac{\nu_{23}}{E_2} & \frac{1}{E_3} & 0 & 0 & 0 \\ 0 & 0 & 0 & \frac{G_{12}}{R_{12}} & 0 & 0 \\ 0 & 0 & 0 & 0 & G_{23} & 0 \\ 0 & 0 & 0 & 0 & 0 & G_{13} \end{bmatrix} \quad (3.47)$$

Note that in the above equation, no reduction is applied on the out-of-plane stiffness components.

3.4 Summary

In this chapter the formulation of the original macroscopic non-local CODAM2 model was briefly reviewed as the tool for capturing the intra-laminar damage modes of a sub-laminate. It was discussed that for cases where failure is governed by discrete macro-crack propagation such as large splits or delamination, continuum damage models cannot correctly describe the propagation of damage through the structure. Discrete cracks redistribute the stresses around the damage zone and consequently alter the load paths within the structure. Moreover, when delamination is dominant, the sub-laminate's fracture energy in presence of extensive delamination zones between the plies becomes difficult to define and measure. Therefore, it is necessary to explicitly model delamination which will then allow the growth of macro-cracks (e.g. splits) in the separated ply. This can be done by using a cohesive-based interface model which will be discussed in Chapter 4. The intra-laminar modes of damage, on the other hand, including matrix cracking and fibre fracture can be captured with the presented enhanced form of the non-local CODAM2 material model in a mesoscopic context. In Chapters 5 and 6, it will be shown that the non-local averaging technique is very effective in predicting the trajectory of in-plane macro-cracks irrespective of the finite element discretization. Therefore, the need to introduce pre-inserted discrete cohesive elements in the plane of a ply to capture the growth of matrix cracks is eliminated which reduces the computational cost significantly.

In this chapter, the enhancements required for considering individual plies as the building blocks of the laminate were introduced. These enhancements and modifications were associated with the prediction of initiation and saturation of matrix and fibre damage modes. The interactive effect of transverse normal and shear stress components on matrix cracking combined with the inherent non-linear shear stress-strain response of unidirectional composites necessitates the use of a stress-based criterion to signal initiation of matrix damage. Therefore, Hashin's failure criteria {{1332 Hashin,Z. 1973; 1327 Hashin,Z. 1980}} were used to identify the onset of both intra-laminar matrix and fibre damage modes. This will also make the process of calibration of damage material properties more straightforward since the initiation and saturation values of the equivalent strain parameters are calculated directly by the material model. The constraining effect of the immediate neighboring plies and the ply thickness on the unidirectional strength

properties were also considered through an approximate analytical model based on combination of fracture mechanics and a shear lag theory introduced by Zhang et al. [278,279]. Moreover, the irreversible nonlinear behaviour of in-plane shear was incorporated in both elastic and damage regimes of the loading. The structure and algorithm of this material model written as a user-defined material model in LS-DYNA are summarized in Appendix B through Appendix F.

The material parameters required for this model include the strength properties of unidirectional plies and the fracture energies associated with fibre fracture and matrix cracking. In Chapter 5, the available methods and standards for extracting strength properties and the fracture energy values are discussed. Specifically, a unique methodology will be proposed to numerically calibrate the in-situ fracture energy of both intra-laminar fibre fracture and intra-laminar matrix cracking (corresponding to matrix crack propagation in a ply constrained by adjacent plies within a laminate). These are the type of quantities that may not be directly measured from standard experiments.

Chapter 4: Inter-laminar Delamination Modelling

4.1 Introduction

For cases where failure is governed by discrete crack propagation such as large splits or delamination, fully continuum damage models often fail to correctly describe the propagation of damage through the structure. In continuum models, these cracks are “smeared” as part of the damage homogenization process. However, in reality, discrete cracks redistribute the stresses around the damaged zone and consequently alter the load paths within the structure.

Delamination in a structure subjected to in-plane loads is a subcritical failure mode [186,207] with possible effect of stiffness loss, local stress concentration in load bearing plies, and a local instability causing its further growth leading to compressive failure.

Elevated levels of inter-laminar stresses caused by impact, eccentricities in structural load paths or geometric discontinuities in the structure can lead to delamination (see Figure 2.2). Some of the structural details which may induce the local out-of-plane loads leading to inter-laminar stresses [59] are (1) free edges (either straight or curved edges) or (2) ply terminations or ply drops at taped sections, (3) bonded or co-cured joints, and (5) bolted joints. In these cases, even when the remote loading is applied in-plane the local stresses that develop around such discontinuities may be out-of-plane.

Two major causes of inter-laminar stresses that can lead to delamination in an in-plane loading condition are free-edges and intra-laminar matrix cracks.

Delamination caused by free Edges

Typically inter-laminar stresses develop near the free edges of a laminated composite. These stresses (Figure 4.1) occur due to the mismatch in engineering properties, i.e. mismatch in Poisson's ratio ν_{xy} and coefficient of mutual influence $\eta_{xy,x}$ between layers of different fibre orientations [96].

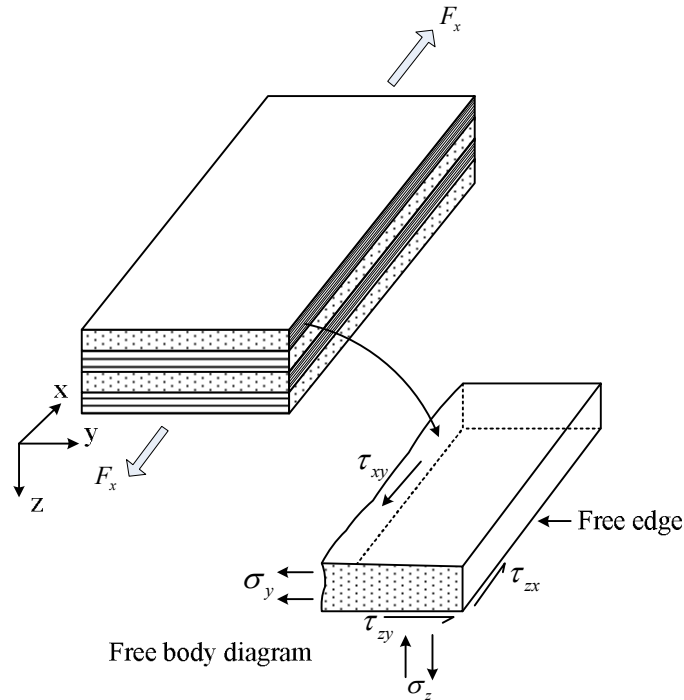


Figure 4.1: Inter-laminar stresses in a ply of a symmetric balanced laminate under axial loading, adapted from [111]

The mismatch in ν_{xy} gives rise to inter-laminar normal σ_z and shear τ_{zy} stresses and the mismatch in $\eta_{xy,x}$ causes inter-laminar shear stress τ_{xz} near the free edge of a laminate (see Figure 4.1). The magnitude of these stresses depends on the severity of the mismatch in ν_{xy} and $\eta_{xy,x}$, elastic and shear moduli, stacking sequence and mode of loading.

The other parameter affecting the inter-laminar stresses is ply thickness. Thick plies tend to promote higher inter-laminar stresses thus causing early delamination. This is obvious from

Figure 4.2 where the critical strain, ϵ_c , for the onset of edge delamination in $[45_n/-45_n/0_n/90_n]_s$ ($n=1, 2, 3$) T300/5208 graphite/epoxy laminates under unidirectional tensile loading is shown [186]. The specimens were 254mm long by 38mm wide and were loaded monotonically in tension at a rate of 44.5 N/sec until a delamination was detected. The load level corresponding to delamination onset was recorded and the corresponding applied stress, σ_c , was calculated. Then, in order to determine the nominal strain at the onset of delamination, σ_c was divided by the modulus of laminate, E_{lam} , calculated from laminated plate theory. As can be seen, the strain at initiation of delamination decreases with increase in ply thickness. It should be noted that the predictions using the approximate solution by O'Brien [186] (Equation (2.1)) are also in agreement with the experimental results and show an inverse relationship between the strain at the onset of delamination and the ply thickness. Similar trends have also been reported for other laminate layups including $[\pm 35/0/90_n]_s$, $[\pm 30/90_n]_s$, $[(\pm 30)_n/90_n]_s$ ($n=1/2, 1, 3/2, 2$) when the thickness of the 90^0 ply increases [185].

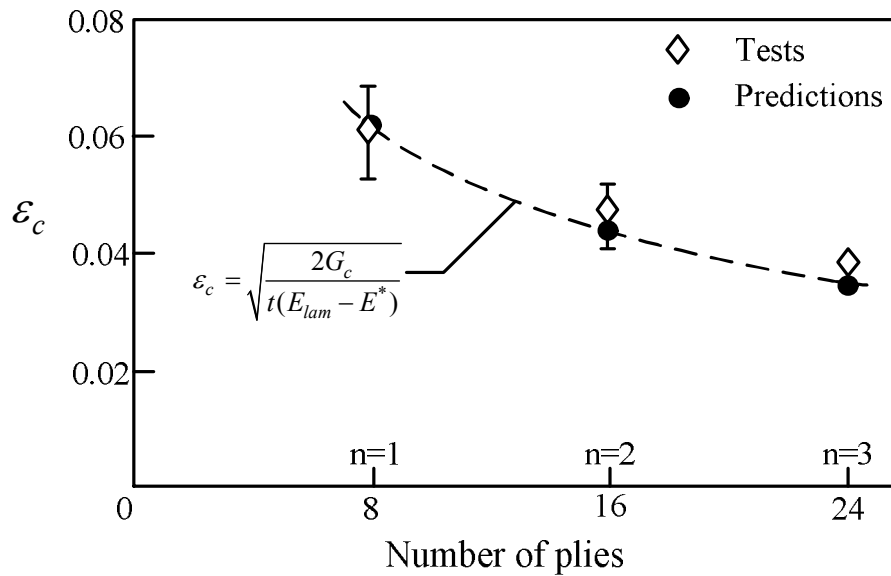


Figure 4.2: Effect of ply thickness on the onset of delamination onset strain, adapted from [186]

Delamination caused by matrix cracks

Another cause of delamination development in a laminate is matrix cracking in off-axis plies. These off-axis ply cracks create inter-laminar stresses as shown in Figure 4.3. In a quasi-isotropic graphite/epoxy laminate $[0/90/\pm 45]_s$, Reifsnider and coworkers [232] have estimated these inter-laminar stresses near the tip of the matrix crack in 90° ply. These inter-laminar stresses frequently cause local delamination which grow along ply interfaces near matrix cracks.

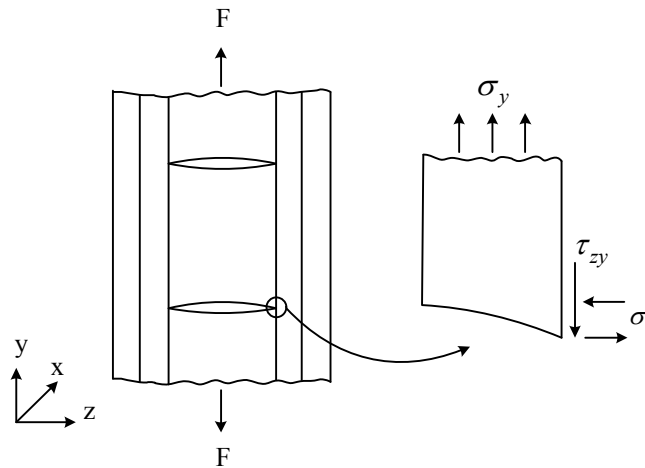


Figure 4.3: Inter-laminar stresses due to matrix cracks in off-axis plies

Prediction of delamination behaviour in composites has been the subject of research for many years. Most of such work has been to determine the stresses in the boundary layer near the free edges whether curved or straight. The problem of determining the edge stresses involves the solution of an interfacial crack between two highly anisotropic fibre composite laminae under general loading conditions. The analytical approaches to such problems have been developed to determine stress intensity factors at the tips of the crack at the interface of two or more isotropic layers or transversely isotropic half planes [40,65,210], or for an edge delamination in an angle ply laminate [259].

Because of the complexities involved analytical solutions to such problem have been rather limited. Therefore, more emphasis has been placed on the use of either finite difference [202,214] or finite element methods [57,125,184,212]. A thorough review of the most recent

numerical methods including finite difference, 2D finite element and 3D finite element methods is summarized in [124]. However, for thick realistic structural laminates, solving edge stress problems tend to be expensive using such methods.

The singular stress states that appear at the neighbourhood of the tip of transverse cracks terminating at the interface end of the delamination cracks and the mechanisms of their further progression have also attracted the attention of a large number of authors. Examples are the characterization of the influence of the bi-material parameters on the singularity of a crack perpendicular to and terminating at the interface between orthotropic materials [42], and studying the actual mechanism of growth of a crack approaching and deflecting at the interface [149,164].

Cohesive zone models as discussed in Section 2.2.3 offer a powerful method to analyze composite delamination problems. Problems of delamination in the absence of large notches or holes have been studied using this method [14,32,53,114,243,262].

Cohesive zone models offer the prospect of determining important issues such as the influence of stacking sequence on delamination crack propagation, free edge delamination initiation and propagation, and delamination around pin holes. Moreover, if damage-mechanics based in-plane failure modes are incorporated into the continuum elements representing the plies, the coupling effects between in-plane damage modes and out-of-plane delamination can be taken into account.

In this work, we will use a cohesive zone model to predict delamination in between the plies while the intra-laminar damage modes are captured by the mesoscopic non-local CODAM2 material model. In the following, the cohesive-zone model used in this work and its limitations are described.

4.2 Cohesive zone model

As mentioned before, the inter-laminar damage mode in this work (i.e. delamination) is modelled using a discrete approach based on cohesive zone model. The potential delamination interfaces between plies in LS-DYNA can be modelled using a cohesive-based tie-break contact known as `*CONTACT_AUTOMATIC_ONE_WAY_SURFACE_TO_SURFACE_TIEBREAK` [158]. The separation between nodal points of the elements from two neighboring plies is triggered by a damage parameter, ω_D , when it reaches its maximum value of one.

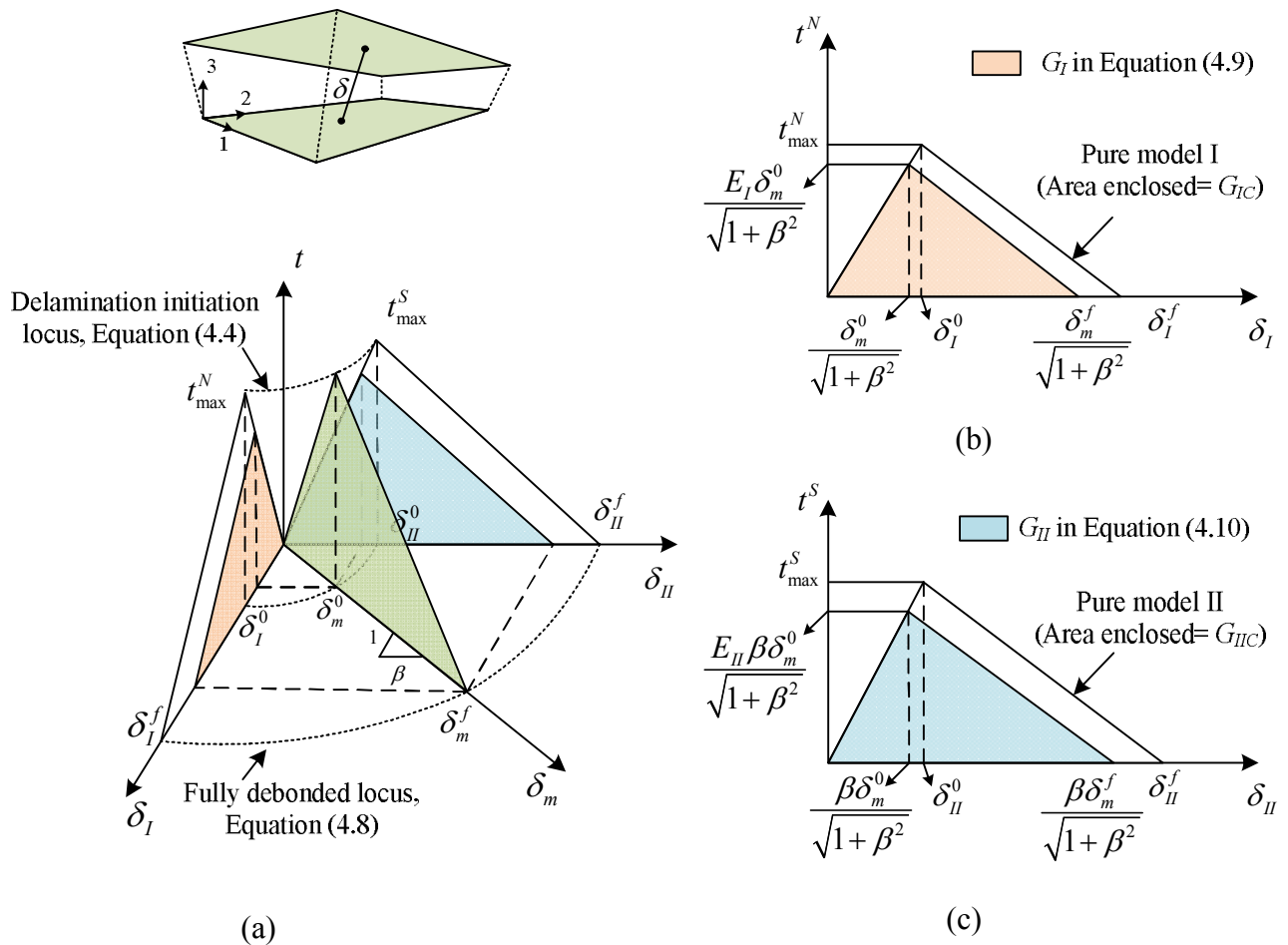


Figure 4.4: Mixed-mode traction separation law, adapted from [158]

Let us consider a point at an interface like the one shown in Figure 4.4(a). The tractions t_i between the top and bottom surfaces of the interface at that point are related to the relative displacement δ_i at the same point for $i = 1, 2, 3$ (Figure 4.4). The index value $i = 1$ corresponds to an opening mode (mode I), while the index values $i = 2$ and 3 correspond to a shear mode (mode II).

The formulation that governs the relationship between the relative displacement, δ_i , and the tractions, t_i , can be illustrated in a three-dimensional mixed-mode map, as used by several authors [32,114,196], by presenting the normal opening mode (mode I) on the $0-t^N-\delta_I$ plane, and the transverse shear mode (mode II) on the $0-t^S-\delta_{II}^f$ plane (see Figure 4.4 (a)). The triangles $0-t_{\max}^N-\delta_I^f$ and $0-t_{\max}^S-\delta_{II}^f$ are the bi-linear responses in the pure opening and pure shear modes, respectively (see Figure 4.4 (b) and (c)). Any point on the $0-\delta_I-\delta_{II}$ plane represents a mixed-mode relative displacement. The shear relative-displacement, δ_{II} , and the magnitude of the relative mixed-mode displacement, δ_m , are defined as:

$$\begin{aligned}\delta_{II} &= \sqrt{\delta_2^2 + \delta_3^2} \\ \delta_m &= \sqrt{\delta_{II}^2 + \langle \delta_I \rangle^2}\end{aligned}\tag{4.1}$$

where the operator $\langle \cdot \rangle$ is the Mc-Cauley bracket defined as $\langle x \rangle = \max\{0, x\}$, $x \in \mathbb{R}$. The mixed-mode ratio, β , that defines the participation of the different modes, is defined as:

$$\beta = \max\left\{0, \frac{\delta_{II}}{\delta_I}\right\}\tag{4.2}$$

Using the mixed-mode ratio, the relative displacements in pure mode I and II are related to the mixed-mode displacement, δ_m , as follows:

$$\delta_I = \frac{\delta_m}{\sqrt{1 + \beta^2}}$$

$$\delta_{II} = \frac{\beta \delta_m}{\sqrt{1 + \beta^2}} \quad (4.3)$$

The initiation of delamination damage mode is predicted by the following quadratic mixed-mode criterion:

$$\left(\frac{\langle t^N \rangle}{t_{\max}^N} \right)^2 + \left(\frac{t^S}{t_{\max}^S} \right)^2 = 1 \quad (4.4)$$

where t^N and t^S are the normal and shear tractions between the top and bottom surfaces of the interface, and t_{\max}^N and t_{\max}^S are peak normal and shear inter-laminar strength values in pure mode I and mode II separation. The shear and normal tractions, t^S and t^N , are defined as:

$$t^S = \sqrt{t_2^2 + t_3^2} = E_{II} \delta_{II} \quad (4.5)$$

$$t^N = t_1 = E_I \delta_I$$

where E_I and E_{II} are the stiffness components corresponding to pure mode I and mode II traction-separation law. The interface stiffness needs to be large enough to assure a stiff connection between the two neighboring layers and small enough to avoid spurious oscillations. With the use of Equation (4.3), the shear and normal tractions, t^S and t^N , can be related to the mixed-mode displacement as follows:

$$t^S = E_{II} \frac{\beta \delta_m}{\sqrt{1 + \beta^2}} \quad (4.6)$$

$$t^N = E_I \frac{\delta_m}{\sqrt{1 + \beta^2}}$$

Therefore, for a given mode ratio, the displacements and tractions corresponding to mode I and II at the onset of delamination can be obtained from Equations (4.3) and (4.6) by replacing, δ_m , with its initiation value δ_m^0 .

The onset relative-displacement, δ_m^0 , is obtained by substituting $t_{\max}^N = E_I \delta_I^0$, $t_{\max}^S = E_{II} \delta_{II}^0$ and Equations (4.3) and (4.6) at the onset of delamination into the mixed-mode initiation criterion of Equation (4.4) which leads to:

$$\delta_m^0 = \delta_I^0 \delta_{II}^0 \sqrt{\frac{1 + \beta^2}{(\beta \delta_I^0)^2 + (\delta_{II}^0)^2}} \quad (4.7)$$

The mixed-mode propagation criterion establishes the state of complete decohesion for different ratios of normal and shear mode energy release rates. There are several criteria that describe mixed-mode propagation (see Table 2-7). The cohesive zone model in LS-DYNA follows the Power Law criterion [264] expressed as:

$$\left(\frac{G_I}{G_{Ic}} \right)^\alpha + \left(\frac{G_{II}}{G_{IIc}} \right)^\alpha = 1 \quad (4.8)$$

where G_{Ic} and G_{IIc} are the mode I and mode II inter-laminar fracture energy values. The power coefficient, α , in the current study is chosen to be one. The energy absorbed by each mode in a mixed-mode loading is equal to the shaded area shown in Figure 4.4(b) and (c):

$$G_I = \frac{E_I \delta_m^0 \delta_m^f}{2\sqrt{1 + \beta^2}} \quad (4.9)$$

$$G_{II} = \frac{E_{II} \beta^2 \delta_m^0 \delta_m^f}{2\sqrt{1 + \beta^2}} \quad (4.10)$$

Substituting the above relations into Equation (4.8), yields the final mixed-mode displacement,

δ_m^f , as:

$$\delta_m^f = \frac{2(1 + \beta^2)}{\delta_m^0} \left[\left(\frac{E_I}{G_{Ic}} \right)^\alpha + \left(\frac{\beta^2 E_{II}}{G_{IIc}} \right)^\alpha \right]^{-\frac{1}{\alpha}} \quad (4.11)$$

Based on the cohesive zone model, the stresses after the onset of delamination are calculated using the damage variable from the following equations:

$$\begin{aligned} t^N &= (1 - \omega_D) E_I \delta_I \\ t^S &= (1 - \omega_D) E_{II} \delta_{II} \end{aligned} \quad (4.12)$$

where the corresponding damage parameter associated with delamination growth, ω_D , is defined based on the mixed-mode displacement δ_m and its corresponding initiation and final values:

$$\omega_D = \frac{(\delta_m - \delta_m^0) \delta_m^f}{(\delta_m^f - \delta_m^0) \delta_m} \quad (4.13)$$

4.2.1 Cohesive element size requirement

In order to obtain accurate representation of the fracture zone using CZM, the tractions in the cohesive zone must be represented properly by the finite element spatial discretization. When the cohesive zone is discretized by too few elements, the distribution of tractions ahead of the crack tip is not represented accurately. The length of the cohesive zone is defined as the distance from the crack tip to the point where the maximum cohesive traction is reached. A robust and accurate prediction using CZM requires the elements to be several times smaller than this cohesive zone length. The length of the cohesive zone is related to the fracture energy, stiffness and strength, but for delamination cracks in laminates, the thickness is an additional factor to be considered [91,246,276]. Different models have been suggested in the literature for determining the length of the cohesive zone length. Irwin [110] estimated the size of plastic zone ahead of crack tip in an infinite ductile body by considering the crack tip zone where the stress exceeds the tensile yield stress. Dugdale [60] calculated the size of cohesive zone by idealizing the plastic region as a narrow strip ahead of crack tip that is loaded by constant yield stress. Following the work by Irwin and Dugdale, Hui [103] estimated the length of the cohesive zone for soft elastic materials, while Rice [209] and Falk et al. [66] estimated the length of the cohesive zone as a function of

the crack growth velocity. Barenblatt [18] used assumptions similar to Dugdale [60] for ideally brittle materials. The length of cohesive zone suggested by these models for the case of plane stress condition have the following generalized form:

$$l_{cz} = ME \frac{G_c}{(t_{\max})^2} \quad (4.14)$$

where E is the Young modulus of the material, G_c is the critical energy release rate, t_{\max} is the maximum interfacial strength, and M is a parameter that depends on the cohesive zone model and is summarized in Table 4-1 for the plane stress conditions.

Table 4-1: Estimated cohesive zone length (l_{cz}) and equivalent value for M in Equation (4.14)

Source	l_{cz}	M
Irwin [110]	$\frac{1}{\pi} E \frac{G_c}{(t_{\max})^2}$	0.31
Hui [103]	$\frac{2}{3\pi} E \frac{G_c}{(t_{\max})^2}$	0.21
Dugdale [60], Barenblatt [18]	$\frac{\pi}{8} E \frac{G_c}{(t_{\max})^2}$	0.4
Rice [209], Falk et al. [66]	$\frac{9\pi}{32} E \frac{G_c}{(t_{\max})^2}$	0.88
Hillerborg et al. [97]	$E \frac{G_c}{(t_{\max})^2}$	1

The above mentioned estimations are for cracks in isotropic materials, but as pointed out by Yang et al. [276], the elastic modulus in the cohesive length equation for orthotropic materials becomes a function of the material's longitudinal modulus, transverse modulus, shear modulus, depth and plane stress or plane strain conditions. It should be noted that the above analytical estimation are for infinite bodies, where material depth has no effect on the cohesive zone length. For analysis of composite delamination, the effects of specimen thickness on cohesive zone length can be critical due to the slender nature of typical laminates. Cox and Yang [276] proposed a formulation for estimating the cohesive zone length in slender laminates, with centred cracks, under mode I and mode II loading, respectively:

$$l_{cz,I} = \left(E'_I \frac{G_c}{(t_{\max}^N)^2} \right)^{1/4} h^{3/4} \quad (4.15)$$

$$l_{cz,II} = \sqrt{\left(E'_{II} \frac{G_c}{(t_{\max}^S)^2} h \right)} \quad (4.16)$$

where h is the laminate half-thickness, E'_I and E'_{II} are equivalent elastic moduli for orthotropic material (see [43]), and t_{\max}^N and t_{\max}^S are the peak stresses in the cohesive law for mode I and II, respectively.

The length of the cohesive zone given by the above analytical solutions are proportional to the fracture energy release rate (G_c) and to the inverse of the interfacial strength t_{\max} . According to Turon et al. [245,246], the length of the cohesive zone is smaller than one or two millimeters for typical graphite–epoxy or glass–epoxy composite materials. Since elements must be several times smaller than the cohesive zone length, very small element sizes are commonly required for robustness and accuracy of the solution. This element size requirement seriously limits the specimen dimensions that can be simulated within reasonable computation time. The number of elements in the cohesive zone is:

$$N_e = \frac{l_{cz}}{l_e} \quad (4.17)$$

where l_e is the element size in the direction of crack growth. Turon et al. [245,246] have proposed an engineering solution to this limitation to increase the length of the cohesive zone in the simulation artificially by reducing the interface strength. The interface strength properties are reduced such that the length of the cohesive zone increases to cover at least three elements. Results presented in [51,245], show that using this approach the computational cost of the simulations is reduced considerably thus rendering possibility of analysing large scale structures.

Alfano and Crisfield [12] observed that variations of the maximum interfacial strength do not strongly influence the predicted results, but that lowering the interfacial strength can improve the

convergence rate of an implicit solution. The result of using a lower interfacial strength is that the length of the cohesive zone and the number of elements in the cohesive zone increase. Therefore, the representation of the softening response of the fracture process ahead of the crack tip is more accurate with a lower interface strength at the expense of altering the stress distribution in the regions near the crack tip [12]. Although the stress concentrations in the bulk material near the crack tip are less accurate when using a reduced interfacial strength value, the mechanics of energy dissipation are properly captured, which ensures the proper propagation of the crack front.

The proposed methods for scaling down the interfacial strength values are mostly given based on estimation of the length of the cohesive zone. Different formulations have been proposed for a prescribed pure mode I or pure mode II cohesive traction laws for plane stress cases in undamaged isotropic materials or unidirectional transversely isotropic materials [18,60,66,97,103,209]. However, no numerical studies have been presented to validate the accuracy of such analytical formulations across a range of material properties, structural geometries and load conditions. For more complex problems, delamination occurs under mixed-mode loading either originating from free-edge inter-laminar stresses between plies with different fibre orientations or from intra-laminar matrix crack tips reaching the ply interfaces. Estimating the cohesive zone length in these cases is not straightforward. Another issue is that the minimum number of elements needed in the cohesive zone is not well established: Moes and Belytschko [176] suggested using more than 10 elements. However, Falk et al. [21] used between 2 and 5 elements in their simulations. Camanho et al. [31], suggested that 3 elements are sufficient for a double cantilever beam (DCB) to predict the propagation of delamination in mode I.

In Chapter 5, a more intuitive approximate method is introduced for reduction of interfacial strength properties for cases where delamination starts as a result of matrix cracks and their migration to the ply interface. Based on this method, the amount of reduction in the interfacial strength properties will implicitly be dependent on the geometry, the ply thickness and the fibre orientation of the plies. Using this simple and practical method, the growth of delamination can be coupled with the growth of intra-laminar matrix damage modes quite effectively.

4.3 Summary

In this chapter the common causes of delamination specially those associated with inter-laminar stresses induced by matrix cracks or created at free edges were discussed. While the intra-laminar damage modes are captured by the mesoscopic non-local CODAM2 material model as proposed in the previous chapter, the inter-laminar delamination between dissimilar plies is captured by the mixed-mode cohesive interface model described in this chapter. A common drawback of cohesive methods is that the cohesive zone has a given length and that robust and accurate simulations require the elements to be several times smaller than this cohesive zone. One engineering solution commonly used in the literature is to artificially increase the length of the cohesive zone in the simulation by reducing the interface strength. However, the estimation of the amount of reduction is not known for any geometry, loading scenario and laminate sequence, since the prediction of the length of the cohesive zone is not well studied or validated for all the cases. In the following chapter, as part of numerical calibration of the inter-laminar damage model, a simple yet intuitive method will be proposed to estimate the amount of reduction for the interface strength properties.

Chapter 5: Model Calibration

In using the proposed methodology of combined continuum and discrete approaches described in Chapters 3 and 4, the damage parameters need to be characterized using a combination of experimental and numerical analysis. In this chapter, the methodology for determining the material parameters associated with the inter-laminar and intra-laminar damage modes will be outlined in detail.

5.1 Inter-laminar model parameters

In this section the calibration of material parameters required for the cohesive interface to capture delamination mode is summarized. The behavior of the cohesive interface is governed by the inter-laminar strength parameters and the inter-laminar fracture energy values which will be discussed in the following.

5.1.1 Inter-laminar damage initiation- numerical calibration

As discussed in Chapter 4, one of the drawbacks in the use of CZM is that very fine meshes are needed to assure a reasonable number of elements are present in the cohesive zone. An engineering solution is to reduce the interfacial strength values in order to increase the size of the cohesive zone artificially and hence accommodate coarser elements to accurately capture the softening behaviour ahead of the crack tip.

In the presence of matrix cracks, the accurate prediction of the singular state of inter-laminar stresses in finite element methods requires an extremely fine mesh which is quite often impractical. In order to capture the onset of delamination stemming from the matrix crack tips using a finite element model with a reasonable mesh size, we propose to scale down the inter-ply strength values based on the value of the operative inter-laminar stresses at the instant when matrix damage in the neighboring ply (plies) is deemed to have occurred. Therefore, we conduct a preliminary finite element analysis step with the same mesh size as in the main model but with

cohesive contact interfaces deactivated to identify the status of inter-laminar stress distribution at locations where matrix cracks and hence delaminations are expected to occur.

The process involves running a model in which each dissimilar ply is modelled with 3D elements through the thickness and the intra-laminar damage modes in the plies are active while the cohesive interface remains intact. For this purpose, the inter-laminar normal and shear strengths, t_{\max}^N and t_{\max}^S are set to high values to inhibit delamination. Alternatively, the plies can be tied together using the constrained contact formulation available in LS-DYNA (*CONTACT_TIED_SURFACE_TO_SURFACE [158]). From this simulation the inter-laminar shear and normal stresses will be obtained over a finite region around the notch tip (or free edge) where matrix damage first occurs. The number of elements inside this region must be large enough to adequately capture the softening behaviour of the cohesive zone model. Based on numerical studies in the literature [245,246] and various numerical case studies using CODAM2, it is deemed that 3-4 elements give reasonable spatial resolution. As schematically shown in Figure 5.1 for the notch tip in an OCT specimen geometry for a given laminate layup, the inter-laminar stresses will be obtained at an interface for a region around a point where matrix damage initially occurs (in this case the points around the notch tip). At the instant when matrix damage initiates in any of the elements of the adjacent plies inside this region, the inter-laminar normal and shear stresses will be averaged over this region. This process will be repeated for all the interfaces through the laminate thickness and the maximum of the averaged inter-laminar normal and shear stresses for all the interfaces will be used as the inter-laminar strength values, t_{\max}^N and t_{\max}^S , in Equation (4.4). The justification behind this procedure is that matrix cracking-induced delamination is the culmination of multiple micro-delaminations, which are initiated when multiple transverse matrix cracks reach the interface, and coalesce to form a macro-delamination. This approach is not only aligned with the practical solution offered by Turon et al. [244], it also implicitly accounts for the effect of ply thickness on the initiation of delamination since the initiation of delamination is indirectly linked to the matrix cracking which is in turn influenced by ply thickness. In this work, the dependency of matrix damage initiation on ply thickness is enabled using the shear lag theory (Section 3.3.2) and details of intra-laminar model calibration are described later in this chapter (Section 5.2).

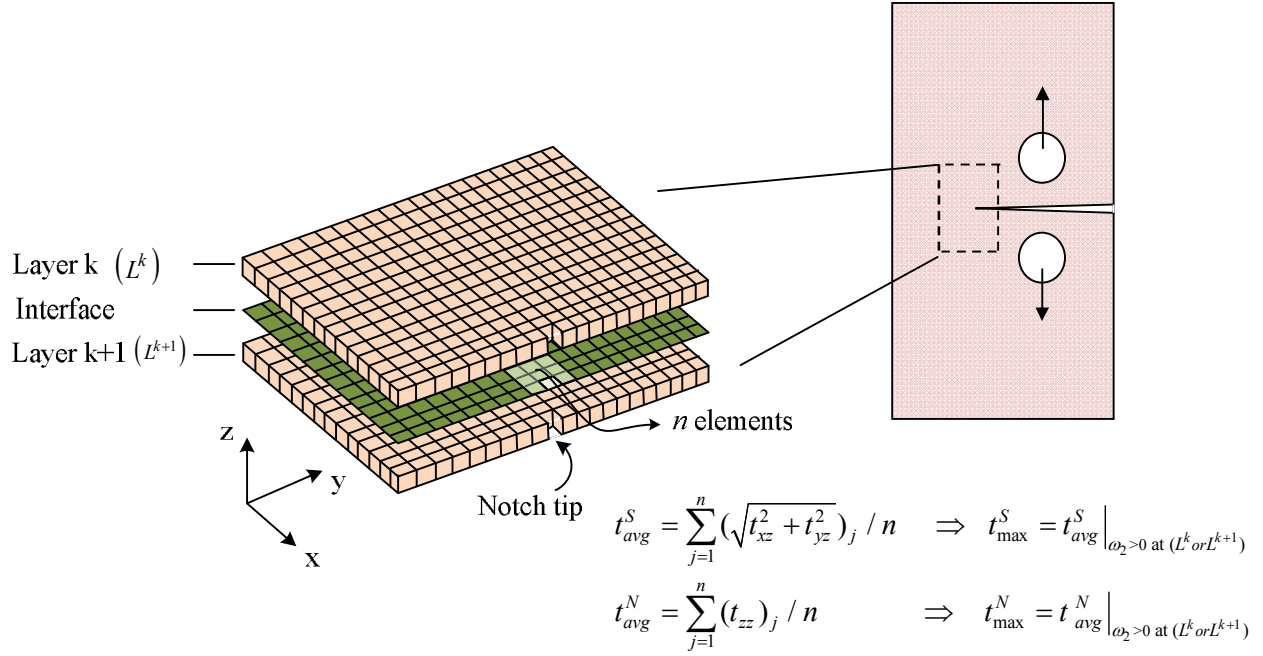


Figure 5.1: Exploded through-thickness view of the region close to the notch tip of OCT specimen showing contact interface between adjacent dissimilar plies modelled using 3D solid or thick shell elements. The averaged interface shear and normal stresses, t_{avg}^S and t_{avg}^N , inside a zone of ‘n’ elements close to the notch tip will be extracted from an elastic (undamaged) tied contact interface. At a time step when intra-laminar matrix damage in adjacent plies initiates (i.e. $\omega_2 > 0$ in L^k or L^{k+1}), the averaged normal and shear stresses are used as the calibrated maximum inter-laminar stresses, t_{max}^S and t_{max}^N , for the cohesive-based contact interface.

5.1.2 Inter-laminar damage progression- Experimental calibration

While the numerically calibrated inter-laminar strength values replace the actual inter-laminar strength properties, the first and second mode of inter-laminar fracture energies, G_{Ic} and G_{IIc} , will not be changed in order to properly capture the mechanics of energy dissipation and progression of delamination. The mode I component of the fracture toughness, G_{Ic} , can be measured using the Double Cantilever Beam (DCB) test ASTM-D 5528 [15]. The mode II component of the fracture toughness, G_{IIc} , can be measured using the Four-Point End Notched

Flexure (4-ENF) test specimen [163,180]. These tests have been the subject of an extensive research throughout the years. A comprehensive review of these tests can be found in [165,187,218].

5.2 Intra-laminar model parameters

In this section the calibration of material parameters required for initiation and saturation of intra-laminar damage modes including fibre and matrix damage modes are described. The available methodologies in the literature are reviewed. For cases where standard tests are not available, a systematic methodology is introduced to obtain the parameters through the correlations of numerical virtual tests with relevant experimental tests.

5.2.1 Intra-laminar damage initiation- Experimental calibration

As discussed in Section 3.3.1.1, the intra-laminar fibre and matrix damage initiation are related to the strength properties of individual plies. These strength properties can be measured by conducting ASTM standard tests on unidirectional laminates [6-8]. While relatively simple to perform, the complete series of tests required to characterize a given material system are expensive both in terms of time and resources. With the extensive research in the field of composites, there exists a body of published characterization data available for many of the widely used material systems (see for example [1,2,121]). These data can also be supplemented by material suppliers and larger material end-users who frequently have libraries of material characterization data for use in design calculations.

Based on what was presented in Section 3.3.2.2, the in-situ in-plane tensile and shear strength properties, Y_T^{is} and S_L^{is} , can be calculated by using Equations (3.36) and (3.38) in order to account for the effect of ply thickness and constraint imposed by neighboring plies on the initiation of matrix damage.

5.2.2 Intra-laminar damage progression- Review of existing experimental methods

As described in Section 3.3.1.2, the progression of the intra-laminar damage is governed by the fracture energy values for the fibre and matrix damage modes. The determination of the fracture energies associated with both fibre and matrix failure modes are more complicated since there are no standard tests available to determine them. Typically notched tests such as compact tension/compression loading geometries are employed to extract fracture toughness of materials. However, the purpose of these tests is to achieve stable and self-similar crack growth which in the case of composites can only be achieved for weakly orthotropic or quasi-isotropic layups.

5.2.2.1 Intra-laminar fibre fracture energy

Different notched geometries have been used in the literature to characterize the intra-laminar fracture behaviour of composites fibre failure mode [35,58,141-144,147]. The following provides a brief review of some of the tests used by researchers to determine the fibre fracture energy.

Leach and Seferis [147] used three-point bend specimens with a $[0]_{40}$ layup to measure the fracture toughness associated with the tensile fibre failure mode of a carbon/PEEK composite, and reported a critical energy release rate of 26 kJ/m^2 .

Jose et al. [118] investigated intra-laminar fracture energy of laminates made of M55J/M18 carbon/epoxy with layup $[0/90]_{15}$, to determine the fracture toughness associated with tensile loading using Over-height Compact Tension (OCT) specimens. The experimental results were compared with finite element simulations using a modified crack-closure integral method. Based on the work by Jose et al. [118], Pinho et al. [200] concluded that the mode I critical energy release rate reported by Jose et al. corresponds to the mode I critical energy release rate for fibre fracture in the 0^0 layers combined with matrix crack propagation in the 90^0 layers. Assuming that those energies are additive, and that the matrix tensile toughness is similar in magnitude to the (inter-laminar) mode I critical energy release rate (i.e. 0.2 kJ/m^2), they reported the critical energy release rate for the fibre tensile failure mode of M55J/M18 carbon/epoxy to be about 31.7

kJ/m^2 . Using the same procedure, Laffan et al. [144] have reported an R-curve for the fibre fracture energy of IM7/8552 CFRP with initiation and propagation values of $112 \pm 9.8 \text{ kJ/m}^2$ and $147 \pm 12 \text{ kJ/m}^2$, respectively. This procedure neglects other damage modes including delamination as well as the interactions between the different layers that are failing in different modes. It is also assumed that a single matrix crack parallel to the pre-crack occurs in the 90° layers.

Pinho et al. [200] also used the same assumption to investigate the intra-laminar toughness associated with fibre breakage in tension and fibre-kinking in compression in unidirectional prepreg composites using Compact Tension (CT) and Compact Compression (CC) specimens made of T300/913 carbon-epoxy for a $[90/0]_{8s}$ layup. The initiation and propagation values of the tensile fibre failure critical energy release rate were determined to be 91.6 kJ/m^2 and 133 kJ/m^2 , respectively. For compressive loading, propagation values could not be obtained directly because of contact in the crushed area of the specimen. The measurement of the energy dissipation associated with longitudinal compressive loading is complex because several dissipative phenomena are involved, such as crack growth, crushing and friction. Later, Donadon et al. [58], presented a numerical and experimental investigation on the mode I intra-laminar fracture energies of a hybrid plain weave composite laminate manufactured using resin infusion under flexible tooling (RIFT) process. The pre-cracked geometries consisted of OCT, double edge notch (DEN) and centrally cracked four-point bending (4PB) test specimens. The authors also presented a methodology based on the numerical evaluation of the strain energy release rate using the J-integral method to derive new geometric correction functions for the determination of the stress intensity factor for composites. They reported a lower scatter in the toughness values using 4PBT specimens. They obtained initiation and propagation toughness values around 2 kJ/m^2 and 10 kJ/m^2 , respectively, in the weft direction. Whereas, initiation and propagation toughness values around 100 kJ/m^2 and 165 kJ/m^2 , respectively, were obtained in the warp direction.

Vaiyda and Sun [248] carried out tensile tests on several centre-notched laminates made of AS4/3501-6 graphite/epoxy with different laminate layups including $[0/90/45/-45]_s$, $[45/-45/90/0]_s$, $[90/0/45/-45]_s$, $[0/15/-15]_s$, $[0/30/-30]_s$, $[0/45/-45]_s$, $[0/90]_{2s}$. They observed from the X-ray results that only the 0° plies exhibited fibre failure whereas the off-axis plies failed along

matrix cracks. Hence, it was proposed that the fracture toughness of the 0^0 plies (K_{Ic}^0) is a constant at failure which means that the laminate fails when the stress in the 0^0 plies reaches the critical value K_{Ic}^0 (i.e. the toughness of 0^0 plies in the event of fibre breakage). Vaiyda and Sun [248] suggested a simple method to estimate this parameter. Using lamination theory, the load carried by the 0^0 plies is related to the applied load on the laminate without accounting for the effect of stress distribution in the damaged zone:

$$\sigma_c^0 = \eta\sigma_c \quad (5.1)$$

where σ_c is the laminate applied stress at failure, σ_c^0 is the remote stress in the 0^0 ply, and η is a parameter that depends on the laminate configuration and the material system and can be calculated using the classical lamination theory. Knowing that the laminate toughness, K_{Ic} , can be expressed as $K_{Ic} = \sigma_c \sqrt{\pi a} f(a)$ and by substituting for σ_c in terms of σ_c^0 , we have:

$$K_{Ic}^0 = \eta K_{Ic} \quad (5.2)$$

Therefore, they suggested that the fracture toughness of the laminate can be related to a single parameter K_{Ic}^0 . They showed that for the above mentioned laminate configurations the calculated K_{Ic}^0 values based on Equation (5.2) lead to a mean value of 110 MPa.m^{1/2} with less than 10% standard deviation.

5.2.2.2 Intra-laminar matrix fracture energy

There is an extensive work on the measurement of inter-laminar matrix fracture energy. However, the intra-laminar fracture characterization is not so well studied owing to some experimental difficulties mostly due to fibre bridging and the effect of constraining plies. This translaminar fracture is commonly characterized by a crack running parallel to fibres through the layers' thickness and is required for transverse matrix cracking analysis.

The intra-laminar mode-I fracture toughness has been measured for a number of unidirectional material systems including graphite/epoxies [98,160], glass/epoxies [189,220], and graphite/thermoplastics [98,147]. Several test geometries have been used, including the double cantilever beam (DCB), CT, 3PB and 4PB, and mixed bending-tension (MBT) tests (see Table 5-1). In all these types of experiments, it has been attempted to confine the matrix crack to a single crack parallel to a transverse intra-laminar starter crack. This can be done by creating a pre-crack using disk cutters [220], diamond coated wires [231], razor blades [113] or by inserting a Teflon film through the thickness of the laminate [199]. In most cases, the magnitude of mode I intra-laminar critical strain energy release rate obtained from a unidirectional laminate configuration is reported to be comparable to its inter-laminar counterpart with a ratio ranging from 0.9 to 1.8.

The amount of work on characterizing the intra-laminar fracture energy dominated by shear mode is very limited in comparison with mode I. As pointed out in [26], mode II fracture toughness is measured by methods based on fracture near a central crack under an applied shear load [270] or flexure of end-notched specimens [157]. Both of these types of tests lead to unstable crack growth, and therefore only a crack initiation fracture toughness can be measured. In contrast, splitting of unidirectional composites near a central hole under longitudinal tensile load is stable, and the entire R-curve may be determined. Bazhenov [26] used this specimen configuration to measure the R-curve for mode II failure for four different unidirectional laminates with reinforcements including, S-glass, carbon UKN-5000 and aramid SVM, Armos and Terlon fibres. Hot-setting epoxy EDT-10 resin was used as a matrix. It was shown that under mode II loading, the difference between fracture toughness at split initiation and that at split growth is significant. It was observed that the fracture toughness increases with increase in split length. The mode II fracture toughness was between 1.35 to 10 kJ/m² depending on split length and fibre type. Except for the initial parts of R-curves for split lengths less than 20mm, the fracture toughness was high, approximately 10-times higher than the typical mode I values (0.2 to 0.8 kJ/m²). For example at a split length of 50 mm, the mode II fracture energy was measured to be between 4 to 10 kJ/m², essentially higher than those at split initiation and mode I loading. The increase in fracture toughness was attributed to the presence of friction and unbroken fibres bridging the opposite sides of the split.

Table 5-1: A summary of experimental studies on measurement of intra-laminar matrix fracture energy for various material systems in unidirectional laminates

Composite materials	Test methods
<p><u>Graphite/epoxies</u> (Hine, Brew et al. 1989) [98] (Slepetz, J.M. and L. Carlson 1975) [225] (Macedo, Pereira et al. 2012) [160]</p>	<p><u>Double cantilever beam (DCB)</u> (Sørensen, Jacobsen 1998) [231] (Iwamoto, Ni et al. 1999b, Iwamoto, Ni et al. 1999a)[112,113]</p>
<p><u>Glass/epoxies</u> (Slepetz, J.M. and L. Carlson 1975) [225] (Shaw Ming Lee 1986) [220] (Parhizgar, Zachary et al. 1982) [189]</p>	<p>(de Moura, Campilho et al. 2010) [54] (Hine, Brew et al. 1988) [99] (Hine, Brew et al. 1989) [98]</p>
<p><u>Graphite/thermoplastics</u> (Leach, Moore 1985) [147] (Hine, Brew et al. 1988) [99] (Hine, Brew et al. 1989) [98]</p>	<p><u>Compact tension (CT)</u> (Slepetz, J.M. and L. Carlson 1975) [225] (Garg 1986a) [77] (Truss, Hine et al. 1997) [241] (Jose, Ramesh Kumar et al. 2001) [118] (Gutkin, Laffan et al. 2011) [85]</p>
	<p><u>Four-point bend (4PB)</u> (Leach, Moore 1985) [147] (Garg 1986a) [77] (Hine, Brew et al. 1989) [98]</p>
	<p><u>Mixed bending-tension (MBT)</u> (Macedo, Pereira et al. 2012) [160]</p>

The measurement of intra-laminar matrix fracture energy from a unidirectional laminate does not take into account the interaction of matrix damage in a laminate with delamination. Moreover, matrix cracking in a multidirectional laminate may not occur as a single crack similar to what can be achieved in an experimental setup for a unidirectional laminate. Often they are in the form of multiple distributed cracks with a combination of mode I and mode II actions. In some numerical studies [87,114], where intra-laminar damage at the ply level is modelled by using discrete elements, this type of damage is treated similarly to delamination. This can be justified by the fact that enough number of potential crack interfaces is inserted in the plies to dissipate the same amount of energy by matrix cracks as in the experiment. Therefore, the intra-laminar matrix fracture energy is assumed to be similar to the inter-laminar fracture energy values. However, in the proposed methodology where we use a continuum damage based approach, the

fracture surfaces caused by all matrix/fibre debonding and matrix cracks are not modelled directly (explicitly). Therefore, the inter-laminar fracture energy values do not represent the correct amount of energy absorbed by this damage mechanism.

5.2.3 Intra-laminar damage progression- Numerical calibration

In this work, we calibrate the intra-laminar fracture energy in tension from the numerical analysis of a set of OCT tests on cross-ply laminates using a series of virtual tests. Cross-ply laminates made of IM7/8552 CFRP material with two different stacking sequences: (i) blocked-ply layup ($[0_4/90_4]_{2s}$), and (ii) a dispersed-ply layup ($[0/90]_{8s}$) in OCT configuration were tested by Li et al. [154] and are used here for extracting intra-laminar fracture energies for both fibre and matrix damage modes. While the dispersed laminate exhibits minor delamination with multiple matrix cracks and fibre breakage confined to a local and measurable damage zone ahead of the notch, the lumped (blocked-ply) laminate shows individual isolated discrete damage modes [154].

The experimental results for the blocked cross-ply laminate that are governed by delamination and splitting (i.e. matrix damage dominated) are used to estimate the appropriate values of the matrix intra-laminar fracture energy. The numerical analyses are performed using a range for fracture energy of matrix cracking while keeping all the other damage parameters constant. The numerical predictions in terms of the global behaviour (e.g. force-displacement) and damage mechanisms are compared against the experimental results to calibrate the intra-laminar matrix fracture energy. Once the intra-laminar matrix fracture energy is calibrated, the same process is repeated for the dispersed cross-ply laminate with its damage behaviour dominated by fibre fracture. The dispersed layup is useful for calibration of the fibre fracture since the extent of delamination and splits is very limited in comparison with the block-ply laminates. In order to validate the final estimated values for intra-laminar fracture energies, they will be used in simulations of quasi-isotropic laminate layups made of the same material system in next chapter (see Section 6.1).

In the following, the numerical calibration for intra-laminar matrix and fibre fracture energies is shown with more details for laminates made of IM7/8552 CFRP unidirectional prepregs. However, the process will be similar for any other material system.

5.2.3.1 Calibration of intra-laminar fracture energies for IM7/8552 CFRP

Figure 5.2 shows the experimental force vs the pin-opening displacement (POD) for both dispersed-ply ($[0/90]_{8s}$) and blocked-ply ($[0_4/90_4]_{2s}$) laminates made of IM7/8552 CFRP unidirectional prepregs [154]. The experimental curves have been shifted left in order to account for initial testing machine and test fixture compliance. The test panels for these specimens were provided by the University of Bristol. The tests were conducted at the University of British Columbia (UBC) to study the progressive damage behaviour of different layups.

For the purpose of comparison of delamination zones, C-scans were conducted¹ at UBC on a few post-mortem specimens (see Figure 5.3). Phased array equipment was used to perform a pulse-echo inspection based on the guidelines provided in References [3-5]. The ultrasonic inspection technique was used with a 64-element, 5.0 MHz phased array equipment. Groups of eight elements were excited at an interval of 1 element. In other words, elements 1 to 8 were excited first, then elements 2 to 9 and so on. A focal depth of 50 mm was used for inspection. From the scan results, the back wall amplitude was analyzed with TomoView software [5] to identify defect areas. The threshold for defect was set at -6dB or a 50% drop of the mean back wall signal. The color palette shown in Figure 5.3 is red for a range from 0% full-screen height (FSH) to 50% of the mean back wall signal, and has black-to-white gradient from 50% of the mean back wall signal to 100% FSH [5].

It can be observed from Figure 5.3 that the dispersed-ply laminate shows a smaller delamination zone in comparison with the blocked-ply laminates. This difference in the damage mechanisms can also be confirmed from the force vs pin-opening displacement (POD) as shown in Figure 5.2

¹ The C-scan on these samples were conducted by Navid Zobeiry at University of British Columbia.

where the blocked-ply laminates show higher failure load and a tougher overall behaviour. This can be associated with the presence of delamination and large splits in the 0^0 plies that delays the fibre breakage as a result of the crack-blunting mechanism.

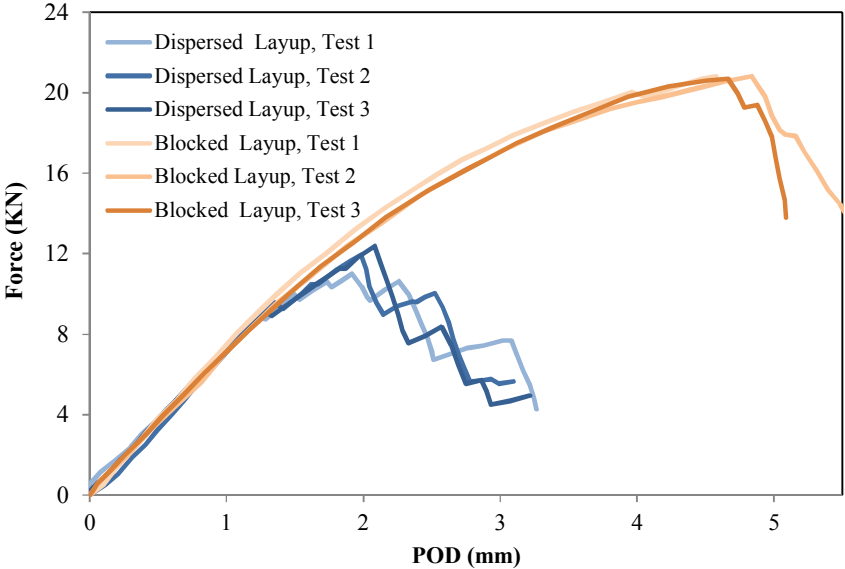


Figure 5.2: Experimentally obtained force vs. pin-opening displacement (POD) curves for both dispersed $[0/90]_{8s}$ and blocked $[0_4/90_4]_{2s}$ cross-ply laminates in OCT specimens [154]

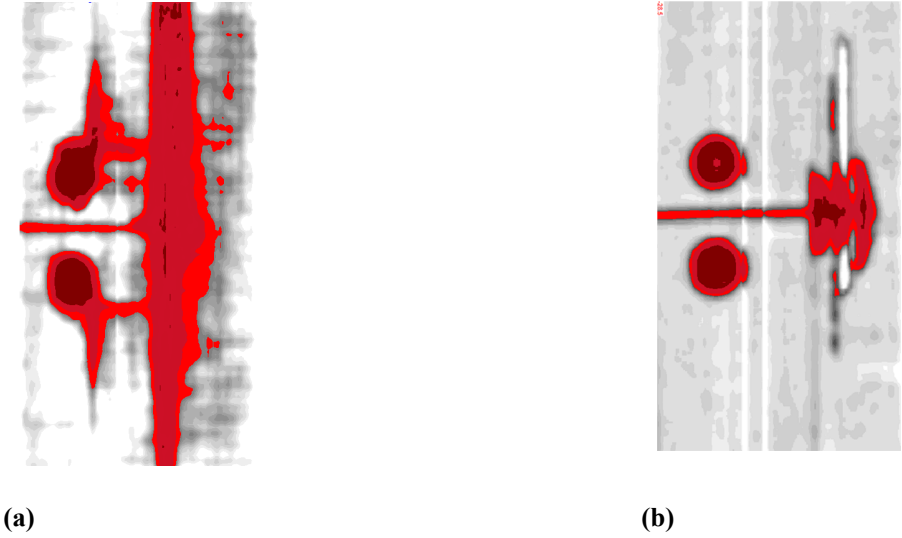


Figure 5.3: C-Scan results showing the delaminated zone in OCT specimens of (a) blocked-ply $[0_4/90_4]_{2s}$ laminate, and (b) dispersed-ply $[0/90]_{8s}$ laminate [154]

5.2.3.1.1 Numerical model setup for OCT simulation

All numerical simulations were carried out using the commercial explicit finite element software package, LS-DYNA [158]. The enhanced CODAM2 material model with all the features described in Chapter 3 is implemented as a user-defined material model in LS-DYNA and was used for the following simulations. Due to symmetry of the layups, in all cases half-models through the thickness were used. The geometry and the finite element mesh of the specimen are shown in Figure 5.4. A prescribed displacement was applied at each of the rigid pins of the models until the Pin Opening Displacement (POD) reached the maximum displacement that was attained in experiments.

Each individual ply was modelled with one layer of reduced-integrated thick shell elements (element formulation 5 in LS-DYNA) in the thickness direction which can capture the through thickness stress distribution. For each ply of elements, one integration point was considered through the thickness given that the loading is in-plane. Moreover, the enhanced CODAM2 material model was assigned to each layer of elements with its own ply orientation. Both blocked-ply and dispersed-ply layups were modelled using this approach. A cohesive-based tie-break contact as explained in Section 4.2 was defined between dissimilar plies to simulate delamination within the laminate. A stiffness based hourglass control (Type 4) was used with stiffness coefficient of 0.5 to prevent zero energy mode shapes due to the presence of only one integration point in the plane of elements.

The in-plane mesh size of the region close to the notch in all models is 0.5 mm and the elements are coarser with increasing distance from the notch tip. For a mesh size of 0.5mm and one in-plane integration point in each element, the non-local averaging radius was chosen to be 1mm to ensure that it covers more than one in-plane integration point in the averaging zone.

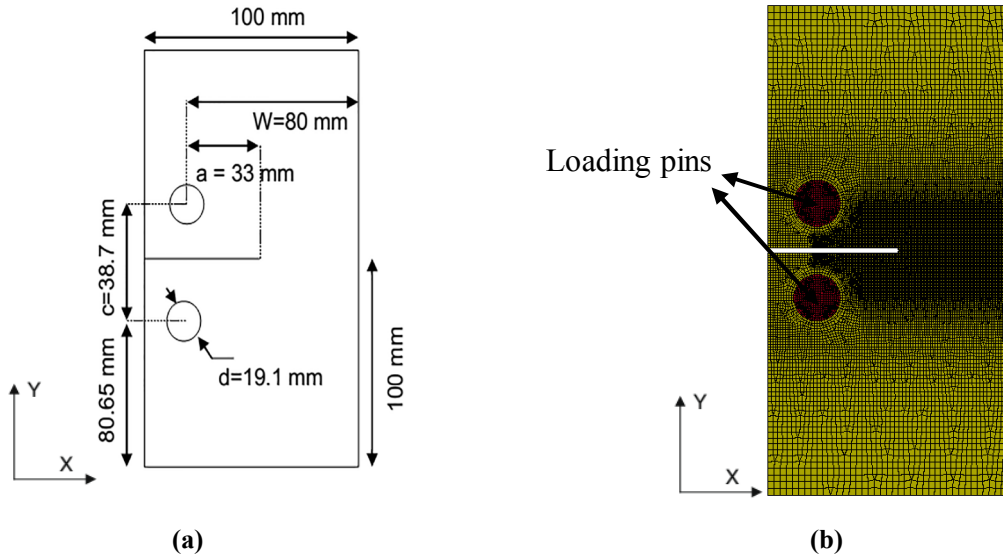


Figure 5.4: (a) OCT specimen geometry and (b) the FE mesh

The initiation of fibre and matrix damage is captured using the Hashin's stress-based failure criteria with the strength properties measured from the standard unidirectional tests. The experimentally measured strength properties for a unidirectional laminate of IM7/8552 CFRP are shown in Table 5-2 [121]. The in-situ transverse tensile and shear strength properties of thin (0.125 mm) and thick (0.5 mm) plies for each laminate layup were also calculated using the procedure described in Section 3.3.2. The in-situ strength properties that were obtained for the thicker plies (0.5mm) are quite in agreement with the reported measurements for unidirectional laminates of IM7/8552 CFRP in [121] (see Table 5-2). This shows that the constraining effect of the adjacent plies in a blocked-ply laminate with ply thickness more than 0.5 mm can be ignored. However, it leads to a relative increase in the in-situ transverse tensile and in-plane shear strength properties of the thin plies (0.125 mm) in the dispersed-ply layups. The calculated in-situ strength properties are shown in Table 5-2 for both thin and thick plies.

Table 5-2: Elastic and damage material parameter (tensile) for plies for [90₄/0₄]_{2s} and [90/0]_{8s} OCT laminates in meso-modelling approach

Experimental properties for unidirectional plies:		
$E_1 = 165 \text{ GPa}$; $E_2 = 9.0 \text{ GPa}$; ^(a) $G_{12}^0 = 5.1 \text{ GPa}$, $\nu_{12} = 0.34$		
$X_T = 2560 \text{ MPa}$, $Y_T = 73 \text{ MPa}$, $S_L = 90 \text{ MPa}$		
Intra-laminar damage parameters for each ply		
Input Parameters	[90 ₄ /0 ₄] _{2s}	[90/0] _{8s}
Longitudinal tensile strength	$X_T = 2560 \text{ MPa}$	$X_T = 2560 \text{ MPa}$
Transverse tensile strength	$Y_T^s = 73 \text{ MPa}$	$Y_T^s = 122 \text{ MPa}$
In-plane shear strength	$S_L^s = 90 \text{ MPa}$	$S_L^s = 98.5 \text{ MPa}$
Fibre fracture energy	$G_1^f = [90 - 150] \text{ kJ/m}^2$	$G_1^f = [90 - 150] \text{ kJ/m}^2$
Fibre fracture energy density ($g_1^f = G_1^f / (0.86r)$)	$g_1^f = [104.7 - 174.4] \text{ N/mm}^2$	$g_1^f = [104.7 - 174.4] \text{ N/mm}^2$
Matrix fracture energy	$G_2^f = [0.65 - 6.5] \text{ kJ/m}^2$	$G_2^f = [0.65 - 6.5] \text{ kJ/m}^2$
Matrix fracture energy density ($g_2^f = G_2^f / (0.65r)$)	$g_2^f = [1 - 10] \text{ N/mm}^2$	$g_2^f = [1 - 10] \text{ N/mm}^2$
Non-local averaging radius	1 mm	1 mm
Inter-laminar damage parameters		
Input Parameters	[90 ₄ /0 ₄] _{2s}	[90/0] _{8s}
Maximum inter-laminar normal stress	$t_{\max}^N = [17 - 30] \text{ MPa}$	$t_{\max}^N = [7 - 10] \text{ MPa}$
Maximum inter-laminar shear stress	$t_{\max}^S = [17 - 30] \text{ MPa}$	$t_{\max}^S = [7 - 10] \text{ MPa}$
Inter-laminar fracture energy, Mode-I	$G_{Ic} = 0.2 \text{ kJ/m}^2$	$G_{Ic} = 0.2 \text{ kJ/m}^2$
Inter-laminar fracture energy, Mode-II	$G_{IIc} = 0.8 \text{ kJ/m}^2$	$G_{IIc} = 0.8 \text{ kJ/m}^2$

^(a) The nonlinear shear stress-strain curve is provided in [121]

5.2.3.1.2 OCT simulation of blocked cross-ply laminates [90₄/0₄]_{2s}

Here, with the use of a reference model for [90₄/0₄]_{2s} laminate, a series of simulations were conducted to estimate the proper intra-laminar matrix fracture energy value, G_2^f . A range of values for G_2^f from 0.65 to 6.5 kJ/m² were considered (see Table 5-2). The input for the material model is the corresponding fracture energy density, g_2^f , which is related to G_2^f with an effective length scale, h_2^c (i.e. $g_2^f = G_2^f / h_2^c$). This length scale as discussed on Section 3.3.1.2 and detailed

in Appendix B is a function of the selected radius of non-local averaging. For the chosen radius of $r = 1\text{mm}$ and a length scale of $h^c = 0.65r$ as suggested in Appendix B, the corresponding matrix fracture energy density g_2^f ranges from 1 to 10 N/mm². In all cases, the intra-laminar fibre fracture energy and all the other mechanical properties were kept the same. In the reference model, it was assumed that $G_1^f = 150\text{kJ/m}^2$ which is closer to the upper bound of the range [100-150] kJ/m² that is reported in [144] for IM7/8552 CFRP material system. However, the effect of using lower values within the reported range for fibre fracture energy will also be discussed. The inter-laminar fracture energy values G_{lc} and G_{llc} were chosen from [121] as listed in Table 5-2. The adjusted maximum inter-laminar shear and normal stress values were obtained using the 3D stress analysis as described in Section 5.1.1 for each numerical case (see Table 5-2).

Upon conducting the numerical analysis for each of the adopted intra-laminar matrix fracture energy values, the resulted force-displacement and damage patterns were investigated and compared against the experimental results conducted by Li et al. [154].

Figure 5.5 displays the predicted force vs POD response of the blocked cross-ply laminate with intra-laminar fracture values between 0.65 to 6.5 kJ/m². For values smaller than 2.6 kJ/m², the peak force is underestimated as a result of insufficient amount of energy dissipation. On the other hand, for values above 2.6 kJ/m², the maximum force is over-predicted. The predicted damage pattern (fringe plots of ω_1 and ω_2) for intra-laminar damage modes in the 0⁰ and 90⁰ layer as well as delamination between them (fringe plots of ω_D) for the case where $G_2^f = 2.6\text{kJ/m}^2$ are shown in Figure 5.6 and Figure 5.7.

The predicted damage pattern is consistent with experimental results [154] where there is negligible fibre breakage and the splits (in the 0⁰ layer) and interface delamination are the dominant damage mechanisms. Although the nature of the predicted damage pattern with all the chosen values of matrix fracture energy is the same, the speed of split growth in the 0⁰ plies is dependent on the available matrix fracture energy. Figure 5.8 shows the increase in the split length as the load increases for different values of intra-laminar matrix fracture values. Note that

the figure shows half of the total split over upper or lower half of the specimen from the notch tip to the upper or lower edge of the specimen. It can be seen that decreasing the available intra-laminar matrix fracture energy leads to an increase in the rate of split growth. This also explains the behaviour in the force-displacement result, where lower value of matrix fracture energy leads to faster saturation of matrix crack that grows in the 0^0 plies. Delamination also grows along with the split and saturates the whole height of the specimen and causes the load drop to occur earlier with decreasing matrix fracture energy. This trend, however, reverses as the intra-laminar matrix fracture energy increases.

Fibre damage did not initiate in any of the above numerical cases with blocked-ply laminates. Therefore, changing the value of fibre fracture energy from 150kJ/m^2 to lower values did not change the response of the laminate. However, as will be shown in the following, the fibre fracture energy can affect the overall response of the dispersed cross-ply laminates as their behaviour is dominated by fibre damage mode.

The correlation between the simulation results and the experimental tests could be done in a more quantitative manner by having more accurate measurements of the damage modes. For example tracking the length of the splits in the 0^0 ply in the experiment could be used as an additional measure for correlating the numerical and experimental results and hence achieving a more accurate value of the matrix fracture energy.

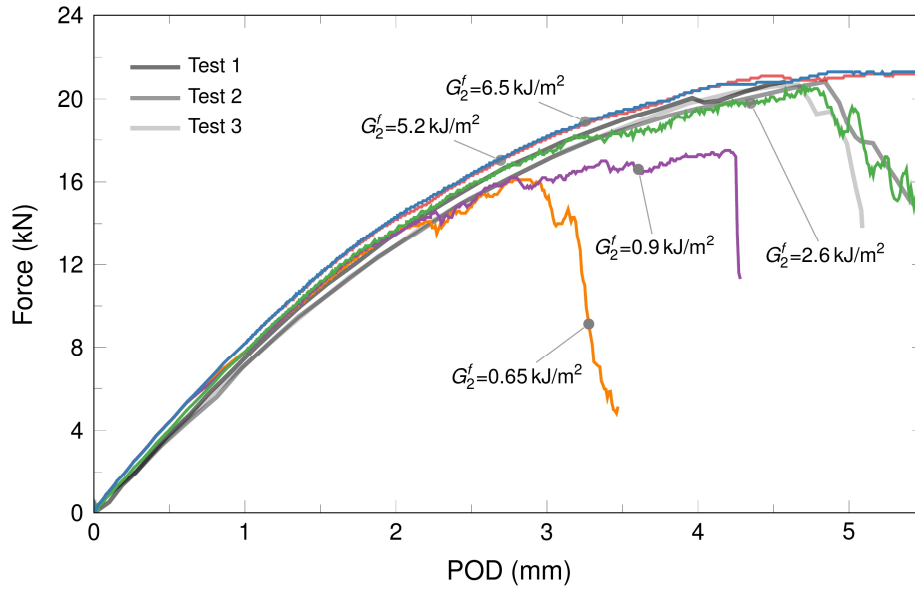


Figure 5.5: Comparison of the experimental and predicted force-displacement curves for $[0_4/90_4]_{2s}$ laminate with different values of matrix fracture energy and fibre fracture energy of 150 kJ/m^2 [154]

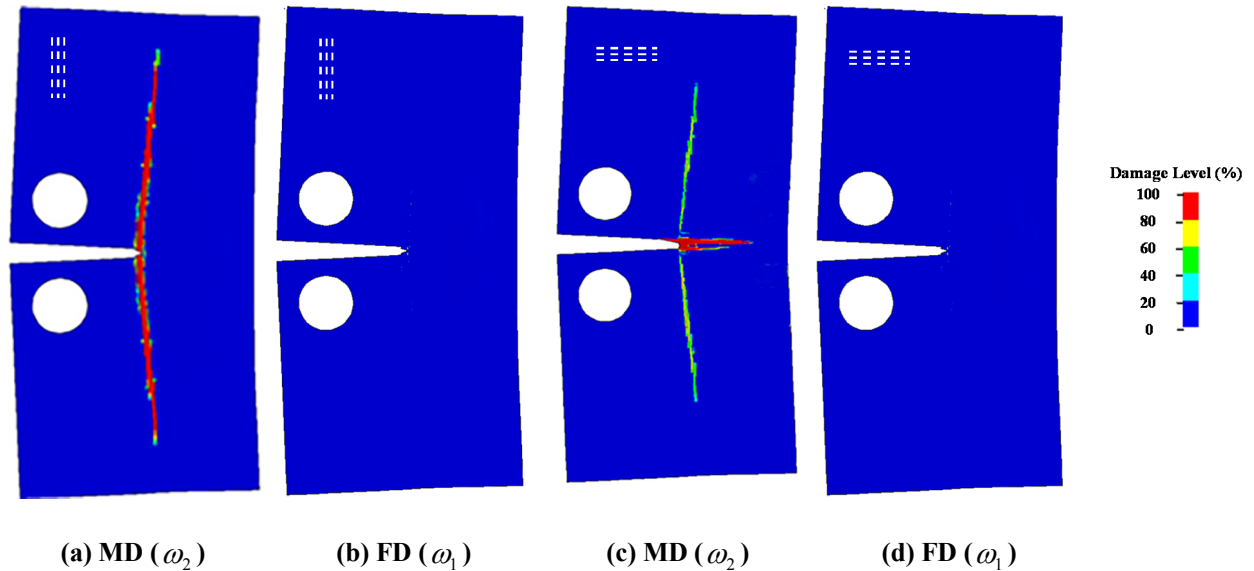


Figure 5.6: Predicted damage patterns for each ply of the $[0_4/90_4]_{2s}$ OCT laminate with $G_2^f = 2.6 \text{ kJ/m}^2$ at $\text{POD}=4.8\text{mm}$, (a) matrix damage in 0° layer, (b) fibre damage in 0° layer, (c) matrix damage in 90° layer and (d) fibre damage in 90° layer

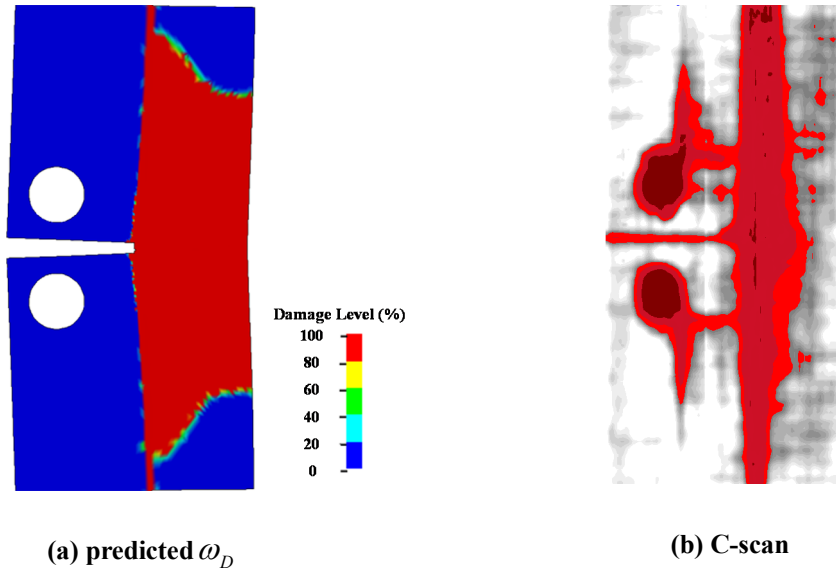


Figure 5.7: Comparison of (a) the predicted delamination zone at $0^\circ/90^\circ$ interface of the $[0_4/90_4]_{2s}$ OCT laminate at $POD=5$ mm with (b) the final measured delamination zone from the C-scan results

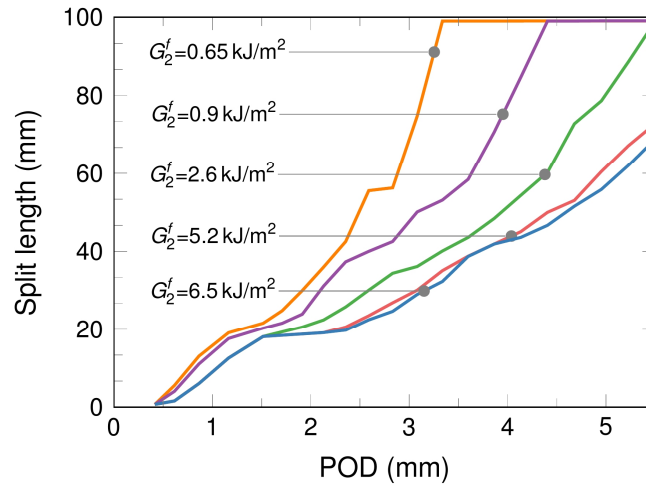


Figure 5.8: Comparison of the predicted split length over half of the specimen height from the notch to the upper boundary in the 0° ply for intra-laminar matrix fracture energy values ranging from 0.65 to 6.5 kJ/m² for the $[0_4/90_4]_{2s}$ blocked-ply OCT laminate

The finite element mesh that was used for the above simulation was in square shape and the edges of the elements were parallel with the global x and y direction of the model (the load is applied in y direction). In order to investigate the effect of mesh structure ahead of the notch tip, a non-structured mesh configuration as shown in Figure 5.9(a) was used for both 0° and 90° plies. The size of the elements is roughly 0.5 mm but the orientation of mesh ahead of the notch tip is not parallel with the global coordinate system and not necessarily square in shape. The above-mentioned laminate layup was simulated using this mesh configuration with the same value of radius for nonlocal averaging and $G_2^f = 2.6 \text{ kJ/m}^2$ (i.e. $g_2^f = 4 \text{ N/mm}^2$). The predicted force vs. POD curve was found to be in good agreement with the experimental results and the predicted matrix damage pattern in each ply is shown in Figure 5.9(b) and (c). Since the obtained predictions are more or less the same, one can conclude that the calibrated parameters obtained from a structured mesh can also be used for a non-structured mesh as long as the non-local approach is used.

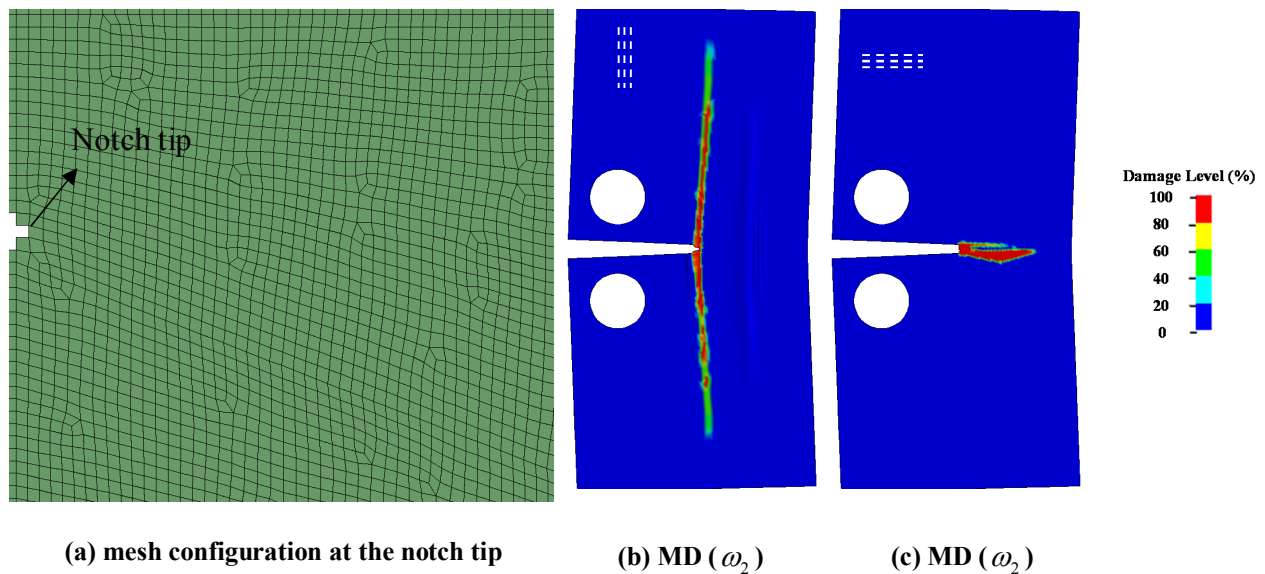


Figure 5.9: (a) An non-structured mesh configuration ahead of the notch tip for the $[0_4/90_4]_{2s}$ OCT laminate, (b) predicted matrix damage in 0° layer, (c) predicted matrix damage in 90° layer for $G_2^f = 2.6 \text{ kJ/m}^2$ at $\text{POD} = 4.8 \text{ mm}$

5.2.3.1.3 OCT simulation of dispersed cross-ply laminates $[0/90]_{8s}$

Similar virtual tests have been performed for thin-ply laminate layup $[0/90]_{8s}$ with fracture energy of matrix cracking ranging from 2.6 to 6.5 kJ/m² and eliminating values lower than 2.6 kJ/m² based on the predictions for blocked-ply laminates. Again, in a reference case, the upper bound of fibre fracture energy (i.e. $G_1^f = 150$ kJ/m²) is used, but the effect of lower values are also studied. The curves in Figure 5.10 show the force-displacement results for the upper and lower bounds $G_2^f = 6.5$ kJ/m² and $G_2^f = 2.6$ kJ/m² that are over-laid on the experimental results. The behaviour shown by the global force-displacement results for each case can be explained by investigating the predicted damage pattern shown in Figure 5.11 through Figure 5.13. The intra-laminar and inter-laminar damage patterns for the case with $G_2^f = 2.6$ kJ/m² are shown in Figure 5.11 and Figure 5.12, respectively, whereas Figure 5.13 shows the damage patterns for $G_2^f = 6.5$ kJ/m². Using the upper bound for matrix fracture energy delays the growth of matrix damage in the 0° plies. Consequently, there is enough time for the stress in the fibre direction to increase and reach the initiation point of fibre breakage before any splits can be formed. Thus, fibre breakage becomes the dominant damage mechanism. In this case delamination zone is also very small. For the lower bound (i.e. $G_2^f = 2.6$ kJ/m²), however, the splits grow to some extent to allow delamination to occur between the plies. However, the splits and delamination are not large enough to redistribute the stress as in the case of the blocked-ply laminate. Therefore, the stress in the fibres increases sufficiently to reach the damage initiation criterion and fibre breakage ensues.

From the above results, we conclude that a value of intra-laminar matrix damage fracture energy of $G_2^f = 2.6$ kJ/m² is sufficient to capture the response of this material system both for blocked and dispersed laminate layup. However, the initiation damage properties for the intra-laminar damage (i.e. the in-situ strength properties) and inter-laminar damage (i.e. the interface strength properties) modes have to be adjusted depending on the ply thickness and laminate layup based on the procedure proposed in this work.

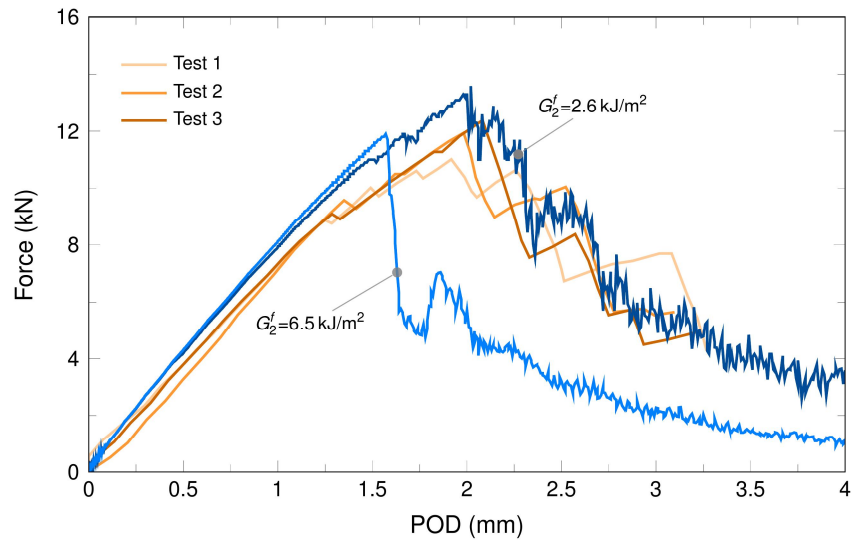


Figure 5.10: Comparison of the experimental and predicted force-displacement curves for the $[0/90]_{8s}$ OCT laminates for a low and a high value of intra-laminar matrix fracture energy and fibre fracture energy of 150 kJ/m^2 [154]

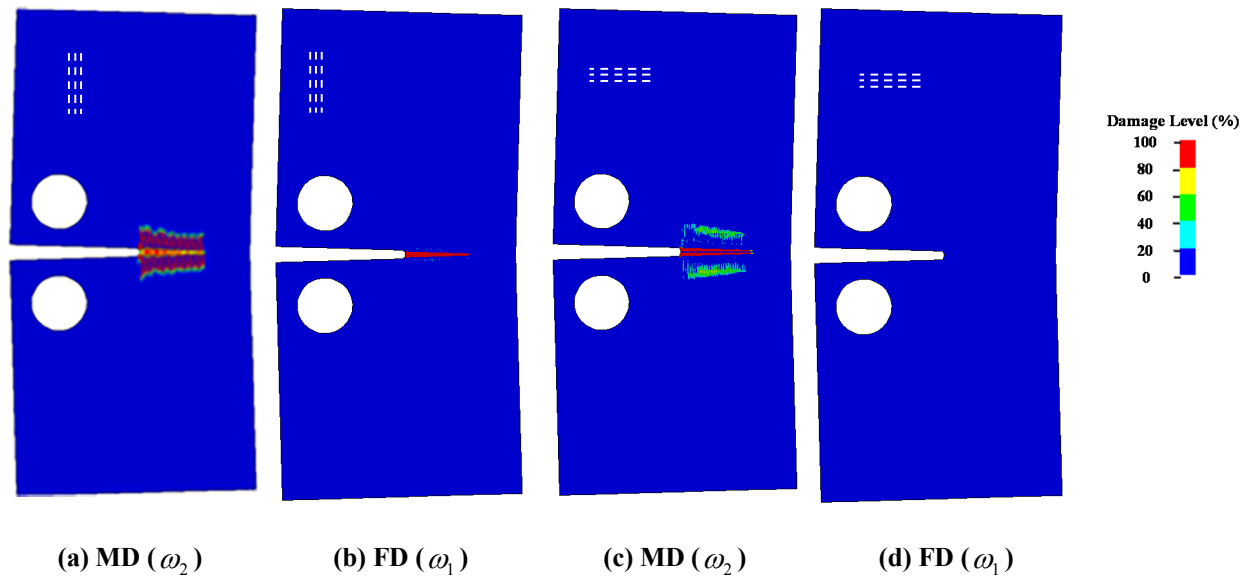
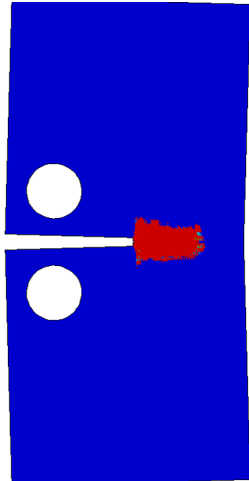
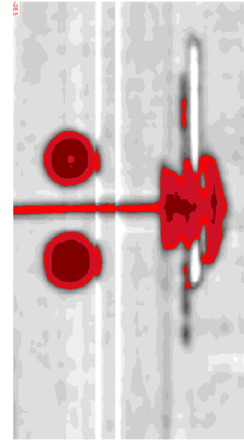


Figure 5.11: Predicted damage patterns for each ply of the $[0/90]_{8s}$ OCT laminate with $G_2^f = 2.6 \text{ kJ/m}^2$ at $\text{POD}=3.8 \text{ mm}$, (a) matrix damage in 0° layer, (b) fibre damage in the 0° layer, (c) matrix damage in 90° layer, and (d) fibre damage in 90° layer

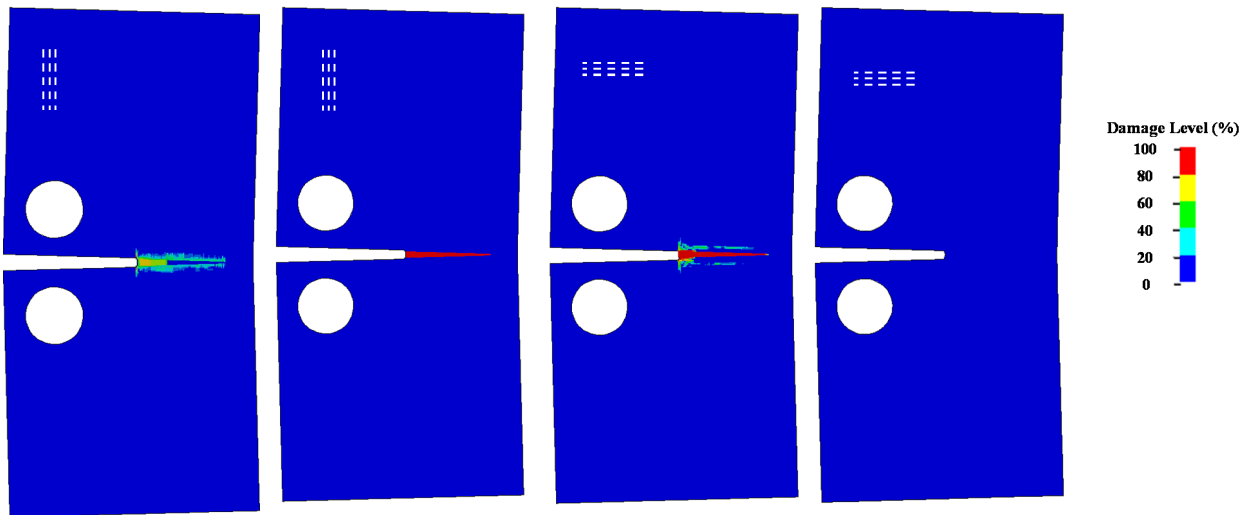


(a) predicted ω_D



(b) C-scan

Figure 5.12: Comparison of (a) the predicted delamination zone at $0^\circ/90^\circ$ interface of the $[0/90]_{8s}$ OCT laminate with $G_2^f = 2.6 \text{ kJ/m}^2$ at $\text{POD}=3.8 \text{ mm}$ with (b) the final measured delamination zone from the C-scan results



(a) MD (ω_2)

(b) FD (ω_1)

(c) MD (ω_2)

(d) FD (ω_1)

Figure 5.13: Predicted damage patterns for each ply of the $[0/90]_{8s}$ OCT laminate with $G_2^f = 6.5 \text{ kJ/m}^2$ at $\text{POD}=3.8 \text{ mm}$, (a) matrix damage in 0° layer, (b) fibre damage in the 0° layer, (c) matrix damage in 90° layer, and (d) fibre damage in 90° layer

Once the matrix fracture energy is calibrated using the reference models of blocked and dispersed cross-ply laminates where fibre fracture was assumed to be equal to an upper bound of 150kJ/m^2 , the effect of lower values for fibre fracture energy is also investigated. It was mentioned that the change in fibre fracture energy did not affect the response of blocked-ply laminates since damage progression was dominated by matrix cracking and delamination. However, the dispersed-ply laminate is a good candidate to study the effect of fibre fracture energy on the progression and overall behaviour of the laminate. For this purpose, the dispersed cross-ply OCT specimen was simulated with a range of fibre fracture energy values between 90 to 150kJ/m^2 , while the matrix fracture energy was kept constant at 2.6kJ/m^2 . Figure 5.14 shows the force-displacement curves overlaid on the experimental results. It can be seen that by reducing the amount of fibre fracture energy, the peak force as well as the post-peak response drops which is a result of the reduction in the saturation strain associated with fibre damage. As the fibre fracture energy is decreased, damage in the 0^0 plies becomes dominated by the fibre damage mode similar to what was shown in Figure 5.13. Therefore, the fibre fracture energy values within the range 140 to 150kJ/m^2 are considered to be acceptable for this material system.

Although the input material parameters are calibrated in a deterministic sense, once some level of confidence is obtained, one can also approach the process of calibration in a probabilistic sense. To this end, the variability in the experimental results can be considered and accordingly a range of variability of the calibrated input parameters can be obtained using a probabilistic approach.

The numerical noise that are observed in the form of high frequency oscillations in the force vs. POD response in Figure 5.5 and Figure 5.14 are associated with the explicit nature of the finite element solution procedure specifically once the intra-laminar and inter-laminar damage modes initiate. Similar behaviour has been observed in numerical solutions that are based on explicit finite element solutions (e.g. [153])

In the following chapter, the numerically calibrated intra-laminar matrix and fibre fracture energies are used for prediction of damage progression in two geometries. In the first case, two quasi-isotropic laminates made of IM7/8552 CFRP material with a dispersed-ply and blocked-

ply laminate layup in an OCT configuration are simulated. In the second case, OHT specimens made of quasi-isotropic laminates of IM7/8552 carbon fibre/epoxy material system with various size and laminate thicknesses are modelled.

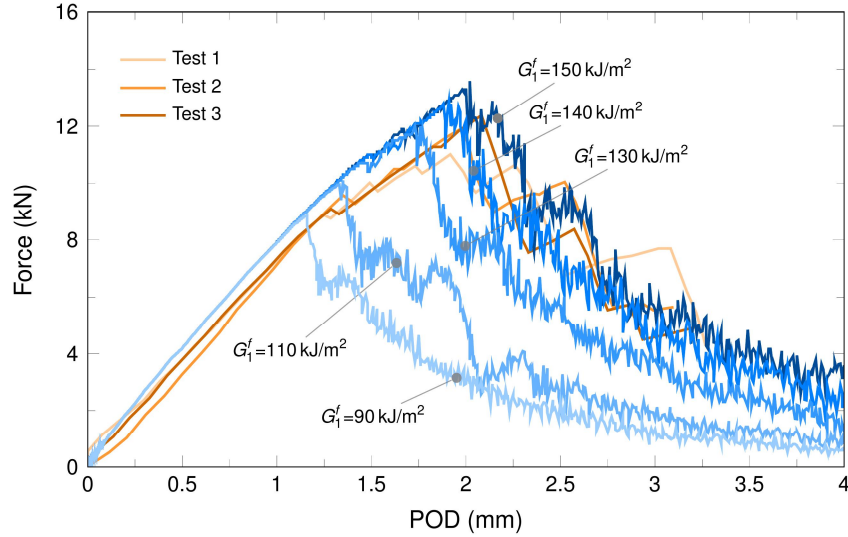


Figure 5.14: Comparison of the experimental and predicted force-displacement curves for the $[0/90]_{8s}$ OCT laminates with $G_2^f = 2.6 \text{ kJ/m}^2$ and a range for fibre fracture energy values, G_1^f [154].

5.3 Summary

In this chapter, the guidelines and procedures to determine the intra-laminar and inter-laminar damage parameters for the mesoscopic non-local CODAM2 material model were presented.

In order to have an accurate prediction of delamination using the cohesive zone model without the need to use very fine mesh, the length of the cohesive zone in the simulation was artificially increased by reducing the interface strength. A simple yet intuitive method was proposed to estimate the amount of reduction for the interface strength properties. The inter-laminar strength properties were adjusted based on the status of inter-laminar stresses that were obtained from a 3D stress analysis on the laminate while delamination was prevented between the plies. The average of inter-laminar stresses within a zone close to the notch or discontinuities where the matrix cracks and delamination were expected to occur first was selected as the inter-laminar

calibrated strength properties. However, the inter-laminar fracture energy values remained unchanged. With this approach, one can eliminate the need to have very fine mesh size to get accurate prediction using the cohesive interfaces. Moreover, it also implicitly accounts for the effect of ply thickness on the initiation of delamination since the initiation of delamination is indirectly linked to the matrix cracking which is in turn influenced by ply thickness. In this work, the dependency of matrix damage initiation on ply thickness is enabled using the shear lag theory (Section 3.3.2).

The methodologies for determining the material constants required for the intra-laminar damage modes were also discussed. Most properties including the elastic moduli and strength properties can be gathered from the standard tests. The effect of the ply thickness on initiation of matrix cracking is considered using the in-situ strength properties that are approximated by the shear lag theory.

While there is more literature available on the characterization of fibre fracture energy, less work has been done for characterization of intra-laminar matrix fracture energy values. A systematic and novel procedure was proposed to calibrate the intra-laminar fracture energies of a material system in tension from a few experiments on over-height compact tension specimens of cross-ply laminates. The intent is to implicitly account for the interaction of matrix cracks with delamination and damage in neighboring plies. These are the type of interacting mechanisms that do not show up in conducted tests on unidirectional laminates. Two types of blocked-ply and dispersed-ply laminates with cross-ply layup were used to calibrate the intra-laminar fracture energy values for IM7/8552 carbon-fibre/epoxy material system. The experimental results for the blocked cross-ply laminate that are governed by delamination and splitting (i.e. matrix damage dominated) were used to estimate the appropriate values of the matrix intra-laminar fracture energy. The numerical analyses were performed using a range for fracture energy of matrix cracking while keeping all the other damage parameters including the fibre fracture energy constant. The numerical predictions in terms of the global behaviour (e.g. force-displacement) and damage mechanisms were compared against the experimental results to calibrate the intra-laminar matrix fracture energy. Moreover, the effect of the experimental range reported for the fibre fracture energy of this material in the literature was investigated. While the response of the

blocked-ply laminate was independent of the fibre fracture energy, the peak force and the post peak response of the dispersed-ply laminate reduced as the fibre fracture energy decreased. The response of the dispersed-ply laminate refined the range of fibre fracture energy that fit the experimental results.

The calibrated material properties for the above mentioned material system will be used in the next chapter for validating the proposed methodology for different layup and loading geometry of the same material system.

Chapter 6: Model Validation

Having calibrated the intra-laminar matrix and fibre fracture energies for the IM7/8552 CFRP material using OCT simulation of blocked and dispersed cross-ply laminates (see Section 5.2.3.1), in this chapter the calibrated model is used to simulate the tensile response of notched laminates of IM7/8552 CFRP with different layup and loading geometry for validating the model.

In Section 6.1, two quasi-isotropic laminates made of IM7/8552 CFRP material with different stacking sequences: (i) a dispersed-ply layup ($[45/90/-45/0]_{2S}$), and (ii) a ply-scaled layup ($[45_4/90_4/-45_4/0_4]_S$) are simulated in OCT test setting [154]. The geometry of the specimens is the same as the cross-ply laminates that were used for calibration. Again, these two laminates were chosen because of their distinct nature of damage modes. The major damage mechanism in the dispersed-ply laminate is fibre fracture in the 0° and 45° layers while delamination is the main failure mechanism in the blocked-ply laminate.

In Section 6.2, the applicability of the proposed methodology as well as the calibrated material properties are examined for the same material system but a different geometry. For this purpose, a series of open-hole specimens that have been tested under tensile loading at the University of Bristol [82] are modelled using the proposed approach. The specimens are made of IM7/8552 CFRP laminates with a quasi-isotropic layup, with varying hole diameter, ply and laminate thickness while keeping the ratios of the hole diameter to specimen width and length constant. It was observed that both strength and failure mechanisms of the open-hole laminates varied with layup configurations. We will demonstrate that the proposed approach captures the dominant failure mechanisms as well as the overall behaviour, including the size and layup effect on the notched strength of the laminate.

6.1 OCT tests on quasi-isotropic laminates

Here, both the blocked-ply and dispersed-ply quasi-isotropic laminates made of IM7/8552 CFRP that were experimentally tested by Li et al. [154] are modelled with the proposed methodology.

The model specifications and the in-plane mesh size are similar to what was described for the cross-ply laminates in Section 5.2.3.1. The mechanical properties and other numerical parameters required for determination of damage initiation for intra-laminar fibre and matrix damage modes are similar to what were used for cross-ply laminate with thin and thick plies. As calibrated in chapter, the intra-laminar matrix fracture energy is selected as $G_2^f = 2.6\text{kJ/m}^2$ and fibre fracture energy is $G_1^f = [140 - 150]\text{kJ/m}^2$. Similar to the cross-ply laminates, the adjusted maximum inter-laminar shear and normal stress values are obtained using the 3D stress analysis as described in Section 5.1.1 (see Table 6-1).

Table 6-1: Inter-laminar damage material parameters for $[45_4/90_4/-45_4/0_4]_s$ and $[45/90/-45/0]_{2s}$ laminates in the combined damage modelling approach for OCT specimens

	$[45_4/90_4/-45_4/0_4]_s$	$[45/90/-45/0]_{2s}$
Maximum inter-laminar normal stress	$t_{\max}^N = 15\text{MPa}$	$t_{\max}^N = 10\text{MPa}$
Maximum inter-laminar shear stress	$t_{\max}^S = 25\text{MPa}$	$t_{\max}^S = 20\text{MPa}$

6.1.1 Simulation results and discussions

The predicted force-displacement response for the dispersed-ply and blocked-ply laminates is shown in Figure 6.1(a) and (b) overlaid by the experimental results. These results are shown for intra-laminar fracture energy values of 150kJ/m^2 and 2.6kJ/m^2 for fibre and matrix damage modes, respectively. Note that the experimental curves have been shifted left in order to account for initial testing machine and test fixture compliance. It can be seen that the current methodology is capable of predicting the overall response of both laminate layup types. The main reason for the more gradual decrease of the stiffness in the blocked-ply laminate compared to the dispersed one is the presence of the splits and delamination. This leads to stress redistribution in the layers and prevents major fibre fracture.

Figure 6.2 shows the predicted matrix cracks (ω_2 distribution) at POD of 2.2 mm predicted close to the ultimate failure load. The surface split in the 45° layer is in good agreement with what has been observed from the experiments [154]. The evolution of the extent of matrix damage in each ply with increasing POD is shown in Figure 6.3. The predicted projection of delamination zones

at $0^\circ/-45^\circ$, $-45^\circ/90^\circ$ and $90^\circ/45^\circ$ interfaces is also shown in Figure 6.4(a) at POD of 2.2mm. Figure 6.4(b) shows the corresponding C-scan results obtained in-house for one of the post-mortem specimens. The predicted direction of delamination growth at different interfaces is found to be in consistent with the C-scan results.

The matrix and fibre damage modes for each ply of the dispersed-ply $[45/90/-45/0]_{2s}$ laminate at POD of 2.2mm are shown in Figure 6.5 and Figure 6.6, respectively. The presence of fibre fracture in the 0° and $\pm 45^\circ$ plies is the major reason for the brittle behaviour of this layup in comparison with the block-ply laminate. The projection of delaminated zone at POD of 2.2 mm is also shown in Figure 6.7 along with the C-scan results for one of the post-mortem specimens. Note that the predicted delamination and the C-scan results provided here might be at slightly different loading points (POD level). However, the shape and the path of the predicted delamination growth are in fairly good agreement with corresponding C-scan results.

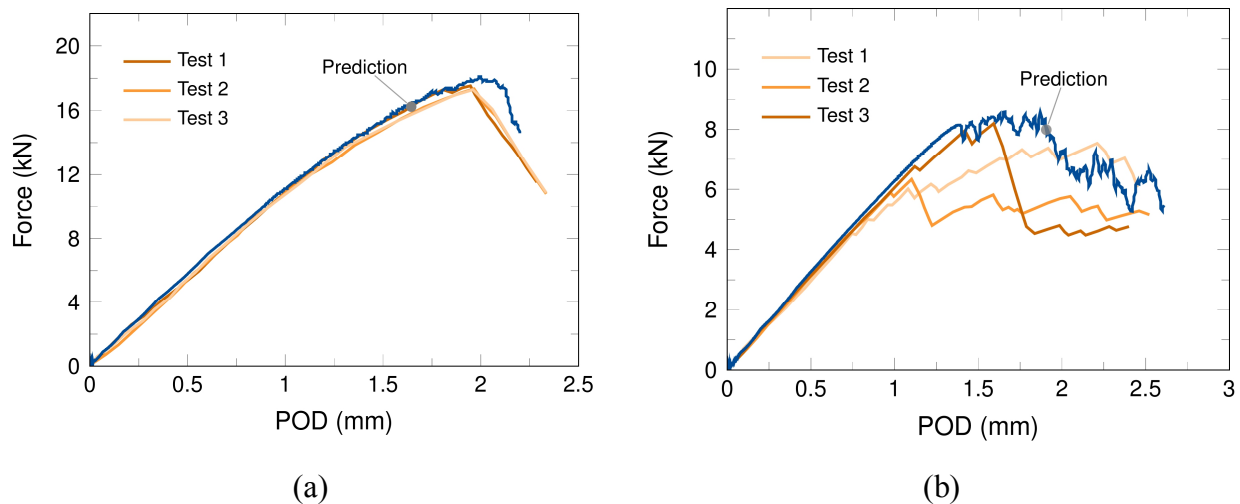


Figure 6.1: Comparison of the experimental and predicted force-displacement curves for (a) $[45_4/90_4/-45_4/0_4]_s$ and (b) $[45/90/-45/0]_{2s}$ laminates under OCT loading geometry [154]

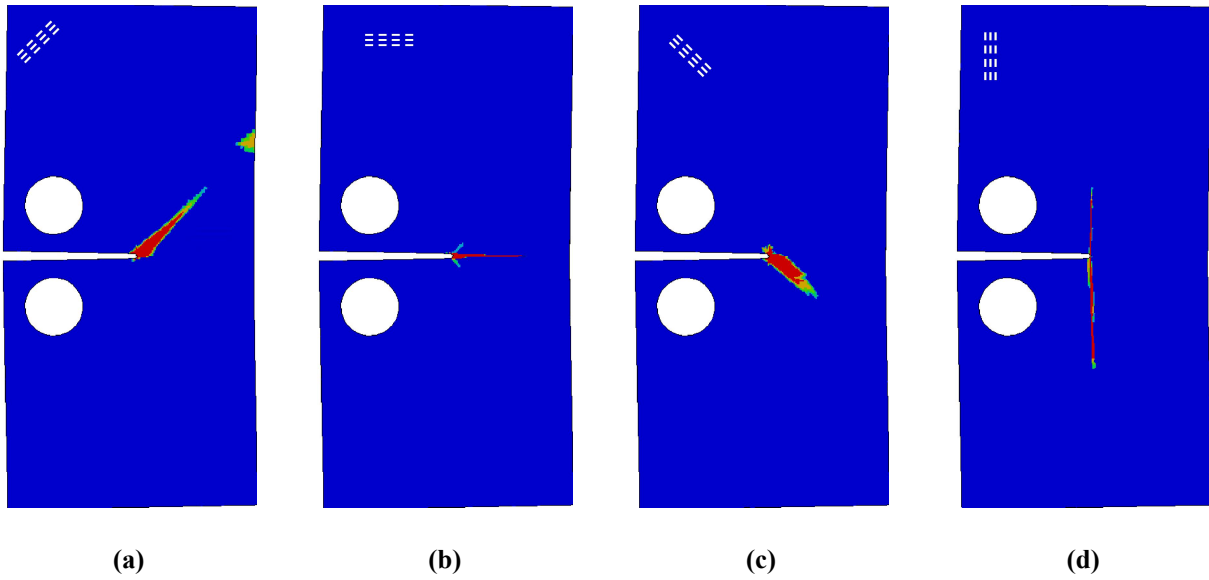


Figure 6.2: Predicted matrix damage pattern (ω_2 distribution) for each ply of the blocked-ply $[45_4/90_4/-45_4/0_4]_s$ laminate at $POD=2.2\text{mm}$

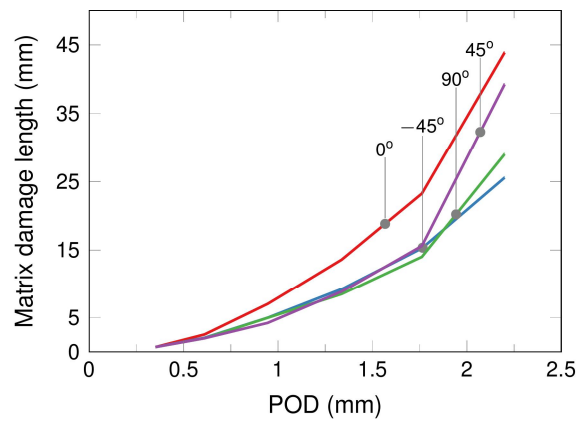


Figure 6.3: Predicted length of matrix damage versus pin opening displacement (POD) for each ply of the blocked-ply $[45_4/90_4/-45_4/0_4]_s$ laminate under OCT loading

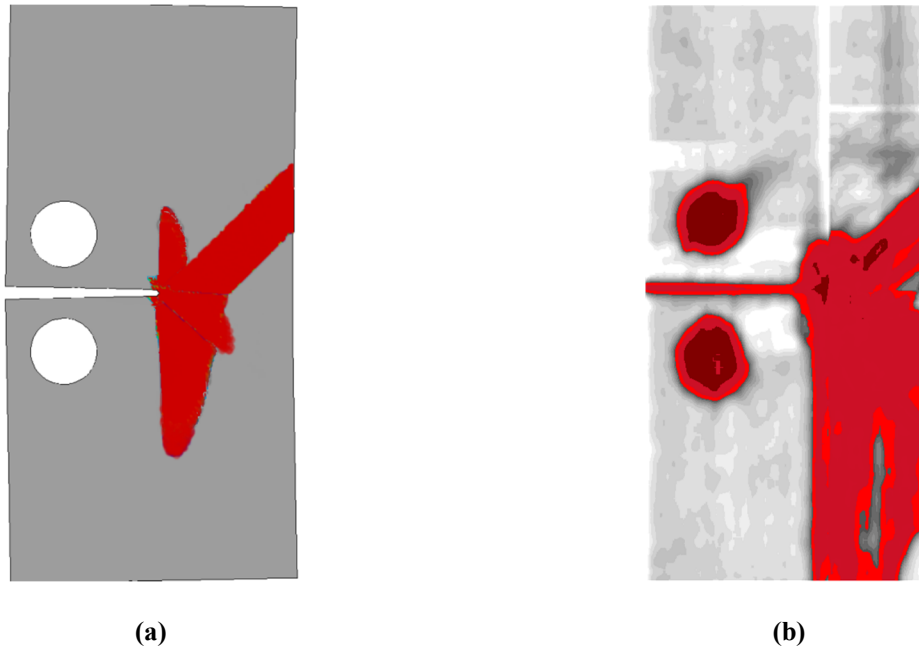


Figure 6.4: Predicted projected delamination zone for $[45_4/90_4/-45_4/0_4]_s$ laminate at $POD=2.2\text{mm}$ and the experimental C-scan result obtained from a corresponding post-mortem specimen

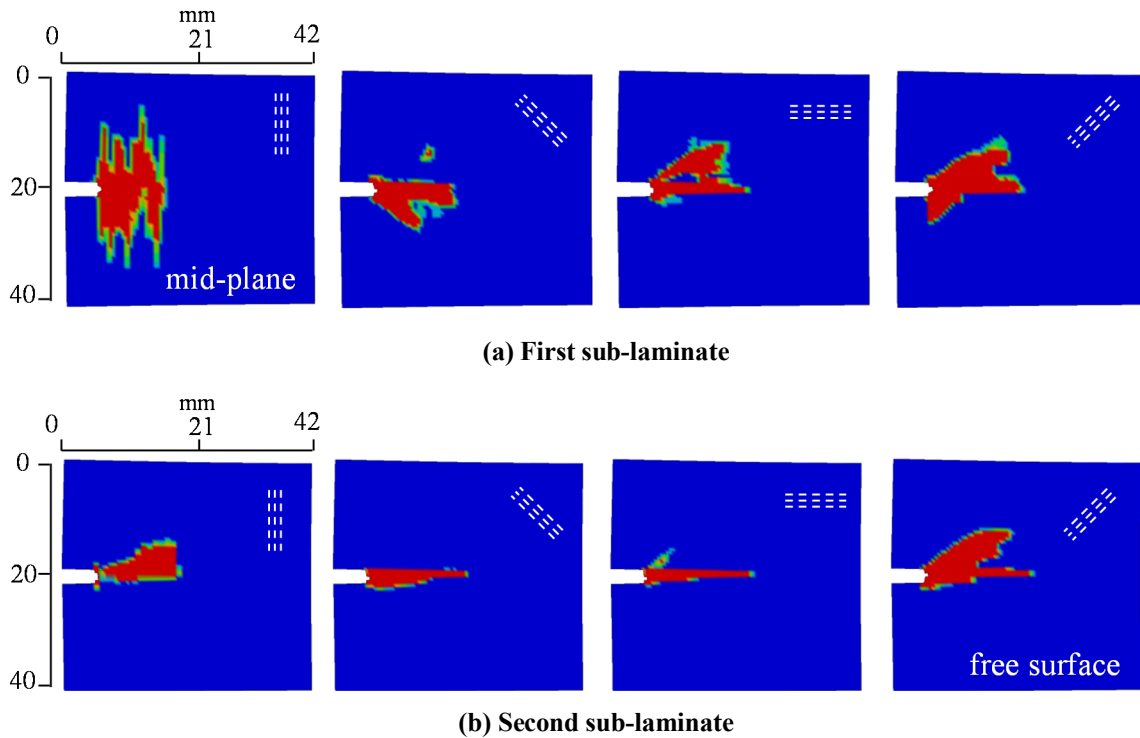


Figure 6.5: Predicted matrix damage pattern (ω_2 distribution) for each ply of the $[45/90/-45/0]_{2s}$ laminate at $POD=2.2\text{ mm}$ for (a) the first and (b) second sub-laminates (from the mid-plane to the free surface)

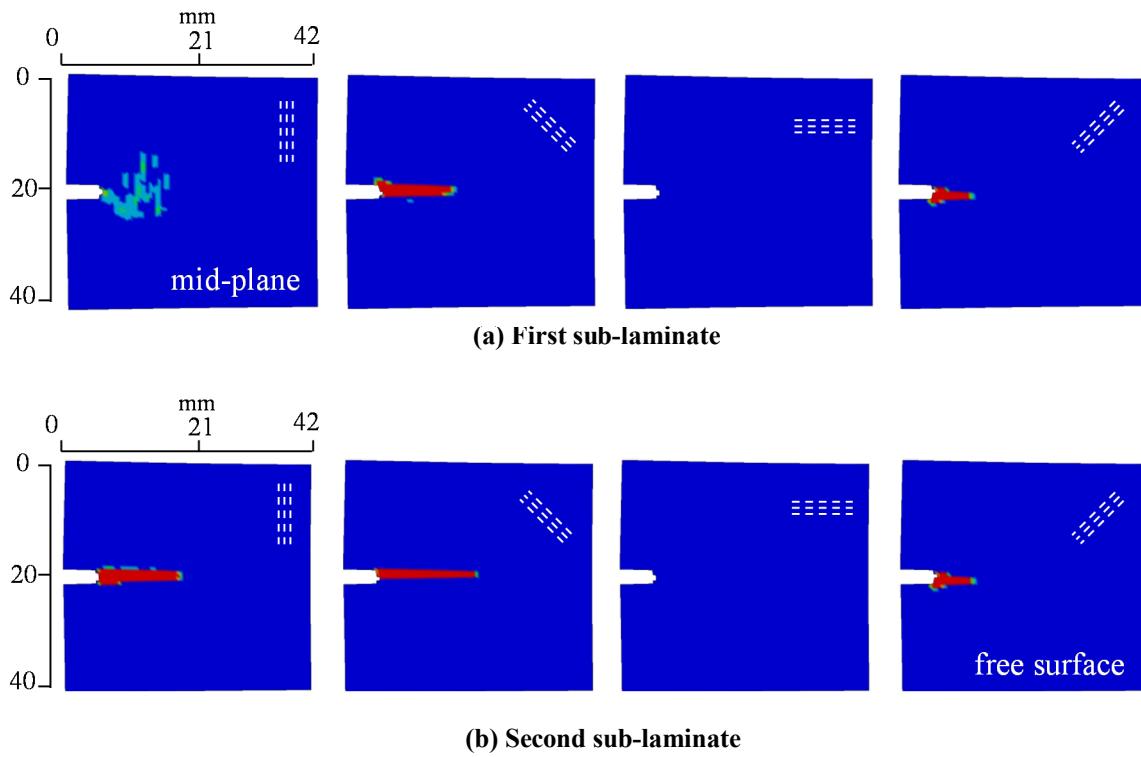


Figure 6.6: Predicted fibre damage pattern (ω_1 distribution) for each ply of the $[45/90/-45/0]_{2s}$ laminate at $POD=2.2$ mm for (a) the first and (b) second sub-laminates (from the mid-plane to the free surface)

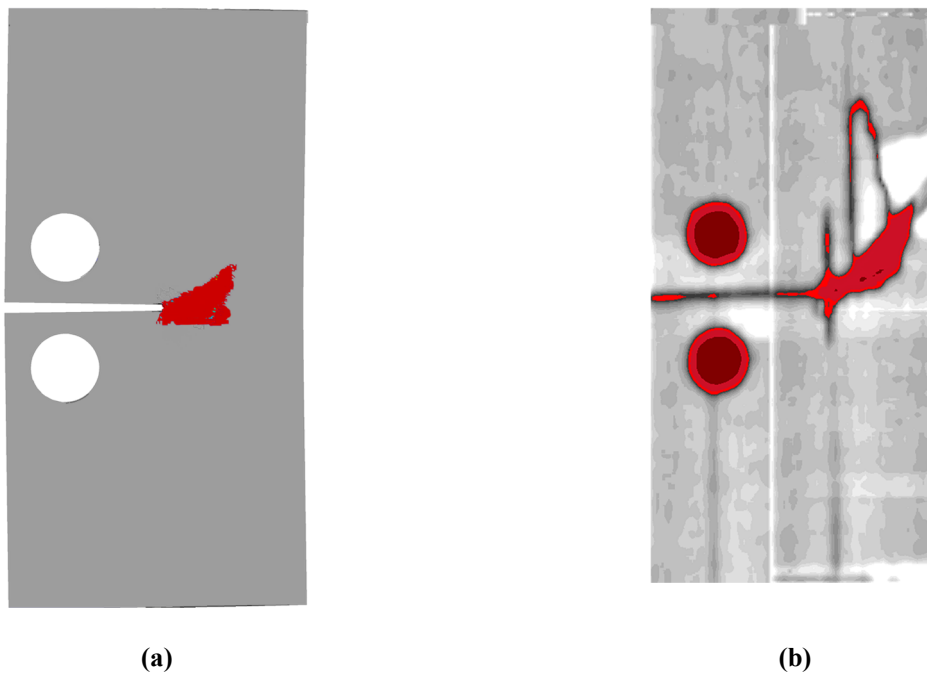


Figure 6.7: Predicted projected delamination zone for $[45/90/-45/0]_{2s}$ laminate at $POD=2.2$ mm and the experimental C-scan result obtained from a corresponding post-mortem specimen

In order to investigate the sensitivity of the response to the chosen value for the fibre fracture energy, Figure 6.8 shows the force vs POD for the dispersed-ply $[45/90/-45/0]_{2s}$ laminate for different values of G_1^f ranging from 140 to 150 kJ/m^2 . It can be seen that with decreasing the amount of fracture energy, the peak force and the post peak response slightly decrease but the predicted response is still within the range of the experimental results.

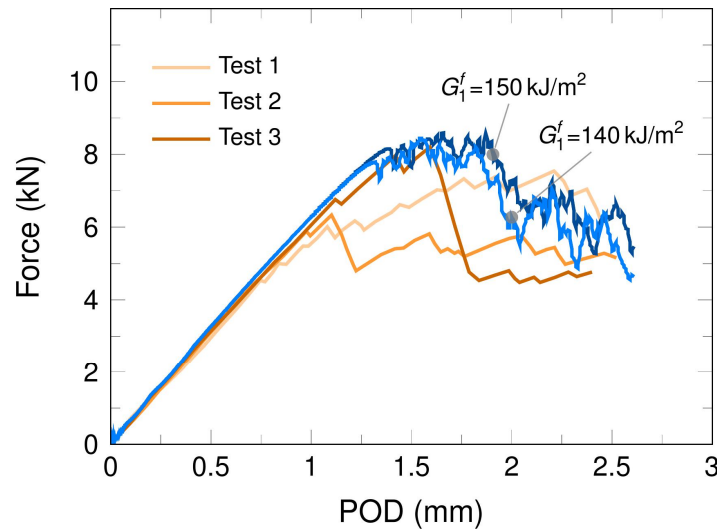


Figure 6.8: Comparison of the experimental [154] and predicted force-displacement curves for $[45/90/-45/0]_{2s}$ OCT laminate with different values of fracture energy for fibre damage mode

The presented numerical results show the advantage of the proposed approach for a laminate layup which is prone to large delamination zones. Without capturing delamination as the major damage mechanism, the predicted damage will be smeared over a finite zone and the behaviour of the laminate will be dominated by fibre fracture. This phenomenon can be shown by simulating the blocked-ply quasi-isotropic laminate $[45_4/90_4/-45_4/0_4]_s$ using the fully continuum damage approach. For this purpose, the model has been setup as previously described (i.e. ply-by-ply) but all the plies are tied together using the constrained contact formulation available in LS-DYNA (*CONTACT_TIED_SURFACE_TO_SURFACE [158]). This will eliminate the occurrence of delamination. The enhanced CODAM2 material model is assigned to each ply with all intra-laminar damage parameters as was used before with $G_1^f = 150 \text{kJ/m}^2$ and $G_2^f = 2.6 \text{kJ/m}^2$. It can be observed from Figure 6.9(a) that without capturing delamination

between the plies, the force-displacement response becomes more brittle. In this case damage is dominated by fibre fracture leading to severe under-prediction of the failure load. This shows that the response of a blocked-ply laminate can be correctly modelled only when the plies are allowed to delaminate at the interfaces, thus redistributing the stresses and resulting in a tougher response.

The application of the fully continuum damage approach to capture the overall response of the dispersed-ply quasi-isotropic laminate $[45/90/-45/0]_{2s}$ is also investigated. For this purpose, two simulations have been conducted. In the first one, all the plies are fully tied together to prevent delamination with all intra-laminar damage parameters as was used before with $G_1^f = 150\text{kJ/m}^2$ and $G_2^f = 2.6\text{kJ/m}^2$. In the second simulation, however, half-thickness of the laminate is modelled by only one layer of thick shell elements with two integration point through the thickness where for each integration point the original sub-laminate-based (macroscopic) CODAM2 material model as described in Section 3.2 is used. As outlined in Section 3.2.4, each integration point will represent the effective strain-softening behaviour of a sub-laminate once its initiation and saturation strain values are calibrated using the characterized damage properties of the sub-laminate. Since the loading is in-plane, one can also get the same result by using only one integration point through the thickness of the elements. The calibrated material properties for this laminate are chosen to be similar to $[45/90/-45/0]_{4s}$ (i.e. eight sub-laminates instead of four) which was characterized by Zobeiry et al. [289]. The calibrated input parameters including the matrix and fibre damage initiation and saturation strains are listed in Table 6-2 [289]. The fibre damage initiation strain of 0.011 is used based on the range of experimentally measured values. Matrix damage initiation strain of 0.008 is also used based on the reported values in the literature [121]. The measured laminate's fracture energy of 105 kJ/m^2 and a damage height equal to 5.0mm, are used to determine the damage saturation strain values [289,290]. Figure 6.9(b) shows the predicted force-displacement (POD) response using both of the above mentioned methodologies (both considered as a fully CDM approach). It is observed that both methods can capture the force-displacement response of the dispersed-ply quasi-isotropic laminate within the range of experimental results. The major predicted damage pattern is fibre fracture in the 0° and $\pm 45^\circ$ layers. Therefore, the fully continuum damage approach may provide a reasonable

prediction of the overall response for cases where delamination is minor. It is observed from Figure 6.9(b) that when delamination is prevented in the ply-by-ply model with the enhanced CODAM2 model, the force-displacement result is showing a more brittle behaviour in comparison with the case where delamination is allowed. This difference is associated with influence of delamination on redistributing the stress in the plies and delaying the initiation of fibre damage.

Table 6-2: Calibrated damage material parameters for $[45/90/-45/0]_{2s}$ laminate using the original sub-laminate based (macroscopic) CODAM2 [289]

Damage property	Symbol	Value
Matrix damage initiation strain	ε_2^i	0.008
Fibre damage initiation strain	ε_1^i	0.011
Damage saturation strain (fibre and matrix)	$\varepsilon_1^s, \varepsilon_2^s$	0.075
Non-local averaging radius (mm)	r	2.0

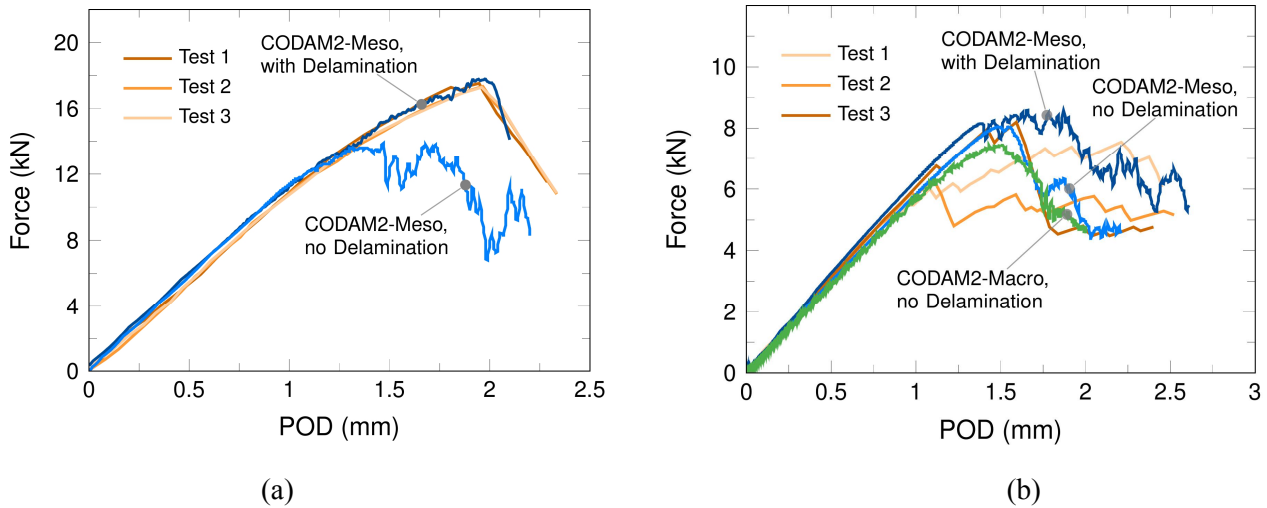


Figure 6.9: Comparison of the experimental and predicted force-displacement curves with and without accounting for delamination for (a) blocked-ply $[45_4/90_4/-45_4/0_4]_s$ and (b) dispersed-ply $[45/90/-45/0]_{2s}$ laminates [154,289]

6.2 Open-hole tensile (OHT) tests on quasi-isotropic laminates

The open-hole tensile (OHT) test is one of the test configurations that is commonly used in aerospace industry for composite design since it is representative of common features in composite components causing stress concentrations such as fastener holes and cutouts. The simulation of damage progression in OHT poses a great challenge due to the complex failure modes and their interaction that depend on fibre and matrix associated in-plane damage modes, stacking sequence, hole diameter, width/diameter ratios, ply thickness and others. The adopted virtual test method must be able to capture the failure scenarios and the dominant damage modes that lead to final failure of the specimen. Without capturing the correct failure mechanisms the notched ultimate strength may not be predicted correctly.

Several modelling strategies have been used recently to simulate the progression of damage and to account for all the possible damage mechanisms. The discrete damage method applied at the ply level in combination with discrete interface methods have gained significant attention, since it automatically takes into account the coupling between the intra-laminar and inter-laminar damage. As an example of this methodology, one can refer to the work by Hallett et al. [87], Achard and Bouvet et al. [11] where a refined complex mesh is made with a layer of elements per ply and interfaces for in-plane matrix crack and delamination. The paths of possible failures are limited to the number of interfaces pre-inserted in the model. Other methods have also been used to account for the discrete nature of matrix cracks. Prabhakar and Waas [203] proposed a triangular finite element that enables the possibility of splitting elements into two parts to capture the matrix crack failure. Methods that are based on XFEM are also used for this purpose. Vander Meer [249,252,253] used phantom node method to capture the in-plane matrix cracks within a limited area close to the hole with very fine mesh. Iarve et al. [105,106,236] used the regularized XFEM method to simulate the hole size effect in thick-ply laminates where the failure occurs in the delamination mode. They have used a minimum crack spacing which is dependent on the maximum size of any element on the crack path with the restriction that two adjacent crack paths have to be separated by several elements. Introducing the matrix cracks in this method will induce additional degrees of freedom and therefore an upper limit for the number of cracks per ply is enforced. This method has shown very good correlation with the

experimental results of thick ply laminates in OHT. They also extended their methodology to model fatigue in open-hole tests [107].

Meso-models using the CDM approach to capture intra-laminar damage modes are also used for this problem. Among them, Song et al. [229], proposed a modeling approach for the analysis of the open-hole tension specimens that consists of different meshes for each ply orientation, such that the element edges were aligned with the ply fibre direction, and cohesive element layers embedded between plies. Tie constraints were then used to connect the individual ply meshes with the cohesive element layers. They used the CDM formulation that is available in Abaqus to capture intra-ply damage modes. They have been able to predict the matrix crack and delamination pattern in blocked ply open hole laminates. However, they have reported that failure loads for specimens exhibiting a delamination failure mode are consistently over predicted. They have attributed this discrepancy to the late onset of delamination to link up damage through the laminate width compared to the experimental results.

The original sub-laminate based non-local CODAM2 was also employed to predict two of the test cases for the third round of World Wide Failure Exercise (WWFEIII) [75]. In these test cases, open hole tensile and compressive specimens of a quasi-isotropic $[45_4/90_4/-45_4/0_4]_s$ IM7/8552 laminate were modeled. For this geometry and material layup, the edge delamination and splitting in the layers, especially in the 0^0 layer have important roles to play in redistribution of stress in the layers. The effect of edge delamination, in this problem, was implicitly accounted for by reducing the in-plane stiffness of the laminate using a damage parameter which was driven by the maximum principal strain. The initiation strain of this damage mode was calculated based on the analytical formulation of O'Brien [186] that defines the critical in-plane strain corresponding to the onset of edge delamination. The stiffness reduction factor according to this damage mode was applied to all stiffness components of the laminate. The paper did not show satisfactory agreements with experiments. Since the sub-laminate was modelled as a block without modelling the ply interface separation, splits and delaminations were not captured.

Camanho et al. [33] also used both Linear Elastic Fracture Mechanics (LEFM) approaches and a local CDM approach for modeling size effect of open hole specimens only with dispersed

laminates. Delamination was not simulated as it was not the driving failure for sub-laminate-level scaled laminates in contrast to ply-blocked laminates. They concluded that a CDM approach can quantify the size effect of such problems more accurately than LEM approaches.

In this chapter, we will show that the proposed method can capture the response of OHT tests in terms of the final strength value, damage patterns and size effect in an efficient manner without the need to use discrete approaches to capture the intra-laminar matrix damage modes.

6.2.1 Test setup

The experimental details are presented fully by Green et al. in [82]. Key details are recounted here for comparison to the numerical results generated.

The specimen design is shown in plan-view in Figure 6.10. It consists of a gauge section of constant cross-sectional area, with width W , thickness t and length L , and a centrally located hole of diameter D . At either end of the gauge section is a gripping region. The specimen gauge length has constant ratios of $W/D=5$ and $L/D=20$ for all specimen sizes.

A quasi-isotropic laminate with stacking sequence $[45_m/90_m/-45_m/0_m]_{ns}$ was used, with 0 being in the direction of the applied loading. The product of m and n is equal to the laminate thickness, i.e. $m, n = 1$ for a 1 mm thick laminate; $m = 2, n = 1$ or $m = 1, n = 2$ for a 2 mm thick laminate; etc. Increasing m increases the number of plies of the same orientation blocked together, i.e. it increases the effective ply thickness. Hereafter, this is referred to as ply-level scaling. Increasing n keeps a constant ply thickness, but increases the laminate thickness by increasing the number of sub-laminates present. From now on this is referred to as sub-laminate-level scaling.

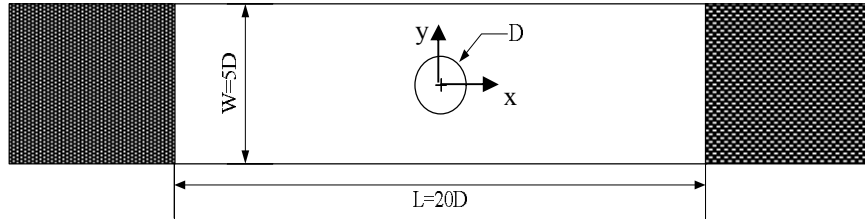


Figure 6.10: Specimen geometry of the open hole tensile laminates

The dimensions of the baseline specimen are scaled by a factor of 2 each time up to a maximum of 4. The minimum hole diameter used is 3.175 mm. Three different scaling routines are used: one-dimensional, two-dimensional and three-dimensional scaling. In the case of one-dimensional scaling only the thickness of the laminate is increased; in two-dimensional scaling, the in-plane dimensions (hole diameter, and hence width and length) are increased but the thickness kept the same. Three-dimensional scaling is where all dimensions are scaled simultaneously. The specimens were loaded using a constant nominal strain rate across the different sizes. A nominal strain rate of 0.78% /min was used, which equates to constant displacement rates of 0.5, 1 and 2 mm/min being used for hole diameters of 3.175, 6.35 and 12.7 mm, respectively. The failure load F_x was taken as being the first significant (greater than 5%) load drop on the load-displacement curve, which corresponded to either fibre failure or extensive delamination throughout the gauge section. The failure strength σ_x was obtained by dividing the failure load with the gross cross-sectional area of the specimen:

$$\sigma_x = \frac{F_x}{Wt} \quad (6.1)$$

Table 6-3 shows the experimental strength results and dominant failure modes from [82] for the tested laminates. The scatter associated with each value is variable in a range of 1% to 8% for the coefficients of variation.

Table 6-3: Experimental gross average failure stresses for laminates (MPa)(cv,%), reference [82]

		Hole Diameter D (mm)					
		Sub-laminate level scaled			Ply-level scaled		
		3.175	6.35	12.7	3.175	6.35	12.7
Laminate thickness (mm)	1	570(7.7)	-	-	-	-	-
	2	500(4.0)	438(2.4)	-	396(5.2)	498(6.5)	-
	4	478(3.1)	433(2.0)	374 (1.01)	275(5.6)	285(5.2)	362 (2.6)
	8	476(5.1)	-	-	202(7.9)	-	-

 Fibre breakage
  Delamination

6.2.2 Model setup

To reduce the model size, only the gauge length was modelled. For the symmetry of the lay-ups, half the thickness of the laminates was modelled and plane symmetric boundary conditions were applied at the mid-plane of the laminates.

The finite element mesh used to discretize the specimens for a region close to the hole are shown in Figure 6.11 for three cases of hole size. The mesh size is about 0.25 mm around the hole edge and increases along the width and height of the specimen to a maximum of 0.5mm along the y -axis at $x=0$. The mesh size along the height of specimen increases to as large as 1.5mm at the free boundaries at $x=L/2$. A pair of prescribed motions with constant rates of 317.5mm/s, 635mm/s and 1270mm/s was applied on the two ends of the specimens with hole diameters of 3.175mm, 6.35mm and 12.7mm, respectively.

Each individual ply was modelled with one layer of reduced-integrated thick shell elements (formulation 5 in LS-DYNA). Moreover, the enhanced CODAM2 material model was assigned to each layer of elements with its own ply orientation. Both blocked-ply and dispersed-ply layups were modelled using this approach. The tie-break contact with cohesive-based damage formulation, as described in Section 4.2, was defined between dissimilar plies to simulate delamination within the laminate. A stiffness based hourglass control (Type 4) was used with

stiffness coefficient of 0.6 to prevent zero energy mode shapes due to the presence of only one integration point in the plane of elements.

All the material properties are adopted similar to what was used in the previous chapter except for the strength parameters related to intra-ply and inter-ply matrix damage modes that are summarized in Table 6-4 for different ply thicknesses. The fracture energy values for matrix and fibre damage modes are assumed to be 2.6 and 140 kJ/m², respectively.

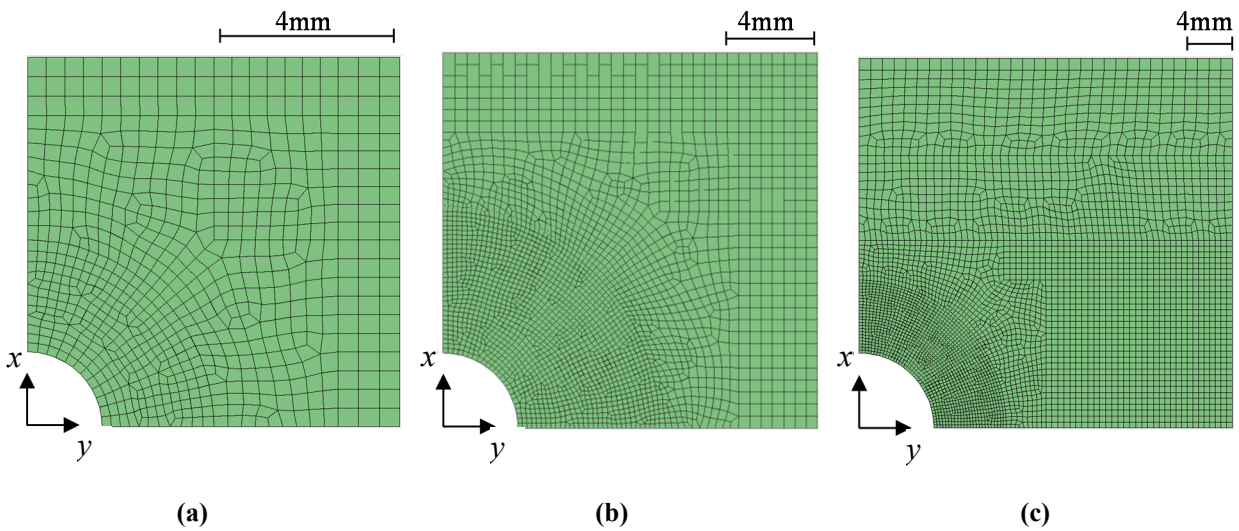


Figure 6.11: Finite element mesh around the hole with width and height of 2.5D for specimens with (a) D=3.175mm, (b) D=6.35mm, (c) D=12.7mm

6.2.3 Simulation results

The predicted failure strength σ_x corresponding to the first load drop greater than 5% and their difference with the experimental measured average strength values reported in [87] are shown in Table 6-5. The load values are divided by the unnotched cross-section width to obtain the resultant stresses. The stress vs opening displacement curves are also shown in Figure 6.12 through Figure 6.14 for D=3.175 mm, D=6.35 mm and D=12.7 mm for different laminate thicknesses. In the following, the numerical results will be discussed and compared against the experimental observations from Reference [82]. The numerical results and the sequence of

damage development are summarized based on the experimental observation of size effect due to ply thickness scaling and in-plane scaling of the specimens.

Table 6-4: Damage material parameters for $[45_m/90_m/-45_m/0_m]_{ns}$ laminates in the combined damage modelling approach for OHT specimens

Intra-laminar damage parameters for each ply				
Input parameters	$[45_m/90_m/-45_m/0_m]_{ns}$			
	m=1, n=1,2,4	m=2, n=1,2,4	m=4, n=1,2,4	m=8, n=1,2,4
Transverse tensile strength	$Y_T^{is} = 122\text{MPa}$	$Y_T^{is} = 90\text{MPa}$	$Y_T^{is} = 73\text{MPa}$	$Y_T^{is} = 73\text{MPa}$
In-plane shear strength	$S_L^{is} = 98.5\text{MPa}$	$S_L^{is} = 94\text{MPa}$	$S_L^{is} = 90\text{MPa}$	$S_L^{is} = 90\text{MPa}$
Inter-laminar damage parameters				
Input parameters	m=1, n=1,2,4	m=2, n=1,2,4	m=4, n=1,2,4	m=8, n=1,2,4
Maximum inter-laminar normal stress	$t_{max}^N = 33\text{MPa}$	$t_{max}^N = 24\text{MPa}$	$t_{max}^N = 21\text{MPa}$	$t_{max}^N = 9\text{MPa}$
Maximum inter-laminar shear stress	$t_{max}^S = 40\text{MPa}$	$t_{max}^S = 29\text{MPa}$	$t_{max}^S = 25\text{MPa}$	$t_{max}^S = 12\text{MPa}$

Table 6-5: Finite element predicted gross average failure stresses for $[45_m/90_m/-45_m/0_m]_{ns}$ laminates (MPa)(difference with average experimental results,%)

Laminate thickness (mm)	Hole Diameter D (mm)					
	Sub-laminate level scaled $[45/90/-45/0]_{ns}$			Ply-level scaled $[45_m/90_m/-45_m/0_m]_s$		
	3.175	6.35	12.7	3.175	6.35	12.7
1	540(5.3)	-	-	-	-	-
2	520(4.0)	440(0.5)		393(5.8)	468(6.0)	-
4	515(7.7)	436(0.7)	357(4.5)	297 (8.0)	305(7.0)	343 (5.2)
8	509 (8.9)	-	-	194(4.0)	-	-

 Fibre breakage  Delamination

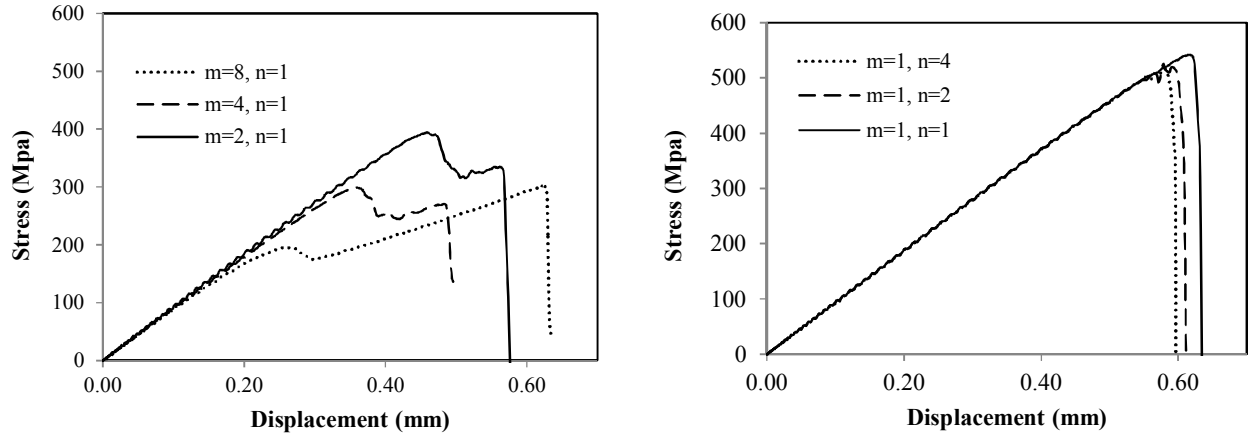


Figure 6.12: Predicted load versus displacement curves of OHT laminates with different laminate thicknesses: (a) ply-level scaled and (b) sub-laminate-level scaled specimens $[45_m/90_m/-45_m/0_m]_{ns}$ with $D=3.175\text{mm}$

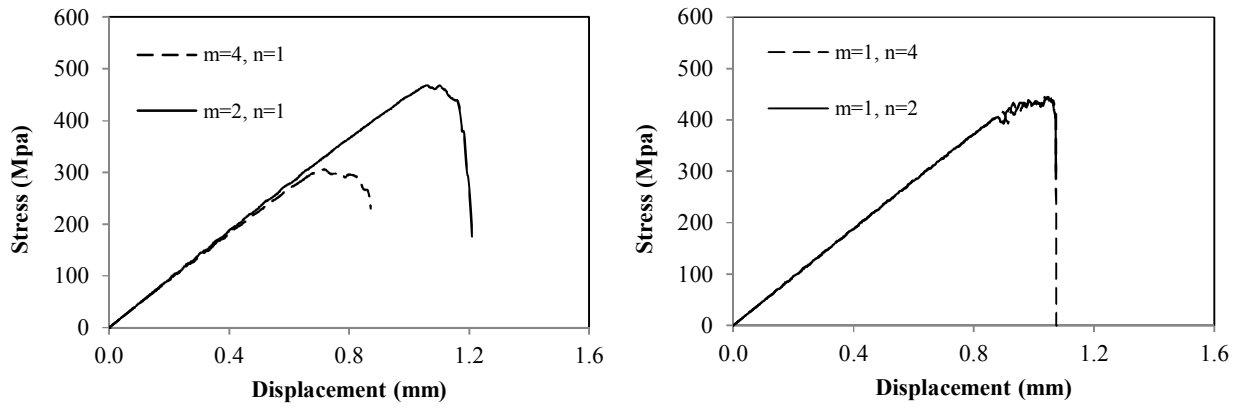


Figure 6.13: Predicted load versus displacement curves of OHT laminates with different laminate thicknesses: (a) ply-level scaled and (b) sub-laminate-level scaled specimens $[45_m/90_m/-45_m/0_m]_{ns}$ with $D=6.35\text{mm}$

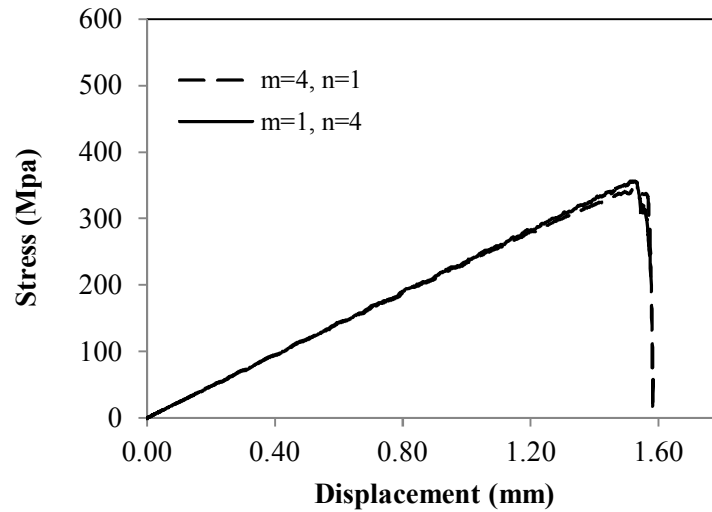


Figure 6.14: Predicted load versus displacement curves of OHT laminates with different laminate thicknesses for a ply-level scaled and a sub-laminate-level scaled specimens $[45_m/90_m/-45_m/0_m]_{ns}$ with $D=12.7\text{mm}$

6.2.3.1 Ply-thickness size-effect

The predicted and experimental results for strength of the ply-scaled specimens with $D=3.175\text{mm}$ and $D=6.35\text{mm}$ are shown in Figure 6.15 along with the average experimental values for the two hole sizes. The load values are divided by the unnotched cross-section width to visualize the size effect. It is seen that the size effect with respect to the ply thickness is captured well with the proposed numerical framework. Without the size effect the maximum load would have linearly scaled with the thickness resulting in a constant maximum far-field stress.

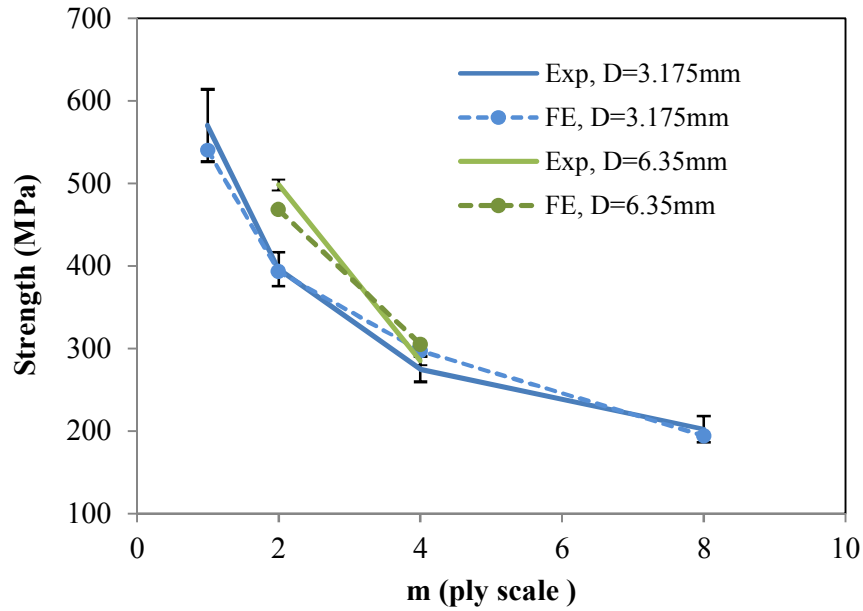


Figure 6.15: Comparison between numerical and experimental strength values for ply-level scaled specimens for D=3.175mm and D=6.35mm.

Figure 6.16 (a) and (b) shows the stress versus the displacement for the 4mm thick specimens with D=3.175 mm and D=6.35 mm when the ply thickness is increased from 0.125 to 0.5mm. It is seen that for single ply laminates ($t_k=0.125\text{mm}$) the behaviour is almost linear until an abrupt failure occurs. The failure corresponds to fibre breakage in the 0° plies. Predicted damage pattern for these thin-ply laminates is shown in Figure 6.17 through Figure 6.19 for D=3.17mm for a post-peak time step as indicated by the red square marker in Figure 6.16(a). Similar damage patterns are also predicted for D=6.35mm and D=12.7mm hole size specimens with 0.125mm thick plies which are not shown here.

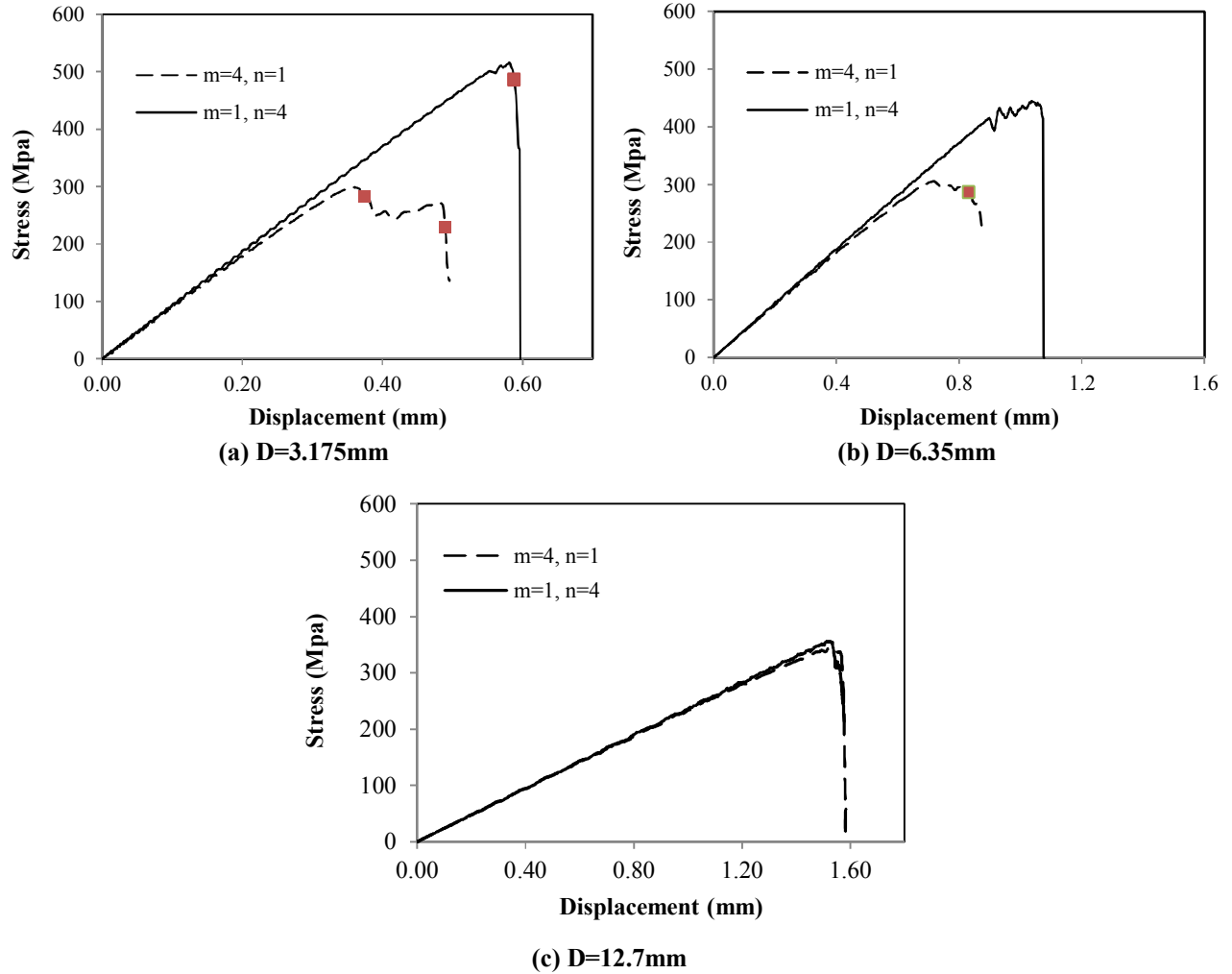


Figure 6.16: Predicted load-displacement curves for 4mm thick specimens with (a) $D=3.175\text{mm}$, (b) $D=6.35\text{mm}$ and (c) $D=12.7\text{mm}$ hole size made of single and quadruple ply thickness

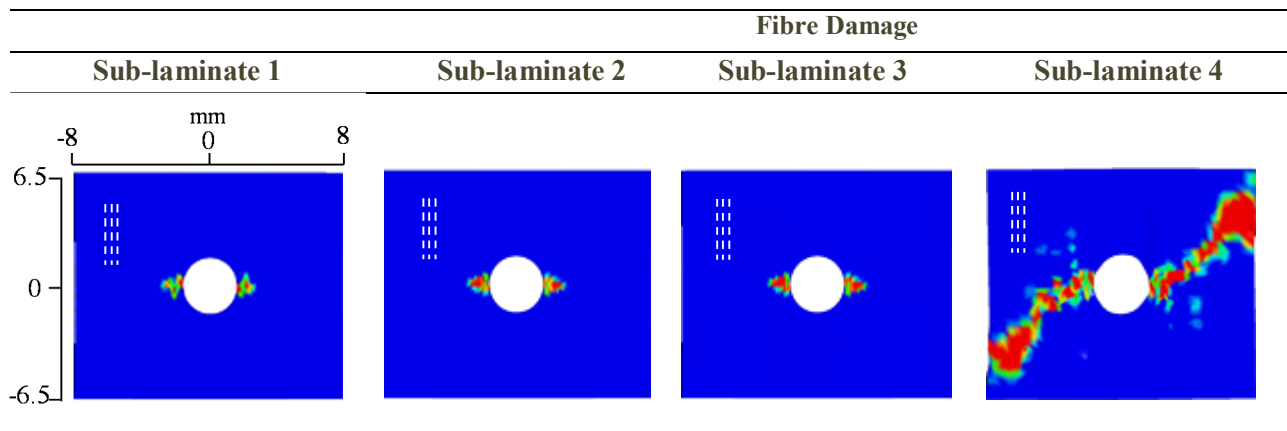


Figure 6.17: State of fibre damage in 0° plies for a time step after failure (marked with red squares in Figure 6.16(a)) for $[45/90/-45/0]_{4s}$ specimen with hole size $D=3.175\text{mm}$

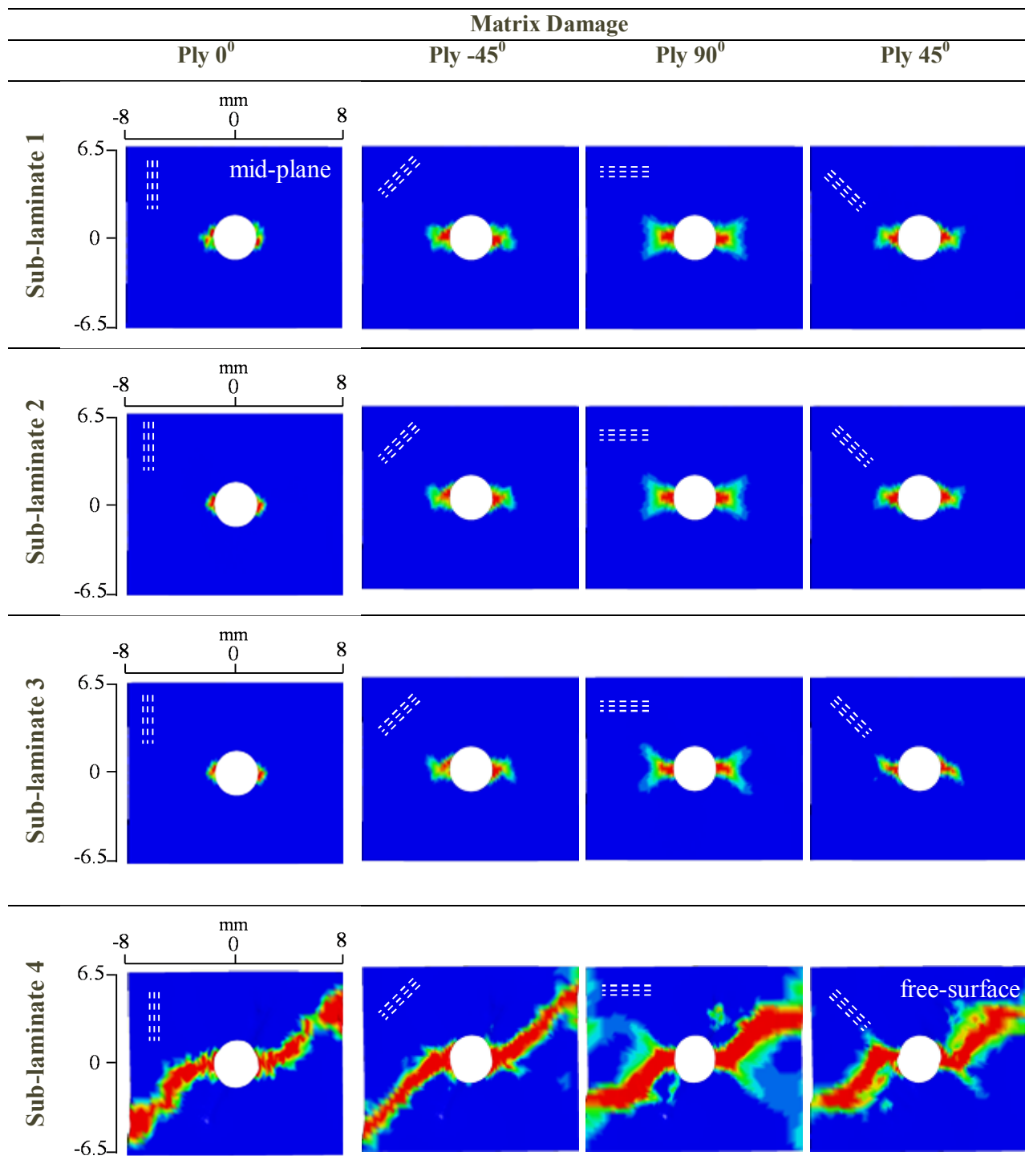


Figure 6.18: State of matrix damage in all the plies for a time step after failure (marked with red squares in Figure 6.16(a)) for $[45/90/-45/0]_4$ s specimen with hole size $D=3.175\text{mm}$

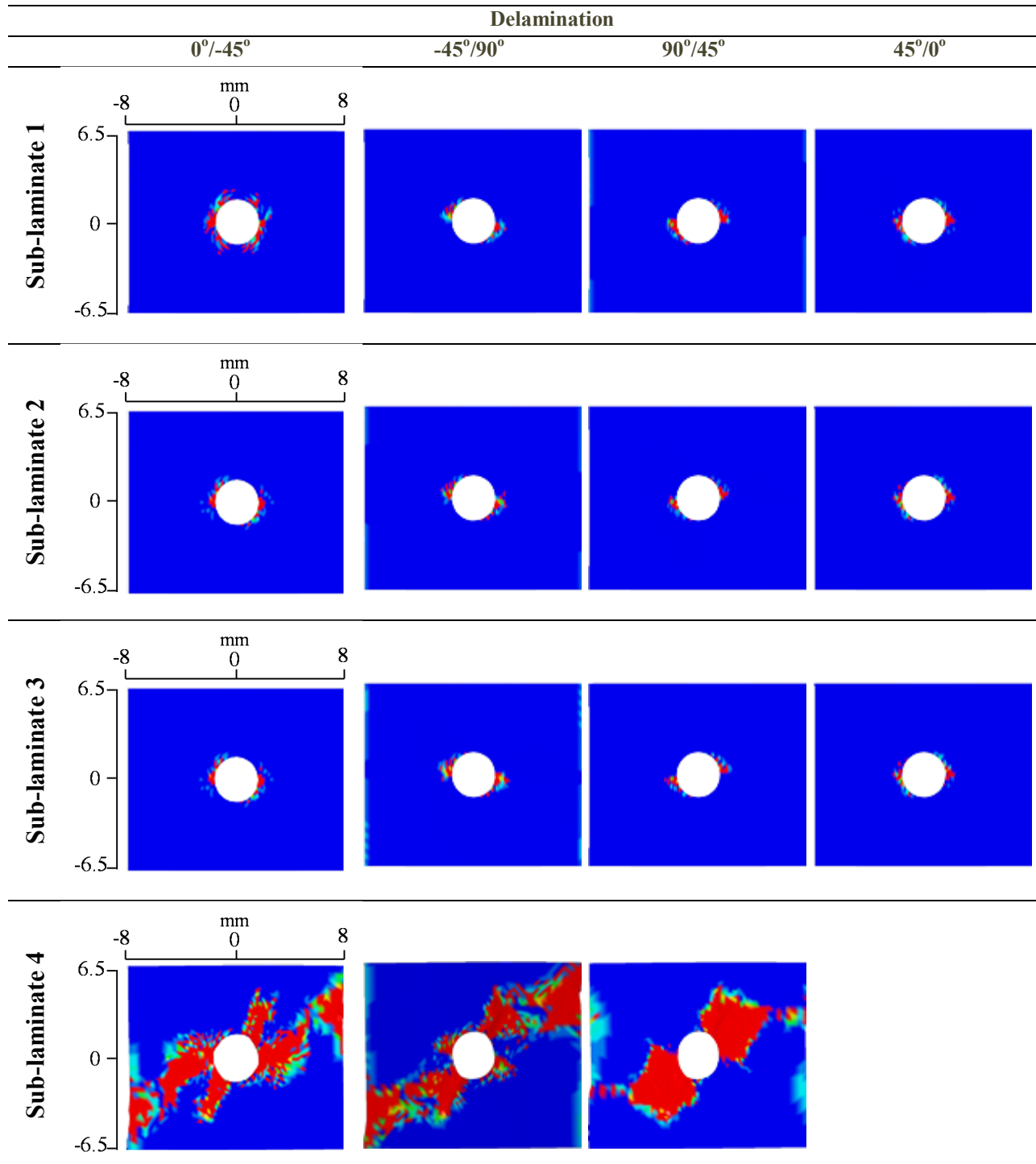


Figure 6.19: State of delamination in all the interfaces for a time step after failure (marked with red squares in Figure 6.16(a)) for $[45/90/-45/0]_{4s}$ specimen with hole size $D=3.175\text{mm}$

It can be seen from Figure 6.16(a) that for thick-ply laminates ($t_k=0.5\text{mm}$), however, the laminate stiffness gradually decreases before the load drop which corresponds to the failure point. Depending on the hole size, the load drop in these laminates can be a series of smaller drops or a single drop. Damage patterns predicted for the thick-ply laminate with $D=3.175\text{mm}$ hole size are shown in Figure 6.20 for two points corresponding to time steps after the first and second load drops as indicated by the red square markers in Figure 6.16(a). Similarly, damage mechanisms for thick-ply laminate with $D=6.35\text{mm}$ hole size are shown in Figure 6.21 for a post-peak time step as indicated by red square marker in Figure 6.16(b). The failure in thick-ply laminates ($t_k=0.5\text{mm}$) is the result of the propagation of delamination as will be discussed in more details in the following.

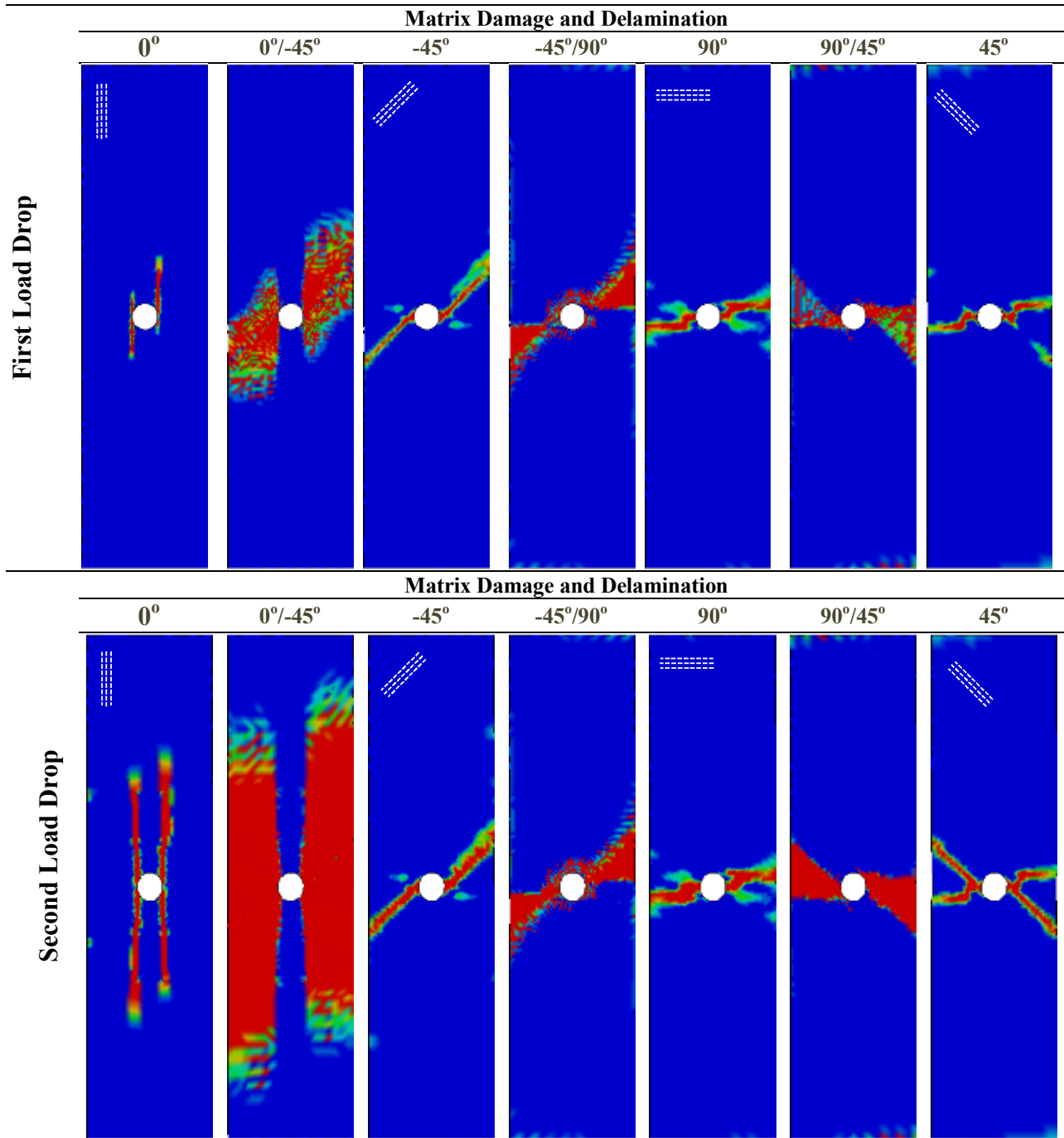


Figure 6.20: State of matrix damage for all plies and delamination at each interface for $[45_4/90_4/-45_4/0_4]_s$ specimen with $D=3.175\text{mm}$ at a time step after the first and second load drop (marked with red squares in Figure 6.16(a))

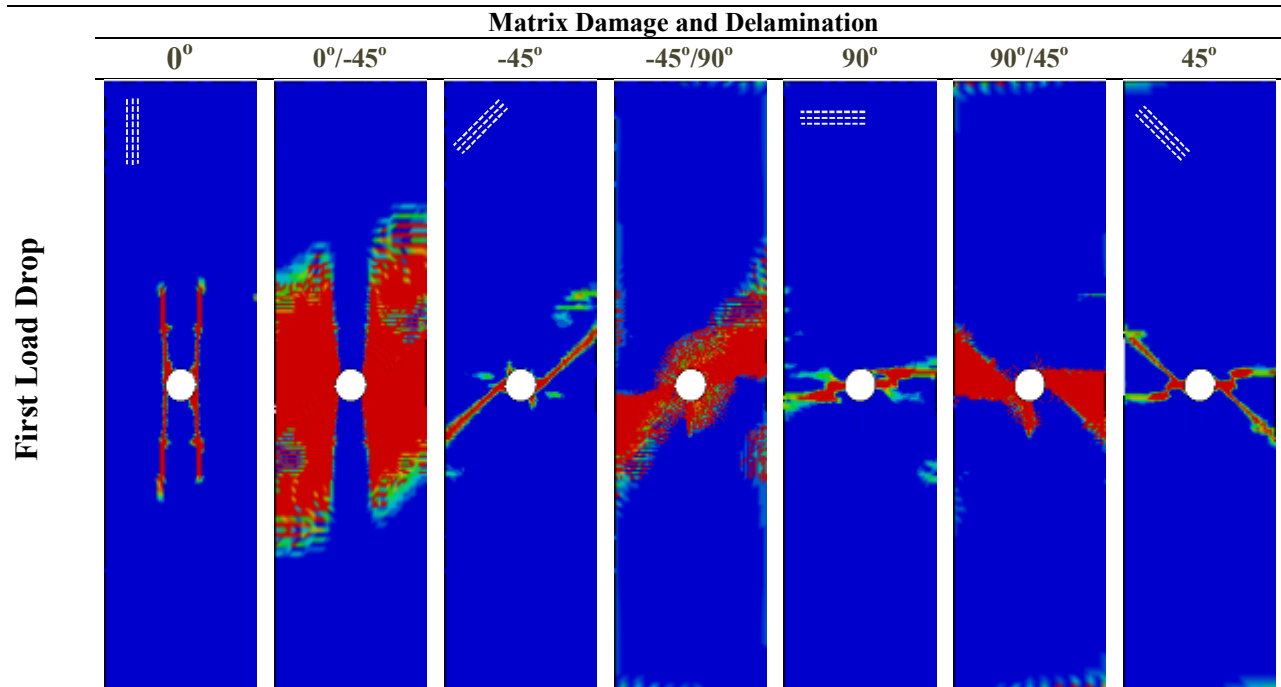


Figure 6.21: State of matrix damage for all plies and delamination at each interface for $[45_4/90_4/-45_4/0_4]_s$ specimen with $D=6.35\text{mm}$ at a time step after the first load drop (marked with red squares in Figure 6.16(a))

In the following the patterns of different damage modes are explained in more detail for both thin and thick-ply laminates.

Thin plies: fibre-dominated failure

According to the experimental studies [82], the failure mode in thin ply specimens is dominated by fibre breakage except for limited delamination mostly concentrated in the vicinity of the hole. The load curve of this type of behaviour is mostly linear with abrupt failure. Similarly, the predicted damage patterns in Figure 6.17 through Figure 6.19 for thin-ply specimen with hole size $D=3.175\text{mm}$ ($[45/90/-45/0]_{4s}$) also shows fibre breakage with matrix cracking and delamination occurring in a limited zone at the free edges of the hole. The extent of delamination and matrix cracking in the sub-laminate closest to the top surface (sub-laminate 4 in Figure 6.18 and Figure 6.19) is larger than the other sub-laminates as a result of the reduced constraining effect from the neighboring plies. The stress-displacement curve of this specimen in Figure 6.16(a) also shows a linear behaviour up to the final abrupt drop which is consistent with the experimental results.

Thick plies: delamination- dominated failure

In thick-ply laminates ($t_k=0.5\text{mm}$), the failure is dominated by delamination. Based on experimental observations [82], the stiffness degradation begins with matrix cracking in the outer 45° layer along the hole edges and then it will propagate across the plies and interfaces until the delamination at the $-45/0$ interface crosses the whole width of the specimen which corresponds to the first load drop of specimen. According to the experiments [82], there can be a single load drop or a series of smaller drops. When a series of load drops are observed, the delamination at the $-45/0$ interface as well as the splits in the 0° plies propagate asymmetrically. However, when the delamination covers the entire gauge section instantaneously and symmetrically on both sides of the hole edge, a single load drop is observed. The experimental results have shown that the asymmetric behaviour in propagation of splits in 0° plies and delamination at $-45/0$ interface is more pronounced in the specimens with smaller hole diameter.

The simulation results of thick-ply specimens, shown in Figure 6.20 and Figure 6.21, are in good agreement with the experimental observations and the predicted evolution of matrix cracking and associated interface delamination. On the load-displacement curve (Figure 6.16(a)), there is a gradual decrease in the slope which is related to the progression of transverse matrix cracks and delamination.

It is seen that at the first load drop in smaller hole size ($D=3.175\text{mm}$) (Figure 6.20), delamination growth path at $-45/0$ interface as well as the associated splits in the 0° layer is asymmetric with respect to the hole centre as a result of the adjacent -45 plies. This is in agreement with what has been observed in the experiments. In comparison, however, the specimen with larger hole size of $D=6.35\text{mm}$ (Figure 6.21) shows a symmetric propagation of the 0° -ply splits in all the four quadrants of specimen which will lead to a single load drop but larger failure load. The same behaviour is also predicted by a fully discrete methodology conducted in [87]. As a result of using a non-local averaging technique, the current model is able to successfully predict the path of transverse matrix cracks propagating in the 0° and off-axis plies.

In conclusion, the predictions have well captured the transition from the fibre-dominated failure mode to the delamination-dominated mode as the thickness of plies increases. Therefore, the introduction of the ply thickness effect for transverse matrix cracking prediction and the coupling between intra-laminar and inter-laminar behaviour are essential requirements for capturing such transition. The dependence of initiation of matrix damage on the ply thickness will allow earlier prediction of such mechanisms for thicker plies. The coupling between matrix damage and delamination onset through the unique calibration procedure for inter-laminar maximum stresses, allows triggering development of delamination which is the characteristic failure mode in the case of thick plies.

6.2.3.2 In-plane size effect

In this section, the focus is on the comparison of results between different sizes of hole and in-plane size of specimens.

Previous studies have shown that in quasi-brittle materials the size effect falls between strength theories, e.g. theory of plasticity (for which there is no size effect) and linear elastic fracture mechanics (LEFM) (for which the size effect is the strongest). This transitional size effect is an indication of the presence of a certain non-negligible characteristic length of the material. In fact, this length is a representation of the size of the fracture process zone (FPZ) [21,22].

The predicted stress values and the corresponding experimental values for thin-ply ($t_k=0.125\text{mm}$) and thick ply ($t_k=0.5\text{mm}$) laminates with total thickness of 4mm are plotted in Figure 6.22 as a function of hole-diameter. There are some differences in terms of splitting pattern of 0° plies in thick-ply laminates where they tend to be more asymmetric in the small specimen in comparison with the largest specimen where less asymmetric splitting pattern is evident. This was already discussed and shown in Figure 6.20 and Figure 6.21 for specimens with $D=3.175\text{ mm}$ and $D=6.35\text{ mm}$, respectively.

Thin-ply: classical fracture mechanics hole-size effect

For thin-ply laminates, the fibre breakage is the dominant damage mechanism for all specimen scales. The increase in hole size leads to a decrease in strength due to an increase in the in-plane dimensions (green dashed line in Figure 6.22). This is consistent with the classical hole size effect based on fracture mechanics. Among these models, one can mention the Whitney-Nuismer hole size model [265].

Thick-ply: inverted hole-size effect

For thick-ply laminates, the failure is dominated by delamination in all the specimen scales. The hole-size effect is, however, the opposite of what is observed in thin plies. An increase in the in-plane dimensions leads to an increase in the strength (blue dashed line in Figure 6.22). In [87], this behaviour was attributed to the fact that in larger coupons the ligament (i.e. the space between the hole edge and the specimen's free edge in y -direction in Figure 6.10) is larger and the propagation of delamination across the whole width of the specimen requires more energy.

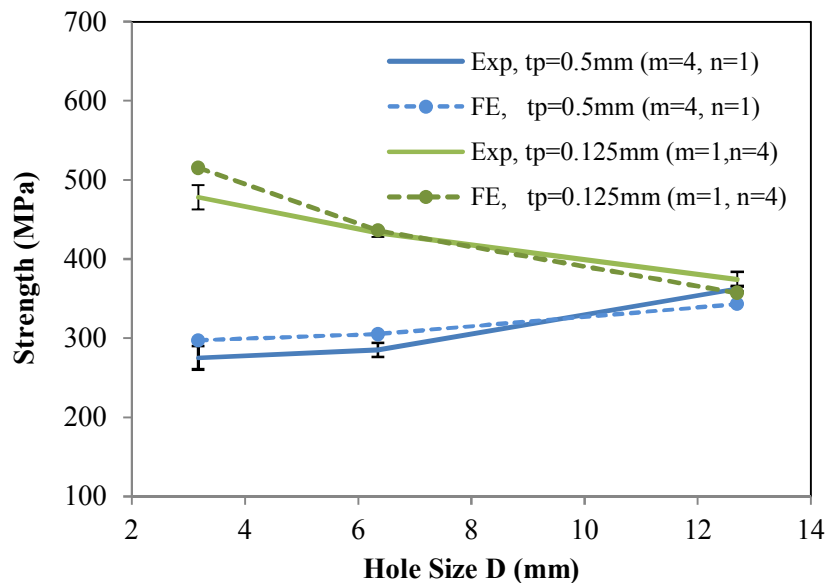


Figure 6.22: Effect of specimen size on the strength of 4-mm thick specimens of $[45/90/-45/0]_{4s}$ and $[45_4/90_4/-45_4/0_4]_s$ laminates with different hole diameter size both in experiments and the predicted results. The strength of thin-ply laminates show a decreasing trend, while the thick-ply laminates exhibit an increasing trend as the hole diameter increases.

Figure 6.23 repeats the results of Figure 6.22 for dispersed layups overlaid by the predictions based on the LEFM-scaled model. The vertical axis in this figure represents the logarithm of the remote stress and the horizontal axis represents the logarithm of the hole diameter. Based on the LEFM, the failure stress of a specimen with a hole diameter D_2 can be calculated from the failure stress of the specimen with a hole diameter D_1 :

$$\sigma_x^{(2)} = \sigma_x^{(1)} \sqrt{\frac{D_1}{D_2}} \quad (6.2)$$

The failure stress measured in the specimens with the largest hole diameter of 12.7 mm was used in the LEFM model to predict the strength of the specimens with other hole diameters.

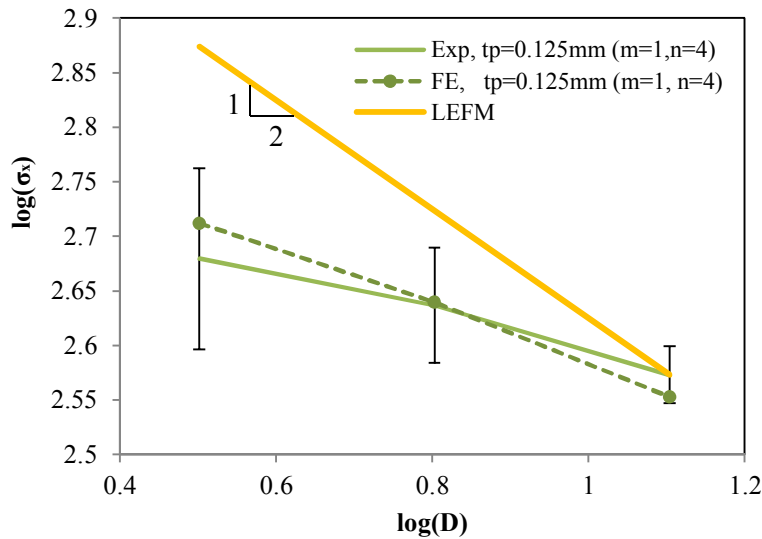


Figure 6.23: Effect of specimen size on the strength of 4-mm thick specimens of [45/90/-45/0]_{4s} with different hole diameter. Comparison of the predictions of the current methodology and LEFM with experiments.

It is seen that the strength is over-predicted for small hole diameters. For small specimens, the damaged region at the edge of the hole cannot be considered to be negligible when compared with the characteristic dimensions of the specimen, and the assumptions of LEFM are not applicable. It should also be noted that the LEFM predictions based on scaled specimens always

result in a line with a slope of $-1/2$ that passes through the baseline point (Figure 6.23). This means that the use of a small hole diameter as the baseline point would result in severe under-predictions of the notched strength of larger specimens. In comparison with LEFM, the nonlocal CODAM2 material model is capable of capturing the size effect by introducing a length scale and capturing the extent of the damage that is dependent on the fracture energy values. The use of discrete interface enables the model to predict the size effect specifically for the case of blocked-ply laminate where its behaviour is dominated by delamination. In this case a reverse size-effect trend is obtained that cannot be predicted by LEFM.

The size effect that is observed from the experiments and are captured well by the proposed methodology are energetic size effect which cannot be predicted by using a statistical approach like the Weibull theory [261]. The Weibull theory is based on the concept that the larger the structure, the higher the probability of presence of defects. It can be shown that in the Weibull theory, the average nominal strength of the material depends on a characteristic size of the specimen which leads to a logarithmic linear relationship between the stress and volume [20]. The application of Weibull theory works best for describing the failure of brittle materials that fail immediately after a microscopic crack becomes macroscopic. However, it suffers from a few limitations for the case of quasi-brittle materials as pointed out by Bazant [20]. The size effect in this formulation is a power law which does not include any characteristic length (i.e. the length of fracture process zone). Moreover, there is no consideration of the failure mechanisms in a mathematical formulation of the structure.

6.3 Summary

In this chapter, the calibrated enhanced CODAM2 material model in combination with cohesive interfaces between the plies was used for prediction of the response and damage progression in quasi-isotropic laminates under two different notched loading geometries for IM7/8552 CFRP material system. In the first case, two quasi-isotropic laminates ($[45_m/90_m/-45_m/0_m]_{ns}$) with a dispersed-ply ($m=1$ and $n=2$) and blocked-ply ($m=4, n=1$) laminate layups in an OCT configuration were simulated. In the second case, OHT specimens with similar material system and layups with various size and laminate thicknesses were modelled.

Overall, the predictions have well captured the transition from the fibre-dominated failure mode to the delamination-dominated as the thickness of plies increases. Therefore, the introduction of the ply thickness effect for transverse matrix cracking prediction and the coupling between intra-laminar and inter-laminar behaviour are essential requirements for capturing such transition. The dependence of initiation of matrix damage on the ply thickness will allow earlier prediction of such mechanism for thicker plies in comparison with thinner ones. The coupling between intra-laminar matrix damage and delamination enables triggering of delamination which is the characteristic failure mode in the case of thick plies.

The predictions have also correctly captured the in-plane size effect for both thin and thick-ply laminates in OHT specimens. The in-plane size effect for the thin ply laminates is consistent with the classical hole size effect as expected based on fracture mechanics. However, for thick plies the failure is mostly dominated by matrix cracking and delamination. An increase in the in-plane dimensions (i.e. an increase in the size of the ligaments) leads to an increase in the strength, since the propagation of delamination across the whole width of specimen requires more energy.

Chapter 7: Conclusions and Future Work

7.1 Conclusions

The development of a proper numerical model representing the physics of damage mechanisms in composite laminates is a challenging task. Although there is a vast body of work with the focus to capture the details of the complex damage process, they are still not being used by engineers in practice due to their high level of complexity and computational cost. The main goal in this study was to present an efficient numerical framework with the potential to model the complex damage process, initiating from matrix cracking, evolving in delamination and fibre breakage, and leading to the ultimate failure of the composite.

A common modelling technique which is used extensively in finite element analysis due to its straightforward implementation and numerical efficiency is the fully continuum damage (CDM) based approach. However, for cases where failure is governed by discrete macro-crack propagation such as large splits or delaminations, a fully continuum-based approach cannot correctly describe the propagation of damage through the structure. The basic assumption of compatibility of displacement/strain fields in the CDM approach is not applicable to delamination-dominated responses. Delamination redistributes the stresses around the damaged zone and consequently alters the load paths within the structure. Moreover, when delamination is dominant, the sub-laminate's fracture energy in presence of extensive delamination zones between the plies becomes difficult to define and measure. Therefore, it is necessary to explicitly model delamination which will then allow the growth of macro-cracks (e.g. splits) in the separated ply. This limitation of the CDM approach is the main motivation of the current work with the goal to capture both delamination and the intra-laminar damage modes including highly localized and discrete forms of damage such as transverse and longitudinal matrix damage (splits).

The main contribution of the presented work was to further enhance the capabilities of the in-house macroscopic CODAM2 material model such that it can be used in a mesoscopic context (see Chapter 3). This material model was used in conjunction with the cohesive interface method

in order to capture the inter-ply separations (see Chapter 4). This improvement allowed efficient and accurate prediction of damage progression in several loading geometries and laminate layups. The methodology also accounted for the in-situ behaviour of the individual plies within the laminate and the change in the stacking sequence. The presented methodology offers more computational efficiency in comparison with fully discrete methodologies where cracks, whether in the form of interface disbonding (delamination) or intra-laminar disbonding of fibre and matrix (i.e. splits), are explicitly represented in the geometry model of the structure. With the use of the non-local capability, the presented enhanced CODAM2 material model can effectively predict the trajectory of in-plane macro-cracks irrespective of the finite element discretization. Therefore, prior knowledge of intra-laminar crack paths and the need to introduce pre-inserted discrete cohesive elements in the plane of a ply is eliminated.

The enhancements required for considering individual plies as building blocks of the laminate were introduced in Chapter 3. These enhancements and modifications were related to the prediction of initiation and saturation of matrix and fibre damage modes. The interactive effect of transverse normal and shear stress components on matrix cracking combined with the inherent non-linear shear stress-strain response of unidirectional composites necessitates the use of stress-based criteria to signal initiation of matrix damage. Hashin's failure criteria were used to identify the onset of intra-laminar matrix and fibre damage modes. The constraining effect of the immediate neighboring plies and the ply thickness on the unidirectional strength properties were considered through an approximate analytical model based on a combination of fracture mechanics and shear lag theory introduced by Zhang et al. [278,279]. Moreover, the irreversible nonlinear behaviour of in-plane shear was introduced in both elastic and damage regimes of loading. The progression of intra-laminar damage modes at the ply level took into account the fracture toughness corresponding to each failure mode.

Another contribution of the current work is to establish a methodology for obtaining the in-situ material properties associated with the initiation and progression of intra-laminar damage modes for the presented advanced non-local CODAM2 material model in the mesoscopic context. Most of these properties including the elastic moduli and strength properties can be gathered from the standard tests. For the material considered in this study, IM7/8552 CFRP, the literature provided

a well-established database. However, the main interest was to obtain the fracture energies associated with the progression of fibre and matrix damage modes (see Chapter 5).

While there is more literature available on the characterization of fibre fracture energy, less work has been done for characterization of intra-laminar matrix fracture energy. In fully discrete models where intra-laminar matrix cracks at the ply level is modelled by using cohesive discrete elements, this type of damage is treated similarly to delamination. This can be justified by the fact that enough number of potential crack interfaces is inserted in the plies to dissipate the same amount of energy by matrix cracks as in the experiment. Therefore, the intra-laminar matrix fracture energy is assumed to be similar to the inter-laminar fracture energy values. However, in the proposed methodology where we use a CDM approach, the fracture surfaces caused by all matrix/fibre debonding and matrix cracks are not modelled directly (explicitly). Thus, the inter-laminar fracture energy values do not represent the correct amount of energy absorbed by this damage mechanism. Therefore, a systematic and unique procedure was proposed to calibrate the intra-laminar fracture energies of a material system in tension from a few experiments on OCT specimens of cross-ply laminates (see Chapter 5). The intent was to implicitly account for the interaction of matrix cracks with delamination and damage in neighboring plies. These are the type of interacting mechanisms that do not show up in tests conducted on unidirectional laminates.

For the purpose of calibration of intra-laminar fracture energy values for IM7/8552 CFRP material system, two types of blocked and dispersed cross-ply laminates with OCT configuration were used. The experimental results for the blocked cross-ply laminate that are governed by delamination and splitting (i.e. matrix damage dominated) were used to estimate the appropriate value of the matrix intra-laminar fracture energy. The numerical analyses were performed using a range of fracture energy values for matrix cracking while keeping all the other damage parameters constant. The numerical predictions in terms of the global behaviour (e.g. force-displacement) and damage mechanisms were compared against the experimental results to calibrate the intra-laminar matrix fracture energy. Moreover, the effect of the experimental range reported for the fibre fracture energy of this material in the literature was investigated. While the response of the blocked-ply laminate was independent of the fibre fracture energy, the peak force

and the post-peak response of the dispersed-ply laminate were found to be sensitive to the fibre fracture energy value.

Another issue that was addressed in this work was the drawback associated with use of cohesive zone model that was used to capture the interface delamination. In order to have an accurate prediction of delamination using the cohesive zone model without the need to use very fine mesh, the length of the cohesive zone in the simulation was artificially increased by reducing the interface strength. A simple yet intuitive method was proposed to estimate the amount of reduction for the interface strength properties (see Chapter 5). The inter-laminar strength properties were adjusted based on the status of inter-laminar stresses that were obtained from a 3D stress analysis on the laminate while delamination was prevented between the plies. The average of inter-laminar stresses within a zone close to the notch or discontinuities where the matrix cracks and delamination were expected to occur first was selected as the inter-laminar calibrated strength properties. However, the inter-laminar fracture energy values remained unchanged. With this approach, one can eliminate the need to have very fine mesh size to get accurate prediction using the cohesive interfaces. Moreover, it also implicitly accounts for the effect of ply thickness on the initiation of delamination since the initiation of delamination is indirectly linked to the matrix cracking which is in turn influenced by ply thickness.

The calibrated material properties for the above mentioned material system were used to validate two loading geometries. In the first case, two quasi-isotropic laminates of IM7/8552 CFRP with a dispersed-ply and blocked-ply laminate layup in an OCT configuration were simulated. In the second case, the same laminates in an OHT loading geometry with various size and laminate thicknesses were modelled.

In conclusion, the model calibrated using correlation between the simulations and experiments on blocked and dispersed cross-ply laminates has found to predict the details of the response of the blocked and dispersed quasi-isotropic laminates under both OCT and OHT loading configurations. In all cases, the model captured the transition from the fibre-dominated failure mode to the delamination-dominated mode with increasing the thickness of ply. The introduction of the ply thickness effect for initiating transverse matrix cracking and the coupling

between intra-laminar and inter-laminar damage were essential requirements for capturing such transition. The dependence of initiation of matrix damage on the ply thickness will allow earlier prediction of such mechanism for thicker plies. The inter-laminar coupling allows to trigger development of delamination which is the characteristic failure mode in the case of thick-ply laminates.

7.2 Contributions

The contributions of this work can be summarized as follows:

- The capabilities of the UBC's in-house macroscopic CODAM2 material model were enhanced so it can be used in a mesoscopic context. This makes the model applicable to a wider range of problems, especially when the damage response of the composite laminate is dominated by matrix cracking and delamination damage modes. These are the type of problems that cannot be simulated with fully CDM models.
- A simple technique was proposed to avoid the use of very fine mesh structure, and couple the interface delamination with matrix damage, which is in turn influenced by ply thickness.
- A novel methodology was proposed for obtaining the in-situ material properties associated with the initiation and progression of intra-laminar damage modes for the presented advanced non-local CODAM2 material model in the mesoscopic context.

7.3 Future works

To make the model capable of simulating a wider range of damage propagation problems for different loading scenarios and material systems, the proposed methodology needs to be further improved. The following are some of the features that will achieve this.

-CODAM2 formulation in compression

One of the enhancements would be to add the capability of simulating the plateau behaviour and residual deformation observed in compressive tests on notched laminated composite specimens

[174,287]. Residual deformation was also observed in low velocity lateral impact tests on composite panels [55,56]. To be able to predict the residual deformations, a coupled damage-plasticity formulation needs to be employed for modelling the behaviour of the material under compressive loading. The damage with plasticity model employed in [74] for an isotropic material was shown to be successful in predicting the unloading behaviour of the impacted plate as well as predicting the residual deformation. The challenge here is to adopt an appropriate plasticity model that is compatible with the fundamentals of CODAM2.

-Automation of delamination

In order to reduce the computational cost of this methodology even further, one can avoid a prior introduction of cohesive interfaces between all the plies by using an automated local cohesive zone (LCZ) methodology [221]. This method allows modelling the structure without a priori definition of the delamination location in the analysis, i.e. delaminations initiate and evolve as the simulation progresses. The continuum elements are split through their thickness and potential paths for delamination growth are seeded into the model adaptively. Combining the enhanced CODAM2 material model with the LCZ eliminates the need to use cohesive zones between all plies and reduces the computational costs. Implementation of the enhanced CODAM2 in the mesoscopic form advanced in this thesis as an addition to the built-in material type MAT219 in LS-DYNA as well as the LCZ method can be of great benefit for engineers in practice.

Bibliography

- [1] Composite Material Handbooks (CMH-17), Volume 1-Guidelines for Characterization of Structural Materials, US Department of Defense 2002.
- [2] Composite Material Handbooks (CMH-17), Volume 2-Materials Properties. , US Department of Defense 2002.
- [3] BAPS 176-018, Ultrasonic Inspection Of Composite Components.
- [4] CRNTD 156-001B, Defect Testing with OmniScan MX2.
- [5] CRNTD 166-001B, Basic Analysis Using TomoView.
- [6] Standard test method for compressive properties of unidirectional or cross-ply fiber-resin composites, ASTM D 3410-87, West Conshohocken (PA), USA: American Society for Testing and Materials (ASTM).
- [7] Standard test method for in-plane shear response of polymer matrix composite materials by test of a $\pm 45^\circ$ laminate, ASTM D 3518/3518M-94, West Conshohocken (PA), USA: American Society for Testing and Materials (ASTM).
- [8] Standard test method for tensile properties of polymer matrix composite materials, ASTM D3039/D 3039M-00. West Conshohocken (PA), USA: American Society for Testing and Materials (ASTM).
- [9] Abdi F, Godines C, DorMohammadi S, Minnetyan L, Static Validation of Composite Open Hole Analysis Technique for Standard and nonstandard Laminate -Part 1. 56th AIAA/ASCE/AHS/ASC Structures, Structural Dynamics, and Materials Conference, American Institute of Aeronautics and Astronautics, 2015.
- [10] Abisset E, Daghia F, Sun XC, Wisnom MR, Hallett SR, Interaction of inter- and intralaminar damage in scaled quasi-static indentation tests: Part 1 – Experiments, Composite Structures. 136 (2016) 712-726.
- [11] Achard V, Bouvet C, Castanié B, Chirol C, Discrete ply modelling of open hole tensile tests, Composite Structures. 113 (2014) 369-381.
- [12] Alfano G, Crisfield MA, Finite element interface models for the delamination analysis of laminated composites: Mechanical and computational issues, Int J Numer Methods Eng. 50 (2001) 1701-1736.
- [13] Allen DH, Searcy CR, Numerical Aspects of a Micromechanical Model of a Cohesive Zone, J Reinf Plast Compos. 19 (2000) 240-248.

- [14] Allix O, Corigliano A, Modeling and simulation of crack propagation in mixed-modes interlaminar fracture specimens, *Int.J.Fract.* 77 (1996) 111-140.
- [15] ASTM D, Standard Test Method for Mode I Interlaminar Fracture Toughness of Unidirectional Fiber-reinforced Polymer Matrix Composites, (2007).
- [16] Babuska I, Melenk JM, Partition of unity method, *Int J Numer Methods Eng.* 40 (1997) 727-758.
- [17] Barbero EJ, de Vivo L, A Constitutive Model for Elastic Damage in Fiber-Reinforced PMC Laminae, *Int J Damage Mech.* 10 (2001) 73-93.
- [18] Barenblatt GI, The Mathematical Theory of Equilibrium Cracks in Brittle Fracture. *Advances in Applied Mechanics*, Elsevier, pp. 55-129.
- [19] Basu S, Waas AM, Ambur DR, Prediction of progressive failure in multidirectional composite laminated panels, *Int.J.Solids Structures.* 44 (2007) 2648-2676.
- [20] Bažant ZP, Size effect on structural strength: a review, *Arch Appl Mech.* 69 (1999) 703-725.
- [21] Bazant ZP, Planas J, Fracture and size effect in concrete and other quasibrittle materials. , CRC Press, Boca Raton, 1998.
- [22] Bazant ZP, Daniel IM, Li Z, Size effect and fracture characteristics of composite laminates, *Journal of Engineering Materials and Technology.* 118 (1996) 317-324.
- [23] Bazant ZP, Di Luzio G, Nonlocal microplane model with strain-softening yield limits, *Int.J.Solids Structures.* 41 (2004) 7209-7240.
- [24] Bazant ZP, Oh BH, Crack band theory for fracture of concrete, *Materiaux et Constructions, Materials and Structures.* 16 (1983) 155-177.
- [25] Bazant ZP, Pijaudier-Cabot G, Nonlocal continuum damage, localization instability and convergence, *Journal of applied mechanics* (1988) 18-7.
- [26] Bazhenov S, Longitudinal splitting in unidirectional fibre-reinforced composites with an open hole, *Composites Sci.Technol.* 58 (1998) 83-89.
- [27] Belytschko T, Black T, Elastic crack growth in finite elements with minimal remeshing, *Int J Numer Methods Eng.* 45 (1999) 601-620.
- [28] Benzeggagh ML, Kenane M, Measurement of mixed-mode delamination fracture toughness of unidirectional glass/epoxy composites with mixed-mode bending apparatus, *Composites Sci.Technol.* 56 (1996) 439-449.

- [29] Borg R, Nilsson L, Simonsson K, Modeling of delamination using a discretized cohesive zone and damage formulation, *Composites Sci.Technol.* 62 (2002) 1299-1314.
- [30] Butalia TS, Wolfe WE, A strain-energy-based non-linear failure criterion: comparison of numerical predictions and experimental observations for symmetric composite laminates, *Composites Sci.Technol.* 62 (2002) 1697-1710.
- [31] Camanho PP DC, Mixed-mode decohesion finite elements for the simulation of delamination in composite materials, NASA/TM-2002-211737 (2002).
- [32] Camanho PP, Davila CG, de Moura MF, Numerical simulation of mixed-mode progressive delamination in composite materials, *J.Composite Mater.* 37 (2003) 1415-1438.
- [33] Camanho PP, Maimí P, Dávila CG, Prediction of size effects in notched laminates using continuum damage mechanics, *Composites Sci.Technol.* 67 (2007) 2715-2727.
- [34] Camanho PP, Dávila CG, Pinho ST, Iannucci L, Robinson P, Prediction of in situ strengths and matrix cracking in composites under transverse tension and in-plane shear, *Composites Part A: Applied Science and Manufacturing.* 37 (2006) 165-176.
- [35] Catalanotti G, Camanho PP, Xavier J, Dávila CG, Marques AT, Measurement of resistance curves in the longitudinal failure of composites using digital image correlation, *Composites Sci.Technol.* 70 (2010) 1986-1993.
- [36] Chaboche JL, Development of continuum damage mechanics for elastic solids sustaining anisotropic and unilateral damage, *Int J Damage Mech.* 2 (1993) 311-329.
- [37] Chamis CC, Murthy PLN, Minnetyan L, Progressive fracture of polymer matrix composite structures, *Theor.Appl.Fract.Mech.* 25 (1996) 1-15.
- [38] Chang FK, Lessard LB, Damage tolerance of laminated composites containing an open hole and subjected to compressive loadings: Part I - Analysis, *Composites.* 22 (1991) 329.
- [39] Chang FK, Chang KY, A progressive damage model for laminated composites containing stress concentrations, *Journal of Composite Materials.* 21 (1987) 834-855.
- [40] Chatterjee SN, Pipes RB, Blake R, Criticality of disbonds in laminated composites. *Effects of Defects in Composite Materials*, ASTM International, 1984.
- [41] Chen BY, Pinho ST, De Carvalho NV, Baiz PM, Tay TE, A floating node method for the modelling of discontinuities in composites, *Eng.Fract.Mech.* 127 (2014) 104-134.
- [42] Chen D, Harada K, Stress singularities for crack normal to and terminating at bimaterial interface on orthotropic half-plates, *Int.J.Fract.* 81 (1996) 147-162.

- [43] Cox BN, Marshall DB, Concepts for bridged cracks in fracture and fatigue, *Acta metallurgica et materialia*. 42 (1994) 341-363.
- [44] Cox B, Yang Q, In quest of virtual tests for structural composites, *Science*. 314 (2006) 1102-1107.
- [45] Crossman FW, Warren WJ, Wang ASD, Law GE, Initiation and growth of transverse cracks and edge delamination in composite laminates Part 2. Experimental correlation, *Journal of Composite Materials*. 14 (1980) 88-108.
- [46] Cui WC, Wisnom MR, Jones M, A comparison of failure criteria to predict delamination of unidirectional glass/epoxy specimens waisted through the thickness, *Composites*. 23 (1992) 158-166.
- [47] Cui W, Wisnom MR, A combined stress-based and fracture-mechanics-based model for predicting delamination in composites, *Composites*. 24 (1993) 467-474.
- [48] Cuntze RG, Freund A, The predictive capability of failure mode concept-based strength criteria for multidirectional laminates, *Composites Sci.Technol*. 64 (2004) 343-377.
- [49] Cusatis G, Beghini A, Bazant ZP, Spectral stiffness microplane model for quasibrittle composite laminates - Part I: Theory, *J.Appl.Mech.Trans.ASME*. 75 (2008) 0210091-0210099.
- [50] Dalgarno R, Robbins D, Fiber-aligned,discrete-layer modeling approaches for progressive failure simulation of open hole composite panels. 53rd AIAA/ASME/ASCE/AHS/ASC Structures, Structural Dynamics and Materials Conference, American Institute of Aeronautics and Astronautics, 2012.
- [51] Davila CG, Camanho PP, Turon A, Effective simulation of delamination in aeronautical structures using shells and cohesive elements, *J.Aircr*. 45 (2008) 663-672.
- [52] Davila C, Jaunky N, Goswami S, Failure criteria for FRP laminates in plane stress. American Institute of Aeronautics and Astronautics, 2003.
- [53] de Borst R, Gutierrez MA, Wells GN, Remmers JJC, Askes H, Cohesive-zone models, higher-order continuum theories and reliability methods for computational failure analysis, *Int J Numer Methods Eng*. 60 (2004) 289-315.
- [54] de Moura MFSF, Campilho RDSG, Amaro AM, Reis PNB, Interlaminar and intralaminar fracture characterization of composites under mode I loading, *Composite Structures*. 92 (2010) 144-149.
- [55] Delfosse D, Poursartip A, Energy-based approach to impact damage in CFRP laminates, *Composites Part A: Applied Science and Manufacturing*. 28 (1997) 647-655.

- [56] Delfosse D, Poursartip A, Coxon BR, Dost EF, Non-penetrating impact behavior of CFRP at low and intermediate velocities, In Composite Materials: Fatigue and Fracture: Fifth Volume. ASTM International (1995) 333-350.
- [57] Di Sciuva M, Multilayered anisotropic plate models with continuous interlaminar stresses, Composite Structures. 22 (1992) 149-167.
- [58] Donadon MV, Falzon BG, Iannucci L, Hodgkinson JM, Intralaminar toughness characterisation of unbalanced hybrid plain weave laminates, Composites Part A: Applied Science and Manufacturing. 38 (2007) 1597-1611.
- [59] Dorey G, Fracture of composites and damage tolerance, AGARD Lecture Series, North Atlantic Organization. (1982).
- [60] Dugdale DS, Yielding of steel sheets containing slits, J.Mech.Phys.Solids. 8 (1960) 100-104.
- [61] Echaabi J, Trochu F, Gauvin R, Review of failure criteria of fibrous composite materials, Polymer Composites. 17 (1996) 786-798.
- [62] Eckold GC, Failure criteria for use in the design environment, Composites Sci.Technol. 62 (2002) 1561-1570.
- [63] Engelstad SP, Action J, Clay SB, Holzwarth R, Dalgarno RW, Robbins D, Assessment of Composite Damage Growth Tools for Aircraft Structure-Part I, (2015) 1876.
- [64] Engelstad SP, Clay S, Assessment of Composite Damage Growth Tools for Aircraft Structure Part II. 57th AIAA/ASCE/AHS/ASC Structures, Structural Dynamics, and Materials Conference, American Institute of Aeronautics and Astronautics, 2016.
- [65] Erdogan F, Gupta G, The stress analysis of multi-layered composites with a flaw, Int.J.Solids Structures. 7 (1971) 39-61.
- [66] Falk ML, Needleman A, Rice JR, A critical evaluation of cohesive zone models of dynamic fracture, Le Journal de Physique IV. 11 (2001) Pr5-43-Pr5-50.
- [67] Fernlund G, Osooly A, Poursartip A, Vaziri R, Courdji R, Nelson K, et al., Finite element based prediction of process-induced deformation of autoclaved composite structures using 2D process analysis and 3D structural analysis, Composite Structures. 62 (2003) 223-234.
- [68] Fernlund G, Rahman N, Courdji R, Bresslauer M, Poursartip A, Willden K, et al., Experimental and numerical study of the effect of cure cycle, tool surface, geometry, and lay-up on the dimensional fidelity of autoclave-processed composite parts, Composites Part A: Applied Science and Manufacturing. 33 (2002) 341-351.

- [69] Fish J, Yu Q, Multiscale damage modelling for composite materials: theory and computational framework, *Int J Numer Methods Eng.* 52 (2001) 161-191.
- [70] Flaggs DL, Kural MH, Experimental Determination of the In Situ Transverse Lamina Strength in Graphite/Epoxy Laminates, *J.Composite Mater.* 16 (1982) 103-116.
- [71] Floyd A, An engineering approach to the simulation of gross damage development in composite laminates, PhD Thesis, Department of Civil Engineering, The University of British Columbia, Vancouver, BC, Canada. (2004).
- [72] Forghani A, A non-local approach to simulation of damage in composite structures, PhD. Thesis, Department of Civil Engineering, The University of British Columbia, Vancouver, Canada. (2011).
- [73] Forghani A, Shahbazi M, Zobeiry N, Poursartip A, Vaziri R, 6 - An overview of continuum damage models used to simulate intralaminar failure mechanisms in advanced composite materials. In: Hallett SR, Camanho PP (Eds.), *Numerical Modelling of Failure in Advanced Composite Materials*, Woodhead Publishing, 2015, pp. 151-173.
- [74] Forghani A, Vaziri R, Computational modeling of damage development in composite laminates subjected to transverse dynamic loading, *J.Appl.Mech.Trans.ASME.* 76 (2009) 051304.
- [75] Forghani A, Zobeiry N, Poursartip A, Vaziri R, A structural modelling framework for prediction of damage development and failure of composite laminates, *J.Composite Mater.* 47 (2013) 2553-2573.
- [76] Forghani A, Zobeiry N, Vaziri R, Poursartip A, Ellyin F, A non-local approach to simulation of damage in laminated composites, *Damage in Composites*, 5 (2013) 279-294.
- [77] Garg AC, Intralaminar and interlaminar fracture in graphite/epoxy laminates, *Eng.Fract.Mech.* 23 (1986) 719-733.
- [78] Ghosh S, Bai J, Raghavan P, Concurrent multi-level model for damage evolution in microstructurally debonding composites, *Mech.Mater.* 39 (2007) 241-266.
- [79] Gotsis PK, Chamis CC, Minnetyan L, Application of progressive fracture analysis for predicting failure envelopes and stress-strain behaviors of composite laminates: a comparison with experimental results, *Composites Sci.Technol.* 62 (2002) 1545-1559.
- [80] Gotsis PK, Chamis CC, Minnetyan L, Prediction of composite laminate fracture: micromechanics and progressive fracture, *Composites Sci.Technol.* 58 (1998) 1137-1149.
- [81] Goyal VK, Johnson ER, Dávila CG, Irreversible constitutive law for modeling the delamination process using interfacial surface discontinuities, *Composite Structures.* 65 (2004) 289-305.

- [82] Green BG, Wisnom MR, Hallett SR, An experimental investigation into the tensile strength scaling of notched composites, *Composites Part A: Applied Science and Manufacturing*. 38 (2007) 867-878.
- [83] Grufman C, Ellyin F, Numerical modelling of damage susceptibility of an inhomogeneous representative material volume element of polymer composites, *Composites Sci.Technol*. 68 (2008) 650-657.
- [84] Grufman C, Ellyin F, Determining a representative volume element capturing the morphology of fibre reinforced polymer composites, *Composites Sci.Technol*. 67 (2007) 766-775.
- [85] Gutkin R, Laffan ML, Pinho ST, Robinson P, Curtis PT, Modelling the R-curve effect and its specimen-dependence, *Int.J.Solids Structures*. 48 (2011) 1767-1777.
- [86] Hallett SR, Numerical investigation of progressive damage and the effect of layup in notched tensile tests, *J.Composite Mater*. 40 (2005) 1229-1245.
- [87] Hallett SR, Green BG, Jiang WG, Wisnom MR, An experimental and numerical investigation into the damage mechanisms in notched composites, *Compos Part A Appl Sci Manuf*. 40 (2009) 613-624.
- [88] Hallett SR, Wisnom MR, Numerical investigation of progressive damage and the effect of layup in notched tensile tests, *J.Composite Mater*. 40 (2006) 1229-1245.
- [89] Han YM, Hahn HT, Croman RB, A simplified analysis of transverse ply cracking in cross-ply laminates, *Composites Sci.Technol*. 31 (1988) 165-177.
- [90] Hansbo A, Hansbo P, A finite element method for the simulation of strong and weak discontinuities in solid mechanics, *Comput.Methods Appl.Mech.Eng*. 193 (2004) 3523-3540.
- [91] Harper PW, Hallett SR, Cohesive zone length in numerical simulations of composite delamination, *Eng.Fract.Mech*. 75 (2008) 4774-4792.
- [92] Hart-Smith LJ, Comparison between theories and test data concerning the strength of various fibre-polymer composites, *Composites Sci.Technol*. 62 (2002) 1591-1618.
- [93] Hart-Smith LJ, Expanding the capabilities of the Ten-Percent Rule for predicting the strength of fibre-polymer composites, *Composites Sci.Technol*. 62 (2002) 1515-1544.
- [94] Hashin Z, Failure criteria for unidirectional fiber composites, *Journal of Applied Mechanics*. 47 (1980) 329-334.
- [95] Hashin Z, Rotem A, A Fatigue Failure Criterion for Fiber Reinforced Materials, *Journal of Composite Materials*. 7 (1973) 448-464.

- [96] Herakovich CT, On the relationship between engineering properties and delamination of composite laminates, *Journal of Composite Materials*, 15 (1981) 336-348.
- [97] Hillerborg A, Modeer M, Petersson P, Analysis of crack formation and crack growth in concrete by means of fracture mechanics and finite elements, *Cem. Concr. Res.* 6 (1976) 773-781.
- [98] Hine PJ, Brew B, Duckett RA, Ward IM, Failure mechanisms in continuous carbon-fibre reinforced PEEK composites, *Composites Sci.Technol.* 35 (1989) 31-51.
- [99] Hine PJ, Brew B, Duckett RA, Ward IM, The fracture behaviour of carbon fibre reinforced poly(ether etherketone), *Composites Sci.Technol.* 33 (1988) 35-71.
- [100] Hinton MJ, Kaddour AS, Soden PD, A further assessment of the predictive capabilities of current failure theories for composite laminates: Comparison with experimental evidence, *Composites Sci.Technol.* 64 (2004) 549-588.
- [101] Hinton MJ, Kaddour AS, Soden PD, A comparison of the predictive capabilities of current failure theories for composite laminates, judged against experimental evidence, *Composites Sci.Technol.* 62 (2002) 1725-1797.
- [102] Hinton MJ, Soden PD, Predicting failure in composite laminates: the background to the exercise, *Composites Sci.Technol.* 58 (1998) 1001-1010.
- [103] Hui C, Jagota A, Bennison S, Londono J, Crack blunting and the strength of soft elastic solids, In *Proceedings of the Royal Society of London A: Mathematical, Physical and Engineering Sciences*, 459 (2003) 1489-1516.
- [104] Hutchinson JW, Suo Z, Mixed Mode Cracking in Layered Materials, *Adv.Appl.Mech.* 29 (1991) 63-191.
- [105] Iarve EV, Mesh independent modelling of cracks by using higher order shape functions, *Int J Numer Methods Eng.* 56 (2003) 869-882.
- [106] Iarve EV, Gurvich MR, Mollenhauer DH, Rose CA, Davila CG, Mesh-independent matrix cracking and delamination modeling in laminated composites, *Int J Numer Methods Eng.* 88 (2011) 749-773.
- [107] Iarve EV, Hoos K, Braginsky M, Zhou E, Mollenhauer DH, Progressive failure simulation in laminated composites under fatigue loading by using discrete damage modeling, *J.Composite Mater.* (2017) 2143-2161.
- [108] Icardi U, Locatto S, Longo A, Assessment of Recent Theories for Predicting Failure of Composite Laminates, *Appl.Mech.Rev.* 60 (2007) 76-86.

- [109] Inglis HM, Geubelle PH, Matouš Karel, Boundary condition effects on multiscale analysis of damage localization, *Philosophical Magazine*. 88 (2008) 2373-2397.
- [110] Irwin GR, Plastic zone near a crack and fracture toughness, *Problems of Fracture Mechanics and Fatigue* (1960) 63-78.
- [111] Isaac M. Daniel, Ori Ishai, *Engineering Mechanics of Composite Materials*. second ed., Oxford University Press, Inc. 2006.
- [112] Iwamoto M, Ni Q, Fujiwara T, Kurashiki K, Intralaminar fracture mechanism in unidirectional CFRP composites — part II: analysis, *Eng.Fract.Mech.* 64 (1999) 747-764.
- [113] Iwamoto M, Ni Q, Fujiwara T, Kurashiki K, Intralaminar fracture mechanism in unidirectional CFRP composites: Part I: Intralaminar toughness and AE characteristics, *Eng.Fract.Mech.* 64 (1999) 721-745.
- [114] Jiang W, Hallett SR, Green BG, Wisnom MR, A concise interface constitutive law for analysis of delamination and splitting in composite materials and its application to scaled notched tensile specimens, *Int J Numer Methods Eng.* 69 (2007) 1982-1995.
- [115] Jirasek M, *Course Notes on Modeling of Localized Elastic Deformation*, (2007).
- [116] Jirásek M, Nonlocal models for damage and fracture: Comparison of approaches, *Int.J.Solids Structures*. 35 (1998) 4133-4145.
- [117] Johnston A, Vaziri R, Poursartip A, A plane strain model for process-induced deformation of laminated composite structures, *Journal of Composite Materials*. 35 (2001) 1435-1469.
- [118] Jose S, Ramesh Kumar R, Jana MK, Venkateswara Rao G, Intralaminar fracture toughness of a cross-ply laminate and its constituent sub-laminates, *Composites Sci.Technol.* 61 (2001) 1115-1122.
- [119] Kachanov LM, Rupture time under creep conditions, *Int.J.Fract.* 97 (1999) 11-18.
- [120] Kaddour AS, Hinton MJ, Smith PA, Li S, The background to the third world-wide failure exercise, *J.Composite Mater.* 47 (2013) 2417-2426.
- [121] Kaddour AS, Hinton MJ, Smith PA, Li S, Mechanical properties and details of composite laminates for the test cases used in the third world-wide failure exercise, *J.Composite Mater.* 47 (2013) 2427-2442.
- [122] Kaddour AS, Hinton MJ, Soden PD, A comparison of the predictive capabilities of current failure theories for composite laminates: Additional contributions, *Compos.Sci.Technol.* 64 (2004) 449-476.

- [123] Kaddour AS, Hinton MJ, Soden PD, A comparison of the predictive capabilities of current failure theories for composite laminates: additional contributions, *Composites Sci.Technol.* 64 (2004) 449-476.
- [124] Kant T, Swaminathan K, Estimation of transverse/interlaminar stresses in laminated composites – a selective review and survey of current developments, *Composite Structures.* 49 (2000) 65-75.
- [125] Kapania R, A review on the analysis of laminated shells, *ASME J.Pressure Vessel Technol.* 111 (1989) 88-96.
- [126] Karihaloo BL, Xiao QZ, Modelling of stationary and growing cracks in FE framework without remeshing: A state-of-the-art review, *Computers and Structures.* 81 (2003) 119-129.
- [127] Kashtalyan M, Soutis C, Effect of delaminations induced by transverse cracks and splits on stiffness properties of composite laminates, *Composites Part A: Applied Science and Manufacturing.* 31 (2000) 107-119.
- [128] Kashtalyan M, Soutis C, Analysis of composite laminates with intra- and interlaminar damage, *Prog.Aerospace Sci.* 41 (2005) 152-173.
- [129] Kongshavn I, Poursartip A, Experimental investigation of a strain-softening approach to predicting failure in notched fibre-reinforced composite laminates, *Composites Sci.Technol.* 59 (1999) 29-40.
- [130] Krajcinovic D, *Continuous damage mechanics revisited: Basic concepts and definitions*, (1985) ASME, New York, NY, USA.
- [131] Krajcinovic D, Silva MAG, Statistical aspects of the continuous damage theory, *International Journal of Solids and Structures.* 18 (1982) 551-562.
- [132] Krueger R, Virtual crack closure technique: History, approach, and applications, *Appl.Mech.Rev.* 57 (2004) 109-143.
- [133] Kuraishi A, Tsai SW, Liu KKS, A progressive quadratic failure criterion, part B, *Composites Sci.Technol.* 62 (2002) 1683-1695.
- [134] Kwon YW, Liu CT, Study of damage evolution in composites using damage mechanics and micromechanics, *Composite Structures.* 38 (1997) 133-139.
- [135] Lacy TE, McDowell DL, Willice PA, Talreja R, On representation of damage evolution in continuum damage mechanics, *Int J Damage Mech.* 6 (1997) 62-95.
- [136] Ladeveze P, LeDantec E, Damage modelling of the elementary ply for laminated composites, *Composites Sci.Technol.* 43 (1992) 257-267.

- [137] Ladeveze P, Multiscale modeling and computational strategies for composites, *Int.J.Numer.Meth.Engng.* 60 (2004) 233-253.
- [138] Ladeveze P, Allix O, Deu J, Leveque D, Mesomodel for localisation and damage computation in laminates, *Comput.Methods Appl.Mech.Eng.* 183 (2000) 105-122.
- [139] Ladeveze P, Nouy A, On a multiscale computational strategy with time and space homogenization for structural mechanics, *Comput.Methods Appl.Mech.Eng.* 192 (2003) 3061-3087.
- [140] Lafarie-Frenot MC, Touchard F, Comparative in-plane shear behaviour of long-carbon-fibre composites with thermoset or thermoplastic matrix, *Composites Sci.Technol.* 52 (1994) 417-425.
- [141] Laffan MJ, Pinho ST, Robinson P, Iannucci L, Measurement of the fracture toughness associated with mode I fibre compressive failure, *Composites Part A: Applied Science and Manufacturing*, 43 (2010) 1930-1938.
- [142] Laffan MJ, Pinho ST, Robinson P, Iannucci L, Measurement of the in situ ply fracture toughness associated with mode I fibre tensile failure in FRP. Part I: Data reduction, *Composites Sci.Technol.* 70 (2010) 606-613.
- [143] Laffan MJ, Pinho ST, Robinson P, Iannucci L, Measurement of the in situ ply fracture toughness associated with mode I fibre tensile failure in FRP. Part II: Size and lay-up effects, *Composites Sci.Technol.* 70 (2010) 614-621.
- [144] Laffan MJ, Pinho ST, Robinson P, McMillan AJ, Translaminar fracture toughness: The critical notch tip radius of 0° plies in CFRP, *Composites Sci.Technol.* 72 (2011) 97-102.
- [145] Laurin F, Carrère N, Maire J-, A multiscale progressive failure approach for composite laminates based on thermodynamical viscoelastic and damage models, *Composites Part A: Applied Science and Manufacturing.* 38 (2007) 198-209.
- [146] Laws N DG, Progressive transverse cracking in composite laminates, *J. Compos. Mater.* 22 (1988) 900-916.
- [147] Leach DC, Moore DR, Toughness of aromatic polymer composites reinforced with carbon fibres, *Composites Sci.Technol.* 23 (1985) 131-161.
- [148] Lee JW, Daniel IM, Progressive transverse cracking of crossply composite laminates, *Journal of Composite Materials.* 24 (1990) 1225-1243.
- [149] Leguillon D, Lacroix C, Martin E, Interface debonding ahead of a primary crack, *J.Mech.Phys.Solids.* 48 (2000) 2137-2161.

- [150] Lemaitre J, Desmorat R, Sauzay M, Anisotropic damage law of evolution, *Eur J Mech A Solids*. 19 (2000) 187-208.
- [151] Li C, Zobeiry N, Chatterjee S, Poursartip A, Advances in the characterization of residual stress in composite structures, Paper presented at the SAMPE Conference, Seattle, WA. (2014).
- [152] Li X, Hallett SR, Wisnom MR, A finite element based statistical model for progressive tensile fibre failure in composite laminates, *Composites Part B: Engineering*. 45 (2013) 433-439.
- [153] Li X, Hallett SR, Wisnom MR, Numerical investigation of progressive damage and the effect of layup in overheight compact tension tests, *Composites Part A: Applied Science and Manufacturing*. 43 (2012) 2137-2150.
- [154] Li X, Hallett SR, Wisnom MR, Zobeiry N, Vaziri R, Poursartip A, Experimental study of damage propagation in Over-height Compact Tension tests, *Composites Part A: Applied Science and Manufacturing*. 40 (2009) 1891-1899.
- [155] Liu K, Tsai SW, A progressive quadratic failure criterion for a laminate, *Composites Sci.Technol*. 58 (1998) 1023-1032.
- [156] Llorca J, Gonzalez C, Molina-Aldareguia J, Segurado J, Seltzer R, Sket F, et al., Multiscale modeling of composite materials: A roadmap towards virtual testing, *Adv Mater*. 23 (2011) 5130-5147.
- [157] Lotter RE, Santare MH, Analysis of Mode I and Mode II interlaminar fracture specimens by a comparative finite element method, *Composites Science and Technology*. 40 (1991) 87-107.
- [158] LS-DYNA Keyword User's Manual, (2015).
- [159] Maa R, Cheng J, A CDM-based failure model for predicting strength of notched composite laminates, *Composites Part B: Engineering*. 33 (2002) 479-489.
- [160] Macedo FS, Pereira AB, de Moraes AB, Mixed Bending-Tension (MBT) test for mode I interlaminar and intralaminar fracture, *Composites Sci.Technol*. 72 (2012) 1049-1055.
- [161] Maimi P, Camanho PP, Mayugo JA, Davila CG, A continuum damage model for composite laminates: Part I - Constitutive model, *Mech.Mater*. 39 (2007) 897-908.
- [162] Maimi P, Camanho PP, Mayugo JA, Davila CG, A continuum damage model for composite laminates: Part II - Computational implementation and validation, *Mech.Mater*. 39 (2007) 909-919.
- [163] Martin R, Elms T, Bowron S, Characterization of mode II delamination using the 4ENF, *Proceedings of the 4th European conference on composites: testing and standardisation*, Lisbon (1998).

- [164] Martin E, Leguillon D, Energetic conditions for interfacial failure in the vicinity of a matrix crack in brittle matrix composites, *Int.J.Solids Structures*. 41 (2004) 6937-6948.
- [165] Martin RH, Interlaminar Fracture Characterization: A Current Review. NASA Contractor Report 18757 (1991).
- [166] Matzenmiller A, Lubliner J, Taylor RL, A constitutive model for anisotropic damage in fiber-composites, *Mech.Mater.* 20 (1995) 125-152.
- [167] McCartney LN, Energy-based prediction of progressive ply cracking and strength of general symmetric laminates using an homogenisation method, *Composites Part A: Applied Science and Manufacturing*. 36 (2005) 119-128.
- [168] McCartney LN, Prediction of ply crack formation and failure in laminates, *Composites Sci.Technol.* 62 (2002) 1619-1631.
- [169] McCartney LN, Predicting transverse crack formation in cross-ply laminates, *Composites Sci.Technol.* 58 (1998) 1069-1081.
- [170] McGregor CJ, Simulation of progressive damage development in braided composite tubes under axial compression, *Composites Part A: Applied Science and Manufacturing* 38 (2005) 2247-2259.
- [171] McGregor CJ, Vaziri R, Poursartip A, Xiao X, Simulation of progressive damage development in braided composite tubes under axial compression, *Composites Part A: Applied Science and Manufacturing*. 38 (2007) 2247-2259.
- [172] McGregor C, Vaziri R, Poursartip A, Xiao X, Axial crushing of triaxially braided composite tubes at quasi-static and dynamic rates, *Composite Structures*. 157 (2016) 197-206.
- [173] McGregor C, Vaziri R, Xiao X, Finite element modelling of the progressive crushing of braided composite tubes under axial impact, *Int.J.Impact Eng.* 37 (2010) 662-672.
- [174] McGregor C, Zobeiry N, Vaziri R, Poursartip A, A constitutive model for progressive compressive failure of composites, *J.Composite Mater.* 42 (2008) 2687-2716.
- [175] Mergheim J, Kuhl E, Steinmann P, A finite element method for the computational modelling of cohesive cracks, *Int J Numer Methods Eng.* 63 (2005) 276-289.
- [176] Moes N, Belytschko T, Extended finite element method for cohesive crack growth, *Eng.Fract.Mech.* 69 (2002) 813-833.
- [177] Moes N, Dolbow J, Belytschko T, Finite element method for crack growth without remeshing, *Int J Numer Methods Eng.* 46 (1999) 131-150.

- [178] Mollenhauer D, Ward L, Iarve E, Putthanasarat S, Hoos K, Hallett S, et al., Simulation of discrete damage in composite Overheight Compact Tension specimens, *Composites Part A: Applied Science and Manufacturing*. 43 (2012) 1667-1679.
- [179] Murakami S, Progress of continuum damage mechanics, *JSME international journal*. 30 (1987) 701-710.
- [180] Murri G, O'Brien T, Interlaminar GIIC evaluation of toughened-resin matrix composites using the end-notched flexure test. 26th Structures, Structural Dynamics, and Materials Conference, American Institute of Aeronautics and Astronautics, 1985.
- [181] Nahas M, Survey of Failure and Post-Failure Theories of Laminated Fiber-Reinforced Composites, *Journal of Composites, Technology and Research*, 8 (1986) 138-153.
- [182] Nguyen VP, Stroeve M, Sluys LJ, Multiscale failure modeling of concrete: Micromechanical modeling, discontinuous homogenization and parallel computations, *Comput.Methods Appl.Mech.Eng.* 201–204 (2012) 139-156.
- [183] Nikishkov Y, Makeev A, Seon G, Simulation of Damage in Composites Based on Solid Finite Elements, *Journal of the American Helicopter Society*. 55 (2010).
- [184] Noor AK, Kim YH, Peters JM, Transverse shear stresses and their sensitivity coefficients in multilayered composite panels, *AIAA J.* 32 (1994) 1259-1269.
- [185] O'Brien TK, Mixed-mode strain-energy-release rate effects on edge delamination of composites. effects of defects in composite materials, ASTM International, 1984.
- [186] O'Brien TK, Characterization of delamination onset and growth in a composite laminate, Basic Mechanisms, Accumulation, Tolerance, and Characterization. ASTM International, (1981).
- [187] O'Brien TK, Interlaminar fracture toughness: the long and winding road to standardization, *Composites Part B: Engineering*. 29 (1998) 57-62.
- [188] Ortiz M, A constitutive theory for the inelastic behavior of concrete, *Mechanics of Materials*. 4 (1985) 67-93.
- [189] Parhizgar S, Zachary L, Sun CT, Application of the principles of linear fracture mechanics to the composite materials, *Int.J.Fract.* 20 (1982) 3-15.
- [190] Paris F, Jackson KE, A study of failure criteria of fibrous composite materials, NASA/CR-2001-210661, (2001).
- [191] Parvizi A, Garrett KW, Bailey JE, Constrained cracking in glass fibre-reinforced epoxy cross-ply laminates, *J.Mater.Sci.* 13 (1978) 195-201.

- [192] Patzak B, Bittnar Z, Design of object oriented finite element code, *Adv.Eng.Software.* 32 (2001) 759-767.
- [193] Peerlings RHJ, de Borst R, Brekelmans WAM, Geers MGD, Localisation issues in local and nonlocal continuum approaches to fracture, *European Journal of Mechanics - A/Solids.* 21 (2002) 175-189.
- [194] Pijaudier-Cabot G, Bažant Z, Nonlocal Damage Theory, *J.Eng.Mech.* 113 (1987) 1512-1533.
- [195] Pinho ST, Dávila CG, Camanho PP, Iannucci L, Robinson P., Failure models and criteria for FRP under in-plane or three-dimensional stress states including shear non-linearity, NASA/TM-2005-213530 (2005).
- [196] Pinho ST, Iannucci L, Robinson P, Formulation and implementation of decohesion elements in an explicit finite element code, *Composites Part A: Applied Science and Manufacturing.* 37 (2006) 778-789.
- [197] Pinho ST, Iannucci L, Robinson P, Physically based failure models and criteria for laminated fibre-reinforced composites with emphasis on fibre kinking. Part II: FE implementation, *Composites Part A: Applied Science and Manufacturing.* 37 (2006) 766-777.
- [198] Pinho ST, Iannucci L, Robinson P, Physically-based failure models and criteria for laminated fibre-reinforced composites with emphasis on fibre kinking: Part I: Development, *Composites Part A: Applied Science and Manufacturing.* 37 (2006) 63-73.
- [199] Pinho ST, Robinson P, Iannucci L, Developing a four point bend specimen to measure the mode I intralaminar fracture toughness of unidirectional laminated composites, *Composites Sci.Technol.* 69 (2009) 1303-1309.
- [200] Pinho ST, Robinson P, Iannucci L, Fracture toughness of the tensile and compressive fibre failure modes in laminated composites, *Composites Sci.Technol.* 66 (2006) 2069-2079.
- [201] Pinho ST, Vyas GM, Robinson P, Response and damage propagation of polymer-matrix fibre-reinforced composites: Predictions for WWFE-III Part A, *J.Composite Mater.* 47 (2013) 2595-2612.
- [202] Pipes RB, Pagano N, Interlaminar stresses in composite laminates under uniform axial extension. *Mechanics of Composite Materials*, Springer, 1994, pp. 234-245.
- [203] Prabhakar P, Waas AM, A novel continuum-decohesive finite element for modeling in-plane fracture in fiber reinforced composites, *Composites Sci.Technol.* 83 (2013) 1-10.
- [204] Puck A, Schürmann H, Failure analysis of FRP laminates by means of physically based phenomenological models, *Composites Sci.Technol.* 62 (2002) 1633-1662.

- [205] Raghavan P, Li S, Ghosh S, Two scale response and damage modeling of composite materials, 40 (2004) 1619-1640.
- [206] Raju I, O'Brien T, Fracture mechanics concepts, stress fields, strain energy release rates, delamination initiation and growth criteria, Delamination behaviour of composites, Delamination behaviour of composites (2008) 3-27.
- [207] Reifsnider KL, Highsmith A, The relationship of stiffness changes in composite laminates to fracture-related damage mechanisms, In Fracture of Composite Materials, Springer Netherlands, (1982) 279-290.
- [208] Reiner J, Veidt M, Dargusch M, Gross L, A progressive analysis of matrix cracking-induced delamination in composite laminates using an advanced phantom node method, J.Composite Mater. 51 (2017) 2933-2947.
- [209] Rice J, The mechanics of earthquake rupture. , Division of Engineering, Brown University 1979.
- [210] Rice J, Sih GC, Plane problems of cracks in dissimilar media, Journal of Applied Mechanics. 32 (1965) 418-423.
- [211] Rice JR, A Path Independent Integral and the Approximate Analysis of Strain Concentration by Notches and Cracks, Journal of Applied Mechanics. 35 (1968) 379-386.
- [212] Rolfes R, Rohwer K, Ballerstaedt M, Efficient linear transverse normal stress analysis of layered composite plates, Comput.Struct. 68 (1998) 643-652.
- [213] Rybicki EF, Kanninen MF, A finite element calculation of stress intensity factors by a modified crack closure integral, Eng.Fract.Mech. 9 (1977) 931-938.
- [214] Salamon NJ, Interlaminar stressess in a layered composite laminate in bending, Fibre Science and Technology. 11 (1978) 305-317.
- [215] Schapery RA, A theory of mechanical behavior of elastic media with growing damage and other changes in structure, Journal of the Mechanics and Physics of Solids. 38 (1990) 215-253.
- [216] Schipperen JHA, An anisotropic damage model for the description of transverse matrix cracking in a graphite–epoxy laminate, Composite Structures. 53 (2001) 295-299.
- [217] Sebaey TA, Costa J, Maimí P, Batista Y, Blanco N, Mayugo JA, Measurement of the in situ transverse tensile strength of composite plies by means of the real time monitoring of microcracking, Composites Part B: Engineering. 65 (2014) 40-46.
- [218] Sela N, Ishai O, Interlaminar fracture toughness and toughening of laminated composite materials: a review, Composites. 20 (1989) 423-435.

- [219] Shahbazi M, Vaziri R, Zobeiry N, An efficient virtual testing framework to simulate the interacting effect of intra-laminar and inter-laminar damage progression in composite laminates, Proceedings of American Society for Composites 2016, Thirty-First Technical Conference, Virginia. (2016).
- [220] Shaw Ming Lee , A Comparison of Fracture Toughness of Matrix Controlled Failure Modes: Delamination and Transverse Cracking, Journal of Composite Materials. 20 (1986) 185-196.
- [221] Shor O, Vaziri R, Adaptive insertion of cohesive elements for simulation of delamination in laminated composite materials, Eng.Fract.Mech. 146 (2015) 121-138.
- [222] Simo JC, Ju JW, Strain- and stress-based continuum damage models—II. Computational aspects, Math.Comput.Model. 12 (1989) 378.
- [223] Simo JC, Ju JW, Strain- and stress-based continuum damage models—I. Formulation, Int.J.Solids Structures. 23 (1987) 821-840.
- [224] Singh CV, Talreja R, A synergistic damage mechanics approach for composite laminates with matrix cracks in multiple orientations, Mech.Mater. 41 (2009) 954-968.
- [225] Slepetz, J.M. and L. Carlson, Fracture of Composite Compact Tension Specimens, (1975).
- [226] Smilauer V, Hoover CG, Bazant ZP, Caner FC, Waas AM, Shahwan KW, Multiscale simulation of fracture of braided composites via repetitive unit cells, Eng.Fract.Mech. 78 (2011) 901-918.
- [227] Soden PD, Hinton MJ, Kaddour AS, Comparison of the predictive capabilities of current failure theories for composite laminates, Composites Sci.Technol. 58 (1998) 1225-1254.
- [228] Soden PD, Kaddour AS, Hinton MJ, Recommendations for designers and researchers resulting from the world-wide failure exercise, Composites Sci.Technol. 64 (2004) 589-604.
- [229] Song K, Li Y, Rose C, Continuum damage mechanics models for the analysis of progressive failure in open-hole tension laminates, 52nd AIAA/ASME/ASCE/AHS/ASC Structures, Structural Dynamics and Materials Conference, (2011) 1861.
- [230] Song J, Areias PMA, Belytschko T, A method for dynamic crack and shear band propagation with phantom nodes, Int J Numer Methods Eng. 67 (2006) 868-893.
- [231] Sorensen BF, Jacobsen TK, Large-scale bridging in composites: R-curves and bridging laws, Composites Part A: Applied Science and Manufacturing. 29 (1998) 1443-1451.
- [232] Stinchcomb WW, Ashbaugh NE, Composite materials: fatigue and fracture. , ASTM International 1993.

- [233] Sun CT, Tao J, Kaddour AS, The prediction of failure envelopes and stress/strain behavior of composite laminates: comparison with experimental results, *Composites Sci.Technol.* 62 (2002) 1673-1682.
- [234] Sun CT, Tao J, Prediction of failure envelopes and stress/strain behaviour of composite laminates1, *Composites Sci.Technol.* 58 (1998) 1125-1136.
- [235] Sun XC, Wisnom MR, Hallett SR, Interaction of inter- and intralaminar damage in scaled quasi-static indentation tests: Part 2 – Numerical simulation, *Composite Structures.* 136 (2016) 727-742.
- [236] Swindeman MJ, Iarve EV, Brockman RA, Mollenhauer DH, Hallett SR, Strength prediction in open hole composite laminates by using discrete damage modeling, *AIAA J.* 51 (2013) 936-945.
- [237] Talreja R, Damage development in composites: mechanisms and modelling, *J.Strain Anal.Eng.Des.* 24 (1989) 215-222.
- [238] Talreja R, Continuum Mechanics Characterization of Damage in Composite Materials, *Proc.R.Soc.Lond., Ser.A: Math.Phys.Sci.* 399 (1985) 195-216.
- [239] Tan SC, Nuismer RJ, A Theory for Progressive Matrix Cracking in Composite Laminates, *J.Composite Mater.* 23 (1989) 1029-1047.
- [240] Tong L, An Assessment of Failure Criteria to Predict the Strength of Adhesively Bonded Composite Double Lap Joints, *Journal of Reinforced Plastics and Composites.* 16 (1997) 698-713.
- [241] Truss RW, Hine PJ, Duckett RA, Interlaminar and intralaminar fracture toughness of uniaxial continuous and discontinuous carbon fibre/epoxy composites, *Composites Part A: Applied Science and Manufacturing.* 28 (1997) 627-636.
- [242] Tsai SW, Wu EM, A General Theory of Strength for Anisotropic Materials, *Journal of Composite Materials.* 5 (1971) 58-80.
- [243] Turon A, Camanho PP, Costa J, Dávila CG, A damage model for the simulation of delamination in advanced composites under variable-mode loading, *Mech.Mater.* 38 (2006) 1072-1089.
- [244] Turon A, Camanho PP, Costa J, Renart J, Accurate simulation of delamination growth under mixed-mode loading using cohesive elements: Definition of interlaminar strengths and elastic stiffness, *Composite Structures.* 92 (2010) 1857-1864.
- [245] Turon A, Dávila CG, Camanho PP, Costa J, An engineering solution for mesh size effects in the simulation of delamination using cohesive zone models, *Eng.Fract.Mech.* 74 (2007) 1665-1682.

- [246] Turon A, Costa J, Camanho PP, Maima P, Analytical and numerical investigation of the length of the cohesive zone in delaminated composite materials. In: Camanho PP, Davila CG, Pinho ST, Remmers JJC (Eds.), *Mechanical Response of Composites*, Springer Netherlands, Dordrecht, 2008, pp. 77-97.
- [247] Tvergaard V, Hutchinson JW, Effect of strain-dependent cohesive zone model on predictions of crack growth resistance, *International Journal of Solids and Structures*. 33 (1996) 3297-3308.
- [248] Vaidya RS, Sun CT, Fracture criterion for notched thin composite laminates, *AIAA J*. 35 (1997) 311-316.
- [249] Van Der Meer FP, Dávila CG, Cohesive modeling of transverse cracking in laminates under in-plane loading with a single layer of elements per ply, *Int.J.Solids Structures*. 50 (2013) 3308-3318.
- [250] Van Der Meer FP, Moes N, Sluys LJ, A level set model for delamination - Modeling crack growth without cohesive zone or stress singularity, *Eng.Fract.Mech*. 79 (2012) 191-212.
- [251] Van Der Meer FP, Sluys LJ, Continuum models for the analysis of progressive failure in composite laminates, *Journal of Composite Materials*. (2009).
- [252] Van Der Meer FP, Sluys LJ, A phantom node formulation with mixed mode cohesive law for splitting in laminates, *International Journal of Fracture*, 158 (2009) 107-124.
- [253] Van Der Meer FP, Sluys LJ, Hallett SR, Wisnom MR, Computational modeling of complex failure mechanisms in laminates, *J.Composite Mater*. 46 (2012) 603-623.
- [254] Van Paepegem W, De Baere I, Degrieck J, Modelling the nonlinear shear stress-strain response of glass fibre-reinforced composites. Part I: Experimental results, *Composites Sci.Technol*. 66 (2006) 1455-1464.
- [255] Van Paepegem W, De Baere I, Degrieck J, Modelling the nonlinear shear stress-strain response of glass fibre-reinforced composites. Part II: Model development and finite element simulations, *Composites Sci.Technol*. 66 (2006) 1465-1478.
- [256] Vogler M, Rolfes R, Camanho PP, Modeling the inelastic deformation and fracture of polymer composites – Part I: Plasticity model, *Mech.Mater*. 59 (2013) 50-64.
- [257] Voyiadjis GZ, Deliktas B, Aifantis EC, Multiscale analysis of multiple damage mechanisms coupled with inelastic behavior of composite materials, *J.Eng.Mech*. 127 (2001) 636-645.
- [258] Voyiadjis GZ, Deliktas B, A coupled anisotropic damage model for the inelastic response of composite materials, *Comput.Methods Appl.Mech.Eng*. 183 (2000) 159-199.

- [259] Wang S, Choi I, The interface crack between dissimilar anisotropic composite materials, *Journal of applied mechanics*. 50 (1983) 169-178.
- [260] Wang A, Fracture mechanics of sublaminar cracks in composite materials, *Journal of Composites, Technology and Research*. 6 (1984) 45-62.
- [261] Weibull W, A Statistical Distribution Function of Wide Availability, *Journal of Applied Mechanics*. 18 (1951) 293-297.
- [262] Wells GN, De Borst R, Sluys LJ, A consistent geometrically non-linear approach for delamination, *Int J Numer Methods Eng*. 54 (2002) 1333-1355.
- [263] Wells GN, Sluys LJ, A new method for modelling cohesive cracks using finite elements, *Int J Numer Methods Eng*. 50 (2001) 2667-2682.
- [264] Whitcomb JD., Analysis of instability-related growth of a through-width delamination, NASA TM-86301 (1984).
- [265] Whitney JM, Nuismer RJ, Stress Fracture Criteria for Laminated Composites Containing Stress Concentrations, *Journal of Composite Materials*. 8 (1974) 253-265.
- [266] Williams K, Vaziri R, Finite Element Analysis of the Impact Response of CFRP Composite Plates, Tenth International Conference on Composite Materials (ICCM/10) (1995).
- [267] Williams KV, Vaziri R, Poursartip A, A physically based continuum damage mechanics model for thin laminated composite structures, *Int J Solids Struct*. 40 (2003) 2267-300.
- [268] Williams KV, Vaziri R, Application of a damage mechanics model for predicting the impact response of composite materials, *Computers and Structures*. 79 (2001) 997-1011.
- [269] Wolfe WE, Butalia TS, A strain-energy based failure criterion for non-linear analysis of composite laminates subjected to biaxial loading, *Composites Sci.Technol*. 58 (1998) 1107-1124.
- [270] Wu EM, Strength and fracture of fiber-reinforced composites, In *Fracture and Fatigue*, ed. L. J. Broutman. Academic Press, New York. (1974).
- [271] Wu L, Noels L, Adam L, Doghri I, A multiscale mean-field homogenization method for fiber-reinforced composites with gradient-enhanced damage models, *Comput.Methods Appl.Mech.Eng*. 233-236 (2012) 164-179.
- [272] Wu L, Noels L, Adam L, Doghri I, Non-local multiscale analyses of composite laminates based on a damage-enhanced mean-field homogenization formulation, 17th International Conference on Composite Structures (ICCS/17), (2013).

- [273] Xia Z, Chen Y, Ellyin F, Meso/micro-mechanical model for damage progression in glass-fiber/epoxy cross-ply laminates by finite-element analysis, *Composites Sci.Technol.* 60 (2000) 1171-1179.
- [274] Xie D, Salvi AG, Sun C, Waas AM, Caliskan A, Discrete cohesive zone model to simulate static fracture in 2D triaxially braided carbon fiber composites, *J.Composite Mater.* 40 (2006) 2025-2046.
- [275] Xie D, Waas AM, Discrete cohesive zone model for mixed-mode fracture using finite element analysis, *Eng.Fract.Mech.* 73 (2006) 1783-1796.
- [276] Yang Q, Cox B, Cohesive models for damage evolution in laminated composites, *Int.J.Fract.* 133 (2005) 107-137.
- [277] Young W. Kwon, David H. Allen, Ramesh Talreja, Multiscale modeling for damage analysis Multiscale modeling and simulation of composite materials and structures, Vol. 47. New York: Springer US (2008).
- [278] Zhang J, Fan J, Soutis C, Analysis of multiple matrix cracking in $[\pm\theta m/90n]_s$ composite laminates. Part 1: In-plane stiffness properties, *Composites.* 23 (1992) 291-298.
- [279] Zhang J, Fan J, Soutis C, Analysis of multiple matrix cracking in $[\pm\theta m/90n]_s$ composite laminates. Part 2: Development of transverse ply cracks, *Composites.* 23 (1992) 299-304.
- [280] Zhang X, Impact damage in composite aircraft structures-experimental testing and numerical simulation, *Proceedings of the Institution of Mechanical Engineers, Part G: Journal of Aerospace Engineering.* 212 (1998) 245-259.
- [281] Zhang Y, Xia Z, Ellyin F, Viscoelastic and damage analyses of fibrous polymer laminates by micro/meso-mechanical modeling, *J.Composite Mater.* 39 (2005) 2001-2022.
- [282] Zinoviev PA, Grigoriev SV, Lebedeva OV, Tairova LP, The strength of multilayered composites under a plane-stress state, *Composites Sci.Technol.* 58 (1998) 1209-1223.
- [283] Zinoviev PA, Lebedeva OV, Tairova LP, A coupled analysis of experimental and theoretical results on the deformation and failure of composite laminates under a state of plane stress, *Composites Sci.Technol.* 62 (2002) 1711-1723.
- [284] Zobeiry N, Poursartip A, 3 - The origins of residual stress and its evaluation in composite materials: *Structural Integrity and Durability of Advanced Composites*, Woodhead Publishing. (2015) 43-72.
- [285] Zobeiry N, Vaziri R, Poursartip A, Characterization of strain-softening behaviour and failure mechanisms of composites under tension and compression, *Composites Part A: Applied Science and Manufacturing.* 68 (2015) 29-41.

- [286] Zobeiry N, Extracting the strain softening response of composites using full-field displacement measurement, PhD Thesis, The University of British Columbia. (2010).
- [287] Zobeiry N, Progressive damage modeling of composite materials under compressive loads, M.A.Sc. Thesis, Department of Civil Engineering, The University of British Columbia, Vancouver, BC, Canada. (2004).
- [288] Zobeiry N, Forghani A, Li C, Gordnian K, Thorpe R, Vaziri R, et al., Multiscale characterization and representation of composite materials during processing, *Philos. Trans. A. Math. Phys. Eng. Sci.* 374 (2016) 20150278.
- [289] Zobeiry N, Forghani A, McGregor C, McClennan S, Vaziri R, Poursartip A, Effective calibration and validation of a nonlocal continuum damage model for laminated composites, *Composite Structures.* 173 (2017) 188-195.
- [290] Zobeiry N, Vaziri R, Poursartip A, Characterization of strain-softening behavior and failure mechanisms of composites under tension and compression, *Composites Part A: Applied Science and Manufacturing.* 68 (2015) 29-41.

Appendices

Appendix A - Derivation of IDEFs in shear lag theory

This section summarizes the process of deriving the formulation for the in-situ damage effective functions (IDEF) $\Lambda_{ij}^{(2)}$ for a constrained cracked ply in the shear lag theory used in Section 3.3.2.1. $\Lambda_{ij}^{(2)}$ indicate the stiffness loss caused by the in-situ damage state of the cracked ply under the constraint conditions.

Considering Figure 3.6, let us assume that $\tilde{\sigma}_{ij}^{(2)}$ and $\tilde{\varepsilon}_{ij}^{(2)}$ are the averaged in-plane microscopic stresses and strains in the cracked layer (Layer 2) averaged across the thickness of the layer to ignore the minor effects of the variation of in-plane displacements and strains inside the layer. The in-plane microstresses $\tilde{\sigma}_{ij}^{(2)}$ are determined with a 2-D shear lag theory. For this purpose, the equilibrium equations in terms of micro-stresses $\tilde{\sigma}_{ij}^{(2)}$ for the cracked layer are expressed as

$$\frac{d\tilde{\sigma}_{j2}^{(2)}}{dx_2} - \frac{\tau_j}{h_2} = 0, \quad j=1,2 \quad (\text{A.1})$$

where τ_j are the interface stresses. Based on the shear lag theory, in absence of delamination, the deformation transformation between the cracked layer and the surrounding constrained layers is through the interface stresses. With the assumption of a linear distribution of the out-of-plane shear stresses along the x_3 -axis with zero condition at the middle plane ($x_3=0$) and top plane ($x_3 = h$) will give:

$$\begin{aligned} \sigma_{j3}^{(2)} &= \frac{\tau_j}{h^{(2)}} x_3, \quad 0 \leq |x_3| \leq h^{(2)}, \quad j=1,2, \\ \sigma_{j3}^{(1)} &= \frac{\tau_j}{h^{(1)}} (h - x_3), \quad h^{(2)} \leq |x_3| \leq h, \quad j=1,2 \end{aligned} \quad (\text{A.2})$$

with $h = h^{(1)} + h^{(2)}$.

Upon writing the out-of-plane constitutive equations in terms of the in-plane displacements, substituting them into Equation (A.2) and integrating with respect to x_3 , yields:

$$\tau_j = K_{j1} (\tilde{u}_1^{(2)} - \tilde{u}_1^{(1)}) + K_{j2} (\tilde{u}_2^{(2)} - \tilde{u}_2^{(1)}) \quad (\text{A.3})$$

where the interface shear stresses τ_j are expressed in terms of the in-plane displacements $\tilde{u}_i^{(1)}$ ($i=1,2$) and $\tilde{u}_i^{(2)}$ ($i=1,2$), averaged across the thickness of the layers, with:

$$\begin{bmatrix} K_{11} & K_{12} \\ K_{12} & K_{22} \end{bmatrix} = \left(\frac{h_1}{3} \begin{bmatrix} \hat{Q}_{55}^{(1)} & \hat{Q}_{45}^{(1)} \\ \hat{Q}_{45}^{(1)} & \hat{Q}_{44}^{(1)} \end{bmatrix}^{-1} + \frac{h_2}{3} \begin{bmatrix} \hat{Q}_{55}^{(2)} & \hat{Q}_{45}^{(2)} \\ \hat{Q}_{45}^{(2)} & \hat{Q}_{44}^{(2)} \end{bmatrix}^{-1} \right)^{-1} \quad (\text{A.4})$$

where $(\hat{Q}_{44}^{(1)}, \hat{Q}_{45}^{(1)}, \hat{Q}_{55}^{(1)})$ and $(\hat{Q}_{44}^{(2)}, \hat{Q}_{45}^{(2)}, \hat{Q}_{55}^{(2)})$ are out-of-plane shear moduli in the constraining layers and the cracked layer.

Substitution of Equation (A.3) into Equation (A.2) and subsequent differentiation of Equation (A.2) with respect to x_2 lead to the equilibrium equations in terms of in-plane micro-stresses and micro-strains:

$$\begin{aligned} \frac{d^2 \tilde{\sigma}_{12}^{(2)}}{dx_2^2} + K_{11} (\tilde{\gamma}_{12}^{(1)} - \tilde{\gamma}_{12}^{(2)}) + K_{12} (\tilde{\varepsilon}_{22}^{(1)} - \tilde{\varepsilon}_{22}^{(2)}) &= 0, \quad j=1,2 \\ \frac{d^2 \tilde{\sigma}_{22}^{(2)}}{dx_2^2} + K_{21} (\tilde{\gamma}_{12}^{(1)} - \tilde{\gamma}_{12}^{(2)}) + K_{22} (\tilde{\varepsilon}_{22}^{(1)} - \tilde{\varepsilon}_{22}^{(2)}) &= 0, \quad j=1,2 \end{aligned} \quad (\text{A.5})$$

In the above equations the micro-strains will be excluded using the constitutive equations for both layers:

$$\begin{cases} \tilde{\sigma}_{11}^{(1)} \\ \tilde{\sigma}_{22}^{(1)} \\ \tilde{\sigma}_{12}^{(1)} \end{cases} = \begin{bmatrix} \hat{Q}_{11}^{(1)} & \hat{Q}_{12}^{(1)} & \hat{Q}_{16}^{(1)} \\ \hat{Q}_{12}^{(1)} & \hat{Q}_{22}^{(1)} & \hat{Q}_{26}^{(1)} \\ \hat{Q}_{16}^{(1)} & \hat{Q}_{26}^{(1)} & \hat{Q}_{66}^{(1)} \end{bmatrix} \begin{cases} \tilde{\varepsilon}_{11}^{(1)} \\ \tilde{\varepsilon}_{22}^{(1)} \\ \tilde{\gamma}_{12}^{(1)} \end{cases} \quad (A.6)$$

$$\begin{cases} \tilde{\sigma}_{11}^{(2)} \\ \tilde{\sigma}_{22}^{(2)} \\ \tilde{\sigma}_{12}^{(2)} \end{cases} = \begin{bmatrix} \hat{Q}_{11}^{(2)} & \hat{Q}_{12}^{(2)} & 0 \\ \hat{Q}_{12}^{(2)} & \hat{Q}_{22}^{(2)} & 0 \\ 0 & 0 & \hat{Q}_{66}^{(2)} \end{bmatrix} \begin{cases} \tilde{\varepsilon}_{11}^{(2)} \\ \tilde{\varepsilon}_{22}^{(2)} \\ \tilde{\gamma}_{12}^{(2)} \end{cases}$$

as well as the equations of global equilibrium of the laminate:

$$h_1 \begin{cases} \tilde{\sigma}_{11}^{(1)} \\ \tilde{\sigma}_{22}^{(1)} \\ \tilde{\sigma}_{12}^{(1)} \end{cases} + h_2 \begin{cases} \tilde{\sigma}_{11}^{(2)} \\ \tilde{\sigma}_{22}^{(2)} \\ \tilde{\sigma}_{12}^{(2)} \end{cases} = (h_1 + h_2) \begin{cases} \bar{\sigma}_{xx} \cos^2 \theta + 2\bar{\sigma}_{xy} \sin \theta \cos \theta \\ \bar{\sigma}_{xx} \sin^2 \theta - 2\bar{\sigma}_{xy} \sin \theta \cos \theta \\ -\bar{\sigma}_{xx} \sin \theta \cos \theta + \bar{\sigma}_{xy} (\cos^2 \theta - \sin^2 \theta) \end{cases} \quad (A.7)$$

In the above equation, $\bar{\sigma}_{xx}$ and $\bar{\sigma}_{xy}$ are the applied stresses as shown in Figure 3.6. Using the generalized plane strain condition $\tilde{\varepsilon}_{11}^{(1)} = \tilde{\varepsilon}_{11}^{(2)}$ and combination of the Equations (A.7) and (A.6), the stresses in the constraining layers (i.e. Layer 1) can be excluded from (A.5) and a coupled second order non-homogeneous system of equations in terms of $\tilde{\sigma}_{12}^{(2)}$ and $\tilde{\sigma}_{22}^{(2)}$ will be obtained.

The solution to such equation for the case of $\theta = 90^\circ$ for the cracked layer leads to:

$$\tilde{\sigma}_{22}^{(2)} = \frac{\Omega_{22}}{L_1} \left[1 - \frac{\cosh(\sqrt{L_1} x_2)}{\cosh(\sqrt{L_1} s)} \right] \bar{\sigma}_x \quad (A.8)$$

$$\tilde{\sigma}_{12}^{(2)} = \frac{\Omega_{12}}{L_2} \left[1 - \frac{\cosh(\sqrt{L_2} x_2)}{\cosh(\sqrt{L_2} s)} \right] \bar{\sigma}_{xy}$$

where

$$L_1 = \frac{K_2}{h_1} \left[\hat{S}_{22}^{(1)} + a_1 \hat{S}_{12}^{(1)} + \chi \left(\hat{S}_{22}^{(2)} + a_1 \hat{S}_{12}^{(2)} \right) \right] \quad (A.9)$$

$$L_2 = \frac{K_1}{h_1} \left[\hat{S}_{66}^{(1)} + \chi \hat{S}_{66}^{(2)} \right]$$

$$\Omega_{22} = \frac{K_2}{h_1} (1 + \chi) (\hat{S}_{22}^{(1)} + a_1 \hat{S}_{12}^{(1)})$$

$$\Omega_{12} = \frac{K_1}{h_1} (1 + \chi) \hat{S}_{66}^{(1)}$$

$$a_1 = - \frac{(\hat{S}_{12}^{(1)} + \chi \hat{S}_{12}^{(2)})}{(\hat{S}_{11}^{(1)} + \chi \hat{S}_{11}^{(2)})}$$

The in-plane micro-stresses in the cracked layer, $\tilde{\sigma}_{ij}^{(2)}$, can be used to evaluate the reduction of the laminate stiffness properties. Instead of a damaged laminate, one considers an equivalent laminate, in which the damaged ply is replaced with an equivalent homogeneous layer with degraded stiffness properties. The constitutive equation of the ‘equivalent layer’ is:

$$\bar{\boldsymbol{\sigma}}^{(2)} = \bar{\mathbf{Q}}^{(2)} \bar{\boldsymbol{\epsilon}}^{(2)} \quad (\text{A.10})$$

where the lamina macro-stresses $\bar{\boldsymbol{\sigma}}^{(2)}$ are obtained by averaging the micro-stresses $\tilde{\sigma}_{ij}^{(2)}$ in Equation (A.8) cross the length of the representative cracked segment:

$$\begin{aligned} \bar{\sigma}_{22}^{(2)} &= \frac{1}{2s} \int_{-s}^s \tilde{\sigma}_{22}^{(2)} dx_2 \\ \bar{\sigma}_{12}^{(2)} &= \frac{1}{2s} \int_{-s}^s \tilde{\sigma}_{12}^{(2)} dx_2 \end{aligned} \quad (\text{A.11})$$

The in-plane stiffness of the equivalent homogeneous layer in the local co-ordinate system, $\bar{\mathbf{Q}}^{(2)}$, is related to the in-plane stiffness matrix of the undamaged material, $\hat{\mathbf{Q}}^{(2)}$, via the in-situ damage effective functions (IDEFs) as stated earlier in Equation (3.27).

Substituting Equation (3.27) into the constitutive equations for the ‘equivalent’ layer, Equation (A.10), gives the IDEFs, $\Lambda_{22}^{(2)}$ and $\Lambda_{66}^{(2)}$ in terms of the lamina macro-stresses $\bar{\boldsymbol{\sigma}}^{(2)}$ and macro-strains $\bar{\boldsymbol{\epsilon}}^{(2)}$.

$$\Lambda_{22}^{(2)} = 1 - \frac{\bar{\sigma}_{22}^{(2)}}{\hat{Q}_{12}^{(2)} \bar{\varepsilon}_{11}^{(2)} + \hat{Q}_{22}^{(2)} \bar{\varepsilon}_{22}^{(2)}}, \quad \Lambda_{66}^{(2)} = 1 - \frac{\bar{\sigma}_{12}^{(2)}}{\hat{Q}_{66}^{(2)} \bar{\gamma}_{12}^{(2)}} \quad (\text{A.12})$$

The macro-strains in the equivalent layer $\bar{\boldsymbol{\varepsilon}}^{(2)}$ in Equation (A.12) are calculated from the combination of constitutive equations and equations of global equilibrium for the laminate assuming that $\bar{\boldsymbol{\varepsilon}}^{(2)} = \bar{\boldsymbol{\varepsilon}}^{(1)}$. Therefore, Equation (A.12) can be simplified by substituting for $\bar{\sigma}_{22}^{(2)}$, $\bar{\sigma}_{12}^{(2)}$, $\bar{\varepsilon}_{11}^{(2)}$, $\bar{\varepsilon}_{22}^{(2)}$ and $\bar{\gamma}_{12}^{(2)}$ such that we will have:

$$\Lambda_{22}^{(2)} = 1 - \frac{1 - \frac{D}{\lambda_1} \tanh\left(\frac{\lambda_1}{D}\right)}{1 + \beta_1 \frac{D}{\lambda_1} \tanh\left(\frac{\lambda_1}{D}\right)} \quad (\text{A.13})$$

$$\Lambda_{66}^{(2)} = 1 - \frac{1 - \frac{D}{\lambda_2} \tanh\left(\frac{\lambda_2}{D}\right)}{1 + \beta_1 \frac{D}{\lambda_2} \tanh\left(\frac{\lambda_2}{D}\right)}$$

with

$$\lambda_1 = h_2 \sqrt{L_1}, \quad \lambda_2 = h_2 \sqrt{L_2}$$

$$\beta_1 = \frac{1}{\chi} \left[\hat{Q}_{22}^{(2)} \left(\hat{S}_{22}^{(1)} + a_1 \hat{S}_{12}^{(1)} \right) + \hat{Q}_{12}^{(2)} \left(\hat{S}_{12}^{(1)} + a_1 \hat{S}_{11}^{(1)} \right) \right] \quad (\text{A.14})$$

$$\beta_2 = \frac{1}{\chi} \hat{Q}_{66}^{(2)} \hat{S}_{66}^{(1)}$$

Once the in-plane stiffness matrix of the cracked ply $\bar{\mathbf{Q}}^{(2)}$ in the local coordinate system $x_1 x_2 x_3$ is determined using Equations (3.27) for any crack density value, it can be transformed to the global coordinate system xyz using standard tensor transformation functions (see Figure 3.8).

Appendix B - Correlation of intra-laminar fracture energy with input fracture energy density and non-local radius

As mentioned in Section 3.3.1.2, in the mesoscopic application of the non-local CODAM2 model, the potential discrete matrix cracks have to be captured in a continuum sense. Therefore, the non-local radius, r , used for averaging should be small enough to capture a narrow width of damage that is representative of the matrix cracks running parallel to the fibre direction. Thus, the value of r is limited to two times the finite element size to ensure that there is more than one element within the averaging zone and also to prevent an excessively large width for discrete cracks.

Once the radius of non-local averaging, r , and the experimental intra-laminar fracture energy values are known, the required inputs for the material model are the fracture energy density values from which the saturation strain of each damage mode is automatically calculated by the material model with the use of Equations (3.23) and (3.24). The focus of this section is to establish the relationship between the experimental fracture energy and the material model input fracture energy density when the non-local CODAM2 is used in a mesoscopic context. Here, we first show this for intra-laminar matrix fracture energy and the same process will be repeated for fibre fracture energy.

As discussed in Section 3.3.1.2, the value of input matrix fracture energy density, g_2^f , is related to the intra-laminar matrix fracture energy, G_2^f , through an effective length scale, h_2^c , such that $g_2^f = G_2^f / h_2^c$. Here, a numerical case study is performed to obtain the value of h_2^c and its dependence on the size of element and the radius of averaging. Unidirectional 90° laminate in an OCT configuration is modelled as shown in Figure B.1 (a) with the fibres parallel to the direction of the initial notch. Two mesh configurations shown in Figure B.1 (b) are used for the analysis in LS-DYNA, one with element size $l_e = 0.5$ mm close to the notch and the other with $l_e = 0.25$ mm. The mesh is generated with thick shell elements with reduced integration formulation which means that each element has only one in-plane integration point. The material system used here is IM7/8552 CFRP and the input elastic moduli, tensile and shear strength properties are given in

Table B-1. The matrix fracture energy density is considered to be constant and equal to $g_2^f = 4N / mm^2$ for both mesh configurations. Note that this is an arbitrary value and is used here to numerically obtain the relation between G_2^f and g_2^f .

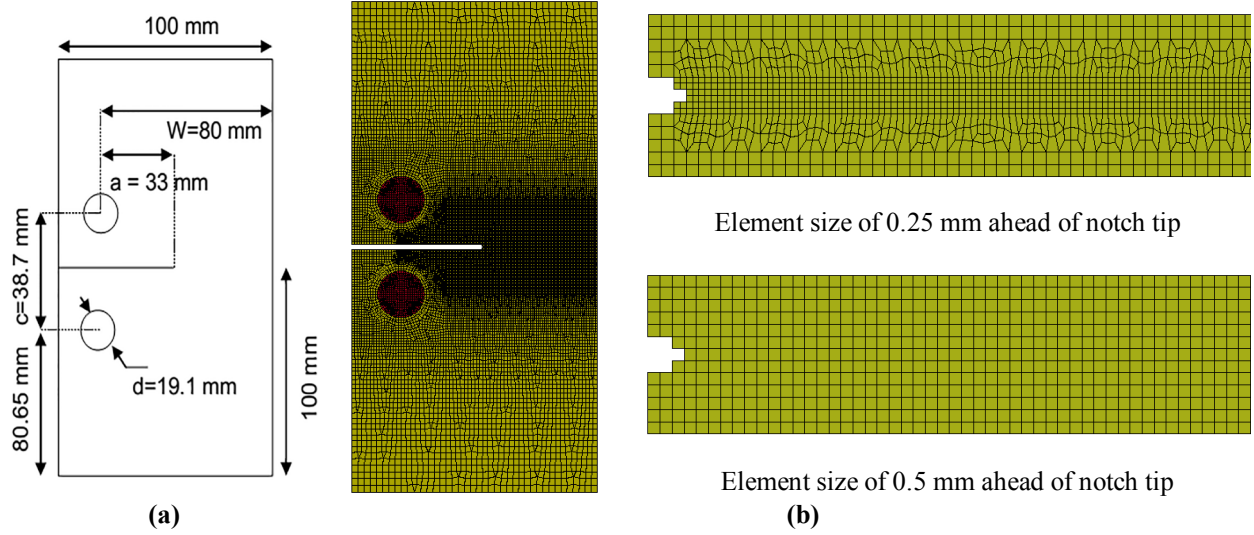


Figure B. 1: (a) OCT specimen geometry and (b) the FE mesh with element size 0.25mm and 0.5mm ahead of notch tip

Table B-1: The material properties of IM7/8552 carbon-epoxy unidirectional lamina [121]

Material	E_1	E_2	$^{(a)} G_{12}^0$	X_T	Y_T	S_L
IM7/8552	165(GPa)	9(GPa)	5.1(GPa)	2560(MPa)	73(MPa)	90(MPa)

(a) The nonlinear shear stress-strain curve is provided in [121]

The specimen is simulated under tensile loading for different values of non-local averaging radius, r , for each element size. For $l_e = 0.25$ mm, the values $r = 0.5, 0.75$ and 1.0 mm and for $l_e = 0.5$ mm, the values $r = 1.0, 1.5$ and 2.0 mm are selected such that for each case 2, 3 and 4 number of neighbor integration points will be present inside the averaging domain (circle) in the direction of crack path.

The predicted fracture energy for each case is calculated based on its definition, that is:

$$G_2^f = \frac{(\Delta W - \Delta U)}{t\Delta a} \quad (\text{B.1})$$

where ΔW is the external work done and ΔU is the change in the strain energy of the system when the crack length advances by an amount Δa and t is the thickness of the laminate. The difference between ΔW and ΔU is equivalent to the shaded area under the load-displacement curve of the specimen shown in Figure B.2.

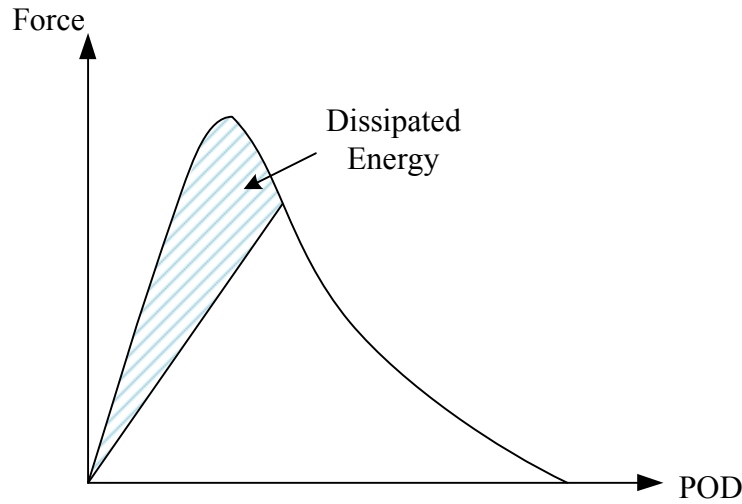


Figure B. 2: Dissipated energy calculated from the area below the load vs. pin-opening displacement (POD) curve

For each numerical case mentioned above, Table B-2 provides the number of integration points, N , inside the averaging domain in the direction of crack path (i.e. $(2r/l_e - 1)$), the predicted fracture energy G_2^f calculated from the force-displacement results using Equation (B.1), and the effective length scale $h_2^c = G_2^f / g_2^f$ where g_2^f is the input fracture energy density (i.e. 4 N/mm^2).

Table B-2: The predicted intra-laminar matrix fracture energy from the simulations of a unidirectional 90° OCT laminate for a given input fracture energy density of 4 N/mm², different non-local radii and element sizes. The effective length scale and its ratio to r are also presented.

l_e (mm)	r (mm)	$N = 2r / l_e - 1$	G_2^f	h_2^c	$\frac{h_2^c}{r}$
0.25	0.50	3	2.6	0.65	1.3
0.25	0.75	5	4.0	1.00	1.3
0.25	1.00	7	4.8	1.20	1.2
0.50	1.00	3	2.6	0.65	0.65
0.50	1.50	5	4.0	1.00	0.67
0.50	2.00	7	5.0	1.25	0.63

It can be seen that as long as the number of integration points within the circle domain of averaging is the same, the length scale, h_2^c , is a constant. Based on these results, for a constant element size, the effective length scale h_2^c is approximately a constant factor of the radius of averaging regardless of the selected value for r (i.e. $1.3r$ for $l_e = 0.25$ mm and $0.65r$ for $l_e = 0.5$ mm). The scale factor for a 0.25mm mesh is two times as large as the one for 0.5 mm mesh size. This model provides a benchmark for finding the relationship between g_2^f and G_2^f for a known mesh size, radius of averaging and fracture energy.

The length scale h_1^c which relates the fracture energy density of fibre to the fibre fracture energy can also be found using the same model setup as that shown in Figure B.2 using a unidirectional 0° lamina. However, the dominant damage mode for a unidirectional 0° lamina in an OCT configuration is the split that grows parallel with fibre direction. Therefore, the transverse tensile strength and in-plane shear strength properties were set to large values in order to prevent any matrix damage to initiate. This will allow the fibre damage mode to occur and be a dominant damage mode. The input value for the fibre fracture energy density in the material model was assumed to be 230 N/mm². The specimen was simulated under tensile loading for different values of non-local averaging radius, r , for each element size. For $l_e = 0.25$ mm, the values $r = 0.5$ and 0.75 mm and for $l_e = 0.5$ mm, the values $r = 1.0$ and 1.5 mm were selected such that for each case 2 or 3 neighbor integration points is located inside the averaging domain (circle) in the direction of crack path. Again, it can be seen that as long as the number of integration points

within the selected domain of averaging is the same, the length scale of h_1^c is constant. In general, h_1^c for fibre fracture energy is slightly larger than h_2^c for matrix fracture energy.

Table B-3: The predicted fibre fracture energy from the simulations of a unidirectional 0° OCT laminate for a given input fracture energy density of 230 N/mm², different non-local radii and element sizes. The effective length scale and its ratio to r are also presented.

l_e (mm)	r (mm)	$N = 2r / l_e - 1$	G_1^f	h_1^c	$\frac{h_1^c}{r}$
0.25	0.50	3	197.8	0.86	1.72
0.25	0.75	5	303.6	1.32	1.76
0.50	1.00	3	197.8	0.86	0.86
0.50	1.50	5	303.6	1.32	0.88

Appendix C - General introduction to user defined features in LS-DYNA

Before laying out the pseudo code for the CODAM2 user material, a short introduction on general layout of a user material model in LS-DYNA is explained here. LS-DYNA provides user-defined interfaces, i.e. the source code which is partly open for customized modifications.

Several user interfaces for the implementation of numerical models or algorithms exist. To be able to modify and incorporate these source codes into the standard LS-DYNA models, a so-called “usermat package” is needed, which is available via local LS-DYNA distributors.

In general, this package is a compressed archive which contains several files such as library files (*.a), object files (*.o), include files (*.inc), Fortran files (*.f) and a Makefile. Most important files for the user are the Fortran files `dyn21.f` and `dyn21b.f`, as well as the Makefile. The last one specifies how to derive the target program, in this case the LS-DYNA executable. It also gives information about the specific Fortran compiler that should be used. If this compiler is installed, then the make command will start compiling the Fortran files and creating a binary executable. This executable can then be operated in the same way as a standard version of LS-DYNA. The next step is to implement the algorithms for materials, elements, or other features into the user subroutines of Fortran files `dyn21.f` and/or `dyn21b.f`. Every time a change is made inside the Fortran files, the files have to be recompiled to update the executable.

All subroutines for the user defined features in LS-DYNA are collected in the files `dyn21.f` and `dyn21b.f` and are ready for editing using any text editor. Mechanical user materials are defined in `dyn21.f`, while user defined elements and cohesive user materials are in `dyn21b.f`, just to give a few examples. The prevailing programming language is Fortran 77.

With the help of the keyword `*MAT_USER_DEFINED_MATERIAL_MODELS` in the input file, one can define the input for the user material interface. If this keyword is used, the main program calls subroutine `usrmat` in `dyn21.f`, and from there, different subroutines are called depending on the element type in use: `urmathn` for solid elements, `urmat2s` for 2D plane stress and 3D shell elements, `urmatb` for beam elements, `urmatd` for discrete elements and `urmatf` for truss beam elements. Those subroutines in turn contain the calls to the user material

subroutines `umatXX`, where it is the objective to compute stresses from strains (see Figure C.1). The letters `XX` stands for a number between 41 and 50 and matches the parameter `MT` specified in the material card `*MAT_USER_DEFINED_MATERIAL_MODELS`. Therefore, up to ten user material subroutines can be implemented simultaneously to update the stresses in solids, shells, beams, discrete beams and truss beams.

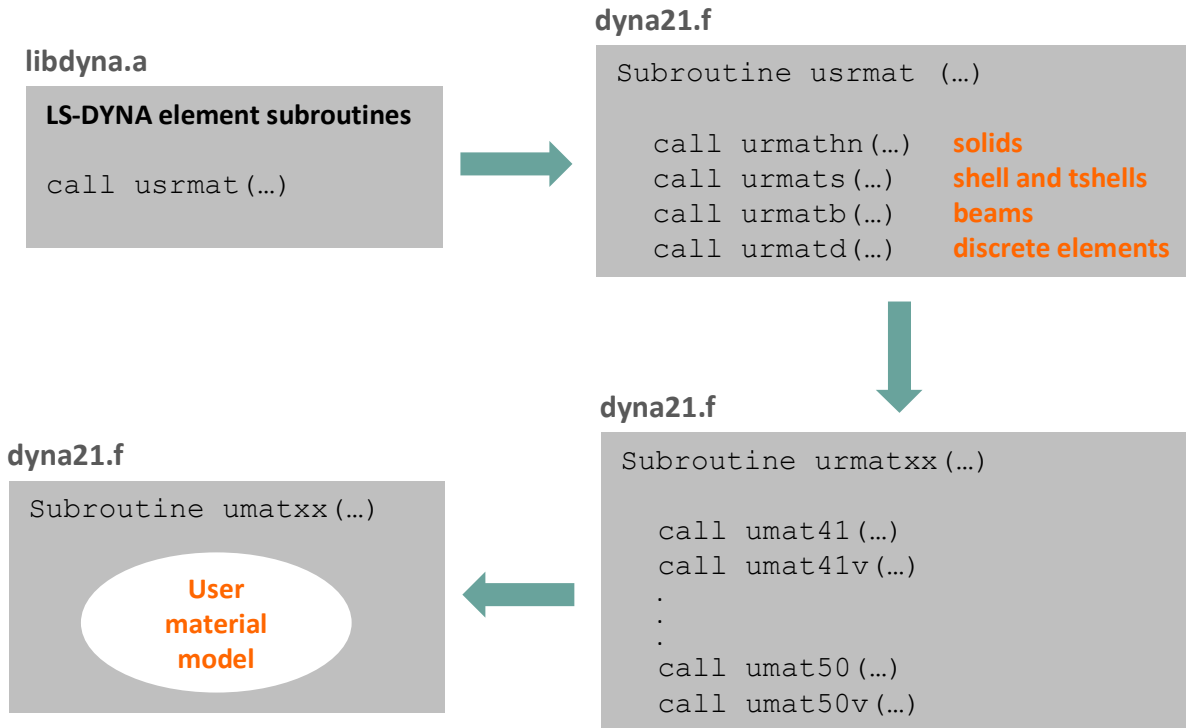


Figure C.1: Schematic of user defined material in LS-DYNA

C.1 User material subroutines

The input arguments to a user material subroutine are material constants defined by `*MAT_USER_DEFINED_MATERIAL_MODELS` in the input file as well as the strain increments, old stresses, old history variables containing user-defined quantities, current time and step size, and others. The output variables are the new (Cauchy) stresses and the updated history values. In the `umatXX` subroutines, which will be modified by the user, the following data structures are initialized for *scalar-type* material subroutines.

sig(6) - stresses in previous time step
eps(6) - strain increments
epsp - effective plastic strain in previous time step
hsv(*) - history variables in previous time step excluding plastic strain
dt1 - current time step size
tt - current time
temper - current temperature
failel - flag indicating failure of element

In the vectorized version of the user-material routines indicated by `umatXXv`, variables are in general stored in vector blocks of length `nlq`, with vector indexes ranging from `lft` to `llt`, which allows for a more efficient execution of the material routine. If this type of user-material subroutine is used, the *vectorization* flag must be set to one (`IVECT=1`) on the material card. CODAM2 material model is also written in this type of subroutine. The data structures for the vectorized subroutine case will be:

sigX(nlq) - stresses in previous time step
dX(nlq) - strain increments
epsps(nlq) - effective plastic strains in previous time step
hsvs(nlq,*) - history variables in previous time step
dtlsiz(nlq) - current time step sizes
tt - current time
temps(nlq) - current temperatures
failels(nlq) - flags indicating failure of elements

where `X` in `sigX` ranges from 1 to 6 for different components. Each entry in a vector block is associated with an element in the finite element mesh for a fix integration point. The number of entries in the history variables array (indicated by `*` in the above) matches the number of history

variables requested on the material card indicated by (NHV). All history variables, are initially zero.

Furthermore, all user-defined material models require a bulk modulus and shear modulus for time step calculations. In addition to the variables mentioned above, the following data can be supplied to the user material routines, regardless of whether vectorization is used or not.

`cm (*)` - material constants array

`crv(lq1, 2, *)` - array representation of curves defined in the keyword deck

The length of material constants array must be specified on the material card (LMC).

A specific material routine, `umatXX` in the scalar case or `umatXXv` in the vectorized case, is now called with any necessary parameters of the ones above, and possibly others as well.

This subroutine is written by the user, and should update the stresses and history variables for the current time. To be able to write different stress updates for different element types, the following character string is passed to the user-defined subroutine:

`etype`- character string that equals `solid`, `shell`, `tshel`, `beam`, `dbeam` or `tbeam`

CODAM2 user material model is coded in vectorized user material subroutine called `umat45v` for which the material input card `*MAT_USER_DEFINED_MATERIAL_MODELS` and the input parameters that will be stored in material array `cm (*)` are described in the APPENDIX D. The list of useful history variables that can be output for visualization is also listed in APPENDIX E. The Pseudo code for the material model is provided in APPENDIX F.

C.2 Load curves in user material subroutines

If the material of interest should require load curves, as in CODAM2 material model for instance, where a curve defines undamaged part of the in-plane shear stress as a function of shear strain, the variable `crv` should be used in the user material subroutine. The curve defined in the keyword deck is represented by points (x_i, y_i) , $i=1, \dots, lq1-1$, stored in the array `crv`

together with a number defining the increments Δx stored in position $lq1$. To be more precise, the first x value is stored in `crv(1,1,*)`, the first y value in `crv(1,2,*)`, the second x value in `crv(2,1,*)`, the second y value in `crv(2,2,*)`, and so on. The increment Δx is stored in `crv(lq1,1,*)`. The third index in the `crv` array represents the internal load curve `id`. This is an approximate representation of a curve in the input deck, where the abscissa range is split into $lq1 - 2$ equidistant intervals and the ordinate values are stored for the $lq1 - 1$ points. Therefore, using this approach may result in loss of the resolution. In order to improve the accuracy, on `*CONTROL_SOLUTION` card the variable `LCINT=lq1-1` can be increased.

The following few lines of code in Fortran file `dyn21.f` has to be used in Fortran code to extract the ordinate value y at the abscissa x for a curve defined by `*DEFINE_LOAD_CURVE` with external curve `id` given by `crvid_ext`.

```

integer crvid_int

$ obtain internal curve id

crvid_int=lcmds(nint(crvid_ext))

$ proceed if curve id is valid

if (crvid_int.gt.0) then

$ obtain increment in x and first x value

xinc=crv(lq1,1,crvid_int)
xbgn=crv(1,1,crvid_int)

$ find interval in which x is situated

ind=aint((x-xbgn)/xinc)+1
ind=min(ind,lq1)
ind=max(ind,1)

$ find slope of that particular segment

slope=(crv(ind+1,2,crvid_int)-crv(ind,2,crvid_int))/
      (crv(ind+1,1,crvid_int)-crv(ind,1,crvid_int))

$ evaluate ordinate value y

```

```
y=crv(ind,2,crvid_int)+slope*(x-crv(ind,1,crvid_int))  
endif
```

Appendix D - Material card for the enhanced CODAM2 user material model

The corresponding material input deck for the enhanced CODAM2 user material model in LS-DYNA is presented in Table D-1. Note that by using the appropriate flags, one can use this material model the same way as MAT219 (i.e. the original formulation of CODAM2 in LS-DYNA) by inputting the relevant parameters. All the material input constants are defined in Table D-2.

Table D-1: *MAT_USER_DEFINED_MATERIAL_MODELS_CODAM2

User	mid	ro	mt	lmc	nhv	iortho	ibulk	ig
Material specs	ivect	ifail	itherm	ihyper	ieos	lmca	unused	unused
Material coords	aopt	mafc	xp	yp	zp	a1	a2	a3
	v1	v2	v3	d1	d2	d3	beta	ievt
Model parameters	E1	E2	G12	V12	V23	nLayers	E3	G23
	Angle 1	Angle 2	Angle 3	Angle 4	Angle 5	Angle 6	Angle 7	Angle 8
	Init MatT	InitFibT	unused	unused	SatMatT	SatFibT	unused	unused
	Init MatC	InitFibC	Alpha1	Alpha2	SatMatC	SatFibC	unused	ShearCurveId
	ErosionFlag	unused	EquivStrFlag	ShearRedFlag	BMod	GMod	unused	unused
	SL	ERParamT	ERParamC	unused	unused	unused	unused	unused

Table D-2: Definition of material constants in the enhanced user material model of CODAM2

Parameter	Description
mid	The <i>id</i> of the material that will be referred to by *part keyword
ro	The material density
mt	The id that specifies the user material subroutine number in Fortran file dyna21.f. It must be set to 45 for CODAM2 which is written in subroutine umat45v
lmc	The maximum number of material constants to be input. Set it to 40.
nhv	Maximum number of history variables to be stored. Set it to 170 (see Remark 1).
iortho	Orthotropic flag (for CODAM2 must be set to 1) : EQ. 0: non orthotropic material EQ. 1: orthotropic material
ibulk	Address of bulk modulus in material constants array in subroutine umat45v. Set it to 36.
ig	Address of shear modulus in material constants array in subroutine umat45v. Set it to 37.
ivect	Vectorization flag (for CODAM2 must be set to 1) EQ. 0: off EQ. 1: on
ifail	Deletion flag (the default for CODAM2 is 0): EQ. 0: No element deletion EQ. 1: Allows element deletion when the first integration point through the thickness of element is identified for erosion based on the ErosionFlag. If ErosionFlag is 0, there will be no element deletion even if ifail=1.. LT. 0: If set to a negative number, its absolute value is the address of NUMINT in the material constant array.

Table D-2: Definition of material constants in the enhanced user material model of CODAM2

Parameter	Description
	NUMINT is the number of failed integration points through the thickness of element that will trigger element deletion. Note that for element deletion, the ErosionFlag has to be non-zero.
Itherm	EQ. 0: If no thermal loading is applied or if the applied thermal loading is handled by using the external *MAT_ADD_THERMAL_EXPANSION (see Remark 2) EQ. 1: CODAM2 itself will handle the thermal loading. For this case, the coefficients of thermal expansion for the material directions 1, 2 has to be given (see Remark 2)
ihyper	Not applicable to CODAM2. Set it to 0.
ieos	Not applicable to CODAM2. Set it to 0.
lmca	Set it to 8 for the extra material constants required for this material model
Aopt mafc xp, yp, zp a1, a2, a3 v1, v2, v3 d1, d2, d3 beta ievt	A coordinate system defined for the part that is assigned by CODAM2. See LS-DYNA manual for different options to define this coordinate system. Note that the direction of fibres for each ply has to be given with respect to first axis of this coordinate system.
E1	The elastic modulus in the fibre direction (i.e. material direction 1)
E2	The elastic modulus transverse to fibre direction (i.e. material direction 2)
E3	The elastic modulus in direction 3. (If set to zero, it will be equal to E_2)
G12	The in-plane shear modulus in 1-2 plane (if nonlinear shear is used, G12 would be the initial modulus)
G23	The shear modulus in 2-3 plane. (If set to zero, it will be equal to $E_2/2(1+\nu_{23})$)
V12	Major Poisson's ratio in 1-2 plane. For transversely isotropic material ν_{13} will be equal to ν_{12} .
V23	Poisson's ratio in 2-3 plane.
nLayers	Number of dissimilar plies in the sub-laminate. If each ply is modelled by one element, nLayers would be 1.
Angle1, ..., Angle 8	The angle of fibres in each ply with respect to the first axis of the coordinate system defined by Aopt option.
Alpha1	Thermal expansion coefficient in direction 1
Alpha2	Thermal expansion coefficient in direction 2 and 3
EquivStrFlag	Equivalent strain formulation: EQ. 1: The equivalent strains for fibre and matrix damage modes are calculated based on Equations (3.4) and (3.5) for a sub-laminate approach (this will be exactly similar to MAT219) EQ. 8: The equivalent strains for fibre and matrix damage modes are calculated based on Equations (3.18) and (3.19) which also accounts for the case where there is nonlinear in-plane shear behaviour.
ShearRedFlag	Shear modulus reduction factor: EQ. 1: $R_{12} = R_1 R_2$ EQ. 2: $R_{12} = R_2$ (this is similar to the formulation of MAT219).
InitMatT	If EquivStrFlag =1: The initiation value for matrix equivalent strain in tension If EquivStrFlag =8: The transverse strength in tension
InitMatC	If EquivStrFlag =1: The initiation value for matrix equivalent strain in compression If EquivStrFlag =1: The transverse strength in compression
InitFibT	If EquivStrFlag =1: The initiation value for fibre equivalent strain in tension If EquivStrFlag =8: The fibre strength in tension
InitFibC	If EquivStrFlag =1: The initiation value for fibre equivalent strain in compression If EquivStrFlag =8: The fibre strength in compression
SatMatT	If EquivStrFlag =1: The saturation value for matrix equivalent strain in tension

Table D-2: Definition of material constants in the enhanced user material model of CODAM2

Parameter	Description
	If EquivStrFlag =8: The fracture energy density for matrix damage g_2^f
SatMatC	If EquivStrFlag =1: The saturation value for matrix equivalent strain in compression If EquivStrFlag =8: The fracture energy density for matrix damage g_2^f
SatFibT	If EquivStrFlag =1: The saturation value for matrix equivalent strain in compression If EquivStrFlag =8: The fracture energy density for fibre damage g_1^f
SatFibC	If EquivStrFlag =1: The saturation value for matrix equivalent strain in compression If EquivStrFlag =8: The fracture energy density for fibre damage g_1^f
ShearCurvEld	EQ.0. : The in-plane shear behaviour is linearly elastic GT.0. : The id for the nonlinear shear stress-strain curve defined by *define_curve.
SL	EQ.0. : if EquivStrFlag =1 GT.0. : if EquivStrFlag =8, this will be the maximum shear strength.
BMod	The bulk modulus of the material for calculation of time step size and hourglass stiffness (see Remark 3)
GMod	The shear modulus of the material for calculation of time step size and hourglass stiffness (see Remark 3)
ErosionFlag	Erosion Flag (see Remark 4) EQ.0: Erosion is turned off. EQ.1: Non-local strain based erosion criterion. EQ.2: Local strain based erosion criterion. EQ.3: Use both 1 and 2 criteria
ERParamT	Erosion parameter in tension (see Remark 4)
ERParamC	Erosion parameter in compression (see Remark 4)

Remark 1:

History variables for CODAM2 are enumerated in Table E-1 in Appendix E. In order to include them in the d3plot database results, the parameters NEIPH (bricks) or NEIPS (shells) on *DATABASE_EXTENT_BINARY has to be set to the desired number of history variables. The maximum number of history variables that can be visualized depends on the number of plies specified in the material input card.

Remark 2:

In order to take into account the residual stresses produced by the temperature change from the cure temperature of composite laminate to room temperature, a thermal load using *LOAD_THERMAL_LOAD_CURVE needs to be defined. The thermal loading should be applied before the mechanical loading. The birth time for the mechanical loading must be bigger than the time where the temperature reaches from zero to the cure temperature decrease.

Along with the temperature load curve, the thermal expansion coefficients in the local direction of material should be specified using the `*MAT_ADD_THERMAL_EXPANSION` which takes the part id of the composite parts and thermal coefficients α_1 , α_2 and α_3 . In this approach, the solver will deduce the thermal strains from the total strains and the remainder will be passed to the user material model to calculate the stress.

Another approach is to specify the thermal expansion coefficients $\alpha_1, \alpha_2, \alpha_3 = \alpha_2$ directly within the CODAM2 user material card instead of using `*MAT_ADD_THERMAL_EXPANSION`. By doing this, the thermal strains in 1, 2 and 3 direction for each ply will be calculated ($\varepsilon_1^T = \alpha_1 \Delta T$, $\varepsilon_2^T = \alpha_2 \Delta T$, $\varepsilon_3^T = \alpha_3 \Delta T$) and subtracted from the total strain to obtain the mechanical strains which will then be used for the mechanical stress calculations. In this case, the `itherm` flag needs to be set to 1 in the user material card.

Remark 3:

The bulk modulus and the shear modulus of material are required by the finite element solver to compute the time step size. Moreover, they will be used if a stiffness-based hourglass control is used for the under integrated elements. It is suggested that:

$$\begin{aligned} \text{BMOD} &= \max(C_{11}, C_{22}, C_{12}) \\ \text{GMOD} &= \max(C_{44}, C_{55}, C_{66}) \end{aligned} \tag{0.1}$$

where C_{11} , C_{22} and C_{12} are the elastic in-plane stiffness components of a unidirectional lamina with the elastic material properties defined in the input card, and C_{44} , C_{55} and C_{66} are three elastic shear stiffness components.

Remark 4:

When `ErosionFlag` > 0, an erosion criterion is checked at each integration point. Elements will be deleted when the erosion criterion is met at any of the integration points if “ifail” in card 2 is set to 1. If “ifail” is set to a negative value, its absolute value specifies the address of

NUMINT in the material constant array. NUMINT is defined as the number of failed integration points through the thickness of element that will trigger element deletion. For example if “ifail” is set to “-42” and the value of the first material constant in card 10 (i.e. 42nd material constant) is set to 3, the element will be deleted only if 3 integration points are failed.

For ErosionFlag= 1, the erosion criterion is met when maximum principal strain exceeds either ERParamT for elements in tension or ERParamC for elements in compression. Elements are in tension when the magnitude of the first principal strain is greater than the magnitude of the third principal strain and in compression when the third principal strain is larger.

When ErosionFlag= 1 and the *Mat_Non-local is also used, the erosion criterion is checked using the non-local (averaged) principal strain.

For ErosionFlag = 2, the erosion criterion is met when the local (non-averaged) maximum principal strain exceeds ERParamT or ERParamC.

For ErosionFlag= 3, both of these erosion criteria are checked.

Appendix E - Post-processing a user-defined material

In order to post process those variable that are defined and saved as history variables in the user material model, the user need to request for those variables to be written in the binary d3plot database that contains all the other results. The number of history variables written to the d3plot database must be requested using the parameters NEIPH (for bricks) and/or NEIPS (for shells) on *DATABASE_EXTENT_BINARY. For instance, if NEIPH (NEIPS) is set to 2, the first two history variables in the history variables array are available for visualization as history var#1 and history var#2 in the d3plot database. By putting NEIPH (NEIPS) equal to NHV, all history variables are written to the d3plot database.

The history variables can be visualized at each individual integration points through the thickness of element or as the average of all those integration points. The history variables that contain the global strains are recorded with respect to the local coordinate axis defined by AOPT in the material input card.

The strain and stress components in the fibre and transverse to fibre directions for each integration point can also be visualized using the corresponding history variables as shown in Table E-1.

Table E-1: History variables for the enhanced CODAM2 model

The history variable	The quantities
Hsvs(2:7)	<p>strains with respect to coordinate system (x,y,z) defined by AOPT in material keyword</p> <p>Hsvs(2): ϵ_{xx}</p> <p>Hsvs(3): ϵ_{yy}</p> <p>Hsvs(4): ϵ_{zz}</p> <p>Hsvs(5): γ_{xy}</p>

Table E-1: History variables for the enhanced CODAM2 model

The history variable	The quantities
	<p>Hsvs(6): γ_{yz}</p> <p>Hsvs(7): γ_{zx}</p>
Hsvs(8:9)	<p>Maximum and minimum principal strains</p> <p>Hsvs(8): ε_{\max}^{prn}</p> <p>Hsvs(9): ε_{\min}^{prn}</p>
Hsvs(10:2n+9)	<p>The damage parameters for fibre and matrix in each layer of the sub-laminate</p> <p>Hsvs(9+(2j-1)): ω_1 - fibre damage in <i>j</i>th layer</p> <p>Hsvs(9+(2j)): ω_2 - matrix damage in <i>j</i>th layer</p>
Hsvs(2n+12: 4n+11)	<p>The non-local averaged equivalent strains used for calculation of fibre and matrix damage.</p> <p>Hsvs(2n+11+(2j-1)): $\bar{\varepsilon}_1^{eq}$ for <i>j</i>th layer</p> <p>Hsvs(2n+11+(2j)): $\bar{\varepsilon}_2^{eq}$ for <i>j</i>th layer</p>
Hsvs(4n+12: 6n+11)	<p>The strains in the fibre and transverse direction of each layer calculated by rotating the strains to the local coordinate of that layer.</p> <p>Hsvs(4n+11+(2j-1)): ε_{11} strain in fibre direction for <i>j</i>th layer</p> <p>Hsvs(4n+11+(2j)): ε_{22} strain in transverse direction for <i>j</i>th layer</p>

Table E-1: History variables for the enhanced CODAM2 model

The history variable	The quantities
hsvs(15n +21:17n+20)	The stresses in the fibre and transverse direction of each layer calculated by rotating the strains to the local coordinate of that layer. Hsvs(15n+20+(2j-1)): σ_{11} stress in fibre direction for <i>j</i> th layer Hsvs(15n+20+(2j)): σ_{22} stress in transverse direction for <i>j</i> th layer
n : number of layers specified in Mat keyword (j=1 ... n)	

Appendix F - Pseudo-code

The following sections present the algorithm that is implemented in the User Material Models of CODAM2 in LS-DYNA for shell and Thick shell element formulations.

1. **Loop** over the integration points (*i*)
2. **Initialize** the current strains with the previous time step's values, $[\boldsymbol{\varepsilon}^{n-1}]_{x,y,z}$, that were saved by history variables: $[\boldsymbol{\varepsilon}^n]_{x,y,z} = [\boldsymbol{\varepsilon}^{n-1}]_{x,y,z}$
3. **Read** the current strain rates, $[\Delta\boldsymbol{\varepsilon}^n]_{x,y,z}$, and add them to the strains from previous time step: $[\boldsymbol{\varepsilon}^n]_{x,y,z} = [\boldsymbol{\varepsilon}^{n-1}]_{x,y,z} + [\Delta\boldsymbol{\varepsilon}^n]_{x,y,z}$. **Save** the current $[\boldsymbol{\varepsilon}^n]_{x,y,z}$ into history variables. From now on the superscript n will be omitted for more clarity in notations.
4. **Initialize** the current stress values for the laminate with zero $[\boldsymbol{\sigma}]_{x,y,z}^{Tot} = 0$
5. **Call** PrincipalStrains subroutine and pass $[\boldsymbol{\varepsilon}]_{x,y,z}$ to **get** the principal strains $[\boldsymbol{\varepsilon}^{prn}]_{x,y,z}$ and **specify** the maximum and minimum principal strains ε_{\max}^{prn} , ε_{\min}^{prn} .
6. **If** $\varepsilon_{\max}^{prn} > \varepsilon_{\min}^{prn}$ and $\varepsilon_{\max}^{prn} > 0$, the status of stress is identified as tensile and go to **step 7**.
Else the status of stress is identified as compressive and go to **step 8**.
7. **Loop** over the number of layers (*j*).
While *j* is less than the total number of layers *n*
If EquivStrainFlag is 1
Set ε_2^i to InitMatT given by the user-material keyword card.
Set ε_2^s to SatMatT given by the user-material keyword card.
Set ε_1^i to InitFibT given by the user-material keyword card.
Set ε_1^s to SatFibT given by the user-material keyword card.
Else If EquivStrainFlag is 8

Set Y_T to InitMatT given by the user-material keyword card.
 Set g_2^f to SatMatT given by the user-material keyword card.
 Set X_T to InitFibT given by the user-material keyword card.
 Set g_1^f to SatFibT given by the user-material keyword card.

End while.

Go to step 9.

8. **Loop** over the number of layers (j).

While j is less than the total number of layers

If EquivStrainFlag is 1

Set ε_2^i to InitMatC given by the user-material keyword card.
 Set ε_2^s to SatMatC given by the user-material keyword card.
 Set ε_1^i to InitFibC given by the user-material keyword card.
 Set ε_1^s to SatFibC given by the user-material keyword card.

Else If EquivStrainFlag is 8

Set Y_C to InitMatT given by the user-material keyword card.
 Set g_2^f to SatMatT given by the user-material keyword card.
 Set X_C to InitFibT given by the user-material keyword card.
 Set g_1^f to SatFibT given by the user-material keyword card.

End while.

Go to step 9.

9. **Start Loop** over the number of layers (j)

10. **Call** rotateStrain and pass $[\varepsilon]_{x,y,z}$ to **get** $[\varepsilon]_{1,2,3}$ in local direction of the ply with angle θ :

$$[\varepsilon]_{1,2,3} = [\mathbf{T}]_{\theta} [\varepsilon]_{x,y,z}$$

11. **Subtract** the thermal strains from the total strains to get the mechanical strains in the three directions 1,2 and 3 .Only if the *itherm* in user-material card is set to 1, the temperature part has non-zero value.

$$(\varepsilon_{ii})_{mech} = \varepsilon_{ii} - \alpha_i \Delta T, \quad i = 1, 2, 3 \quad (\text{The subscript } mech \text{ will be suppressed in the following.})$$

12. **Save** ε_{11} and ε_{22} in the fibre and in-plane transverse directions into history variables for visualization.

13. **Save** the maximum in-plane shear strain that has been experienced up to time t^n :

$$\mathbf{If} \left| \gamma_{12}(t^n) \right| > \left| \gamma_{12}(t^{n-1}) \right|$$

$$\gamma_{12}^{\max}(t^n) = \left| \gamma_{12}(t^n) \right|$$

Else

$$\gamma_{12}^{\max}(t^n) = \gamma_{12}^{\max}(t^{n-1})$$

End

14. **Call** subroutine `localStress` and pass $[\boldsymbol{\varepsilon}]_{1,2,3}$, γ_{12}^{\max} , the element type and **get** the undamaged effective stresses of the ply.

For Shell elements:

$$\begin{bmatrix} \sigma_{11} \\ \sigma_{22} \\ \tau_{12} \end{bmatrix} = \frac{1}{D} \begin{bmatrix} E_1 & \nu_{12}E_2 & 0 \\ \nu_{12}E_2 & E_2 & 0 \\ 0 & 0 & DG_{12}(\gamma_{12}) \end{bmatrix} \begin{bmatrix} \varepsilon_{11} \\ \varepsilon_{22} \\ \gamma_{12} \end{bmatrix}$$

$$D = 1 - \nu_{12}\nu_{21}$$

For Thick shell elements:

$$\begin{bmatrix} \sigma_{11} \\ \sigma_{22} \\ \sigma_{33} \\ \tau_{12} \\ \tau_{23} \\ \tau_{13} \end{bmatrix} = \frac{1}{D} \begin{bmatrix} (1 - \nu_{23}\nu_{32})E_1 & (\nu_{21} + \nu_{23}\nu_{31})E_1 & (\nu_{31} + \nu_{21}\nu_{32})E_1 & 0 & 0 & 0 \\ & (1 - \nu_{31}\nu_{13})E_2 & (\nu_{32} + \nu_{31}\nu_{12})E_2 & 0 & 0 & 0 \\ & & (1 - \nu_{21}\nu_{12})E_3 & 0 & 0 & 0 \\ & & & DG_{12}(\gamma_{12}) & 0 & 0 \\ & & & & DG_{23} & 0 \\ & sym. & & & & DG_{13} \end{bmatrix} \begin{bmatrix} \varepsilon_{11} \\ \varepsilon_{22} \\ \varepsilon_{33} \\ \gamma_{12} \\ \gamma_{23} \\ \gamma_{13} \end{bmatrix}$$

$$D = 1 - \nu_{23}\nu_{32} - \nu_{12}\nu_{21} - 2\nu_{31}\nu_{12}\nu_{23} - \nu_{31}\nu_{13}$$

15. **Calculate** the elastic in-plane shear strain:

$$\gamma_{12}^e = \gamma_{12} - \gamma_{12}^p$$

16. **Initialize** the damage parameters for fibre and matrix damage (i.e. ω_1 , ω_2) with their values from previous time step that had been saved into history variables:

$$\omega_1 = (\omega_1)^{n-1}$$

$$\omega_2 = (\omega_2)^{n-1}$$

17. **Set** the non-local equivalent strain functions $\bar{\varepsilon}_2^{eq}$ and $\bar{\varepsilon}_1^{eq}$ to the corresponding history variables that contain the averaged equivalent strains from the previous time step. The averaging is done by LSDYNA using a Gaussian weight function.

$$\bar{\varepsilon}_2^{eq} = \left(\bar{\varepsilon}_2^{eq} \right)^{n-1}$$

$$\bar{\varepsilon}_1^{eq} = \left(\bar{\varepsilon}_1^{eq} \right)^{n-1}$$

18. **Calculate** the current local equivalent strain functions.

$$\varepsilon_1^{eq} = |\varepsilon_{11}|$$

$$\varepsilon_2^{eq} = \sqrt{(\varepsilon_{22})^2 + (\gamma_{12}^e)^2}$$

19. **Save** the current local equivalent strains into history variables that will be passed to LSYNA for averaging. The averaging can be done only when stress state of all the integration points in the model is updated. Those history variables will then be used in **step 17** as the non-local equivalent strain for the next time step.

20. **If** EquivStrainFlag is 1, the parameters for calculation of damage including $\varepsilon_2^i, \varepsilon_2^s, \varepsilon_1^i$ and ε_1^s are already saved in **steps 8** and **9**. **Go to step 24**.

21. **Else if** EquivStrainFlag is 8, **calculate** F_1 and F_2 as follows.

$$F_1 = \left(\frac{\hat{\sigma}_{11}}{X_T} \right)^2 \text{ for tension}$$

$$F_1 = \left(\frac{\hat{\sigma}_{11}}{X_C} \right)^2 \text{ for compression}$$

$$F_2 = \left(\frac{\hat{\sigma}_{22}}{Y_T} \right)^2 + \left(\frac{\hat{\tau}_{12}}{S_L} \right)^2 \text{ for tension}$$

$$F_2 = \left(\frac{\hat{\sigma}_{22}}{2S_T} \right)^2 + \left[\left(\frac{Y_C}{2S_T} \right)^2 - 1 \right] \frac{\hat{\sigma}_{22}}{Y_C} + \left(\frac{\hat{\tau}_{12}}{S_L} \right)^2 \text{ for compression}$$

22. **If** $F_1 \geq 1$ and $\varepsilon_1^i = 0$ **then**

Fibre damage will be initiated in this time step. **Obtain** the initiation value of equivalent strain for fibre damage using the current strain components.

$$\varepsilon_1^i = \bar{\varepsilon}_1^{eq}$$

$$\varepsilon_1^s = \frac{2g_1^f}{X}$$

Else

Fibre damage has not initiated yet.

$$\varepsilon_1^i = 0$$

End if

23. **If** $F_2 \geq 1$ **and** $\varepsilon_2^i = 0$ **then**

Matrix damage will be initiated in this time step. **Obtain** the initiation and saturation value of equivalent strain for matrix damage using the current strain components.

$$\varepsilon_2^i = \bar{\varepsilon}_2^{eq}$$

$$T = \frac{(\hat{\sigma}_{22}\varepsilon_{22} + \hat{\tau}_{12}\gamma_{12}^e)}{\sqrt{(\varepsilon_{22})^2 + (\gamma_{12}^e)^2}}$$

$$\varepsilon_2^s = \frac{2g_2^f}{T}$$

Else

Matrix damage has not initiated yet.

$$\varepsilon_2^i = 0$$

End if

24. **If** $\bar{\varepsilon}_1^{eq} > \varepsilon_1^i$ **and** $\varepsilon_1^i > 0$ **then**

Calculate a temporary damage parameter

$$\tilde{\omega}_1 = \frac{\bar{\varepsilon}_1^{eq} - \varepsilon_1^i}{\varepsilon_1^s - \varepsilon_1^i} \frac{\varepsilon_1^s}{\bar{\varepsilon}_1^{eq}}$$

Else

$$\tilde{\omega}_1 = 0.$$

End

If $\tilde{\omega}_1 \geq 1$, **then** $\tilde{\omega}_1 = 1$ **End**

If $\omega_1 > \tilde{\omega}_1$ **then**

$\omega_1 = \tilde{\omega}_1$ and save ω_1 into its corresponding history variable to be passed to next time step.

End If

25. **If** $\bar{\varepsilon}_2^{eq} > \varepsilon_2^i$ and $\varepsilon_2^i > 0$ **then**

Calculate a temporary damage parameter,

$$\tilde{\omega}_2 = \frac{\bar{\varepsilon}_2^{eq} - \varepsilon_2^i}{\varepsilon_2^s - \varepsilon_2^i} \frac{\varepsilon_2^s}{\bar{\varepsilon}_2^{eq}}.$$

Else

$$\tilde{\omega}_2 = 0.$$

End

If $\tilde{\omega}_2 \geq 1$, **then** $\tilde{\omega}_2 = 1$ **End**

If $\omega_2 > \tilde{\omega}_2$ **then**

$\omega_2 = \tilde{\omega}_2$ and save ω_2 into its corresponding history variable to be passed to next time step.

End If

26. **Calculate** the stiffness reduction coefficients

$$R_2 = 1 - \omega_2$$

$$R_1 = 1 - \omega_1$$

$$R_{12} = R_2 R_1$$

27. **Call** subroutine `localStress` and pass $[\varepsilon]_{1,2,3}$, γ_{12}^{\max} , R_2 , R_1 , R_{12} and the element type and get the stresses of the damaged ply.

For Shell elements:

$$\begin{bmatrix} \sigma_{11} \\ \sigma_{22} \\ \tau_{12} \end{bmatrix} = \begin{bmatrix} \frac{R_1 E_1}{1 - R_1 R_2 \nu_{12} \nu_{21}} & \frac{R_1 R_2 \nu_{12} E_2}{1 - R_1 R_2 \nu_{12} \nu_{21}} & 0 \\ & \frac{R_2 E_2}{1 - R_1 R_2 \nu_{12} \nu_{21}} & 0 \\ sym & & R_{12} G_{12}(\gamma_{12}) \end{bmatrix} \begin{bmatrix} \varepsilon_{11} \\ \varepsilon_{22} \\ \gamma_{12} \end{bmatrix}^{(k)}$$

For Thick shell elements:

$$\begin{bmatrix} \sigma_{11} \\ \sigma_{22} \\ \sigma_{33} \\ \tau_{12} \\ \tau_{23} \\ \tau_{13} \end{bmatrix} = \frac{1}{D} \begin{bmatrix} (1 - R_2 \nu_{23} \nu_{32}) R_f E_1 & (\nu_{21} + \nu_{23} \nu_{31}) R_1 R_2 E_1 & (\nu_{31} + R_2 \nu_{21} \nu_{32}) R_1 E_1 & 0 & 0 & 0 \\ & (1 - R_1 \nu_{31} \nu_{13}) R_2 E_2 & (\nu_{32} + R_1 \nu_{31} \nu_{12}) R_2 E_2 & 0 & 0 & 0 \\ & & (1 - R_1 R_2 \nu_{21} \nu_{12}) E_3 & 0 & 0 & 0 \\ & & & DR_{12} G_{12} (\gamma_{12}) & 0 & 0 \\ & & & & DG_{23} & 0 \\ & sym. & & & & DG_{13} \end{bmatrix} \begin{bmatrix} \epsilon_{11} \\ \epsilon_{22} \\ \epsilon_{33} \\ \gamma_{12} \\ \gamma_{23} \\ \gamma_{13} \end{bmatrix}$$

$$D = 1 - R_2 \nu_{23} \nu_{32} - R_1 R_2 \nu_{12} \nu_{21} - 2R_1 R_2 \nu_{31} \nu_{12} \nu_{23} - R_1 \nu_{31} \nu_{13}$$

28. **Transform** the damaged stresses of the ply back to the global direction:

$$[\sigma]_{x,y,z} = [T^{-1}][\sigma]_{1,2,3}$$

29. **Divide** the ply stresses by the total number of plies and **add** it to the total stress of the laminate

$$[\sigma]_{x,y,z}^{Tot} = [\sigma]_{x,y,z}^{Tot} + \frac{[\sigma]_{x,y,z}}{nLayer}$$

30. **If** j is less than the number of layers, **go to step 10**. Otherwise, **go to step 31**.

31. **Pass** the total stresses of the laminate, $[\sigma]_{x,y,z}^{Tot}$, to the solver for calculation of nodal force, nodal displacement and strain increments.

32. **Go to step 1**.